ENABLE IRON FLUORIDE CONVERSION ELECTRODE MATERIALS FOR HIGH ENERGY-DENSITY LITHIUM-ION BATTERIES

by

LINSEN LI

A dissertation submitted in partial fulfillment of

the requirements for the degree of

DOCTOR OF PHILOSOPHY

(CHEMISTRY)

at the

UNIVERSITY OF WISCONSIN–MADISON

2015

Date of final oral examination: June 12th, 2015

The dissertation is approved by the following members of the Final Oral Committee:

Song Jin, Professor – Chemistry
Kyoung-Shin Choi, Professor – Chemistry
Shannon Stahl, Professor – Chemistry
Dane Morgan, Professor – Materials Science and Engineering
Paul Evans, Professor – Materials Science and Engineering

PREFACE

ENABLE IRON FLUORIDE CONVERSION ELECTRODE MATERIALS FOR HIGH ENERGY-DENSITY LITHIUM-ION BATTERIES

LINSEN LI, PHD

UNIVERSITY OF WISCONSIN–MADISON

2015

The large-scale deployment of transportation and grid-level energy storage systems depends on scalable and inexpensive energy-storage solutions. Li-ion battery (LIB) is widely considered as the technology of choice to meet the future energy challenge but a substantial increase in energy density is needed. Conversion cathode materials represented by inexpensive iron fluorides (FeF_3 and FeF_2) and their derivatives (such as oxyfluorides, $Fe^{II}_{(1-x)}Fe^{III}_xO_xF_{2-x}$) hold the promise to significantly increase the energy density by enabling multiple Li-ion storage. However, this promise has yet to be realized due to some fundamental challenges commonly observed among all conversion electrode materials, such as fast capacity decay and an unusually large voltage hysteresis. The key to addressing these challenges lies in a better understanding of the electrochemical reaction mechanism, preferentially under *operando* conditions and across multiple length scales (from single particle to entire electrode), and rational designs of battery materials and electrode architecture. To this end, my graduate research has been primarily

focused on the syntheses, electrochemical characterization, and *in situ* mechanistic studies of the FeF_3 conversion cathode materials.

Chapter 1 reviews the promising properties and fundamental challenges facing conversion electrode materials, and our endeavors in understanding and addressing those challenges by using FeF_3 as the model system. First, I discussed the potential of conversion electrode materials to significantly increase the energy density of the LIBs and several fundamental challenges that have been hindering their progress towards practical applications, such as capacity decay and voltage hysteresis. Then I described my multifaceted efforts in understanding the physical origins of the challenges, which include rational syntheses of FeF_3 materials with distinctive microstructure, internal porosity, and morphology, electrochemical characterization, and *in situ* mechanistic studies using synchrotron X-ray techniques and *in situ* transmission electron microscopy (TEM). By holistically evaluating the experimental results and the density functional theory simulations (DFT) done by our collaborators, I was able to reveal a complete and consistent reaction mechanism for the FeF_3 conversion electrode, which is basically symmetrical during discharge and charge but strongly influenced by reaction kinetics. Further, I showed that both capacity decay and voltage hysteresis are problems that are kinetic in nature, which in principle can be mitigated by optimizing material transport properties and rationally designing the electrode architecture. Finally, in light of the mechanistic understanding, I discussed promising strategies to improve the performance of conversion electrode materials for high energy-density LIBs.

In Chapter 2, I reported the inexpensive and scalable synthesis of FeF_3 nanowires (NWs) and investigation of their application as a high-capacity LIB cathode. The FeF_3 NW cathode yielded a discharge capacity as high as 543 mAh g^{-1} at the first cycle and retained a capacity of 223 mAh g^{-1} after 50 cycles at room temperature under the current of 50 mA g^{-1}. Moreover, high-resolution TEM revealed the existence of continuous networks of Fe in the lithiated FeF_3 NWs, which provides electron transport pathway within the solid material and proved important to the excellent electrochemical performance of the FeF_3 NW electrode. The loss of active material (FeF_3) caused by the increasingly ineffective reconversion process during charging was found to be a major factor responsible for the capacity loss upon cycling.

In Chapter 3, I reported the development of an innovated X-ray spectro-imaging technique that can visualize electrochemically-driven phase transformations at the nanoscale and the application of this technique to study the reaction mechanism of the FeF_3 conversion cathode. During the active cycling of two specially designed samples with distinctive microstructure and porosity, I observed concurrent reaction behavior across many particles but significant inhomogeneity at the single-particle level, faster and more complete Li-storage occurring in porous polycrystalline FeF_3, and incomplete charge reaction following a pathway different from conventional belief. These results reveal that the electrochemical reactions of the FeF_3 conversion electrode are strongly influenced by reaction kinetics. Further, the different pathway observed during charge shakes foundation of the traditionally believed model for explaining the large voltage hysteresis.

Chapter 4 covers in-depth mechanistic studies, primarily focused on understanding the origin of the large voltage hysteresis. In this chapter, I used *in situ* synchrotron X-ray absorption

spectroscopy (XAS) to track changes in Fe oxidation states and local bonding structure during cycling of three iron fluoride model samples, FeF_2 nanowires, FeF_3 NWs, and FeF_3 microwires (MWs). Combining results from *in situ* TEM experiments and hybrid functional DFT calculations (HSE06), I showed that the reaction pathway of the FeF_3 cathode is basically symmetrical and as follows: rhombohedral FeF_3 $\rightarrow$ trirutile $Li_{0.25}FeF_3$ $\rightarrow$ trirutile $Li_{0.5}FeF_3$ $\rightleftarrows$ rutile FeF_2 + LiF $\rightleftarrows$ Fe + 3LiF. I also found that reaction homogeneity (completeness and spatial distribution of each electrochemical reaction) is strongly influenced by reaction kinetics in these multiple-step reaction processes. Based on the new mechanistic understanding and results from galvanostatic intermittent titration technique (GITT) experiments, I conclude that the large voltage hysteresis observed in the FeF_3 cathode is due to a combination of iR (Ohmic) drop, kinetic overpotentials, and difference in apparent potentials which are result of different spatial distributions of electrochemically relevant phases. These results have general implications for understanding voltage hysteresis in other conversion electrode materials and suggest new strategies to minimize its adverse effect.

In Chapter 5, I reported the synthesis and electrochemical characterization of another promising high-capacity conversion cathode material FeS_2 (pyrite), which was prepared in large quantity and high purity *via* thermal sulfidation of the FeF_3 NWs. The pyrite NW electrode exhibited excellent capacity retention when it was cycled in a limited voltage window (thus limited amount of capacity) using a 1 M LiTFSi/TEGDME electrolyte. In order to fully utilize the charge storage capability of pyrite, it is important to minimize the dissolution of active materials. Solid-state batteries may be a promising approach.

The following appendices provide either complementary information to the accomplished work presented in the main chapters or describe my other first-author works that different in research topic and/or in progress. Specifically, Appendix 1, 2, 3, and 4 provide additional experimental details and data pertaining to Chapters 2, 3, 4, and 5, respectively.

Appendix 5 and 6 reported the synthesis and post-growth doping of α-Fe_2O_3 (hematite) NWs and their application in photoelectrochemical water-splitting cells. The hematite NWs were prepared by thermal oxidation of the hydrated FeF_3 NWs.

Appendix 7 describes an on-going work in collaboration with Professor Ming Tang group at Rice University. I developed a synthesis of $LiFePO_4$ microrods that are grown along the <010> direction, where the one-dimensional lithium-ion channels are located. I applied the X-ray spectroimaging technique described in Chapter 3 to study the electrochemical delithiation of the $LiFePO_4$ microrods under *operando* conditions. The results not only provide visual evidence for the anisotropic lithium-ion transport in $LiFePO_4$ but also reveal some interesting phase transformation behaviors that have long been debated.

The body of work reviewed here directly targets at the fundamental challenges facing the conversion electrode materials. We have revealed the reaction mechanism and the physical origins of the voltage hysteresis and capacity decay through integrated theory-experimental studies. The new insights on FeF_3 conversion mechanism point to directions to improve other conversion cathode materials and enable their practical application in high energy-density Li-ion batteries, which will be a great leap forward for electrochemical energy storage technologies. The hard X-ray spectro-imaging technique also provides a unique and powerful approach to

elucidate reaction mechanism and diagnose possible failure modes of other electrode materials and could revolutionize studies of other complex phase transformations that are not electrochemically driven.

ACKNOWLEDGMENTS

First and foremost, I would like to dedicate my sincere gratitude to my father Li Li and my mother Mei Liu. Without your constant love, support, encouragement, and kind understanding in me, I would not have been able to reach where I am today in my life journey. I also appreciate the support from my grandparents, aunts, and uncles, who always care about me and are willing to help me grow up intellectually, mentally, and emotionally.

Second, I would like express my deepest appreciation to my PhD advisor and mentor, Professor Song Jin, perhaps as much as that I have for my parents. He provides exceptional coaching in both work and life. I truly appreciate his support, encouragement, opportunities that he offered and/or opened up for me, and the trust and freedom in exploring my research interest during my graduate studies. I have always been impressed by his passion, knowledge, and judgement for scientific research, dedication to details, and excellent time and emotional management skills and benefited significantly from my interaction with him. It has been an honor working for/with him in the last five years. I am looking forward to an opportunity in academia to apply the knowledge and skills Song taught me.

Third, I would especially like to thank Professor Dane Morgan, Professor Jordi Cabana (UIC/LBNL), Dr. Jun Wang (BNL), and Dr. Feng Wang (BNL), who I have been closely working with. They, along with my advisor Professor Song Jin, opened up many exciting research opportunities for me and essentially shaped me who I am as a scientist. I have learned immeasurable lessons and gained great inspiration on academic research from them.

My thanks also go to my other committee members, Professor Kyoung-Shin Choi, Professor Shannon Stahl, and Professor Paul Evans, for reading the draft of this dissertation and providing many insightful comments that improved the presentation and contents of this dissertation.

It has been great enjoyment to work with all of the members of the Jin Group, past and present. I would especially like to thank Dr. Stephen A. Morin (now a professor in University of Nebraska-Lincoln) and Dr. Fei Meng, who trusted me, mentored me, and constantly challenged me to become better during my graduate school years. I also must thank senior members in the Jin Group, Dr. Jeremy M. Higgins, Dr. John P. Degrave, Dr. Mark A. Lukowski, Dr. Rachel S. Selinsky, Dr. Matthew S. Faber, and Dr. Miguel Cabán-Acevedo, for helping me getting started here, teaching me various lab techniques, having insightful discussion, and having fun camping/drinking/playing fantasy football together. Special thanks to Nicholas Kaiser and Miguel for playing pool with me every Friday. Furthermore, I am grateful to three awesome classmates, Dr. Audrey Forticaux, Dr. Ankit Pokhrel (soon-to-be), and Salih Hacialioglu. I treasured our conversation and discussion in the lab and beyond that, the first/second year "bonding group" and our friendship. Last but not least, I want to express my appreciation to other people in the Jin Group that I have been closely working with, Dr. Yanghai Yu, Dr. Ryan Franking, Dr. Marc Estruga, Dr. Dong Liang, Dr. Steven N. Girard, Dr. Xingwang Zhang, Dr. Hanfeng Liang (soon-to-be), Qi Ding, Lichen Xiu, Yongping Fu, Matthew Stolt, Wenjie Li, and two motivated undergrads, Liyang Gan and Tyler Slade. It has been truly joyful and productive experience working with you, and I have gained much inspiration from our interaction.

Next I would like to acknowledge many colleagues outside of the Jin Group, including Dr. Ryan Jacobs (soon-to-be, MSE at UW-Madison), Dr. Karen Yu-chen Chen-Wiegart, Dr. Jiajun Wang,

Dr. Peng Gao (now a professor at Peking University, China) and Dr. Wei Zhang at Brookhaven National Laboratory, and Dr. Young-Sang Yu at the Lawrence Berkeley National Laboratory. Our collaboration is invaluable experience to me. I have learned so much about density-functional theory (DFT) modeling, transmission X-ray microscopy, and *in situ* transmission electron microscopy from you.

Certainly, I would not make through these five years of graduate school without all the support and encouragement from my friends, both in Madison and elsewhere. Dr. Di Zhu, Dr. Ranran Liu, and Li Ke took care of me in the first four years and we had a lot fun playing cards. I also would like to thank Fei Wang (Fudan University, China), Hao Zeng, Dr. Yan Wang, Dr. Yuxuan Wang, Dr. Zhen Liu, Jia Xu, Xiaomeng Lu, Anqi Wang, and Linghong Zhang for always being supportive and caring to me.

Lastly, I would like to express my sincere appreciates to my fiancée Yingmei (Sophia) Lao. Her vision, encouragement, quiet patience and unwavering love are undeniably the bedrock upon which the past eight years of my life have been built. She has been tremendous source of inspiration for me since we got to know each other at Fudan University in 2007, and will always be.

–Linsen Li

06/05/2015

TABLE OF CONTENTS

APPENDIX 7 INHOMOGENEOUS PHASE TRANSFORMATION DURING THE ELECTROCHEMICAL DELITHIATION OF $LiFePO_4$ MICRORODS

LIST OF FIGURES

LIST OF TABLES

CHAPTER 1

Challenges and Strategies: Conversion Electrode Materials for High Energy-Density Lithium-Ion Batteries

1.1 Introduction

Lithium-ion batteries (LIBs), since their invention in 1991, have achieved tremendous commercial success as power sources for consumer electronics due to their superior energy density, power density, and long cycle-life in comparison with other rechargeable batteries.[1] They are now being considered as promising solution to future large-scale energy challenges, such as electrical vehicle and grid-level energy storage.[1-3] A typical LIB consists of a cathode and an anode separated by a polymer separator and an organic liquid electrolyte containing a lithium salt, which transports charge (Li^+) inside the battery between the cathode and the anode. Current LIBs are predominantly built on intercalation chemistry, which consists of topotactic insertion/removal of Li^+ into/from the host lattice of electrode materials. Representative examples include $LiCoO_2$, $LiMn_2O_4$, $LiFePO_4$, $LiNi_{1/3}Mn_{1/3}Co_{1/3}O_2$ (all are cathodes), and graphite (anode). Intercalation/deintercalation reaction introduces a small volume change to the crystal lattice of electrode materials without causing structural collapse and/or phase segregation, which is the key to good rate capability and long cycle-life. However, the energy density achievable with intercalation (500–600 Wh $kg^{-1}_{active\ material}$) is inherently limited by number of

interstitial sites in the host lattice (typically < 1 per formula).[1] Going beyond current LIB requires the development of energy storage technology based on new electrode materials and/or new chemistries, among which Li−O_2 and Li−sulfur have attracted most of the attention due to their significantly higher theoretical energy density.[4] Important advances have been made for Li−O_2 and Li−sulfur batteries over the past decade, but significant challenges remain to be overcome before they can become practically viable.[4] Meanwhile, we and a few other research groups elected to explore another approach to realizing high energy-density storage, which is based on heterogeneous conversion reaction to reversibly store multiple lithium-ions in transition metal fluorides, sulfides, and oxides.[5-22] During cycling, the electrode is cycled a binary metal fluoride, sulfide, or oxide (charged state) and a nanocomposite made of metal and LiF or Li_2X (X = O or S, discharged state).

$$MF_x + xLi^+ + xe^- = M + xLiF$$

$$M_xX_y + 2yLi^+ + 2ye^- = xM + yLi_2X,\ X = O \text{ or } S$$

The past decade has witnessed tremendous advances in preparation of conversion electrode materials that exhibit high specific energy densities (and power capability), mainly through nanostructuring and/or making nanocomposite with conductive carbon materials.[5] However, further interest from practical applications have been discouraged by several fundamental drawbacks (illustrated in Figure 1), such as the unusually large voltage hysteresis (voltage gap) between discharge and charge steps, large irreversible capacity loss in the 1st cycle, and additional capacities caused by electrolyte decomposition. The voltage hysteresis is most problematic. It typically ranges from several hundred mV to ~2 V,[5] comparable to that of a Li-O_2

battery[4] but much higher than that of a Li-sulfur battery (200–300 mV)[4] or a typical intercalation electrode material (several tens mV) at similar rates.[23] It leads to a high degree of round-trip energy inefficiency that is unacceptable in practical applications.

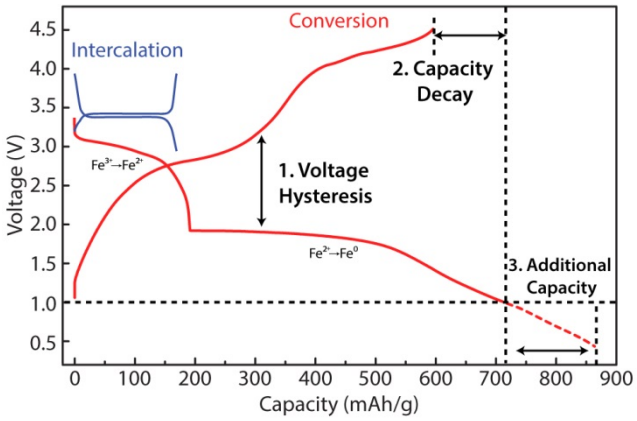

Figure 1.1 | Challenges for Conversion Cathode Materials. The typical voltage profile of an FeF_3 electrode is used for illustrating the challenges. The voltage profile of a $LiFePO_4$ electrode is included for comparison.

The key to addressing these challenges lies in fully understanding the electrochemical conversion/reconversion mechanism. To this end, we elected to perform mechanistic studies using the Fe-based conversion cathode materials as model systems, including FeF_3 (main focus), FeF_2 and FeS_2 (pyrite). These materials can theoretically deliver very large capacities at relatively positive voltages (see **Table 1**),[24] enabling attractive energy densities (>1000 Wh $kg^{-1}_{\text{active material}}$) that are 2–3 times higher than that of the current LIBs based on intercalation chemistry.

Table 1.1 | Li-storage capacities and Electromotive Force (EMF) values for FeF_3, FeF_2, and FeS_2

Materials	Li-Storage Capacity (mAh g^{-1})	Electromotive Force (V)
FeF_3	712	2.742
FeF_2	571	2.664
FeS_2	891	1.861

A systematic approach was taken in our studies. We first designed and developed rational syntheses of iron fluoride materials with different microstructure and internal porosity and comparatively evaluated their electrochemical properties. Then we examined the cycled (lithiated and delithiated) samples by *ex situ* transmission electron microscopy (TEM) to gain preliminary insights into the phase and structural changes during cycling. Further, we tracked changes in Fe oxidation states and local bonding structure during cycling at different length scales using *in situ* hard X-ray spectro-imaging, X-ray absorption near-edge structure spectroscopy (XANES) and extended X-ray absorption fine structure spectroscopy (EXAFS). To corroborate the experimental findings, we performed a detailed multicomponent phase analysis using DFT calculations of materials in the Li-Fe-F ternary system. Complementary information was gleaned from *in situ* TEM and galvanostatic intermittent titration technique (GITT) experiments. By holistically evaluating the results, we confirmed the reaction pathway of the FeF_3 electrode and revealed the origins of voltage hysteresis and capacity loss over cycling.

1.2 Rational Syntheses of Iron Fluorides

Chemical syntheses of FeF_3 as well as other transition metal fluorides are much less explored compared with their oxide or sulfide counterparts due to serious safety concern over the highly corrosive fluorine-containing reagents, such as fluorine gas (F_2), hydrofluoric acid (HF), and ammonium fluoride (NH_4F). Specialized setup is required for a vapor-phase reaction that involves F_2. While a solution synthesis can be done with a plastic reactor, it is quite challenging to combine metal ions and fluorine ions because the corresponding metal oxide/hydroxides are often less soluble than the metal fluoride. As a result, nanostructured FeF_3 samples are more commonly prepared by high-energy ball-milling process.[10, 11, 13] These samples, when mixing with excessive amount of conductive carbon materials, can achieve near theoretical Li-storage capacity at an elevated temperature (70 °C) and a small current density (7.58 mA g^{-1}, ~1/94 C).[10] However, their poor rate capability makes them less favorable as model samples for *in situ* X-ray studies, which are often time-constrained due to limited amount of assigned beam-times.

To address the synthetic challenge and prepare FeF_3 samples with well-defined morphology and improved electrochemical properties, we proposed to perform the solution synthesis in ethanol and control the supersaturation for crystal growth. Ethanol was chosen as the solvent FeF_3 and $FeF_3{\cdot}3H_2O$ are slightly soluble in water (5.92 g/100 g H_2O at 25 °C). HF and iron (III) nitrate nonahydrate [$Fe(NO_3)_3{\cdot}9H_2O$] were used as the fluorine (F^-) and iron (Fe^{3+}) sources, respectively and they were mixed first to make stable FeF_6^{3-} complex ($K_f \approx 1 \times 10^{16}$). In this ethanol-based synthesis, water (H_2O) is also a reactant.

$$FeF_6^{3-} + xH_2O \rightleftarrows FeF_3(H_2O)_x + 3F^- \quad (x = 3,\ 0.33,\ \text{or}\ 0)$$

By adjusting the ratio between Fe^{3+}, F^-, and H_2O, we were able to grow one-dimensional α-$FeF_3 \cdot 3H_2O$ (rhombohedral, $R\bar{3}m$, a = 9.5135 Å, c = 4.7882 Å) wires with tunable diameters (20 nm–2 μm),[16, 19, 25] β-$FeF_3 \cdot 3H_2O$ crystals (tetragonal, $P4/n$, a = 7.846 Å, c = 3.877 Å),[26] FeF_3 polyhedra (cubic, $Fd\bar{3}m$, a = 10.325 Å),[19] and $FeF_3 \cdot 0.33H_2O$ nanoparticles (orthorhombic, $Cmcm$, a = 7.423 Å, b = 12.73 Å, c = 9.526 Å).[26] **Figure 1.2** shows the crystal Structure and morphology of various iron fluoride/fluoride-hydrates. All of these samples can be converted to the thermodynamically stable FeF_3 (rhombohedral $R\bar{3}c$, a = 5.2 Å, c = 13.323 Å) by heating under argon at 350 °C.[16, 19, 26] In particular, the wire samples became porous FeF_3 due to loss of lattice water.

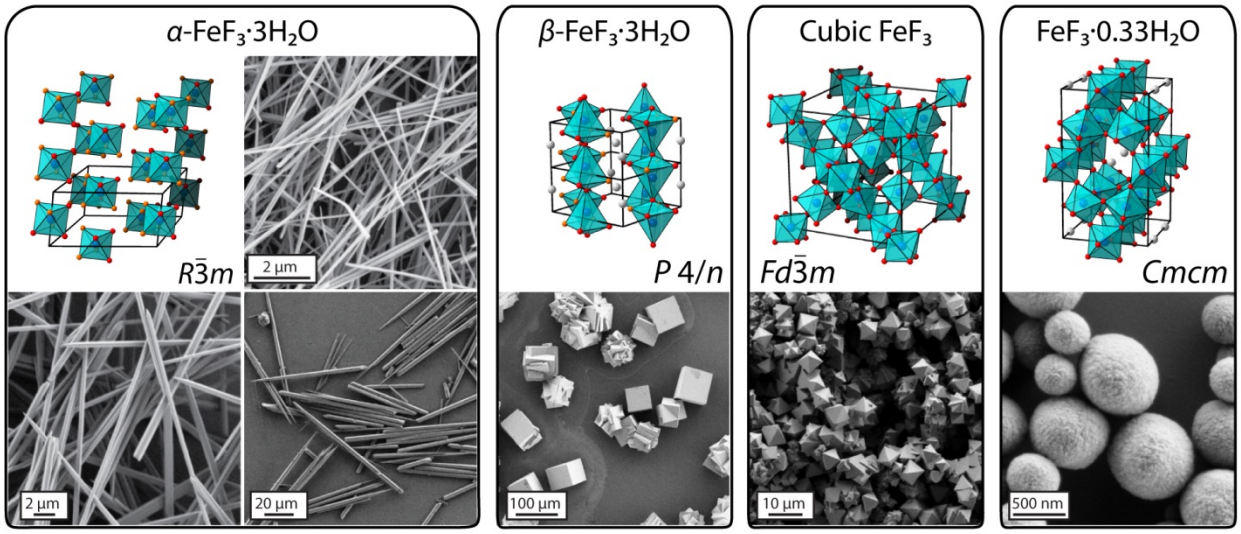

Figure 1.2 | Crystal structure and morphology of various iron fluoride/fluoride-hydrates. Fe, F, O, and crystallization H_2O are represented by blue, red, orange, and silver spheres. H atoms are omitted for brevity.

1.3 Electrochemical Characterization

We evaluated the electrochemical properties of FeF_3 polyhedra, nanowires (NWs), and microwires (MWs) by galvanostatic cycling test at a current of 1/10 C (1 C = 712 mAh g^{-1})[16] and made some interesting observations by comparing the voltage profiles of these three samples during the 1st cycle (**Figure 1.3**). The porous NWs and MWs could both achieve near theoretical Li-storage capacity (712 mAh g^{-1}). However, the MWs lost the sloping plateau at the higher voltage region (>1.7 V). The non-porous polyhedra achieved only ~1/3 of the theoretical capacity and did not show a long and flat voltage plateau which corresponds to the conversion reaction ($Fe^{2+} \rightarrow Fe$). Capacity loss and large voltage hysteresis were observed in all three electrodes.

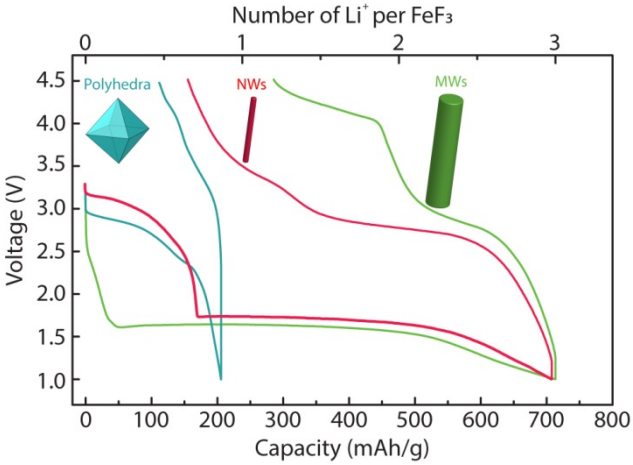

Figure 1.3 | Comparison of 1st cycle electrochemical performance of FeF_3 polyhedra, NWs, and MWs. All three cells were cycled at rate of 1/10 C (71.2 mAh g^{-1}).

We evaluated the long-term performance of the FeF_3 NWs by galvanostatic cycling in the voltage window of 4.5–1.5 V at a current of 50 mA g^{-1} (**Figure 1.4a**). The FeF_3 NWs were found

to exhibit a discharge capacity as high as 543 mAh g^{-1} (relative to the mass of FeF_3 NWs) in the 1st cycle and retained a capacity of 223 mAh g^{-1} after 50 cycles (**Figure 1.4b**), which is larger than the practical capacity of $LiCoO_2$ (~140 mAh g^{-1}). To the best of our knowledge, this is the best performance ever achieved on an FeF_3 electrode in the voltage window of 4.5–1.5 V in terms of capacity and rate capability. However, the fast capacity fading, gradual loss of the high voltage sloping plateau, and large voltage hysteresis (marked by orange arrows **Figure 1.4a**) were still observed. In order to address these fundamental challenges, it is critically important to understand the correlation between the voltage profile and the phase and microstructural changes that occur in the electrode.

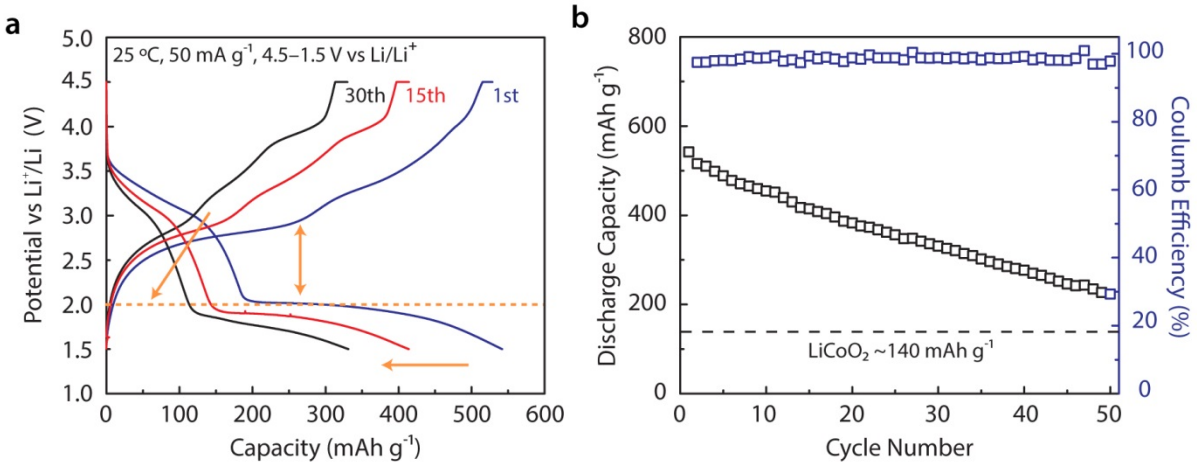

Figure 1.4 | Galvanostatic cycling performance of the FeF_3 NWs. a. Voltage profiles for the 1st, 15th, and 30th discharge-charge cycles of the FeF_3 NW electrode tested under the current of 50 mA g^{-1} (~1/14.3 C) at ~25 °C; Capacity decay, gradual loss of the high-voltage sloping plateau, and voltage hysteresis are indicated by orange arrows. **b.** Discharge capacity and Coulombic efficiency of the FeF_3 NW electrode versus cycle number in comparison with the practical capacity of $LiCoO_2$ (~140 mAh g^{-1});

1.4. *Ex Situ* Mechanistic Studies

To understand the changes that occur to the FeF_3 electrode during cycling, we first examined the morphology of the FeF_3 NWs before and after the galvanostatic cycling test using scanning electron microscopy (SEM, **Figure 1.5a**).[16] The NWs became tortuous due to volume expansion but did not fracture. This observation suggests that the capacity loss may not be simply explained by loss of electrical contact, which is the common problem for many other lithium alloy anodes, such as Si,[27] Ge,[28] Sn,[29] and SnO_2[30]. Additionally, the electrode after cycling appeared relatively clean even without extensive rinsing, which indicates that the FeF_3 electrode does not suffer from severe electrolyte decomposition. This behavior is different from many other conversion anode materials that operates at lower voltages (<1.0 V), in which case solid-electrolyte-interface layer are produced by electrolyte decomposition and additional electrochemical capacity (capacity that exceeds the theoretical value) is observed.[31-34]

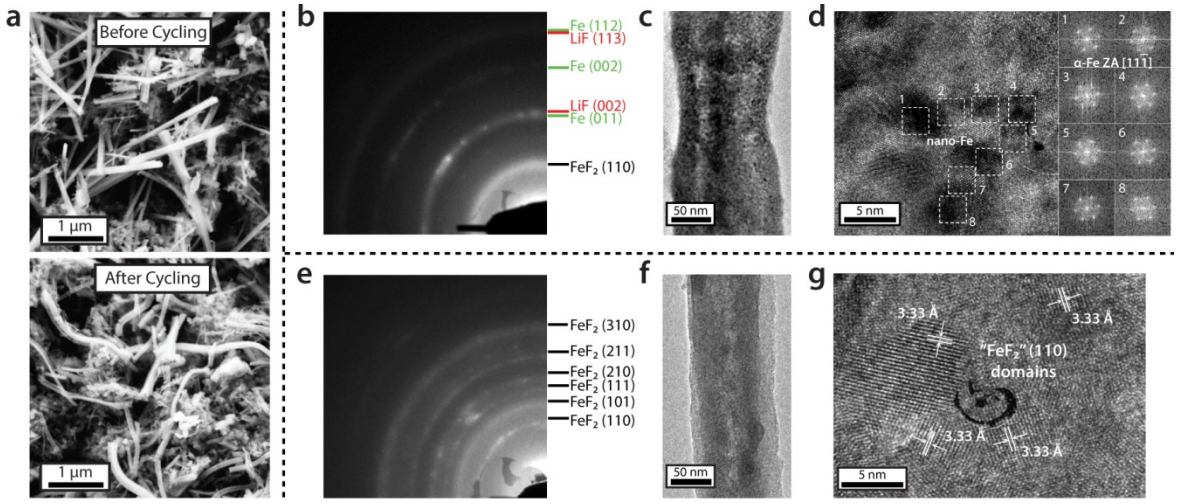

Figure 1.5 | Microstructural characterization of the cycled FeF_3 NWs. a. SEM images of the FeF_3 electrode before and after cycling; **b-d.** SAED pattern and HRTEM images of the FeF_3 NW

electrode lithiated (discharged) to 1.5 V; **e-f**. SAED and high-resolution TEM images of the FeF_3 NW electrode delithiated (charged) to 4.5 V

The phase and microstructure of the cycled electrode was examined using selected-area electron diffraction (SAED) and high-resolution TEM (HRTEM). The FeF_3 electrode was made of metallic Fe, LiF, and a rutile phase (later confirmed to be rutile FeF_2 by *in situ* XAS and DFT calculations) when it was lithiated (discharged) to 1.5 V (**Figure 1.5b**). The LiF phase appears to be amorphous, since its diffraction is quite weak. HRTEM revealed that metallic Fe existed as interconnected nanodomains (~3 nm in diameter, **Figure 1.5c** and **d**). Similar microstructure feature was also observed in the lithiated FeF_2 nanoparticles reported previously.[15] The interconnected Fe domains provide the internal pathway for electron transport and likely facilitate the lithiation reaction. On the other hand, the amorphous LiF provides the medium for Li^+ transport, which may be the slower process compared with the electron transport and limits the rate of the electrochemical reaction. When electrode was charged to 4.5 V, the electrode material was made of a phase highly similar to rutile FeF_2 (in terms of lattice spacing) instead of the rhombohedral FeF_3 in the pristine electrode (**Figure 1.5e**). The interconnected Fe nanodomains were no longer visible (**Figure 1.5f**). The NW was made of interconnected "FeF_2" nanodomains (**Figure 1.5g)**. Based on these observations, the capacity decay of the FeF_3 electrode can be satisfactorily explained by incomplete charge reaction since the Fe^{3+} oxidation state and the original crystal structure are not recovered. However, there used to be a controversy over the exact phase identity and Fe oxidation state of the electrode material after charge. Previous DFT-GGA+*U* calculations suggests the existence of a defect trirutile $Fe^{3+}F_3$ phase,[12] which cannot be differentiated from the rutile FeF_2 phase by SAED or HRTEM. We were able to

address this controversy by careful *in situ* X-ray studies and higher-level DFT calculations and confirmed that the phase we observed in TEM was rutile FeF_2, which are discussed in later sections.

1.5 *In situ* Hard X-ray Spectro-Imaging

We have used several *in situ* X-ray techniques to track the phase and structural evolution of the FeF_3 electrode across different length scales and enable complementary insights into the reaction mechanism. Specifically, we developed an innovated X-ray spectro-imaging technique to visualize electrochemically-driven solid-state phase transformations at the nanoscale and applied it to the study electrochemical reaction dynamics of the FeF_3 electrodes.[19] This technique takes advantage of the strong and deeply penetrating hard X-rays generated by synchrotron radiation and the chemical and elemental sensitivity with a full-field imaging capability provided by the transmission X-ray microscopy (TXM) coupled with X-ray absorption near-edge structure spectroscopy (XANES).[35-37] It provides a unique approach to visualize progression of a electrochemical reaction in a realistic battery electrode in a large (tens of microns) field-of-view (FOV) with nanoscale spatial resolution. Unlike *in situ* TEM experiments that often have to be carried out using specialized sample holders in electrochemical conditions drastically different from those in a practical battery,[38] hard X-ray based experiments can be conveniently performed in relevant and realistic conditions using a much simpler cell design (**Figure 1.6a**).[39-42] In the *operando* experiments (**Figure 1.6a)**, synchrotron monochromatic X-rays are directed to transmit through a perforated 2032-type coin-cell containing the FeF_3 cathode and all the other key components of a realistic battery, such as carbon black, polymeric binder, and a liquid electrolyte. The resulted absorption-contrast images are projected onto a lens-coupled full-field

CCD detector using a zone-plate and recorded. **Figure 1.6b** illustrate general procedures to generate chemical phase maps. First, a series of images are collected by scanning the energy across the Fe *K*-edge (7112 eV) in a step size of 2 eV, one image at each energy. Then, the XANES spectra at each pixel are constructed by plotting normalized X-ray absorption versus energy. They are fitted to reference spectra collected from standard compounds ($Fe^{3+}F_3$, $Fe^{2+}F_2$, and Fe) to determine ratio between different Fe-containing phases so that RGB colors can be accordingly assigned to generate a phase map. As Fe of various oxidation states interacts with X-ray differently, their spatial distribution at different states of discharge/charge reveals progression of the electrochemical reaction in the FeF_3 cathode

Although operando hard X-ray spectro-imaging technique was used to study electrochemical reactions before, it demands large microparticles or aggregates of small particles (several microns in total size) with strong X-ray absorption signal, in which cases chemical phase maps could be generated using simple data processing methods by approximating the X-ray absorption of the study material to the experimentally determined total X-ray absorption.[39-42] However, those approaches ignored background absorption and thus cannot accurately determine actual X-ray absorption of smaller and weakly absorbing samples at single-particle level under *operando* conditions. In order to study small and more electrochemically active samples, such as the FeF_3 MWs, we proposed and developed a conceptually new data analysis method to reliably account for background absorption and accurately determine the X-ray absorption of the study material. Enabled by this technological advance, we were able to visualize the progression of electrochemical discharge reaction in the FeF_3 electrode under *operando* conditions.

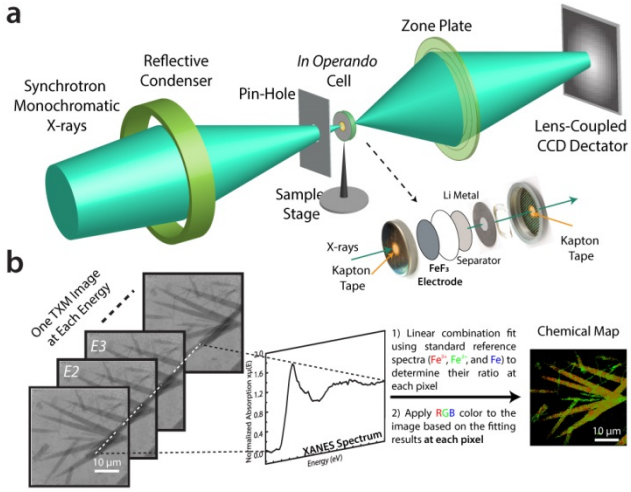

Figure 1.6 | Schematic illustration of the experimental setup and the data analysis method to generate chemical phase map.

We followed the electrochemical reactions in an electrode containing both the single-crystalline, non-porous polyhedra and polycrystalline, mesoporous MWs to reveal the relation between structure and electrochemical properties. The *operando* cell was discharged at a constant current of ~1/15 C (~47.5 mA/g) to 1.5 V (**Figure 1.7a**) and then charged 4.5 V. TXM images were recorded in dynamic conditions at different states of discharge/charge and were processed by our new method to generate the chemical phase maps (**Figure 1.7b**). During discharge (map 1–5 in **Figure 1.7b**), we found that the electrochemical reaction proceeded faster and more completely in the MWs than the polyhedra. This observation not only explains difference in their voltage profiles (**Figure 1.3**), but also reveals the importance of porous structure in promoting the lithiation reaction by reducing the Li^+/electron transport distance. During charge (map 6–9 in **Figure 1.7b**), Fe was gradually converted into FeF_2 but not reach FeF_3, leading to a capacity loss.

Even though all the particles were concurrently reacting (not shown here, see ref. X), we noticed significant reaction inhomogeneity at single-particle level (**Figure 1.7b**). In both the MW and the polyhedra, some regions reacted faster than the other, as evidenced by the non-uniform color distribution. This reaction behavior is likely controlled by reaction kinetics, as larger-size domains may be converted slower. Because reaction inhomogeneity is related to current distribution, it is better to be minimized to avoid current hotspots, which is a safety hazard.

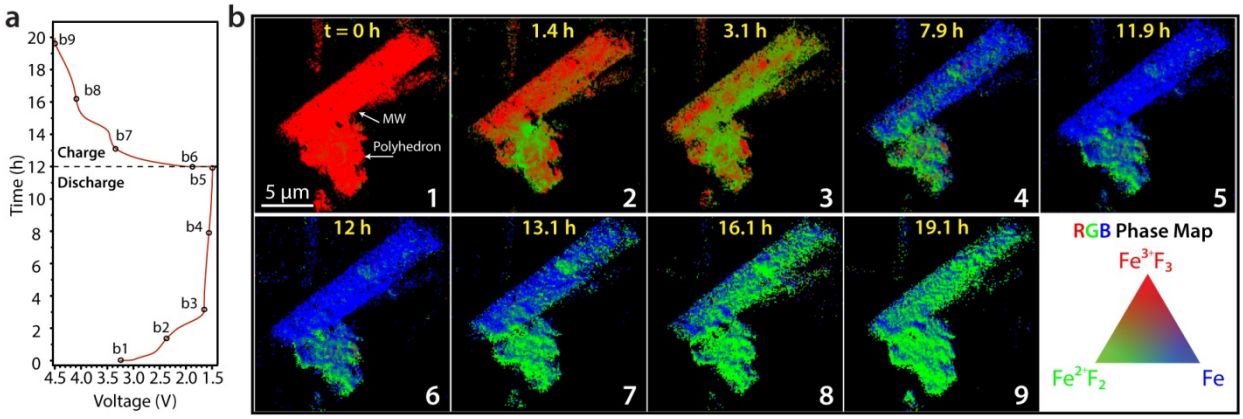

Figure 1.7 | Visualization of the electrochemical reaction of FeF_3 cathodes using hard X-ray spectro-imaging. a. Voltage profile of the *operando* cell that contains an FeF_3 cathode of mixed polyhedra and MWs. The cell was discharged at rate of ~1/15 C to 1.5 V and then charged to 4.5. The small black circles indicate the states of discharge/charge where the data were collected to construct chemical phase maps. **b.** Chemical phase maps showing how the electrochemical reactions proceeded in the FeF_3 electrode. Red, green, and blue pixels represent Fe (+III), Fe (+II), and metallic Fe, respectively.

Another important implication of our results is the indication of a different charge reaction pathway from the previous understanding. First-principles calculations previously suggested that

a number of Fe (+III) containing compounds form sequentially during charge, which seemingly offered a plausible explanation for the voltage hysteresis between discharge and charge.[12] However, the *operando* investigation herein clearly shows Fe (+II)-containing compounds formed first and Fe (+II) was slowly converted to Fe (+III) at high voltage during charge. A thorough (re)investigation using integrated experimental and theoretical approaches would be useful to address this discrepancy between our results and the previous simulation.

1.6 *In situ* X-ray absorption spectroscopy

Although hard X-ray spectro-imaging provides chemical information (Fe oxidation states) at the single-particle level in a visually striking way (**Figure 1.7b**), its energy resolution (~2 eV) is not good enough to differentiate some intermediate phases containing both Fe^{2+} and Fe^{3+}. Additionally, EXAFS is not possible at this moment because the XAS spectra collected by the TXM setup and this technique is too noisy. Therefore, local structure and chemical bonding information are also not available. In order to fully under the reaction mechanism of the FeF_3 electrode, we turned to *in situ* synchrotron X-ray absorption spectroscopy (XAS) to track changes in Fe oxidation states and local bonding structure during cycling of thee model samples, FeF_2 NWs, FeF_3 NWs, and FeF_3 MWs.[43]

We first studied the reaction mechanism of an FeF_2 cathode using *in situ* XAS (**Figure 1.8a**) as a comparison to the FeF_3 cathode, because Li-FeF_2 is a simpler conversion/reconversion system (ideally only Fe^{2+} and Fe^0 are involved) than Li-FeF_3 (Fe^{3+}, Fe^{2+}, and Fe^0 are involved). Based on XANES spectra and EXAFS patterns (contour plots in **Figure 1.8a**), We found that the discharge and charge reactions were highly symmetrical ($FeF_2 + 2Li^+ + 2e^- \rightleftarrows Fe + 2LiF$).

However, the electrode could be overcharged at the end of the charge process so that it became a multiple phase mixture containing Fe, Fe^{2+}, and Fe^{3+}, not the pure rutile FeF_2 phase.

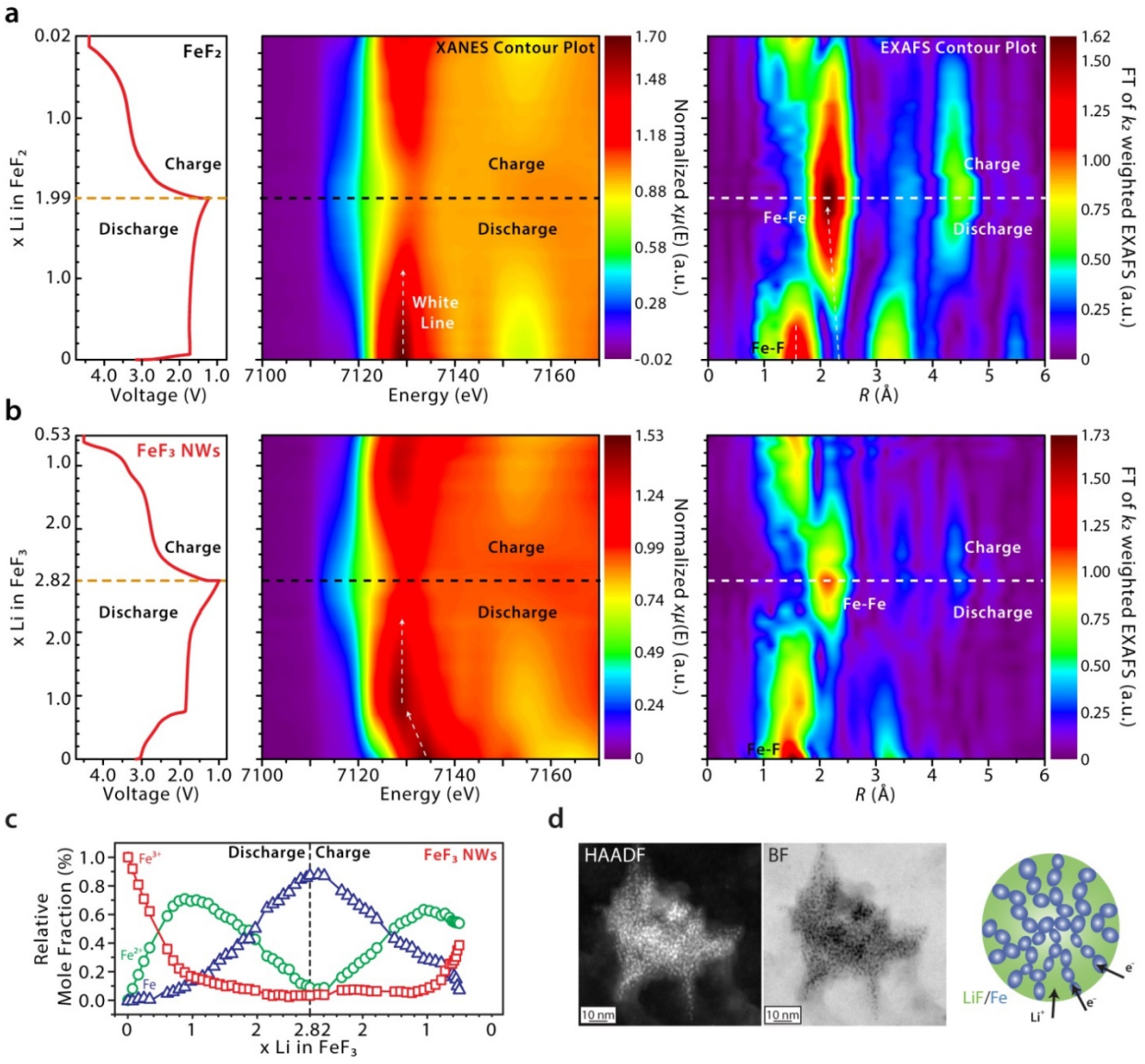

Figure 1.8 | *In situ* XAS and TEM studies on FeF_2 and FeF_3 NW electrodes. a. Voltage profile and *in situ* XANES spectra and EXAFS patterns contour plots of an FeF_2 NW electrode. The three plots share the same y-axis. The FeF_2 NW electrode was discharged at 1/12 C (1 C = 571 mA g^{-1} for FeF_2) and charged at 1/6 C. XAS spectra were recorded every 18 minutes; **b.**

Voltage profile and *in situ* XANES spectra and EXAFS patterns contour plots of an FeF_3 NW electrode. The three plots share the same y-axis. The FeF_3 NW electrode was discharged and charged at 1/10 C (1 C = 712 mA g^{-1} for FeF_3). XAS spectra were recorded every 18 minutes; **c.** Phase evolution during the cycling of the FeF_3 NW electrode, which is estimated by linear combinational fitting analysis of the XANES spectra. **d.** High-angle annular dark-field, bright-field STEM images and schematic illustration showing the microstructure of a bundle of fully lithiated FeF_3 NWs, which is made of interconnected Fe domains surrounded by LiF. The STEM images were recorded in the *in situ* TEM experiment.

We found that the reaction pathway of the FeF_3 cathode is also quite symmetrical (contour plots in **Figure 1.8b** and phase evolution plot in **Figure 1.8c**) and in the conversion/reconversion region (only Fe^{2+} and Fe are involved) the XANES spectra and EXAFS patterns are highly similar to those of the FeF_2 electrode (**Figure 1.8a**). Specifically, in the higher-voltage sloping plateau, EXAFS patterns show that the local structure deviates from that of the rhombohedral FeF_3 and became increasing rutile FeF_2 like upon lithiation, which suggests the formation of rutile structured Li_xFeF_3 phases (later confirmed by DFT-HSE calculations). *In situ* TEM experiments were also performed to understand the microstructural evolution during lithiation, which shows that the lithiation (discharge) initiates at the surface and propagates toward the interior of each active domain and the final product is made of interconnected Fe domains surrounded by LiF. Because delithiation (charge) is very difficult to do using current *in situ* TEM technique (dry cell), we could only use the microstructure of the fully lithiated FeF_3 (made of interconnected Fe and LiF) to predict what is most likely to happen during the charge process. Because Li^+ ions can be extracted most easily at the electrolyte/electrode (now made of Fe/LiF)

interface, the charge reaction likely initiates at the outside of the electrochemically active particles.

By comparing the phase evolutions in the FeF_3 NW and MW electrodes, we also note that kinetic limitations can cause one reaction not proceed completely over the entire particle domain before the subsequent one being forced to initiate in the pre-reacted region under galvanostatic condition. The MWs consist of larger active domains (and thus smaller surface area) than the NWs and are more likely be limited by reaction kinetics (longer distance for Li^+/electron transport). Therefore the rutile FeF_2 phase (green color) produced in the initial lithiation on the outside is further lithiated to produce LiF and Fe (blue color) before the interior FeF_3 domains (red) can begin to react (see schematic illustration in **Figure 1.9**). The occurrence of reduction of Fe^{2+} to Fe dictates the voltage profile so that the high-voltage sloping plateau is lost and the second flat plateau becomes much longer (**Figure 1.3**).

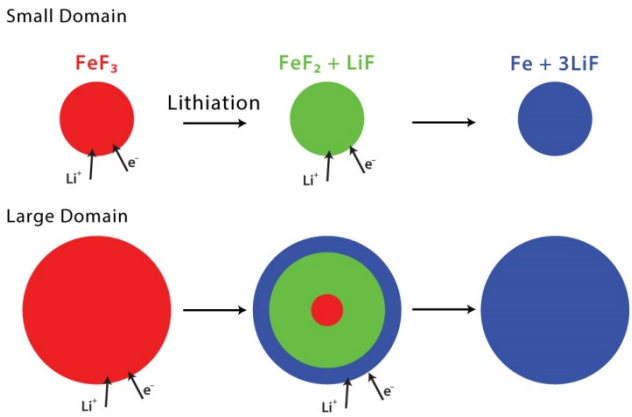

Figure 1.9 | Schematic illustration of the multiple-step lithiation process in a small and a large active domains.

1.7 DFT calculations and reaction pathway of the FeF_3 electrode

The experimentally observed reaction pathway of the FeF_3 electrode is in disagreement with the one calculated from past DFT-GGA+*U* simulations and the associated models,[12] which claim that FeF_3 is first lithiated to $Li_x[Fe^{3+}_{1-x}Fe^{2+}_x]F_3$ before full reduction of Fe to LiF/Fe during discharge, and a series of Fe^{3+}-containing compounds ($Li_{3-3x}Fe^{3+}_xF_3$) form sequentially during charge before formation of a defect trirutile FeF_3. This mechanistic understanding is the basis for a seemingly reasonable explanation for the large voltage hysteresis of the FeF_3 electrode because the presence of different phases (and with Fe at different oxidation states) during discharge and charge would indeed lead to different potentials in the electrochemical system. However, this model cannot be justified our experimental data.

In order to reconcile the discrepancy between our experimental results and the previous DFT-GGA+*U* calculations, we performed a detailed multicomponent phase analysis using DFT calculations of materials in the Li-Fe-F ternary system. The DFT calculations were performed using hybrid HSE functions, which have been shown to more accurately reproduce experimental formation energies and Li insertion voltages for transition metal-containing compounds than GGA- or GGA+*U*-based DFT. **Figure 1.10a** is a plot of the relevant portion of the HSE-DFT ternary Li-Fe-F phase diagram where the FeF_3 and FeF_2 lithiation reactions occur.

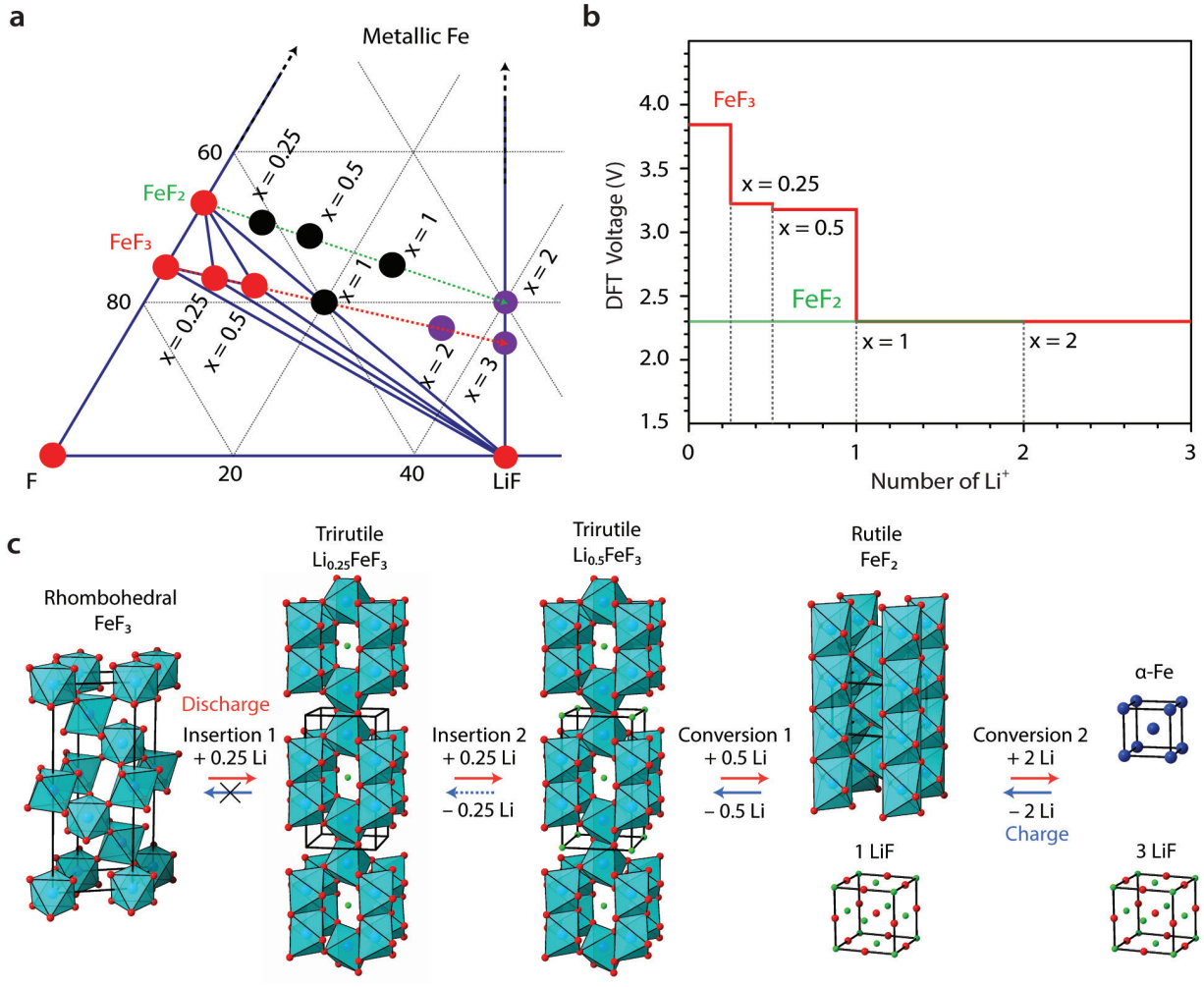

Figure 1.10 | DFT-HSE calculation results and FeF_3 reaction pathway. a. DFT calculated Fe-Li-F phase diagram using the HSE approach. The lithiation pathways for FeF_3 and FeF_2 are indicated by the red and green dashed arrows, respectively. Red dots represent stable phases, black dots represent unstable lithiated phases and purple dots indicate relevant compositions where no lithiated compound was calculated. The fraction of lithiation x for Li_xFeF_2 and Li_xFeF_3 are labeled for both pathways. **b.** Calculated DFT voltage curves for FeF_3 and FeF_2 at different states of lithiation. **c.** Discharge and charge reaction pathways of the FeF_3 electrode, which are

derived from both the experimental and DFT calculation results. Li, Fe, and F atoms are represented by green, blue, and red spheres.

Upon lithiation, FeF_2 immediately begins to dissociate upon lithiation to precipitate metallic Fe and LiF (green dashed line in **Figure 1.10a**). This three-phase region persists over the entire lithiation path until $x_{Li} = 2$, at which point the reduction from Fe^{2+} to metallic Fe is complete and produces a two phase mixture of metallic Fe and LiF. In delithiation of the Fe/LiF (1:2 in mole ratio), FeF_2 should be formed as the stable phase but $Li_{0.5}FeF_3$ may also be produced from FeF_2 if there is excess LiF.

The stable lithiation path for FeF_3 (red dotted line in **Figure 1.10a**) shows direct Li intercalation when $x \leq 0.5$. Upon lithiation to $x_{Li} = 0.25$, the pristine rhombohedral FeF_3 phase is no longer stable, and a phase change to the defected trirutile ($Li_{0.25}FeF_3$) structure occurs. This defected trirutile phase is stable up to $x_{Li} = 0.5$ ($Li_{0.5}FeF_3$), after which dissociation to FeF_2 and LiF occurs because no more interstitial sites for lithium insertion are available. When $x_{Li} = 1$, all Fe^{3+} has been reduced to Fe^{2+} and the system is a two-phase mixture of FeF_2 and LiF. Further lithiation promotes the reduction of Fe^{2+} to metallic Fe, which is exactly the same process as the lithiation of FeF_2. In delithiation of Fe/LiF (1:3 in mole ratio), FeF_2 should be formed as the stable phase first; $Li_{0.5}FeF_3$ can be produced later from the FeF_2 and the excess LiF.

Figure 1.10b shows the calculated DFT lithiation voltages. Since they are representative of equilibrium voltages, in which case no polarization or kinetic overpotential is included, they are higher than those experimentally observed when a current was applied (voltage profiles in **Figure 1.8a** and **b**). As the experimental battery was allowed to relax to approach equilibrium

conditions, its voltages would become closer to the DFT calculated values. This trend is indeed seen from the GITT measurements after relaxation, which is shown in the later section.

These DFT-HSE calculation results are in good agreement with the *in situ* XAS data. Therefore, we can propose complete and consistent reaction pathways for FeF_3 (and FeF_2) cathodes, which is basically symmetrical and as follows: rhombohedral FeF_3 $\rightarrow$ trirutile $Li_{0.25}FeF_3$ $\rightarrow$ trirutile $Li_{0.5}FeF_3$ $\rightleftarrows$ rutile FeF_2 + LiF $\rightleftarrows$ Fe + 3LiF (**Figure 1.10c**). It is difficult for the electrode to return to trirutile $Li_{0.25}FeF_3$ and/or rhombohedral FeF_3 due to kinetic limitations.

1.8 Origins of the Large Voltage Hysteresis in the FeF_3 Electrode

According to the reaction pathway derived from the *in situ* XAS data and DFT-HSE06 calculations, the large voltage hysteresis in the FeF_3 electrode cannot be explained by the system the system progressing through fundamentally different reaction pathways and the existence of different intermediate phases during discharge and charge.

To better understand the possible causes of the large voltage hysteresis, we performed GITT experiments on the FeF_3 NW and MW electrodes, respectively (**Figure 1.11**). **Figure 11b** provides a close-up view of the GITT process. In the discharge half-cycle (red curve), as soon as the current is removed, the voltage first suddenly increases a small value, and then gradually increases as the electrode approaches equilibrium condition. The opposite occurs in the charge half-cycle (Figure **1.11b**, blue curve). We find that the voltage after the 4 h relaxation (V_{relax}, black dashed lines in **Figure 1.11a**) largely correlates with the composition of the electrodes inferred from the *in situ* XAS results. **Figure 1.11c** shows how much the voltage relaxes after 4 h for the FeF_3 NW and MW electrodes, respectively, at different states of lithiation. During

discharge, we observe that the voltage relaxes more in the MW electrode than the NW electrode (Figure **Figure 1.11c**), which is a result of the reaction inhomogeneity: the intermediate phase $Fe^{2+}F_2$ is being further lithiated to produce LiF and Fe on the outside despite the presence of unreacted FeF_3 at the interior of the active particle. After all the FeF_3 is consumed, the magnitude of the voltage relaxation in the MW and the NW electrode becomes comparable. **Figure 1.11 d** shows the remaining voltage difference at the same state of lithiation between discharge and charge steps after the 4 h relaxation (V_{gap}) for both the MW and NW electrodes. V_{gap} can become slightly smaller based on its changing trend if the relaxation time is further increased but will not become zero.

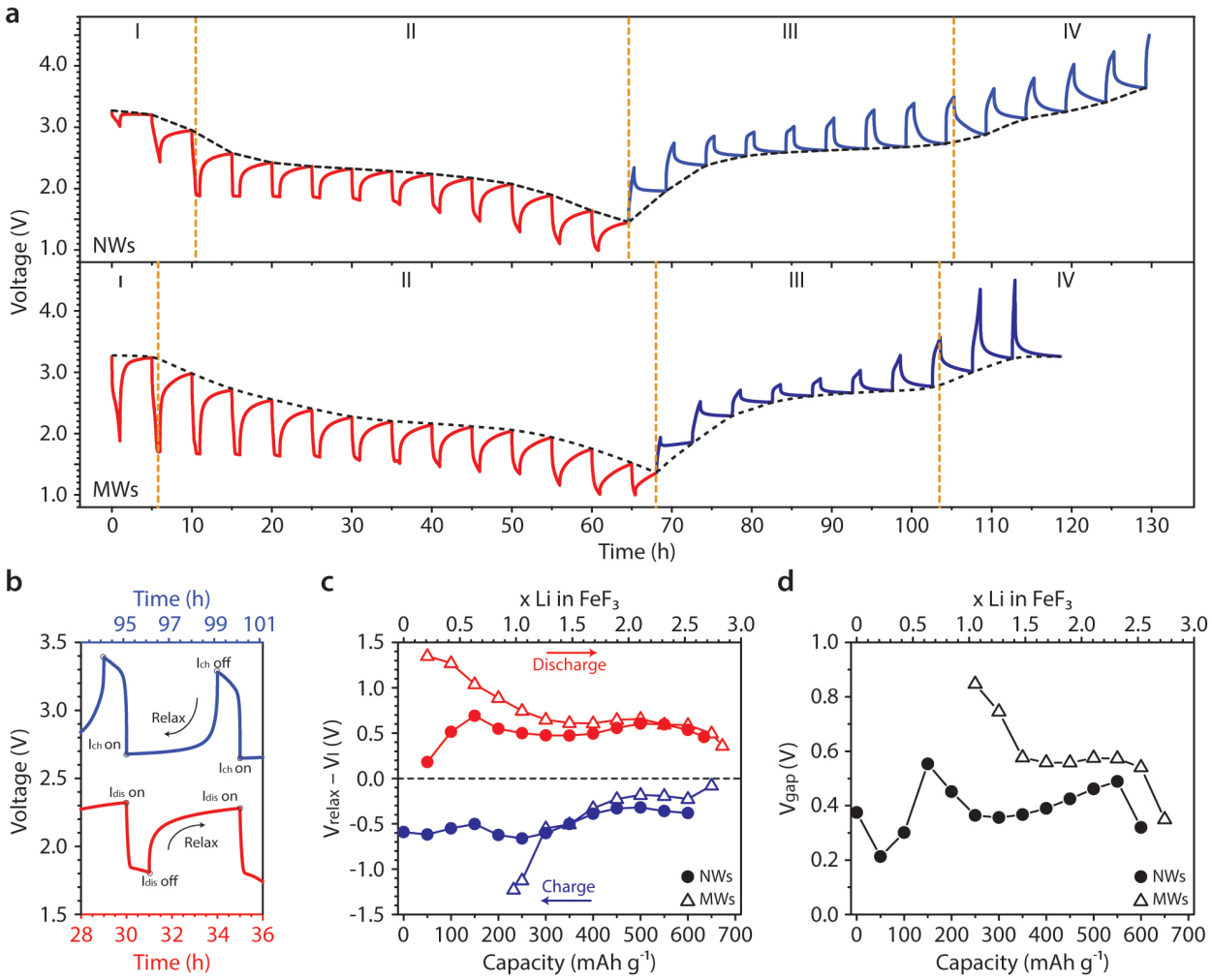

Figure 1.11 | GITT results and analysis. a. GITT profiles of a FeF_3 NW electrode and a MW electrode. The cells were discharged and charged at a rate of 50 mA g^{-1} for 1h and then allowed to relax 4 hours. **b.** Zoom-in view of the GITT curve for the NW electrode. **c.** Voltage change after the 4 h relaxation at different states of discharge and charge of the NW and MW electrodes, respectively. **d.** Voltage difference between discharge and charge steps after the 4 h relaxation at the same state of lithiation of the NW and MW electrodes, respectively.

By integrating all experimental and theoretical simulation results, we can identify the following components that likely contribute to the large voltage hysteresis of FeF_3. The first one is the Ohmic iR voltage drop, which is the sudden voltage jump after the current is removed and typically <50 mV. The second component consists of various kinetic overpotentials that are required to nucleate new phases, drive phase transformations, and overcome interfacial penalty for making nanophases. These kinetic overpotentials are manifested in the voltage "spikes" during the extended voltage relaxation. However, their magnitudes are not straightforward to quantify using the GITT results, because the active particles undergo significant phase transformations and cannot achieve truly a homogeneous composition over the entire particle simply through Li^+ diffusion during the relaxation. Reverse-step potentiostatic intermittent titration technique (PITT) may be a more suitable approach to quantitatively evaluate the kinetic overpotentials in conversion electrode materials.[44] The third component is the difference in spatial distribution of the electrochemically relevant phases during discharge and charge steps and the way these phases are connected in the electrochemical system (i.e. access to Li^+ and electron). For example, at states of lithiation close to x_{Li} = 3 per FeF_3, during discharge the intermediate phase FeF_2 is located at the interior of the active particles while Fe and LiF are on the outside and have contact with the electrolyte and current collector; by contrast, during charge the intermediate phase FeF_2 is formed on the outside while Fe is located inside and may be screened or even isolated from the electrochemical system, by the electrically and ionically insulating FeF_2 phase. Such a difference in phase distribution yields a difference in apparent potentials, which cannot be eliminated by voltage relaxation. This compositional inhomogeneity mechanism for driving hysteresis is likely to play a role in many kinetically limited conversion

materials where during Li insertion (extraction) the most reduced (oxidized) phases are present at the active surface and drive the potential down (up) compared the theoretical OCV. Interesting comparisons may also be made with Li-sulfur[45] and Li-oxygen[46] batteries during discharging/charging: after voltage relaxation, a voltage gap remains in the Li-sulfur system possibly due to presence of different Li_2S_n (n= 8, 6, 4, 2, and 1) phases, but approaches zero in the Li-oxygen system because there is only Li_2O_2.

1.9 Strategies to improve the performance of the FeF_3 electrode

The mechanistic understandings provide the basis for developing new strategies to address the challenge facing conversion electrode materials. There are two important considerations. One is to confine the electrochemically-driven phase transformation locally so that the converted phases are in close contact and can be readily reconverted during reconversion. The other one is to provide efficient electron and Li-ion conduction pathways. Therefore, one straightforward approach is to construct a composite electrode consisting of nanostructured active particles whose size must be comparable to the length scale of the conversion reaction (<10 nm for FeF_3) and directly connected to electrically conductive scaffolds. This is expected to minimize the voltage hysteresis caused by compositional inhomogeneity as well as iR drop. This approach seems quite promising because the beneficial effect has already been observed in the case of $FeCl_3$ conversion anode when ultra-small $FeCl_3$ nanoparticles are embedded between graphene layers to make a graphite intercalation compound (GIC).[47] The $FeCl_3$-GIC electrode shows a moderate voltage gap (<200 mV) between discharge and charge steps and excellent reversibility when cycled at a current of 50 mA g^{-1}. However, sufficient amount of FeF_3 material needs to be embedded so that the overall volumetric energy density is not severely compromised. Another

approach that deserves further exploration is incorporating another cation or anion into the metal fluoride lattice to lower the kinetic overpotentials (similar to a "catalyst") by improving ionic and electronic transport properties and creating a more disordered microstructure.[22, 48] This approach may be more promising than the first one in terms of available energy density because no additional inactive components is introduced. One example is $Cu_yFe_{1-y}F_2$ solid-solution, in which case that Fe in FeF_2 is partially substituted by Cu. The ternary fluoride electrode exhibits reversible Cu and Fe redox reactions with smaller hysteresis than the pure FeF_2 electrode. One major challenge is to preserve the beneficial effect in repeated cycling, as Cu is rapidly lost through Cu^+ dissolution into the liquid electrolyte.[22, 49] Additionally, it will also be interesting to explore materials with flexible host structure so that conversion/reconversion can proceed more easily.

1.10 Summary and Outlook

Through an multifaceted study that involves material synthesis, electrochemical characterization, *in situ* X-ray/TEM studies, and DFT simulations, we reveal that the reaction pathway of the FeF_3 cathode is basically symmetrical and as follows: rhombohedral $FeF_3 \rightarrow$ trirutile $Li_{0.25}FeF_3 \rightarrow$ trirutile $Li_{0.5}FeF_3 \rightleftarrows$ rutile FeF_2 + LiF $\rightleftarrows$ Fe + 3LiF. Side reactions caused by electrolyte decomposition can be minimized by cycling the battery at voltage larger 1 V. We find that reaction homogeneity (completeness and spatial distribution of each electrochemical reaction) strongly depends on reaction kinetics in these multiple-step reaction processes. The irreversible capacity loss is caused by the poor reaction kinetics in recovering the Fe^{3+} oxidation state during charge. The large voltage hysteresis observed in the FeF_3 cathode is due to a combination of iR (Ohmic) drop, kinetic overpotentials, and difference in spatial distributions of

electrochemically relevant phases, which are kinetic in nature and therefore can certainly be mitigated by facilitating Li^+ and electron transport in the electrode. Promising approaches, including but not limited to nanostructure engineering and incorporation of other ions, can help reduce the hysteresis to a reasonable level to eventually enable practical applications. These studies provide the long-awaited conceptual breakthrough in understanding and tackling the large voltage hysteresis in conversion electrode materials[48-50] and will guide future efforts to improve their performance in lithium-ion batteries.

1.11 References

1. Armand, M., Tarascon, J. M., Building better batteries. *Nature* **451,** 652-657 (2008).

2. Bruce, P. G., Energy storage beyond the horizon: Rechargeable lithium batteries. *Solid State Ionics* **179,** 752-760 (2008).

3. Goodenough, J. B., Kim, Y., Challenges for Rechargeable Li Batteries. *Chem. Mater.* **22,** 587-603 (2009).

4. Bruce, P. G., Freunberger, S. A., Hardwick, L. J., Tarascon, J.-M., Li-O_2 and Li-S batteries with high energy storage. *Nature Mater.* **11,** 19-29 (2012).

5. Cabana, J., Monconduit, L., Larcher, D., Palacín, M. R., Beyond Intercalation-Based Li-Ion Batteries: The State of the Art and Challenges of Electrode Materials Reacting Through Conversion Reactions. *Adv. Mater.* **22,** E170-E192 (2010).

6. Poizot, P., et al., Nano-sized transition-metal oxides as negative-electrode materials for lithium-ion batteries. *Nature* **407,** 496-499 (2000).

7. Morcrette, M., et al., A reversible copper extrusion-insertion electrode for rechargeable Li batteries. *Nat Mater* **2,** 755-761 (2003).

8. Li, H., Richter, G., Maier, J., Reversible Formation and Decomposition of LiF Clusters Using Transition Metal Fluorides as Precursors and Their Application in Rechargeable Li Batteries. *Adv. Mater.* **15,** 736-739 (2003).

9. Balaya, P., Li, H., Kienle, L., Maier, J., Fully Reversible Homogeneous and Heterogeneous Li Storage in RuO_2 with High Capacity. *Adv. Funct. Mater.* **13,** 621-625 (2003).

10. Badway, F., Cosandey, F., Pereira, N., Amatucci, G. G., Carbon Metal Fluoride Nanocomposites: High-Capacity Reversible Metal Fluoride Conversion Materials as Rechargeable Positive Electrodes for Li Batteries. *J. Electrochem. Soc.* **150,** A1318-A1327 (2003).

11. Badway, F., Pereira, N., Cosandey, F., Amatucci, G. G., Carbon-Metal Fluoride Nanocomposites: Structure and Electrochemistry of FeF_3:C. *J. Electrochem. Soc.* **150,** A1209-A1218 (2003).

12. Doe, R. E., Persson, K. A., Meng, Y. S., Ceder, G., First-Principles Investigation of the Li−Fe−F Phase Diagram and Equilibrium and Nonequilibrium Conversion Reactions of Iron Fluorides with Lithium. *Chem. Mater.* **20,** 5274-5283 (2008).

13. Yamakawa, N., Jiang, M., Key, B., Grey, C. P., Identifying the Local Structures Formed during Lithiation of the Conversion Material, Iron Fluoride, in a Li Ion Battery: A Solid-State NMR, X-ray Diffraction, and Pair Distribution Function Analysis Study. *J. Am. Chem. Soc.* **131,** 10525-10536 (2009).

14. Kim, S.-W., et al., Fabrication of FeF_3 Nanoflowers on CNT Branches and Their Application to High Power Lithium Rechargeable Batteries. *Adv. Mater.* **22,** 5260-5264 (2010).

15. Wang, F., et al., Conversion Reaction Mechanisms in Lithium Ion Batteries: Study of the Binary Metal Fluoride Electrodes. *J. Am. Chem. Soc.* **133,** 18828-18836 (2011).

16. Li, L., Meng, F., Jin, S., High-Capacity Lithium-Ion Battery Conversion Cathodes Based on Iron Fluoride Nanowires and Insights into the Conversion Mechanism. *Nano Lett.* **12,** 6030-6037 (2012).

17. Li, C., Mu, X., van Aken, P. A., Maier, J., A High-Capacity Cathode for Lithium Batteries Consisting of Porous Microspheres of Highly Amorphized Iron Fluoride Densified from Its Open Parent Phase. *Adv. Energy Mater.* **3,** 113-119 (2013).

18. Liu, J., et al., Carbon-Encapsulated Pyrite as Stable and Earth-Abundant High Energy Cathode Material for Rechargeable Lithium Batteries. *Adv. Mater.* **26,** 6025-6030 (2014).

19. Li, L., et al., Visualization of electrochemically driven solid-state phase transformations using operando hard X-ray spectro-imaging. *Nat. Commun.* **6,** 6883 (2015).

20. Yersak, T. A., et al., Solid State Enabled Reversible Four Electron Storage. *Adv. Energy Mater.* **3,** 120-127 (2013).

21. Li, L., Caban-Acevedo, M., Girard, S. N., Jin, S., High-purity iron pyrite (FeS_2) nanowires as high-capacity nanostructured cathodes for lithium-ion batteries. *Nanoscale* **6,** 2112-2118 (2014).

22. Wang, F., et al., Ternary metal fluorides as high-energy cathodes with low cycling hysteresis. *Nat. Commun.* **6,** 6668 (2015).

23. Dreyer, W., et al., The thermodynamic origin of hysteresis in insertion batteries. *Nat Mater* **9,** 448-453 (2010).

24. Li, H., Balaya, P., Maier, J., Li-Storage via Heterogeneous Reaction in Selected Binary Metal Fluorides and Oxides. *J. Electrochem. Soc.* **151,** A1878-A1885 (2004).

25. Li, L., et al., Facile Solution Synthesis of α-$FeF_3 \cdot 3H_2O$ Nanowires and Their Conversion to α-Fe_2O_3 Nanowires for Photoelectrochemical Application. *Nano Lett.* **12,** 724-731 (2012).

26. Li, L., Jin, S., ***Unpublished Result***.

27. Chan, C. K., et al., High-performance lithium battery anodes using silicon nanowires. *Nat Nano* **3,** 31-35 (2008).

28. Chan, C. K., Zhang, X. F., Cui, Y., High Capacity Li Ion Battery Anodes Using Ge Nanowires. *Nano Lett.* **8,** 307-309 (2008).

29. Yang, J., Winter, M., Besenhard, J. O., Small particle size multiphase Li-alloy anodes for lithium-ionbatteries. *Solid State Ionics* **90,** 281-287 (1996).

30. Courtney, I. A., Dahn, J. R., Electrochemical and In Situ X‐Ray Diffraction Studies of the Reaction of Lithium with Tin Oxide Composites. *J. Electrochem. Soc.* **144,** 2045-2052 (1997).

31. Badway, F., et al., Metal Oxides as Negative Electrode Materials in Li-Ion Cells. *Electrochem. Solid-State Lett.* **5,** A115-A118 (2002).

32. Larcher, D., et al., Effect of Particle Size on Lithium Intercalation into α-Fe_2O_3. *J. Electrochem. Soc.* **150,** A133-A139 (2003).

33. Hu, Y.-Y., et al., Origin of additional capacities in metal oxide lithium-ion battery electrodes. *Nature Mater.* **12,** 1130-1136 (2013).

34. Boesenberg, U., et al., Asymmetric pathways in the electrochemical conversion reaction of NiO as battery electrode with high storage capacity. *Sci. Rep.* **4,** (2014).

35. Wang, J., et al., Automated markerless full field hard x-ray microscopic tomography at sub-50 nm 3-dimension spatial resolution. *Appl. Phys. Lett.* **100,** 143107 (2012).

36. Meirer, F., et al., Three-dimensional imaging of chemical phase transformations at the nanoscale with full-field transmission X-ray microscopy. *J. Synchrotron. Radiat.* **18,** 773-781 (2011).

37. Andrews, J. C., Weckhuysen, B. M., Hard X-ray Spectroscopic Nano-Imaging of Hierarchical Functional Materials at Work. *ChemPhysChem* **14,** 3655-3666 (2013).

38. Huang, J. Y., et al., In Situ Observation of the Electrochemical Lithiation of a Single SnO_2 Nanowire Electrode. *Science* **330,** 1515-1520 (2010).

39. Wang, J., Chen-Wiegart, Y.-c. K., Wang, J., In situ chemical mapping of a lithium-ion battery using full-field hard X-ray spectroscopic imaging. *Chem. Commun.* **49,** 6480-6482 (2013).

40. Wang, J., Chen-Wiegart, Y.-c. K., Wang, J., In operando tracking phase transformation evolution of lithium iron phosphate with hard X-ray microscopy. *Nature Commun.* **5,** 4570 (2014).

41. Yang, F., et al., Nanoscale Morphological and Chemical Changes of High Voltage Lithium–Manganese Rich NMC Composite Cathodes with Cycling. *Nano Lett.* **14,** 4334-4341 (2014).

42. Yu, Y.-S., et al., Nonequilibrium Pathways during Electrochemical Phase Transformations in Single Crystals Revealed by Dynamic Chemical Imaging at Nanoscale Resolution. *Adv. Energy Mater.* **5,** 1402040 (2014).

43. Li, L., et al., The Origin of Large Voltage Hysteresis in Metal Fluoride Lithium-Ion Battery Conversion Electrodes. *to be sumitted* (2015).

44. Ko, J. K., et al., Transport, Phase Reactions, and Hysteresis of Iron Fluoride and Oxyfluoride Conversion Electrode Materials for Lithium Batteries. *ACS Appl. Mater. Interfaces* **6,** 10858-10869 (2014).

45. Cuisinier, M., et al., Unique behaviour of nonsolvents for polysulphides in lithium-sulphur batteries. *Energy Environ. Sci.* **7,** 2697-2705 (2014).

46. Cui, Z. H., Guo, X. X., Li, H., Equilibrium voltage and overpotential variation of nonaqueous Li-O_2 batteries using the galvanostatic intermittent titration technique. *Energy Environ. Sci.* **8,** 182-187 (2015).

47. Wang, F., et al., Graphite Intercalation Compounds (GICs): A New Type of Promising Anode Material for Lithium-Ion Batteries. *Adv. Energy Mater.* **4,** 1300600 (2014).

48. Wiaderek, K. M., et al., Comprehensive Insights into the Structural and Chemical Changes in Mixed-Anion FeOF Electrodes by Using Operando PDF and NMR Spectroscopy. *J. Am. Chem. Soc.* **135,** 4070-4078 (2013).

49. Hua, X., et al., Comprehensive Study of the CuF_2 Conversion Reaction Mechanism in a Lithium Ion Battery. *J. Phys. Chem. C* **118,** 15169-15184 (2014).

50. Lee, D. H., et al., Understanding improved electrochemical properties of NiO-doped NiF_2-C composite conversion materials by X-ray absorption spectroscopy and pair distribution function analysis. *Phys. Chem. Chem. Phys.* **16,** 3095-3102 (2014).

CHAPTER 2

High-Capacity Lithium-Ion Battery Conversion Cathodes Based on Iron Fluoride Nanowires and Insights into the Conversion Mechanism

2.1 Abstract

The increasing demands from large-scale energy applications call for the development of lithium-ion battery (LIB) electrode materials with high energy density. Earth-abundant conversion cathode material iron trifluoride (FeF_3) has a high theoretical capacity (712 mAh g^{-1}) and the potential to double the energy density of the current cathode material based on lithium cobalt oxide. Such promise has not been fulfilled due to the non-optimal material properties and poor kinetics of the electrochemical conversion reactions. Here, we report for the first time a high-capacity LIB cathode that is based on networks of FeF_3 nanowires (NWs) made via an inexpensive and scalable synthesis. The FeF_3 NW cathode yielded a discharge capacity as high as 543 mAh g^{-1} at the first cycle and retained a capacity of 223 mAh g^{-1} after 50 cycles at room temperature under the current of 50 mA g^{-1}. Moreover, high-resolution transmission electron microscopy revealed the existence of continuous networks of Fe in the lithiated FeF_3 NWs after discharging, which is likely an important factor for the observed improved electrochemical

---

This chapter was originally published in *Nano Lett.* **12,** 6030-6037 (2012), in collaboration with F. Meng and S. Jin.

performance. The loss of active material (FeF_3) caused by the increasingly ineffective reconversion process during charging was found to be a major factor responsible for the capacity loss upon cycling. With the advantages of low cost, large quantity, and ease of processing, these FeF_3 NWs are not only promising battery cathode materials, but also provide a convenient platform for fundamental studies and further improving conversion cathodes in general.

2.2 Introduction

Lithium-ion batteries (LIB) have revolutionized portable electronics and become the dominant power sources for mobile devices due to their superior energy density in comparison with other rechargeable batteries.[1-3] Current LIB technology is built on intercalation chemistry, which involves Li^+ topotactic intercalation/deintercalation into/from the host lattice of electrode materials represented by lithium cobalt oxide ($LiCoO_2$) and graphite.[3] Intercalation/deintercalation reaction mostly introduces small volume change to the crystal lattice of electrode materials without causing structural collapse and/or phase segregation, which enables high-performance LIB with good rate capability and long lifetime.[3] However, current LIB fall short of the ever-increasing energy demand from large-scale application such as electrical vehicles and grid-level energy storage.[1-5] This is largely due to the intrinsic limit of intercalation electrode materials, which typically allows no more than one Li^+ per structural unit to be inserted into the host lattice. Going beyond current LIB requires the development of energy-storage technology based on new electrode materials and/or new chemistries, among which Li-O_2 and Li-S have attracted most attention due to their significantly higher theoretical energy density.[6] Important advances have been made for Li-O_2[7] and Li-S[8] batteries recently, but

significant challenges remain to be overcome before they can become a commercial success.[6] High energy storage can also be realized by utilizing conversion electrode materials as battery cathode that undergoes electrochemical conversion/rconversion upon cycling.[3, 9-11] A very promising and representative example is iron trifluoride (FeF_3), which can theoretically react with three Li^+ and deliver a high capacity of 712 mAh g^{-1} at an average potential of ~2.7 V,[12] enabling a high theoretical energy density of 1950 Wh kg^{-1}.

$$FeF_3 + 3Li^+ + 3e^- \rightleftarrows 3LiF + \alpha\text{-}Fe \quad (4.5–1.5\ V\ vs\ Li^+/Li)$$

In the discharge reaction, FeF_3 (space group $R\bar{3}c$, ReO_3-type structure) is electrochemically reduced with Li^+ uptake to form a nanocomposite consisting of α-Fe nanodomains embedded in a LiF matrix (Figure 2.1a).[13-15] The large interface between the two phases likely facilitates subsequent decomposition of the nanocomposite upon a reverse bias on charging[9] and enables the deconversion reaction to form the defect-trirutile FeF_3 (Figure 2.1a) .[13-15] In addition to its high energy density, FeF_3 is also an earth-abundant material that is much less expensive than the current $LiCoO_2$ cathode material.[16] These attributes make FeF_3 a very promising cathode material. However, significant challenges have so far prevented these promises from being fulfilled. Because of the insulating character of FeF_3[17] and significant structural transformation upon cycling, FeF_3 electrodes made of large FeF_3 particles (with crystallite size > 150 nm) severely suffered from sluggish kinetics and could only exhibit a low capacity of about 140 mAh g^{-1} in the voltage window of 4.5–1.5 V even at 70 °C and a small current of 7.58 mA g^{-1}.[13]

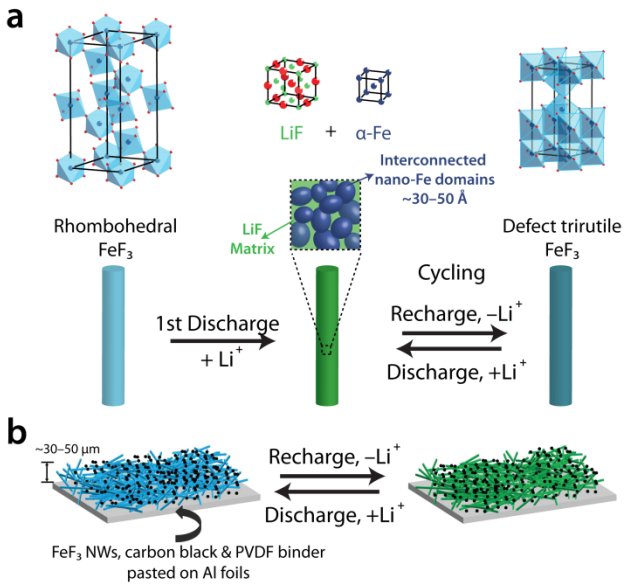

Figure 2.1 | Schematic illustrations of the structural changes. (a) Schematics of the crystal structure and microstructure changes that occur in FeF_3 cathode material during electrochemical cycling. Blue, green and red spheres correspond to Fe, Li, and F atoms, respectively; (b) Schematic illustration of the entangled network of FeF_3 NWs mixed with carbon black and PVDF binder as lithium-ion battery cathode. The carbon black is represented by small black dots and the PVDF binder is not shown for clarity.

Nanostructuring FeF_3 cathodes can potentially alleviate these problems. The decrease in particle size from bulk to nanoscale leads to reduced ion/electrode transport distance and increased surface area,[1] which facilitate conversion reaction kinetics and improve the electrochemical cycling performance of FeF_3 cathodes.[13, 16, 18-21] Previous FeF_3 electrodes are usually made from nanocomposites of FeF_3 nanoparticles (NPs) and conductive carbon *via* an energy-intensive ball-milling process.[13, 14, 16, 18, 20, 22] Even though high capacities have been reported in a few cycles, they were only accessible at elevated temperature and/or small

currents[13, 14] or at the presence of a large amount of carbon (50% wt).[20] Furthermore, the commonly observed capacity fading and voltage hysteresis remain significant challenges for the FeF_3 cathode,[9] and despite significant experimental and theoretical efforts,[13-16, 22] complete understanding of the conversion mechanism of FeF_3 conversion cathodes is still lacking.

One-dimensional (1D) nanostructured electrodes usually exhibit enhanced reversible capacities and longer cycling lives relative to their micrometer-sized/bulk counterparts due to their better capability to withstand stress arising from large structural change upon battery cycling and their better electrical connectivity.[23-26] Even though the success has been mostly achieved on anode materials to date, the performance of conversion cathodes could benefit even more from the nanowire (NW) morphology because of their large structural transformation in the electrochemical conversion/deconversion reaction. Moreover, NWs provide a defined 1D-nanostructure to perform fundamental studies at the microscopic level[27, 28] and better understand the challenges facing the FeF_3 conversion cathode. We have previously achieved the inexpensive and scalable solution-synthesis of α-$FeF_3 \cdot 3H_2O$ NWs[29] under low supersaturation conditions without surfactants and/or catalysts, following the design of dislocation-driven NW growth.[30-34] Here, we report a high-capacity FeF_3 cathode based on FeF_3 NWs that are prepared for the first time by dehydrating the α-$FeF_3 \cdot 3H_2O$ precursor NWs. The electrochemical properties of the FeF_3 cathodes made of nanocomposites of FeF_3 NWs, carbon black and polyvinylidene difluoride (PVDF) binder (Figure 2.1b) were investigated by cyclic voltammetry (CV), galvanostatic cycling, and electrochemical impedance spectroscopy (EIS). The FeF_3 NW cathode exhibited greatly improved room-temperature cycling performance compared to the previously reported FeF_3 cathodes based on FeF_3/C nanocomposites. Furthermore, we took advantage of the

improved electrochemical properties and the well-defined 1D nanostructure of the FeF_3 NWs to investigate the microstructural change and failing mechanism of the FeF_3 conversion cathode. *Ex situ* transmission electron microscopy (TEM) studies revealed for the first time that interconnected Fe nanodomains were formed in the lithiated FeF_3 NWs. EIS and TEM characterizations performed on the electrochemically cycled NWs also led to new insights into the cause of capacity fading for FeF_3 conversion cathode.

2.3 Results and Discussion

To prepare the FeF_3 NWs, first the hydrated α-$FeF_3 \cdot 3H_2O$ NWs were synthesized *via* an procedure improved upon our previous work[29] (see Supporting Information for experimental details). Figure 2.2a shows the SEM images of the as-synthesized α-$FeF_3 \cdot 3H_2O$ NWs with about 30–180 nm in diameter and 2–15 μm in length in high density, consistent with our previous work.[29] These hydrated NWs were dehydrated in an inert atmosphere (argon) at 350 °C to produce the FeF_3 NWs (Figure 2.2b) for the first time. The α-$FeF_3 \cdot 3H_2O$ NWs underwent complex phase transformations during the dehydration and mixtures of other phases could be obtained at lower dehydration temperatures (< 350 °C, see Figure A1.1 and Table A1.1). After dehydration, the NW morphology was well preserved (Figure 2.2b), but the diameter of NWs slightly decreased according to the size survey of the NWs before and after dehydration (Figure 2c). This can be explained by the loss of water molecules in the crystal lattice and a large increase in crystal density [$\rho(\alpha\text{-}FeF_3 \cdot 3H_2O)$ = 2.20 g cm^{-3}, while $\rho(FeF_3)$ = 3.87 g cm^{-3} and $\rho(FeF_2)$ = 4.09 g cm^{-3}]. PXRD (Figure 2.2d) clearly shows that the phase identity of the NWs is α-$FeF_3 \cdot 3H_2O$ (space group $R\bar{3}m$, a = 9.5135 Å, c = 4.7882 Å)[35] before and rhombohedral

FeF_3 (space group $R\bar{3}c$, JCPDS No. 33-0647, a = 5.2 Å, c = 13.323 Å) with some impurity FeF_2 (space group $P4_2/mnm$, JCPDS No. 45-1062, a = 4.7035 Å, c = 3.3056 Å) phase after the dehydration. Further examination of the dehydrated iron fluoride NWs using TEM revealed that these NWs were mostly polycrystalline and porous after the loss of water molecules. As shown in Figure 2e for one representative example, the dehydrated NWs have many voids and rough surfaces. Internal pores can also be observed more clearly in Figure 2.2f and 2.2g at higher magnification. This porous structure of the FeF_3 NWs can be advantageous for battery application due to the increased surface area and smaller domain size that further reduce the diffusion distances of Li^+ and electrons.[1, 26] High-resolution TEM (HRTEM) reveals that most of the NWs contain separate nanodomains of rhombohedral FeF_3 and tetragonal FeF_2, as highlighted in Figure 2f and 2g. The commonly observed lattice fringes match with the (012) and (104) crystal planes of FeF_3 and the (110) plane of FeF_2, respectively, all of which are consistent with the three most intense diffraction peaks in the PXRD diffractogram (Figure 2d). Interestingly, a few NWs (< 5% among all the objects examined) completely decomposed to form quasi-single-crystalline FeF_2 (Figure A1.2), as revealed by the selected area electron diffraction (SAED) pattern (Figure A1.2a inset). The corresponding HRTEM micrograph of the FeF_2 NW (Figure A1.2b) further confirms that the NW is a single crystal with its axial direction along <110>. As the first example of rationally controlled synthesis of transition metal fluoride NWs. the scalable and inexpensive approach to produce iron fluoride NWs discussed herein suggests a potentially general strategy to make other interesting transition metal fluoride NWs.

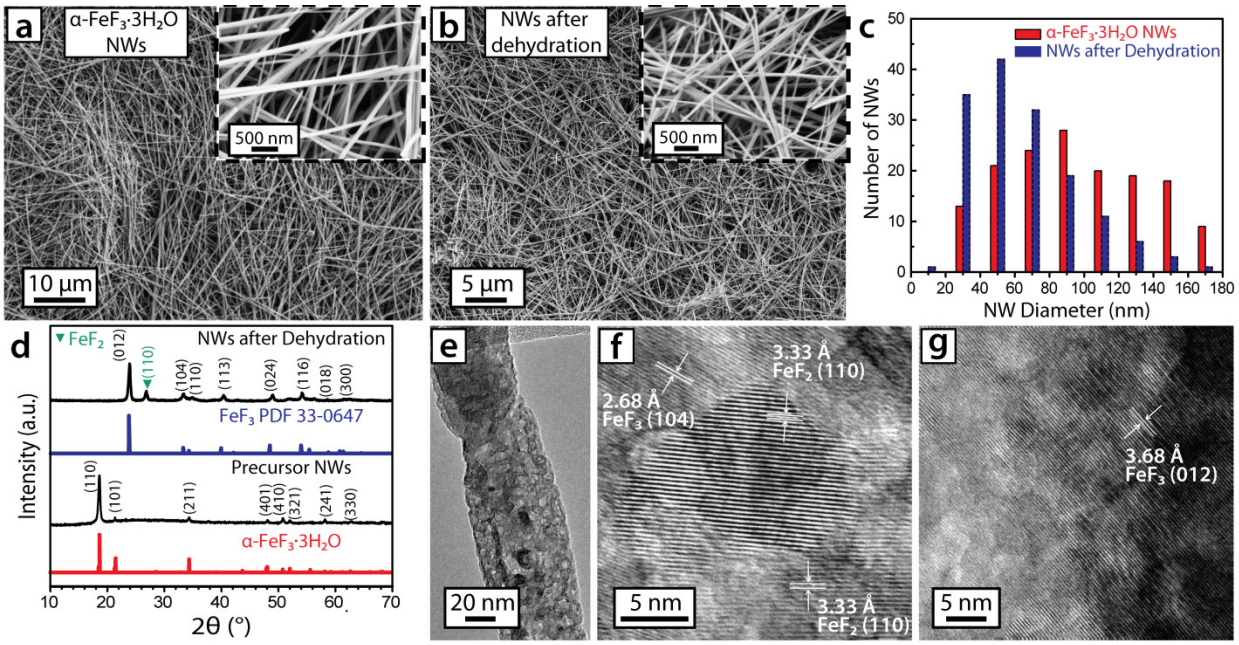

Figure 2.2 | Structural characterization of the FeF_3 NWs. (a) SEM images of the precursor α-$FeF_3 \cdot 3H_2O$ NWs in a large quantity prepared from a solution synthesis; (b) SEM images of the NWs after dehydration showing well preserved NW morphology; (c) Size distribution of the NWs before and after dehydration. The average diameter of the NWs decreased from 96 nm to 60 nm after the dehydration; (d) PXRD of the NWs before and after the dehydration in comparison with the reference diffractograms of α-$FeF_3 \cdot 3H_2O$ and rhombohedral FeF_3, respectively. There is some FeF_2 impurity phase, as denoted by the inverted green triangle; (e) A representative TEM image of the dehydrated NWs showing many voids and a rough surface; (f) and (g) are the magnified HRTEM images of the NW in (e), showing the nanodomains of rhombohedral FeF_3 and tetragonal FeF_2 in the same NW.

We carried out electrochemical measurements on the electrodes that were made by simply mixing the FeF_3 NWs, carbon black and PVDF binder in N-methyl-2-pyrrolidone (NMP) in a

weight ratio of 7:2:1 and pasting the resulting slurry onto aluminum foils, which is similar to the conventional battery packing process. This led to a bulk nanocomposite electrode made of networks of FeF_3 NWs interdispersed with carbon black NPs that has a loading of active materials of about 2 mg cm^{-2} and a thickness of 30–50 μm (see the scheme in Figure 2.1b). These FeF_3 NW electrodes are quite different from many previously reported NW battery electrodes that are based on NW arrays directly grown on metallic current collectors.[23-25]

We first measured the cyclic voltammogram (CV) of the FeF_3 NW electrode to qualitatively examine the reaction mechanism between FeF_3 and lithium (Figure 2.3a). The cathodic (lithiation) scan of the first cycle exhibits more reducing peak position at ~1.5 V. This may be attributed to the slower reaction kinetics in the first cycle to lithiate FeF_3 with larger domain size (reconverted FeF_3 has smaller domain size).[13] The CV (Figure 2.3a) is largely comparable with the previous results obtained on the FeF_3 nanocomposite electrodes (but limited to the first two cycles).[18, 22] The subsequent cycles show consistent cathodic and anodic peak positions, demonstrating the reversibility of the conversion/deconversion reaction. There are two pairs of redox peaks observed in the CV. The first pair of redox peaks at ~3.0 V (cathodic peak) and ~3.4 V (anodic peak) corresponds to the redox reactions between phases containing Fe^{3+} and Fe^{2+}. The second pair of redox peaks at ~1.7 V (cathodic peak) and ~2.8 V (anodic peak) should be attributed to the redox reactions between phases containing Fe^{2+} and metallic Fe^0. There also seems to be some electrolyte oxidation (3.9–4.2 V) in the first anodic scan, which becomes less obvious in subsequent cycles. More details on the reaction mechanism between FeF_3 and lithium have been discussed by Yamakawa et al[14] and Doe et al[15].

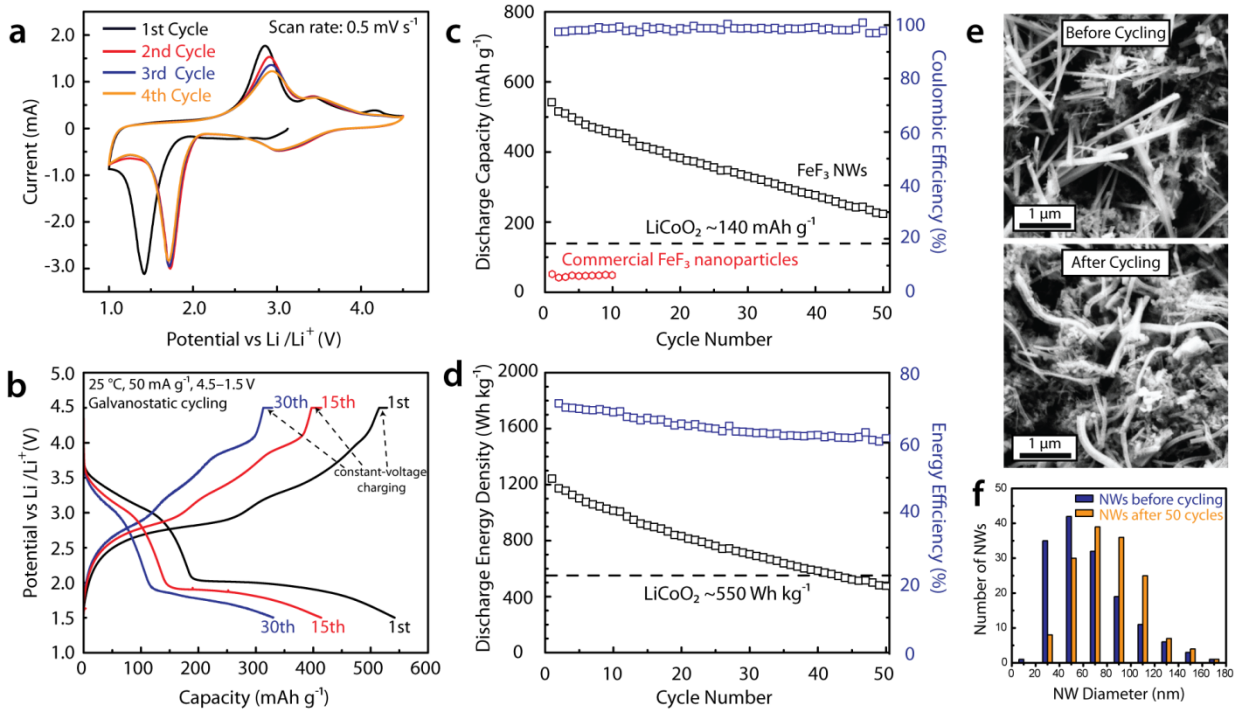

Figure 2.3 | Electrochemical and structural characterization of the FeF_3 NW cathode. (a) Cyclic voltammogram of the FeF_3 NW electrode scanned between 4.5 V and 1.0 V *vs* Li/Li^+ at a scan rate of 0.5 mV s^{-1}. The first four cycles are shown; (b) Voltage profiles for the 1st, 15th, and 30th discharge-charge cycles of the FeF_3 NW electrode tested under a current of 50 mA g^{-1} (1/14.2 C rate) at ~25 °C. Note that an additional constant-voltage charging step is performed after the constant-current charging step at 4.5 V until the current drops to 1/10 of its original value; (c) Discharge capacity and Coulombic efficiency of the FeF_3 NW electrode *vs* cycle number in comparison with the discharge capacity of the FeF_3 cathode made with commercial FeF_3 powder (the open red hexagons) and the practical capacity of $LiCoO_2$ (~140 mAh g^{-1}, the dashed line). Note that all the reported capacity performance in this paper was calculated based on the mass of the FeF_3 NWs only; (d) Discharge energy density and energy efficiency of the FeF_3 NW electrode *vs* cycle number shown along with the energy density of $LiCoO_2$ cathode

(~550 Wh kg^{-1}), which is calculated using an average voltage of 3.9 V and a capacity of ~140 mAh g^{-1}; (e) SEM images before and after the discharge-charge of 50 cycles showing the NW morphology mostly preserved; (f) Size distribution of the NWs before and after the cycling test showing slightly increased NW diameter after 50 cycles.

The lithium storage capability of the FeF_3 NW cathode was evaluated using discharge/charge cycling in the voltage window of 4.5–1.5 V at ~25 °C. The voltage profile (Figure 2.3b) shows a two-stage electrochemical conversion process, which is consistent with the previous results[13-16, 22] and the CV (Figure 2.3a). The FeF_3 NW cathode was found to exhibit a significantly higher capacity than the FeF_3 NP cathode (Figure 2.3c, the open black squares *vs* the open red hexagons) made from the commercial FeF_3 powder (with average grain size > 200 nm, see Figure A1.3). The FeF_3 NW cathode could yield a discharge capacity as high as 543 mAh g^{-1} (relative to the mass of FeF_3 NWs) at the first cycle and retain a capacity of 223 mAh g^{-1} after 50 cycles at a current of 50 mA g^{-1} (1/14.2 C rate), which are higher than the practical capacity of $LiCoO_2$ (~140 mAh g^{-1}, the dash line in Figure 2.3c) despite the fast capacity fading. We have also calculated the Coulombic efficiency (CE) of the Li/FeF_3 NW battery (Figure 2.3c, the open blue squares), which is defined as the ratio between discharge capacity ($Q_{discharge}$) and charge capacity (Q_{charge}). Note that the lithium-free FeF_3 cathode is initially at charged state and undergoes discharging in the 1st cycle so that the Coulombic efficiency is only calculated from the 2nd cycle to the 50th cycle using the following equation:

$$CE\ of\ cycle\ \#N = \frac{Q(discharge)\ of\ Cycle\ \#\ (N+1)}{Q(charge)\ of\ Cycle\ \#N},\ N \text{ is an integer and } N \geq 1.$$

The CE was found to be larger than 96% (Figure 2.3c), which seems to indicate encouraging charge-storage efficiency. However, further research is neccessary to rule out other possible side reactions such as electrolyte decomposition during battery cycling before this data can be accurately interpreted.[9] When cycled at a larger current of 200 mA g^{-1} (1/3.6 C rate), the FeF_3 NW cathode could still achieve a high discharge capacity about 470 mAh g^{-1} at the first cycle and retain a capacity of 147 mAh g^{-1} after 50 cycles (Figure A1.4). To the best of our knowledge, this is the best room-temperature (~25 °C) performance reported for a FeF_3 conversion cathode in terms of capacity, capacity retention, and rate capability in the voltage window of 4.5–1.5 V (A comparison with two previously reported results[13, 18] is shown in Figure A1.6a.) Note that blending the conductive carbon black with the FeF_3 NWs to make the composite is necessary to achieve this performance, as battery cells packed with pure FeF_3 NWs did not exhibit high capacity. Despite this improved performance, the capacity fading commonly observed for FeF_3 cathodes,[13, 18, 19] even though has been mitigated, has not been completely eliminated. After 100 cycles, the capacity of FeF_3 NW cathodes declined to only about 100 mAh g^{-1} (Figure A1.5). We will further discuss the cause of capacity fading later. We believe that the improved performance of the FeF_3 NW cathode may be attributed to the high surface-area of the NW electrode and the favorable NW morphology to accommodate structural strains occurring in the conversion/deconversion reactions. After 50 cycles, the NWs became tortuous but remained continuous and still appeared to have good electrical contact with the conductive carbon (Figure 2.3e). A slight increase in NW diameter was observed after cycling according to the size survey (Figure 2.3f), which could be related to the massive structural transformation and volumetric changes occurred in the conversion/deconversion reaction.[9] We also would like to point out that

the highest capacity was achieved on the cells that underwent one cycle of CV scan before the discharge/charge test. Such "activated" cells consistently yielded higher capacities relative to the non-activated ones (Figure A1.6a). EIS results revealed that the charge-transfer resistance was greatly reduced after the one cycle of CV scan (Figure A1.6b), which may give rise to better reaction kinetics and consequently the enhanced cycling performance. Further studies are needed to understand this "activation" process at the microscopic level.

As the result of the high capacity, the Li/FeF_3 NW battery delivered a high energy density (a product of capacity and voltage) of about 1243 Wh kg^{-1} (relative to the mass of FeF_3 NWs only) in the first cycle and maintained an energy density of 477 Wh kg^{-1} after 50 cycles at a current of 50 mA g^{-1} (Figure 2.3d). After further improvements to mitigate the capacity fading, it is promising that FeF_3 NW cathodes could double the energy density of the current $LiCoO_2$ cathode (~550 Wh kg^{-1}, relative to the mass of $LiCoO_2$ only). However, lithium-containing anodes such as the protected lithium metal anode,[36] lithium metal alloy,[37] prelithiated graphite[38] or silicon[39], or other new materials need to be explored to pair with the lithium-free FeF_3 cathode so that full batteries with higher energy-density can be achieved.

Despite the encouraging capacity and energy density, the large voltage hysteresis between the charge and discharge half-cycle (see Figure 2.3b) remains a great challenge for FeF_3 cathode.[9] Such hysteresis causes energy inefficiency, consuming extra energy for any amount stored (Figure 2.3d, energy efficiency = discharge energy density/charge energy density). Previous studies suggest that the hysteresis may be attributed to the intrinsically different reaction pathways on discharging and charging[15] but the kinetic contribution to the hysteresis should also be considered.[22] Further investigation on the origin of the voltage hysteresis is highly

desirable so that strategies can be designed to minimize it or at least make it more tolerable for practical applications. Few research efforts have been focused on this direction so far, which may be partially due to the lack of high-quality FeF_3 nanomaterials with good electrochemical properties and well-defined nanostructure. Therefore, the readily synthesized FeF_3 NWs reported herein can be used as a convenient platform to carry out fundamental studies and understand the challenges facing the FeF_3 conversion cathode.

In order to understand the phase and structural changes of FeF_3 cathode upon cycling as well as their potential relationship with the improved performance, we set out to investigate the microstructure of the FeF_3 NW cathode. The defined 1D nanostructure of NWs enabled more straightforward microstructural characterization on the electrochemically tested samples.[27, 28] We have examined at least 5 NW ensembles using SAED and more than 15 individual NWs using HRTEM for each of the TEM samples recovered from the cells at the first discharged (1.5 V) and first recharged (4.5 V) states, respectively. The representative SAED pattern (Figure 2.4a) shows that upon discharged to 1.5 V the FeF_3 NWs are electrochemically reduced to form LiF and α-Fe (with some unreacted FeF_2 phase left). Low-resolution TEM (LRTEM, Figure 2.4b) image reveals interesting features: small dark nanodomains (3–5 nm) can be clearly seen all over the lithiated NW. Further HRTEM characterization confirms that these dark nanodomains are single-crystal α-Fe oriented along the direction of $[11\bar{1}]$ zone axis (Figure 2.4c). We examined this more closely and took 8 selective-area fast Fourier transform (FFT) patterns all showing the same $[11\bar{1}]$ zone axis to highlight the interconnectivity between these α-Fe nanodomains (Figure 2.4c, see Figure A1.7 for an additional example). It appears that the Fe nanodomains are interconnected through their common {110} family planes to form a continuous network, which

is observed for the first time for FeF_3 cathodes. Similar microstructural feature has been previously observed in the lithiated FeF_2/C nanocomposites, which essentially have the same conversion product (LiF and α-Fe) when discharged to 1.5 V.[10] We believe that such continuous networks of metallic Fe nanodomains can provide internal conductive pathway inside the NWs, which wires up the active material domains, facilitates local electron transport, and thus improves the cycling performance. In the previously reported FeF_3/C nanocomposite electrodes,[13, 18, 20] the conversion of FeF_3 to form the Fe network may be more difficult because nanocomposite electrodes commonly suffer from phase separation and particle agglomeration which significantly increases the Li^+/electron transport distance.[10] This may provide some explanation for the improved performance our FeF_3 NW cathodes compared to those based on FeF_3/C nanocomposites.

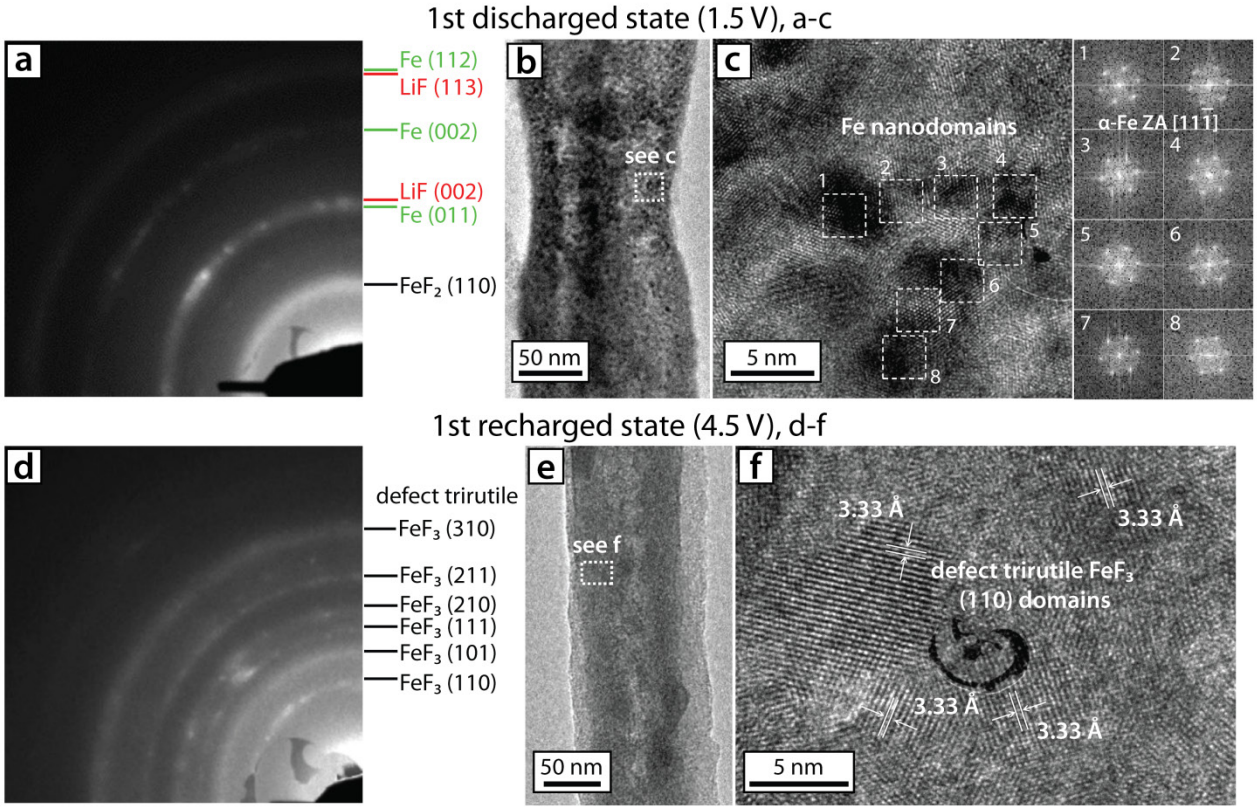

Figure 2.4 | Microstructural characterization of the FeF_3 NW cathodes at the first cycle. (a) Representative SAED pattern for an ensemble of NWs at the 1st discharged (lithiated) state showing the presence of LiF, α-Fe and some unreacted FeF_2 phase; (b) TEM image of a single lithiated FeF_3 NW with many small dark nanodomains (3–5 nm) clearly visible; (c) HRTEM image and FFT analysis confirming that the dark nanodomains are single-crystal α-Fe oriented along the direction of $[11\bar{1}]$ zone axis. These Fe nanodomains are interconnected to form a continuous network through the common {110} family planes. The interconnectivity between adjacent α-Fe nanodomains are highlighted in the HRTEM image; (d) Representative SAED pattern for an ensemble of NWs at the 1st recharged (delithiated) state showing that the NWs are reconverted to form defect-trirutile FeF_3; (e) TEM image of a single delithiated NW with no

small dark nanodomains observable; (f) HRTEM image showing multiple nanodomains of defect-trirutile FeF_3 in the delithiated NW shown in (e). The feature in the center of (f) is a known defect in the camera of the TEM at the time of the experiment.

When the FeF_3 NW cathode is recharged to 4.5 V, the SAED (Figure 2.4d) and the HRTEM (Figure 2.4f) show that the nanocomposite of LiF and Fe is completely reconverted to form defect-trirutile FeF_3 instead of the initial rhombohedral FeF_3, which is consistent with previous reports.[13, 15] No small dark spots could be seen anywhere in the LRTEM image (Figure 2.4e). The HRTEM image (Figure 2.4f) shows the recharged (delithiated) NWs are nanocrystalline with multiple defect-trirutile FeF_3 (110) nanodomains, confirming the nanocrystalline nature of the recharged (delithiated) NWs.

We also investigated the cause of capacity fading, which is a problem commonly observed for FeF_3 cathodes[13, 18] but has not been examined closely before. Previously reported FeF_3 cathodes based on FeF_3/C nanocomposites could only be cycled under very small currents at room temperature, which may have so far limited most studies to the first few cycles.[14, 22] The respectable electrochemical activities exhibited by the FeF_3 NW cathodes and their convenient characterization by TEM can facilitate our more in-depth investigations into the failure mechanism of FeF_3 cathodes. We first measured the impedance of a Li/FeF_3 cell using EIS to qualitatively examine the reaction kinetics of Li^+ transfer before electrochemical cycling, after 20 cycles, and after 50 cycles at the charged state (4.5 V). The obtained impedance data was interpreted in terms of Nyquist plots (Z_{real} *vs* $-Z_{im}$) shown in Figure 2.5. Each of them consists of a squashed semicircle in the high-frequency region and a quasi-sloping line in the low-frequency region. We fitted the data over the range from 200 kHz to 1 Hz to the equivalent circuit shown in

the inset of Figure 5, which is similar to the circuits used to analyze the EIS data for other conversion electrode materials.[40, 41] It consists of a ohmic resistance (R_Ω), a interfacial charge-transfer resistance (R_{ct}), a constant-phase-element (CPE, in place of a capacitor due to the squashed feature of the high-frequency semicircles), a Warburg element (Z_w, representing solid diffusion of the Li^+ in the electrode material) and a capacitance (C) reflecting the accumulation/consumption of Li^+ ions in the electrode material's bulk. Even though a single R_{ct} is used to fit the data due to the observation of one squashed semicircle, it may correspond to more than one interfacial charge-transfer processes which have comparable time constants. The R_{ct} (diameter of the semicircle) increased from 8.9 Ω before cycling to 23.6 Ω after 50 cycles, which may be attributed to a possible formation of solid-electrolyte-interface (SEI) layer due to the undesirable reaction(s) between the electrode material and the electrolyte. The detailed formation mechanism of SEI can be very complex for a conversion electrode material because of the dynamic nature of conversion reaction and the presence of metallic nanodomains which may catalyze the decomposition of the electrolyte.[42] Such SEI layer likely causes a weakened electrical contact between the current collector and FeF_3 NWs and slower Li^+ transfer kinetics, which could lead to capacity fading. On the other hand, the increase in the R_{ct} could also be related to the possible presence of LiF/Fe interface.[22] This is unexpected for the electrode at the charged state because the LiF and Fe phases are supposed to be fully reconverted to FeF_3 after recharging, which is indeed the case for the electrode at the 1st recharged state (see Figure 2.4d-f). Such incomplete reconversion of the LiF and Fe to FeF_3 could directly cause the capacity fading due to the loss of active material (FeF_3).

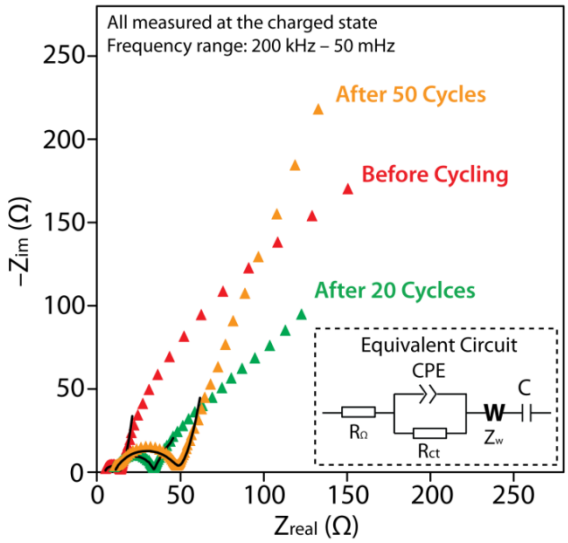

Figure 2.5 | Electrochemical impedance studies. Nyquist plots measured from the same FeF_3 NW electrode after different number of cycles. Symbols represent experimental spectra and continuous lines are the fitted data using the equivalent circuit shown in the inset. The charge-transfer resistance (diameter of the semicircle) increased as the cycle number increased.

While the results based on the EIS measurements hinted at the failure mechanism of the FeF_3 NW cathode, a more complete understanding at the microscopic level could potentially be achieved by direct observation of the microstructural change of the FeF_3 cathode. We therefore investigated and compared the phase and microstructure of the FeF_3 NW cathodes at the 50^{th} discharged state and 50^{th} recharged state respectively using TEM and SAED. For each of the TEM samples, we have examined at least 5 NW ensembles using SAED and more than 15 individual NWs using HRTEM to make sure that the reported results are representative. The SAED pattern (Figure 2.6a) shows that the phases that are present at the 50^{th} discharged state of the FeF_3 NW cathode are LiF and α-Fe. The TEM images in Figure 2.6b and 6c reveal the microstructural feature similar to that observed at the first discharged state (Figure 2.4a-c); dark

single-crystal nanodomains of α-Fe are interconnected through the common {110} family planes. More striking observation was made on the NWs at their ***50th recharged state***. The SAED pattern in Figure 2.6d shows that a significant amount of LiF and α-Fe are still present and not fully reconverted to form defect-trirutile FeF_3 as expected. Nanodomains of both FeF_3 (Figure 2.6f) and α-Fe (Figure 2.6g) were observed in the same NW (Figure 2.6e). This is quite different from the observation made on the FeF_3 NW cathode at its first recharged state (Figure 2.4d-f), where the full recovery of FeF_3 was realized. This new observation based on microstructural characterization corroborates our earlier analysis based on the EIS results and further suggests that the incomplete reconversion of Fe and LiF causes loss the of active material (FeF_3), which should be considered as the major factor responsible for the capacity fading upon cycling. It is interesting to ask that why the reconversion process, which was quite complete at the 1st cycle (see Figure 2.4d-f), became less effective at the 50th cycle and what exactly made it ineffective. It is also unclear that how the unconverted Fe left behind in previous cycles might affect the conversion reaction that involved new Fe formation in subsequent cycles. To answer these more difficult questions, future work should focus on better understanding the nucleation and growth of different nanophases in FeF_3 conversion cathodes during prolonged cycling and *in situ* TEM studies (nanobatteries built with FeF_3 NWs in a TEM) may be an interesting direction.[27, 28]

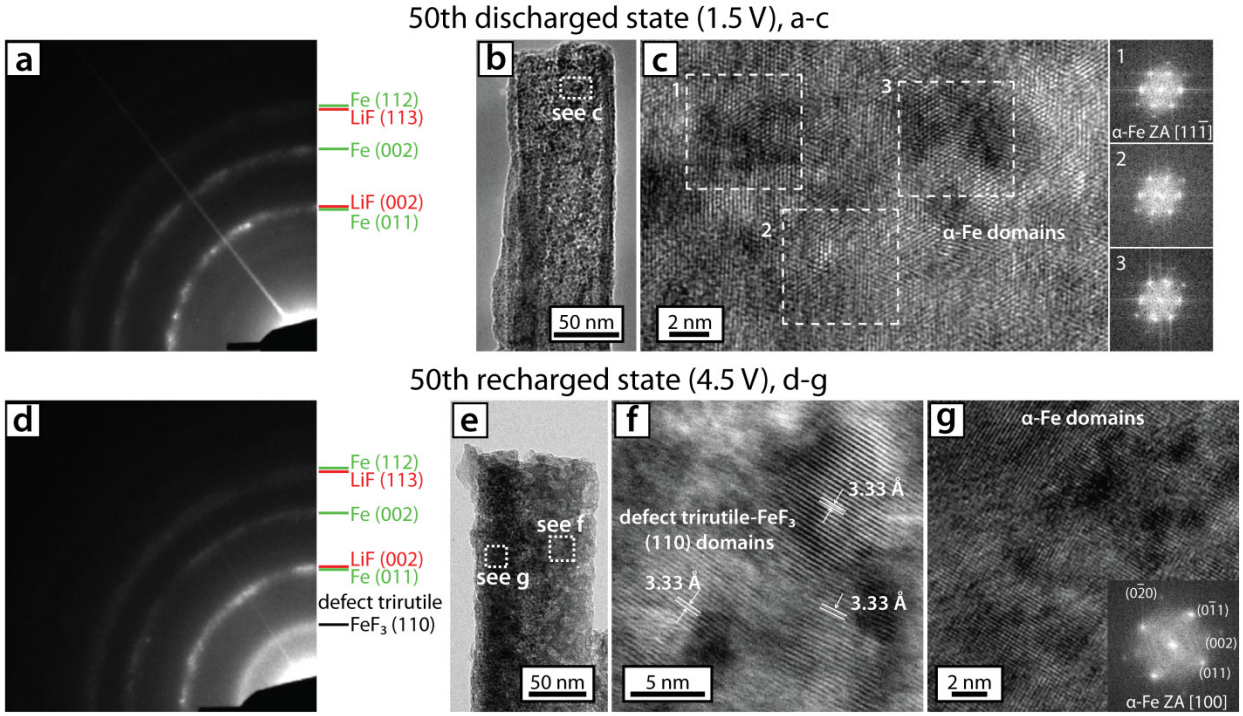

Figure 2.6 | Microstructural characterization of the FeF_3 NW cathodes at the 50th cycle. (a) Representative SAED pattern for an ensemble of NWs at the 50st discharged (lithiated) state showing the presence of LiF and α-Fe; (b) TEM image of a single lithiated FeF_3 NWs at its 50th discharged state; (c) HRTEM image and the associated FFT analysis showing the continuous network of α-Fe; (d) Representative SAED pattern for an ensemble of NWs at the 50st recharged (delithiated) state showing the presence of LiF and α-Fe, and some defect-trirutile FeF_3. The incomplete reconversion of LiF and α-Fe to form FeF_3 during charging caused the active material loss and the capacity decline upon cycling; (e) TEM image of a single delithiated NW at the 50th recharged state; (f) and (g) are the HRTEM images showing nanodomains of defect-trirutile FeF_3 and single-crystal α-Fe observed in the same NW shown in (e).

2.4 Summary and Outlooks

In summary, we have developed a better FeF_3 cathode that is based on a simple bulk nanocomposite of FeF_3 NWs, carbon black, and PVDF binder and used it as a platform to understand the challenges facing the FeF_3 conversion cathode. Porous FeF_3 NWs were prepared from α-$FeF_3 \cdot 3H_2O$ NWs by temperature-controlled dehydration in an inert atmosphere. The FeF_3 NW cathodes exhibited greatly improved electrochemical performance at room temperature, which may be attributed to the large surface area, the favorable morphology to accommodate transformation strains, and the internal conductive pathway provided by the continuous network of Fe nanodomains. TEM characterization revealed the interconnectivity between adjacent Fe nanodomains in fully lithiated FeF_3 NWs. Moreover, the improved rate capability and capacity retention of the FeF_3 NW cathode at room temperature allowed mechanistic investigation beyond the first few cycles. The increasingly ineffective reconversion of α-Fe and LiF to defect-trirutile FeF_3 during charging was found to be a major factor causing the capacity loss upon cycling. Possible fruitful directions to further improve FeF_3 conversion battery electrodes may include, but not are not limited to, using thinner and more porous FeF_3 NWs to further improve reaction kinetics, controlling the nucleation and growth of the relevant nanophases to enhance reversibility, and making FeF_3 NW/carbon nanotube or graphene nanocomposite electrodes to allow better electrical conductivity. These FeF_3 NWs herein reported have not only realized the most promising FeF_3 conversion cathode in terms of capacity and cycling performance, but also could provide a convenient platform for future research such as *in situ* TEM studies, due to their large quantity, ease of processing and good electrochemical properties. Thorough understanding

on the origins of capacity fading and voltage hysteresis could ultimately allow for the application of conversion cathodes in high energy-density batteries.

2.5 References

1. Bruce, P. G., Energy storage beyond the horizon: Rechargeable lithium batteries. *Solid State Ionics* **179,** 752-760 (2008).

2. Goodenough, J. B., Kim, Y., Challenges for Rechargeable Li Batteries†. *Chem. Mater.* **22,** 587-603 (2009).

3. Armand, M., Tarascon, J. M., Building better batteries. *Nature* **451,** 652-657 (2008).

4. Goodenough, J. B., Evolution of Strategies for Modern Rechargeable Batteries. *Acc. Chem. Res.* **ASAP,** DOI: 10.1021/ar2002705 (2012).

5. Duduta, M., et al., Semi-Solid Lithium Rechargeable Flow Battery. *Adv. Energy Mater.* **1,** 511-516 (2011).

6. Bruce, P. G., Freunberger, S. A., Hardwick, L. J., Tarascon, J.-M., Li-O_2 and Li-S batteries with high energy storage. *Nature Mater.* **11,** 19-29 (2012).

7. Peng, Z., Freunberger, S. A., Chen, Y., Bruce, P. G., A Reversible and Higher-Rate Li-O2 Battery. *Science* **337,** 563-566 (2012).

8. Ji, X., Lee, K. T., Nazar, L. F., A highly ordered nanostructured carbon-sulphur cathode for lithium-sulphur batteries. *Nature Mater.* **8,** 500-506 (2009).

9. Cabana, J., Monconduit, L., Larcher, D., Palacin, M. R., Beyond Intercalation-Based Li-Ion Batteries: The State of the Art and Challenges of Electrode Materials Reacting Through Conversion Reactions. *Adv. Mater.* **22,** E170-E192 (2010).

10. Wang, F., et al., Conversion Reaction Mechanisms in Lithium Ion Batteries: Study of the Binary Metal Fluoride Electrodes. *J. Am. Chem. Soc.* **133,** 18828-18836 (2011).

11. Poizot, P., et al., Nano-sized transition-metal oxides as negative-electrode materials for lithium-ion batteries. *Nature* **407,** 496-499 (2000).

12. Li, H., Balaya, P., Maier, J., Li-Storage via Heterogeneous Reaction in Selected Binary Metal Fluorides and Oxides. *J. Electrochem. Soc.* **151,** A1878-A1885 (2004).

13. Badway, F., Cosandey, F., Pereira, N., Amatucci, G. G., Carbon metal fluoride nanocomposites - High-capacity reversible metal fluoride conversion materials as rechargeable positive electrodes for Li batteries. *J. Electrochem. Soc.* **150,** A1318-A1327 (2003).

14. Yamakawa, N., Jiang, M., Key, B., Grey, C. P., Identifying the Local Structures Formed during Lithiation of the Conversion Material, Iron Fluoride, in a Li Ion Battery: A Solid-State NMR, X-ray Diffraction, and Pair Distribution Function Analysis Study. *J. Am. Chem. Soc.* **131,** 10525-10536 (2009).

15. Doe, R. E., Persson, K. A., Meng, Y. S., Ceder, G., First-Principles Investigation of the Li-Fe-F Phase Diagram and Equilibrium and Nonequilibrium Conversion Reactions of Iron Fluorides with Lithium. *Chem. Mater.* **20,** 5274-5283 (2008).

16. Badway, F., Pereira, N., Cosandey, F., Amatucci, G. G., Carbon-Metal Fluoride Nanocomposites. Structure and electrochemistry of FeF_3:C. *J. Electrochem. Soc.* **150,** A1209-A1218 (2003).

17. Li, R. F., Wu, S. Q., Yang, Y., Zhu, Z. Z., Structural and Electronic Properties of Li-Ion Battery Cathode Material FeF_3. *J. Phys. Chem. C* **114,** 16813-16817 (2010).

18. Kim, S.-W., et al., Fabrication of FeF_3 Nanoflowers on CNT Branches and Their Application to High Power Lithium Rechargeable Batteries. *Adv. Mater.* **22,** 5260-5264 (2010).

19. Li, C., Mu, X., van Aken, P. A., Maier, J., A High-Capacity Cathode for Lithium Batteries Consisting of Porous Microspheres of Highly Amorphized Iron Fluoride Densified from Its Open Parent Phase. *Adv. Energy Mater.* ***3*****,** 113-119 (2012).

20. Li, T., et al., Reversible Three-Electron Redox Behaviors of FeF_3 Nanocrystals as High-Capacity Cathode-Active Materials for Li-Ion Batteries. *J. Phys. Chem. C* **114,** 3190-3195 (2010).

21. Ma, D.-l., et al., Three-dimensionally ordered macroporous FeF_3 and its in situ homogenous polymerization coating for high energy and power density lithium ion batteries. *Energy Environ. Sci.* **5,** 8538-8542 (2012).

22. Liu, P., et al., Thermodynamics and Kinetics of the Li/FeF_3 Reaction by Electrochemical Analysis. *J. Phys. Chem. C* **116,** 6467-6473 (2012).

23. Chan, C. K., et al., High-performance lithium battery anodes using silicon nanowires. *Nature Nanotech.* **3,** 31-35 (2008).

24. Chan, C. K., Zhang, X. F., Cui, Y., High Capacity Li Ion Battery Anodes Using Ge Nanowires. *Nano Lett.* **8,** 307-309 (2007).

25. Li, Y. G., Tan, B., Wu, Y. Y., Mesoporous Co_3O_4 nanowire arrays for lithium ion batteries with high capacity and rate capability. *Nano Lett.* **8,** 265-270 (2008).

26. Szczech, J. R., Jin, S., Nanostructured silicon for high capacity lithium battery anodes. *Energy Environ. Sci.* **4,** 56-72 (2011).

27. Huang, J. Y., et al., In Situ Observation of the Electrochemical Lithiation of a Single SnO_2 Nanowire Electrode. *Science* **330,** 1515-1520 (2010).

28. Liu, X. H., Huang, J. Y., In situ TEM electrochemistry of anode materials in lithium ion batteries. *Energy Environ. Sci.* **4,** 3844-3860 (2011).

29. Li, L., et al., Facile Solution Synthesis of α-$FeF_3 \cdot 3H_2O$ Nanowires and Their Conversion to α-Fe_2O_3 Nanowires for Photoelectrochemical Application. *Nano Lett.* **12,** 724-731 (2012).

30. Morin, S. A., Bierman, M. J., Tong, J., Jin, S., Mechanism and Kinetics of Spontaneous Nanotube Growth Driven by Screw Dislocations. *Science* **328,** 476-480 (2010).

31. Jin, S., Bierman, M. J., Morin, S. A., A New Twist on Nanowire Formation: Screw-Dislocation-Driven Growth of Nanowires and Nanotubes. *J. Physc. Chem. Lett.* **1,** 1472-1480 (2010).

32. Meng, F., Jin, S., The Solution Growth of Copper Nanowires and Nanotubes is Driven by Screw Dislocations. *Nano Lett.* **12,** 234-239 (2011).

33. Hacialioglu, S., Meng, F., Jin, S., Facile and mild solution synthesis of Cu_2O nanowires and nanotubes driven by screw dislocations. *Chem. Commun.* **48,** 1174-1176 (2012).

34. Estruga, M., et al., Large-scale solution synthesis of α-AlF3$\cdot 3H_2O$ nanorods under low supersaturation conditions and their conversion to porous α-AlF_3 nanorods. *J. Mater. Chem.* **22,** 20991-20997 (2012).

35. Karraker, D. G., Smith, P. K., .alpha.- and .beta.-ferric fluoride trihydrate revisited: crystal structure and iron-57 Moessbauer spectra. *Inorg. Chem.* **31,** 1118-1120 (1992).

36. Choi, N. S., et al., Protective coating of lithium metal electrode for interfacial enhancement with gel polymer electrolyte. *Solid State Ionics* **172,** 19-24 (2004).

37. Besenhard, J. O., Yang, J., Winter, M., Will advanced lithium-alloy anodes have a chance in lithium-ion batteries? *J. Power Sources* **68,** 87-90 (1997).

38. Jarvis, C. R., Lain, M. J., Yakovleva, M. V., Gao, Y., A prelithiated carbon anode for lithium-ion battery applications. *J. Power Sources* **162,** 800-802 (2006).

39. Liu, N., et al., Prelithiated Silicon Nanowires as an Anode for Lithium Ion Batteries. *ACS Nano* **5,** 6487-6493 (2011).

40. Reddy, M. V., et al., α-Fe_2O_3 Nanoflakes as an Anode Material for Li-Ion Batteries. *Adv. Funct. Mater.* **17,** 2792-2799 (2007).

41. Reddy, M. V., Madhavi, S., Subba Rao, G. V., Chowdari, B. V. R., Metal oxyfluorides $TiOF_2$ and NbO_2F as anodes for Li-ion batteries. *J. Power Sources* **162,** 1312-1321 (2006).

42. Gmitter, A. J., et al., Formation, dynamics, and implication of solid electrolyte interphase in high voltage reversible conversion fluoride nanocomposites. *J. Mater. Chem.* **20,** 4149-4161 (2010).

CHAPTER 3

Visualization of Electrochemically-Driven Solid-State Phase Transformations Using *Operando* Hard X-ray Spectro-Imaging

3.1 Abstract

In situ techniques with high temporal, spatial, and chemical resolution are the key to understanding ubiquitous solid-state phase transformations, which are crucial to many technological applications. Hard X-ray spectro-imaging can visualize electrochemically-driven phase transformations but demands considerably large samples with strong absorption signal so far. Here we show a conceptually new data analysis method to enable *operando* visualization of mechanistically-relevant weakly-absorbing samples at the nanoscale and study electrochemical reaction dynamics of iron fluoride (FeF_3), a promising high-capacity conversion cathode material. In two specially designed samples with distinctive microstructure and porosity, we observe homogeneous phase transformation during both discharge and charge, faster and more complete Li-storage occurring in porous polycrystalline FeF_3, and further, incomplete charge reaction following a pathway different from conventional belief. These new mechanistic insights provide guidelines for designing better conversion cathode materials to realize the promise of high-capacity lithium-ion batteries.

This work was originally published in *Nature Commun.* **6**, 6883, (2015), in collaboration with Y.-c. K. Chen-Wiegart, J. Wang, P. Gao, Q. Ding, Y.-S. Yu, F. Wang, J. Cabana, J. Wang, and S. Jin.

3.2 Introduction

Solid-state phase transformations are ubiquitous and important to numerous applications[1]. They are not only the primary way to make technologically important materials (such as martensitic steel, inorganic ceramics, and thin-film absorbers for solar cells), but also lie at the heart of electrochemical energy storage, in which the insertion and extraction of charge storage ions (such as Li^+ and Na^+) are always accompanied by electrochemically-driven solid-state phase transformations[2]. There has been significant interest in monitoring and probing these transformation processes over the last few decades in the hope of gaining mechanistic understanding to guide further optimization and bring technological benefits. The most commonly used techniques to analyze characteristics of phase transformations include *in situ* X-ray diffraction (XRD)[3], neutron diffraction[4], X-ray absorption spectroscopy (XAS)[5, 6], and solid-state nuclear magnetic resonance (NMR)[6]. These techniques enable valuable insights into changes in long-range structure, local bonding and chemical environment, elemental composition, and oxidation state. However, they only reveal average information over a large sample volume (micrometer to millimeter scale). Recently, the remarkable advances in *in situ* transmission electron microscopy (TEM) have made it possible to probe phase transformation down to nanoscale[7-10]. When coupled with electron diffraction (ED) and/or electron energy-loss spectroscopy (EELS), *in situ* TEM serves as a perfect diagnostic tool to track nanoscale morphological and structural changes as well as new phase nucleation and propagation with nanoscale spatial resolution. However, TEM-based experiments require restrictively thin samples (100 nm or below) and must be compatible with the high vacuum environment inside the microscope. These limitations complicate the experimental design and the straightforward correlation of the observed phenomena to what actually occur under realistic conditions.

Furthermore, TEM-based techniques are inherently incapable of probing the bulk of a working device, such as a battery or a fuel cell electrode, which is typically made of multiple components assembled at micro- or larger length scales.

Hard X-ray spectro-imaging provides an innovated approach to visualize electrochemically-driven solid-state phase transformations at the nanoscale[11]. Taking advantage of the strong and deeply penetrating hard X-rays generated by synchrotron radiation and the chemical and elemental sensitivity with a full-field imaging capability provided by the transmission X-ray microscopy (TXM) coupled with X-ray absorption near-edge structure spectroscopy (XANES)[12, 13], progression of a electrochemical reaction in a realistic battery electrode can be visualized in a large (tens of microns) field-of-view (FOV) with nanoscale spatial resolution. Unlike *in situ* TEM experiments that often have to be carried out using specialized sample holders in electrochemical conditions drastically different from those in a practical battery[7-9], hard X-ray based experiments can be conveniently performed in relevant and realistic conditions using a much simpler cell design[14-17]. Proof-of-concept *operando* hard X-ray spectro-imaging experiments have been recently demonstrated by using large microparticles[18-21] or aggregates of small particles[20] (several microns in total size) with strong X-ray absorption signal, in which cases chemical phase maps could be generated using simple data processing methods by approximating the X-ray absorption of materials under study to the experimentally determined total X-ray absorption. However, those approaches ignored background absorption and thus cannot accurately determine actual X-ray absorption of smaller and weakly absorbing samples at single-particle level under *operando* conditions. In order to study small particles, which, in fact, are more electrochemically active and mechanistically relevant, we herein propose and develop a

conceptually new data analysis method to reliably determine X-ray absorption of study materials and for the first time realized *operando* studies of phase evolution in a high-capacity Li-ion battery conversion cathode with nanoscale chemical resolution.

Here the conversion reaction of iron fluoride (FeF_3) was chosen as a demonstration example for *operando* mechanistic studies. FeF_3 is a promising prototype conversion cathode material with extremely high Li-storage capacity (712 mAh g^{-1})[22-29], 4–5 times higher than current intercalation cathode materials such as $LiCoO_2$ (~140 mAh g^{-1}) and $LiFePO_4$ (~mAh g^{-1}). This is achieved by utilizing all of the oxidation states of Fe through an electrochemical conversion reaction to enable multiple electron transfer and Li-ion storage.

$$FeF_3 + 3Li^+ + 3e^- \rightleftarrows 3LiF + Fe \quad (1)$$

Consequently, batteries based on a FeF_3 conversion cathode (theoretical voltage ~2.7 V)[23] and a suitable lithium-containing anode, such as a protected lithium metal anode[30], hold the promise to significantly increase the energy density of current Li-ion battery technology[22, 31]. However, such promise has yet to be realized due to challenges associated with the significant phase transformation and structural rearrangement during cycling. Two prominent ones are capacity decay and a large voltage hysteresis[24, 26, 32-34]. Solving these challenges requires a better understanding of the electrochemical reaction mechanism under *operando* conditions, especially the recharge reaction, which has been surprisingly under-researched compared with the discharge reaction[35, 36]. Here we use the improved *operando* hard X-ray spectro-imaging to track the phase evolution of FeF_3 cathodes during cycling and reveal how electrochemical reactions progress kinetically and spatially, which provides insights essential to rationally designing electrode microstructure to achieve fast kinetics and high reversibility. We also discover evidences across

different length scales that suggest a charge reaction pathway different from traditional belief, which advances the understanding on the causes of capacity decay and voltage hysteresis.

3.3 Results

3.3.1 Improved experimental setup and new data analysis method

In the *operando* experiments (Figure 3.1a), synchrotron monochromatic X-rays are directed to transmit through a perforated 2032-type coin-cell (Figure 3.1b and 1c) containing the FeF_3 cathode and all the other key components of a realistic battery, such as carbon black, polymeric binder, and a liquid electrolyte (Figure 3.1d). The holes in the coin-cell, which are sealed using Kapton tape (Figure 3.1c,d), need to be small to ensure a small cell impedance. The resulted absorption-contrast images are projected onto a lens-coupled full-field CCD detector using a zone-plate and recorded.

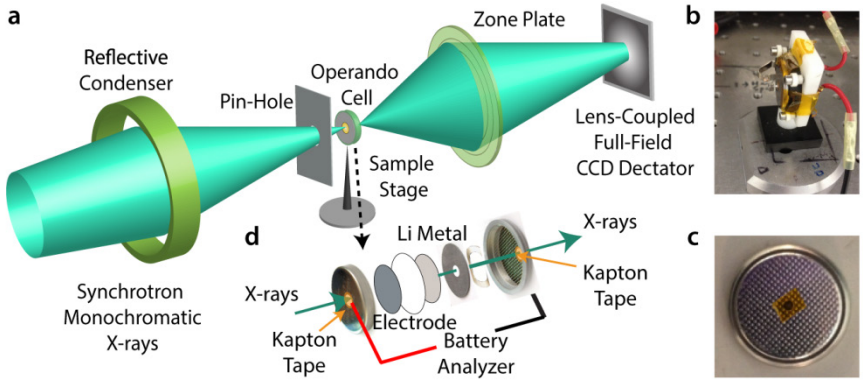

Figure 3.1 | Schematic illustration of the TXM experimental setup. (**a**) Sketch of the full-field transmission X-ray microscope. Photographs of (**b**) the custom-built cell holder and (**c**) a perforated coin cell used for the *operando* studies. (**d**) Schematic illustration of the *operando* cell containing the FeF_3 electrode and all the other key components of a realistic battery.

Figure 3.2a–f illustrate general procedures to realize chemical phase mapping; a detailed comparison between previous methods (Figure 3.2a-d) and our new method (Figure 3.2a, b, e, f) are discussed later in the manuscript. First, a series of images are collected by scanning the energy across the Fe *K*-edge (7112 eV) in a step size of 2 eV, one image at each energy (Figure 3.2a). Then, the XANES spectra at each pixel are constructed by plotting normalized X-ray absorption versus energy (Figure 3.2b and c, or b and e). They are fitted to reference spectra collected from standard compounds ($Fe^{3+}F_3$, $Fe^{2+}F_2$, and Fe) to determine ratio between different Fe-containing phases so that RGB colors can be accordingly assigned to generate a phase map (Figure 3.2d or f). As Fe of various oxidation states interacts with X-ray differently, their spatial distribution at different states of discharge/charge reveals progression of the electrochemical reaction in the FeF_3 cathode.

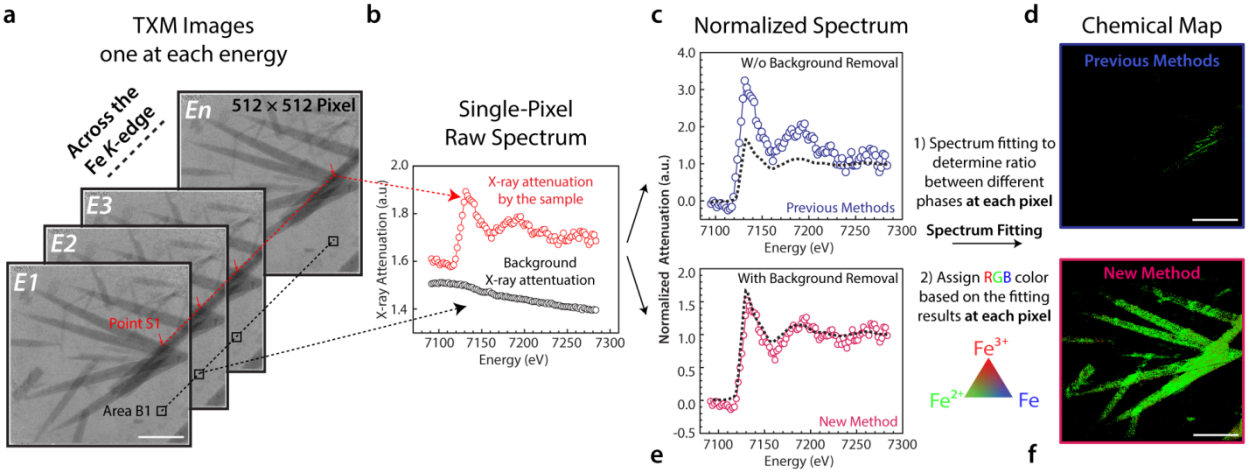

Figure 3.2 | Construction of the chemical phase maps using the new data analysis method. (**a**) A series of TXM image (512 × 512 pixels) collected by scanning across the Fe K-edge, one image at each energy. The *operando* cell was discharged to ~2.0 V when the data were collected. Scale bar is 10 μm. (**b**) XANES spectra from the areas with and without the study sample,

respectively. The background spectrum contains information on X-ray attenuation by all the other components in the *operando* cell. (**c**) XANES spectrum directly normalized without background removal using previously reported methods, which is clearly off the scale compared with a reference spectrum collected from FeF_2 powder (black dashed line). When the spectra at all pixels are processed the same way and fitted, only very few pixels could be preserved, leading to the unsatisfactory chemical map in (**d**). In contrast, (**e**) shows the spectrum correctly normalized by subtracting the background X-ray attenuation first before the normalization. The reference spectrum collected from FeF_2 powder (black dashed line) is shown as a comparison. (**f**) High-quality chemical phase maps constructed by fitting the background-subtracted normalized spectra at each pixel.

We have developed a conceptually new data analysis method to enable *operando* spectro-imaging of small samples with weak absorption signal (more details available in A2.1 Supplementary Methods). In *operando* experiments, the X-rays are not just absorbed by the Fe-containing active material, but also attenuated by all other battery components in the pathway of the beam, such as the carbon black, polymeric binder, separator and liquid electrolyte, which may be considered as an internal background as a whole. Previous methods depend heavily upon strong X-ray absorption of large samples (tens of microns in size) and consider that the X-ray absorption of materials under study is approximately equal to the experimentally determined total X-ray absorption[18-21], in which background absorption is omitted. This approximation is no longer valid for smaller and weakly absorbing samples, such as the porous microwires (MWs) examined here (effective thickness < 1 μm when porosity is considered). It results in improperly normalized XANES spectra (Figure 3.2c) and consequently unsatisfactory chemical phase maps

(Figure 3.2d and see an example of complete comparison in Figure A2.1 and A2.2). We propose and show that the X-ray absorption of the Fe-containing active material can be determined more accurately by subtracting an internal background spectrum from the total X-ray attenuation over the whole imaging area of 512 × 512 pixels. We use the X-ray attenuating information readily available from an area in the same FOV, where the X-rays only pass through the other battery components but not the Fe-containing active material (Figure 3.2a, black box), to more accurately represent the internal background absorption spectrum (Figure 3.2b, black circles). We then subtract such background from the total X-ray absorption spectrum (Figure 3.2b, red circles) at each pixel to determine the actual X-ray absorption of the study material. We also note that background absorption can be mathematically fitted to allow high-quality normalization within a single XANES spectrum[37, 38], but such methods are extremely calculation-intensive to implement when dealing with a considerably large number of spectra (512 × 512 spectra) in spectro-imaging. After internal background removal using our new method, the XANES spectrum (Figure 3.2e) at each pixel can be correctly normalized and fitted to a linear combination of standard reference spectra, enabling high-quality chemical phase mapping under *operando* battery conditions (Figure 3.2f). Note that even though the intrinsic spatial resolution is dictated by the current instrumentation (~25 nm for camera binning 1)[13], the new data analysis method helps determine the X-ray absorption of weakly absorbing samples more accurately at single-particle level so that many more image pixels that contain meaningful chemical information are preserved. These improvements enable the chemical phase mapping of samples that are smaller in size (hundreds of nanometers) than those reported before (several microns in total size)[18-21].

3.3.2 FeF_3 model samples and *in situ* electrochemical cell

Our *operando* experiments also benefit from two specially designed FeF_3 samples with well-defined morphologies of polyhedron (Figure 3.3a) and MWs (Figure 3.3b). These two samples are synthesized for the first time by rationally controlling super-saturation[26, 39-41] (see Methods for synthetic details) and are quite different in microstructure, porosity, and electrochemical activity. The FeF_3 polyhedra are single-crystalline (as proven by the ED pattern in Figure 3.3a inset), non-porous (Figure A2.3) and can only reach ~1/3 of the theoretical Li-storage capacity in the conventional battery test (Figure A2.5), while the MWs are polycrystalline (Figure 3.3b inset), mesoporous, grain-boundary-rich (Figure A2.4), and almost reach full capacity (Figure A2.5). We made an electrode containing both the polyhedra and MWs to enable comparative study and reveal the relation between structure and electrochemical properties. Porous carbon paper (~110 μm in thickness) was used as the current collector for this electrode. It is quite transparent to hard X-rays but still robust enough for handling, which is critical to the *operando* spectro-imaging experiment. More details on the electrode and cell preparation can be found in A2.1 Supplementary Methods. The *operando* cell was discharged at a constant current of ~1/15 C (~47.5 mA/g) to 1.5 V (Figure 3.3c). TXM images were recorded in dynamic conditions at different states of discharge/charge in two different locations. The data were processed by our new approach and fitted to the standard reference spectra (Figure 3.3d) to generate the chemical phase maps shown in Figure 3.3e (FOV 1) and 2f (FOV 2). Similar *operando* studies were also carried out in an electrode containing only FeF_3 MWs cycled in potentiostatic mode (Figure A2.6).

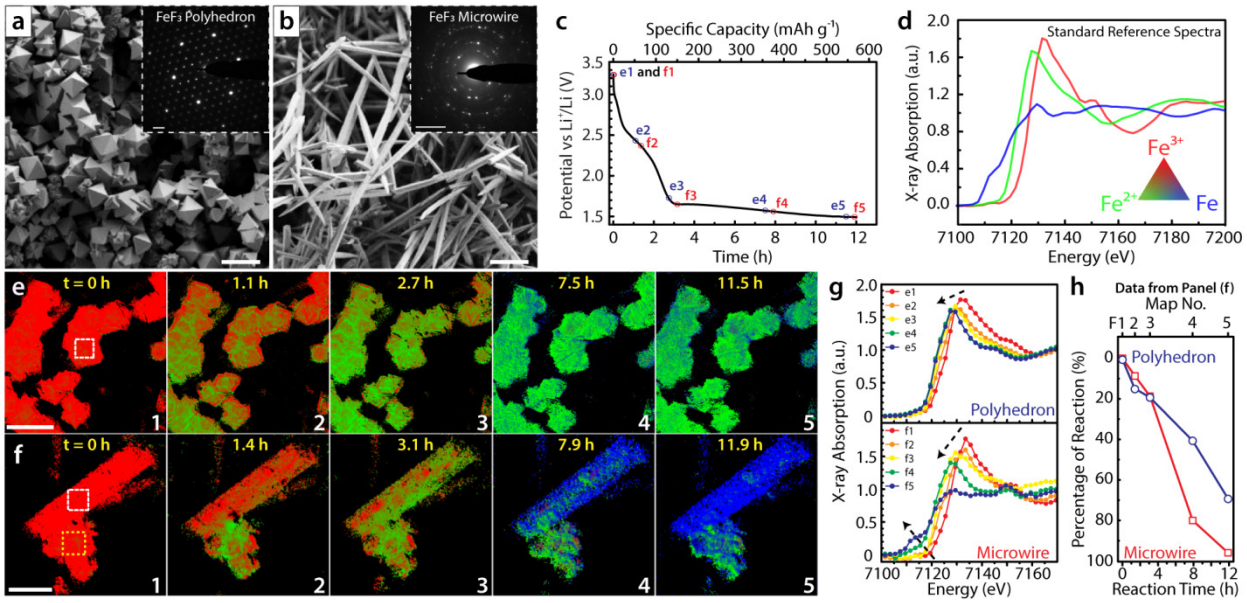

Figure 3.3 | Visualization of the discharge reaction of FeF_3 cathodes using hard X-ray spectro-imaging. (**a, b**) Scanning electron micrographs of the FeF_3 polyhedra and MWs. Insets are ED patterns taken on an individual polyhedron and an individual MW showing that the polyhedron is single-crystalline while the MW is polycrystalline. Scale bars are 10 μm in the two panels and 5 nm^{-1} in their insets. (**c**) Discharge voltage profile of the *operando* cell that contains a FeF_3 cathode of mixed polyhedra and MWs. The cell was discharged at rate of ~1/15 C to 1.5 V. The small black circles indicate the states of discharge where the data were collected to construct chemical phase maps. (**d**) Reference spectra collected from standard compounds ($Fe^{3+}F_3$, $Fe^{2+}F_2$, and Fe). (**e**) and (**f**) are two series of chemical phase maps showing how the electrochemical discharge reaction proceeded in two different regions of the mixed FeF_3 electrode. Scale bars are 10 μm and 5 μm, respectively. Red, green, and blue pixels represent Fe (+III), Fe (+II), and metallic Fe, respectively. (**g**) shows two series of XANES spectra taken from two selected areas of the mixed electrode, indicated by the white boxes in the first maps of (**e**)

and (**f**), which shows that the discharge reaction of the MW was more complete than that of the polyhedron. This is further confirmed by a quantitative comparison in reaction progress (consumption of FeF_3) between a MW and a polyhedron (**h**). The data were taken from two selected areas indicated by the white and yellow boxes in the first map of (**f**).

3.3.3 *Operando* visualization of FeF_3 electrochemical reaction

Enabled by the technological advances in spectro-imaging, we first visualized the progression of electrochemical discharge reaction in the FeF_3 conversion cathode. Two consecutive phase transformations consistent with the sequential lithiation reaction of FeF_3[26, 32, 33] were observed in both the polyhedra and MWs (Figure 3.3e and f). First, from the open-circuit voltage 3.24 V to 1.62 V, red pixels were gradually replaced by green pixels (Figure 3.3e and f, map 1 to 3), which is related to the initial Li^+ intercalation into FeF_3 with Fe (+III, red color) being reduced to Fe (+II, green color). Then, in the sloping voltage plateau between 1.62 V to 1.5 V, blue pixels appeared at the expense of the green pixels (Figure 3.3e and f, map 4 to 5), indicating the formation of metallic Fe (blue color) through the conversion reaction. However, while the first reduction could proceed to completion in both FeF_3 samples, the progression of the second reduction is clearly quite different. The conversion from Fe (+II) to metallic Fe was incomplete for the polyhedra (Figure 3.3e, map 5). Compared with the reference spectra (Figure 3.3d), selected-area XANES spectra taken on the polyhedron reveals that Fe (+II) and metallic Fe coexisted in the end (Figure 3.3g, top panel). The contrast in electrochemical activity is further highlighted in Figure 3.3f, in which one MW and one polyhedron are situated side by side. The MW became mostly metallic Fe (mostly blue) whereas the polyhedra did not react completely (still a lot of green) at the end of discharge (Figure 3.3f, map 5). The change in

XANES spectra taken on the MWs (Figure 3.3g) is consistent with the successive reduction of Fe (+III) to Fe (+II) and then to metallic Fe. Quantitative comparison of the reaction progress based on spectrum fitting (Figure 3.3h) also confirms that the MWs react faster and more completely than the polyhedra. These observations not only explain the difference in discharge capacity in our conventional battery tests (Figure A2.5) but also reveal the importance of porous and grain-boundary-rich structure to promote the complete three-Li^+ storage for FeF_3 conversion cathodes. During discharge, electron transport may become less of a concern once metallic iron precipitates out and starts propagating to form a conductive network within the solid[8, 26, 35, 42]. Therefore, the key to achieving high capacity likely depends on efficient Li^+ transport to trigger the Fe and LiF precipitation after the structure is saturated with Li^+ [8]. This process could be facilitated by the porous and grain-boundary-rich structure of the MWs.

Furthermore, we were able to visualize the spatial dynamics of the electrochemical reaction over a large area (tens of microns) thanks to the unique capability of TXM-XANES in spatially resolving chemical identification in a large FOV. As shown by the concurrent color change in the ensemble of polyhedra (Figure 3.3e) and MWs (Figure A2.6), the electrochemically-driven phase transformations in the FeF_3 cathode are relatively homogenous, indicating the absence of preferential reaction sites during discharge. All particles were actively discharging, though some local regions on individual particles appeared to react more slowly. Because these experiments were carried out on both single-crystalline and polycrystalline FeF_3 samples under *operando* conditions, we believe this observation reveals the inherent reaction characteristics of FeF_3 conversion cathodes. Interestingly, this behavior is different from that of the $LiFePO_4$ intercalation cathode material, in which significant inhomogeneities (i.e. active particle fraction <

100%) were observed and believed to be a major limiting factor for further improving high-rate performance[43, 44]. Therefore, this *operando* visualization of FeF_3 (active particle fraction = 100%) suggests that it could be feasible for conversion cathode material to achieve better rate capability than what was traditionally believed[22, 24], likely via further nanostructure engineering[26].

Our *operando* experiments further enabled the investigation of the charge reaction of the FeF_3 cathode. This unique charge (delithiation) study has not been possible so far using *in situ* TEM techniques due to the instability of organic electrolyte under electron beam and/or the difficulty of applying a controlled constant current. The *operando* cell was charged at the same rate of ~1/15 C to 4.5 V (Figure 3.4a) and chemical phase maps at four different states of charge are shown in Figure 3.4b. The electrochemical reaction occurred uniformly everywhere in the sample, similar to what was observed during discharge. The overall phase transformation during charge is in agreement with metallic Fe gradually converting into Fe (+II) as the voltage increases, but not reaching Fe (+III). This can be clearly seen from the chemical phase maps as well as their corresponding XANES spectra (Figure 3.4c) taken from a selected area of the MW. The relative mole fraction of different Fe oxidation states during both discharge and charge was determined by spectrum fitting and shown in Figure 3.4d. When the charge process finished at the cut-off voltage of 4.5 V, the dominant oxidation state was Fe (+II) (~70%, Figure 3.4d), which is consistent with what was suggested by the previous *ex situ* TEM-EELS studies on the recharged FeF_3/C electrodes[45]. There was also some metallic Fe that did not react during recharge (~30%, Figure 3.4d). The *operando* studies in potentiostatic mode showed the same phase transformation behavior (Figure A2.6).

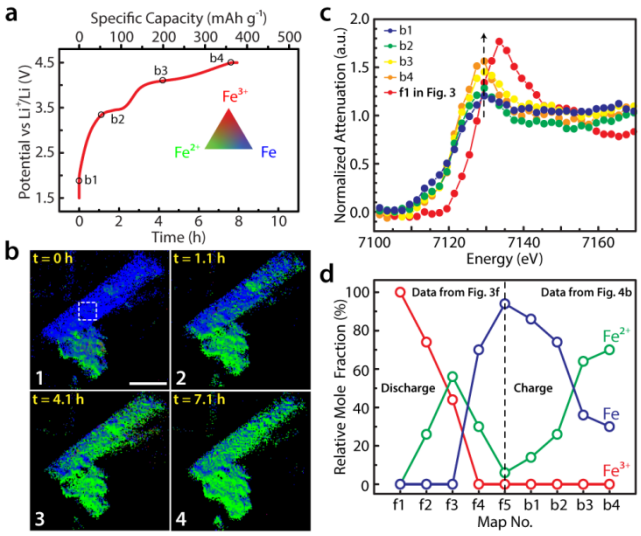

Figure 3.4 | Visualization of the charge reaction of FeF_3 cathodes using hard X-ray spectro-imaging. (**a**) Voltage profile of the *operando* cell that was recharged at ~1/15 C to 4.5 V. The small black circles indicate the states of charge where the data were collected to construct the series of chemical phase maps in (**b**), which show the progression of electrochemical reaction during charge. Scale bar is 5 μm. (**c**) XANES spectra taken from a selected area of the MW, marked by the white box in the first maps of (**b**), showing the change in X-ray absorption during charge. The XANES spectrum of the pristine FeF_3 electrode is shown for comparison. (**d**) The mole fraction of the Fe species in different oxidation states in the same selected area (indicated by the white box) of map 1 to 5 of Figure 3.3**f** (discharge) and map 1 to 4 of panel (**b**) (charge), determined by linear combination fitting using reference spectra.

3.3.4 Phase transformations over a large area of the electrode

In order to confirm what we observed locally in the two FOVs represents the global changes that occurred in the whole electrode, we collected additional data from a few other areas at the end of discharge and charge. The resulting chemical phase maps give consistent pictures (Figure

A2.7). Furthermore, we carried out an *operando* XAS experiment on a FeF_3 MW electrode cycled at ~1/12 C rate. The larger size X-ray beam (~0.5−1.0 mm) in the spectroscopy experiment allows the tracking of phase transformation over a much larger area of the electrode. The observed changes in XAS spectra collected at different states of discharge (Figure 3.5a) and charge (Figure 5b) during continuous cycling (Figure 3.5c) are in agreement with what we observed locally in a single MW (Figure 3.3g and 4c) and the corresponding chemical phase maps (Figure 3.3f and 4b), indicating that the electrochemical reaction is relatively homogeneous over a large area of the electrode. We further performed spectrum fitting to determine the ratio between different Fe oxidation states during cycling (Figure 3.5d). Fitting details and representative best fits are shown in Table A2.1 and Figure A2.8, respectively. The fitting result corroborates our findings in the spectro-imaging experiments (Figure 3.4d). The charge reaction went through Fe (+II) containing intermediate phases (green bar in Figure 3.5d) and Fe (+III, red bar in Figure 3.5d) was barely recovered when recharged to 4.5 V, but could indeed be formed if a constant-voltage charging step was applied following the constant-current charging. *Ex situ* XAS spectra (Figure A2.9) were also collected from electrodes that were cycled to different states of discharge/charge. The result is consistent with those obtained under *operando* conditions.

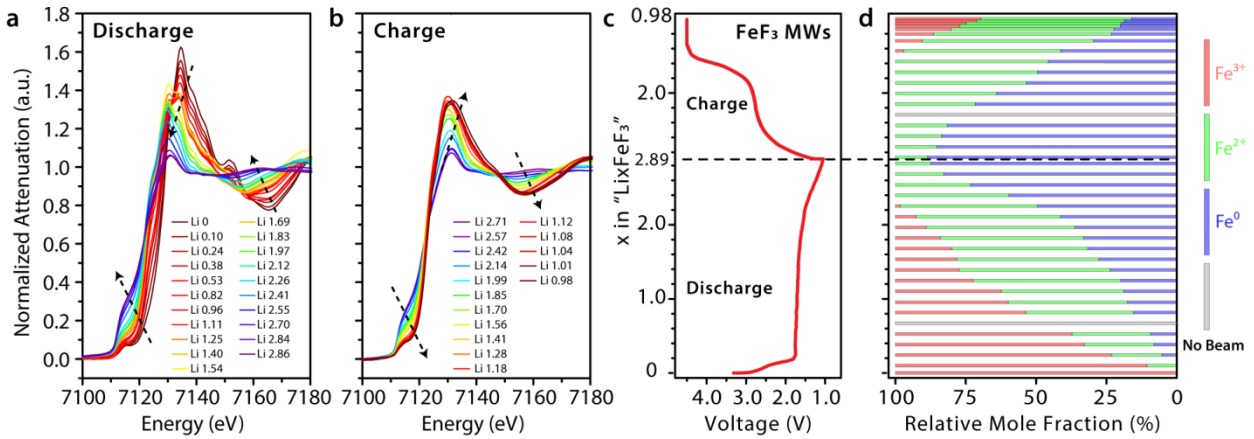

Figure 3.5 | *Operando* XAS on a FeF_3 MW cathode. XANES spectra collected at different states of discharge (**a**) and charge (**b**). (**a**) and (**b**) share the same vertical axis. The arrows indicate the changing trend in XANES spectra during discharge and charge. (**c**) Discharge and charge voltage profile of the *operando* cell cycled at a rate of ~1/12 C. After the constant-current charging, a constant-voltage charging step was applied until the current dropped to ~1/50 C. (**d**) The mole fraction of the Fe species in different oxidation states at different states of discharge and charge, which is calculated by linear combinational fitting of the XANES spectra. (**c**) and (**d**) share the same vertical axis.

3.4 Discussion

Our investigation of the charge reaction across different length scales provides a plausible explanation for the 1st cycle capacity loss, which is a problem commonly observed for FeF_3 cathodes[24, 26, 32] but poorly understood. We found that the capacity loss was caused by the incomplete reconversion of Fe to Fe (+III) during charge, which appears to be a kinetically limited process considering the slow diffusion of iron and fluoride ions. Another important implication is the indication of a different charge reaction pathway from the previous

understanding. First-principles calculations previously suggested that a number of Fe (+III) containing compounds form sequentially during charge, which seemingly offered a plausible explanation for the voltage hysteresis between discharge and charge[33]. However, the *operando* investigation herein shows Fe (+II)-containing compounds formed first and Fe (+II) was slowly converted to Fe (+III) at high voltage during charge. A thorough (re)investigation using integrated experimental and theoretical approaches would be useful to address this discrepancy between our results and the previous simulation.

3.5 Summary and Outlooks

We have developed an *operando* X-ray spectro-imaging technique empowered by a new data analysis method to more accurately account for the internal background absorption and determine the X-ray absorption of weakly absorbing samples to enable the first visualization of the electrochemical reaction in high-capacity FeF_3 cathodes at the nanoscale. These studies reveal the importance of porous nanostructure in achieving fast conversion reaction kinetics and high capacity for FeF_3 cathodes, which could be a structural design principle generally applicable to other conversion electrode materials. Further, more research efforts should focus on the charge reaction, which appears to be kinetically slow even for a highly active porous nanostructured FeF_3 cathode and is confirmed as the bottleneck to utilize the full capacity of conversion electrode materials upon cycling. This work also provides guidelines in experimental design of *in situ* electrochemical cell fabrication, background subtraction, and data analysis method to facilitate *operando* mechanistic studies of other electrode materials[46, 47] to elucidate reaction pathways and diagnose possible failure mechanisms. The temporal and spatial resolution of the chemical phase mapping will be further improved with the full commissioning of brighter

synchrotron light sources, together with the development of lensless imaging methods[48] and better data processing algorithms. This will ultimately allow *operando* studies of other complex solid-state phase transformations that are not electrochemically driven and lead to beneficial solutions towards many technological applications.

3.6 Methods

3.6.1 Synthesis of FeF_3 microwires and polyhedra

FeF_3 microwires (MWs) were prepared by thermal dehydration of α-$FeF_3 \cdot 3H_2O$ MWs at 350°C for 2.5 h in argon atmosphere. The precursor α-$FeF_3 \cdot 3H_2O$ MWs were synthesized by reacting $Fe(NO_3)_3 \cdot 9H_2O$ and HF aqueous solution in ethanol with a concentration ratio of $c(Fe^{3+})$: c(HF) : $c(H_2O)$ ≈ 53.2 mM: 500 mM: 11575 mM at 60 °C for 18 h. Rhombohedral phase FeF_3 polyhedra were prepared by thermal conversion of the metastable cubic phase FeF_3 polyhedra at 350°C for 30 min in argon atmosphere. The precursor cubic phase FeF_3 polyhedra were synthesized by reacting $Fe(NO_3)_3 \cdot 9H_2O$ and HF aqueous solution in ethanol with a concentration ratio of $c(Fe^{3+})$: c(HF) : $c(H_2O)$ ≈ 20 mM: 100 mM: 4670 mM at 60 °C for 24 h. More synthetic details can be found in the A2.1 Supplementary Methods.

3.6.2 Materials characterization

Scanning electron microscopy (SEM) images were acquired using a LEO 55 VP scanning electron microscope at 5 kV. Transmission electron microscopy (TEM) images and electron diffraction (ED) patterns were acquired using either a Tecnai T-12 (120 kV) or a FEI Titan TEM (200 kV). Powder X-ray diffraction (PXRD) data were collected on a Bruker D8 diffractometer using Cu Kα radiation. The Brunauer–Emmet–Teller (BET) surface area and pore size

distribution of the FeF_3 MWs were calculated from nitrogen adsorption–desorption isotherms measured by a Quantachrome Autosorb-1 gas sorption analyzer. *Ex situ* electrochemical measurements were performed on electrodes made of 70 wt% active material, 20 wt% carbon black and 10 wt% binder. CR2032-type coin cells were assembled in an argon-filled glovebox, using Li metal as the counter/quasi-reference electrode, 1 M $LiPF_6$ in EC/DMC (1/1 by volume) as the electrolyte, and electrolyte-soaked polyethylene-polypropylene films as the separator. Electrochemical impedance spectroscopy (EIS) and galvanostatic cycling were performed using either a Biologic SP-200 or a VMP-3 Potentiostat/Galvanostat controlled by EC-Lab software.

3.6.3 *Operando* hard X-ray spectro-imaging and data processing

The *operando* hard X-ray spectro-imaging experiments were performed using the full-field transmission X-ray microscope (FFTXM) at beamline X8c, National Synchrotron Light Source (NSLS), Brookhaven National Laboratory (BNL), using a perforated 2032-type coin cell with holes on both sides sealed by Kapton tapes. The holes were sealed using Kapton tapes and need to be small to ensure a small cell impedance. The o*perando* measurements were performed on electrodes made of 30 wt% FeF_3 active material (polyhedra and MWs 1:1 by weight, or MWs only), 50 wt% carbon black and 20 wt% binder (see a representative SEM image in Figure A2.10). Note that both carbon black and binder are transparent to hard X-rays. Thin aluminum foils (~8 μm thickness) or carbon papers (~110 μm thickness) are used as current collectors for the FeF_3 electrodes. The cell was put into a custom-built holder mounted on a motorized *X, Y, Z,* θ stage and aligned so that the X-ray beam could transmit through. A field of view of 40 × 40 μm^2 with a 2048 × 2048 CCD camera was used. The cell was continuously cycled in galvanostatic or potentiostatic mode and absorption-contrast images (X-ray transmitted through

the sample) and reference background images (X-ray passing through air) were collected in sequence under dynamic conditions. To track the phase transformations in the electrode, a full series of TXM images were collected at each state of discharge and charge. Each TXM image series was collected by scanning across the Fe *K*-edge (7112 eV) from 7091 to 7285 eV, with a step size of 2 eV, and taking one TXM image at each energy step, which contains 512 × 512 XANES spectra when using 4 × 4 binned camera binning. The exposure time for each image was 4 seconds. Each chemical phase map took ~8 minutes to finish. After collection each set of data, the area of study (FOV 1) was allowed to rest for ~16 min (not exposed to X-rays) to minimize any potential impact induced by the X-ray beam, during which a new set of data was taken in another area of study (FOV 2) and background reference images (X-ray passing through air) were also recorded after that. The output pixel size is ~80 nm (camera binning 4).

The XANES spectrum at each pixel was normalized using our new method and then fitted with the linear combination of standard reference spectra collected from FeF_3, FeF_2, and Fe powders under the same conditions using TXM. The rutile FeF_2 was used to represent all the possible rutile related Fe^{2+}-containing phases. This is a reasonable approximation because it was reported that the Li_xFeF_3 (when x ≈ 1.0) phase contains structural features that are found in the rutile FeF_2 structure.[23] The spectrum fitting was carried out by minimizing the ***R*** value (a measure of misfit) for each spectrum at each pixel, which is defined as:

$$\boldsymbol{R} = \sum_{\boldsymbol{Ei}}^{\boldsymbol{Ef}} (\boldsymbol{dataE} - \boldsymbol{refE})^2 / \sum_{\boldsymbol{Ei}}^{\boldsymbol{Ef}} \boldsymbol{dataE}^2 \qquad (2)$$

where ***Ei*** is 7091 eV, ***Ef*** is 7285 eV, ***dataE*** is the normalized spectrum at each pixel for the given energy ***E,*** and ***refE*** is the possible fitting reference value that is a linear combination of X-ray attenuation of FeF_3, FeF_2, and Fe. *R values* were minimized at each pixel to find the best-

matched phase combination of different Fe oxidation states so that Red-Green-Blue (Red: Fe^{3+}, Green: Fe^{2+}, Blue: Fe) colors can be assigned accordingly to generate the chemical phase maps. We applied an *R-value* filter (misfit filter) to the resulting phase map and only pixels with $R < 0.08$ were displayed in order to give the most accurate chemical phase information. See full details in A2.1 Supplementary Methods.

3.6.4 *Operando* X-ray absorption spectroscopy

The *operando* X-ray absorption experiments were performed at beamline X18A, NSLS, BNL, using a perforated 2032-type coin cell with holes on both sides sealed by Kapton tapes. The measurements were performed on electrodes made of 70 wt% FeF_3 active material, 20 wt% carbon black and 10 wt% binder. The measurements were performed in transmission mode using a Si (111) double-crystal monochromator, which was detuned to ~35% of its original maximum intensity to eliminate the high order harmonics in the beam. A reference X-ray absorption spectrum of Fe (*K*-edge 7112 eV) was simultaneously collected using a standard Fe foil. Energy calibration was done using the first inflection point of the Fe *K*-edge spectrum as the reference point. The X-ray absorption data were processed and analyzed using IFEFFIT-ATHENA. Standard reference spectra from FeF_3, FeF_2, and Fe powders were collected to carry out spectrum fitting and determine the ratio between different Fe oxidation states. *Ex situ* spectra were also collected from electrodes cycled to different states of discharge and charge. The electrodes were recovered from coin cells disassembled in the glovebox and sealed in between two pieces of Kapton tape.

3. 7 References

1. Kostorz, G., *Phase transformations in materials*. New ed. (Wiley-VCH: Weinheim : Chichester, 2001).

2. Chiang, Y.-M., Building a better battery. *Science* **330,** 1485-1486 (2010).

3. Liu, H., et al., Capturing metastable structures during high-rate cycling of $LiFePO_4$ nanoparticle electrodes. *Science* **344,** (2014).

4. Sharma, N., et al., Structural changes in a commercial lithium-ion battery during electrochemical cycling: An in situ neutron diffraction study. *J. Power Sources* **195,** 8258-8266 (2010).

5. Yu, X., et al., Understanding the rate capability of high-energy-density Li-rich layered $Lli_{1.2}Ni_{0.15}Co_{0.1}Mn_{0.55}O_2$ cathode materials. *Adv. Energy Mater.* **4,** 1300950 (2014).

6. Hu, Y.-Y., et al., Origin of additional capacities in metal oxide lithium-ion battery electrodes. *Nature Mater.* **12,** 1130-1136 (2013).

7. Huang, J. Y., et al., In situ observation of the electrochemical lithiation of a single SnO_2 nanowire electrode. *Science* **330,** 1515-1520 (2010).

8. Wang, F., et al., Tracking lithium transport and electrochemical reactions in nanoparticles. *Nature Commun.* **3,** 1201 (2012).

9. Gu, M., et al., Demonstration of an electrochemical liquid cell for operando transmission electron microscopy observation of the lithiation/delithiation behavior of Si nanowire battery anodes. *Nano Lett.* **13,** 6106-6112 (2013).

10. Liao, H.-G., et al., Facet development during platinum nanocube growth. *Science* **345,** 916-919 (2014).

11. Andrews, J. C., Weckhuysen, B. M., Hard X-ray spectroscopic nano-imaging of hierarchical functional materials at work. *ChemPhysChem* **14,** 3655-3666 (2013).

12. Meirer, F., et al., Three-dimensional imaging of chemical phase transformations at the nanoscale with full-field transmission X-ray microscopy. *J. Synchrotron. Radiat.* **18,** 773-781 (2011).

13. Wang, J., et al., Automated markerless full field hard X-ray microscopic tomography at sub-50 nm 3-dimension spatial resolution. *Appl. Phys. Lett.* **100,** 143107 (2012).

14. Ebner, M., Marone, F., Stampanoni, M., Wood, V., Visualization and quantification of electrochemical and mechanical degradation in Li ion batteries. *Science* **342,** 716-720 (2013).

15. Nelson, J., et al., In operando X-ray diffraction and transmission X-ray microscopy of lithium sulfur batteries. *J. Am. Chem. Soc.* **134,** 6337-6343 (2012).

16. Chao, S.-C., et al., Study on microstructural deformation of working sn and SnSb anode particles for Li-ion batteries by in situ transmission X-ray microscopy. *J. Phys. Chem. C* **115,** 22040-22047 (2011).

17. Weker, J. N., et al., In situ nanotomography and operando transmission X-ray microscopy of micron-sized Ge particles. *Energy Environ. Sci.* **7,** 2771-2777 (2014).

18. Wang, J., Chen-Wiegart, Y.-c. K., Wang, J., In situ chemical mapping of a lithium-ion battery using full-field hard X-ray spectroscopic imaging. *Chem. Commun.* **49,** 6480-6482 (2013).

19. Yang, F., et al., Nanoscale morphological and chemical changes of high voltage lithium–manganese rich NMC composite cathodes with cycling. *Nano Lett.* **14,** 4334-4341 (2014).

20. Wang, J., Chen-Wiegart, Y.-c. K., Wang, J., In operando tracking phase transformation evolution of lithium iron phosphate with hard X-ray microscopy. *Nature Commun.* **5,** 4570 (2014).

21. Yu, Y.-S., et al., Nonequilibrium pathways during electrochemical phase transformations in single crystals revealed by dynamic chemical imaging at nanoscale resolution. *Adv. Energy Mater.* Early View, **5,** 1402040 (2014).

22. Cabana, J., Monconduit, L., Larcher, D., Palacín, M. R., Beyond intercalation-based Li-ion batteries: The state of the art and challenges of electrode materials reacting through conversion reactions. *Adv. Mater.* **22,** E170-E192 (2010).

23. Li, H., Balaya, P., Maier, J., Li-storage via heterogeneous reaction in selected binary metal fluorides and oxides. *J. Electrochem. Soc.* **151,** A1878-A1885 (2004).

24. Badway, F., Cosandey, F., Pereira, N., Amatucci, G. G., Carbon metal fluoride nanocomposites: High-capacity reversible metal fluoride conversion materials as rechargeable positive electrodes for Li batteries. *J. Electrochem. Soc.* **150,** A1318-A1327 (2003).

25. Badway, F., Pereira, N., Cosandey, F., Amatucci, G. G., Carbon-metal fluoride nanocomposites: Structure and electrochemistry of FeF_3:C. *J. Electrochem. Soc.* **150,** A1209-A1218 (2003).

26. Li, L., Meng, F., Jin, S., High-capacity lithium-ion battery conversion cathodes based on iron fluoride nanowires and insights into the conversion mechanism. *Nano Lett.* **12,** 6030-6037 (2012).

27. Li, H., Richter, G., Maier, J., Reversible formation and decomposition of LiF clusters using transition metal fluorides as precursors and their application in rechargeable Li batteries. *Adv. Mater.* **15,** 736-739 (2003).

28. Li, C., Mu, X., van Aken, P. A., Maier, J., A high-capacity cathode for lithium batteries consisting of porous microspheres of highly amorphized iron fluoride densified from its open parent phase. *Adv. Energy Mater.* **3,** 113-119 (2013).

29. Kim, S.-W., et al., Fabrication of FeF_3 nanoflowers on cnt branches and their application to high power lithium rechargeable batteries. *Adv. Mater.* **22,** 5260-5264 (2010).

30. Zheng, G., et al., Interconnected hollow carbon nanospheres for stable lithium metal anodes. *Nature Nanotech.* **9,** 618-623 (2014).

31. Armand, M., Tarascon, J. M., Building better batteries. *Nature* **451,** 652-657 (2008).

32. Yamakawa, N., Jiang, M., Key, B., Grey, C. P., Identifying the local structures formed during lithiation of the conversion material, iron fluoride, in a Li ion battery: A solid-state NMR, X-ray diffraction, and pair distribution function analysis study. *J. Am. Chem. Soc.* **131,** 10525-10536 (2009).

33. Doe, R. E., Persson, K. A., Meng, Y. S., Ceder, G., First-principles investigation of the Li-Fe-F phase diagram and equilibrium and nonequilibrium conversion reactions of iron fluorides with lithium. *Chem. Mater.* **20,** 5274-5283 (2008).

34. Liu, P., et al., Thermodynamics and kinetics of the Li/FeF_3 reaction by electrochemical analysis. *J. Phys. Chem. C* **116,** 6467-6473 (2012).

35. Wang, F., et al., Conversion reaction mechanisms in lithium ion batteries: Study of the binary metal fluoride electrodes. *J. Am. Chem. Soc.* **133,** 18828-18836 (2011).

36. Zhang, W., et al., In situ electrochemical xafs studies on an iron fluoride high-capacity cathode material for rechargeable lithium batteries. *J. Phys. Chem. C* **117,** 11498-11505 (2013).

37. Ravel, B., Newville, M., Athena, Artemis, Hephaestus: Data analysis for X-ray absorption spectroscopy using IFEFFIT. *J. Synchrotron. Radiat.* **12,** 537-541 (2005).

38. Weng, T.-C., Waldo, G. S., Penner-Hahn, J. E., A method for normalization of X-ray absorption spectra. *J. Synchrotron. Radiat.* **12,** 506-510 (2005).

39. Morin, S. A., Bierman, M. J., Tong, J., Jin, S., Mechanism and kinetics of spontaneous nanotube growth driven by screw dislocations. *Science* **328,** 476-480 (2010).

40. Meng, F., Morin, S. A., Forticaux, A., Jin, S., Screw dislocation driven growth of nanomaterials. *Acc. Chem. Res.* **46,** 1616-1626 (2013).

41. Li, L., et al., Facile solution synthesis of α-$FeF_3 \cdot 3H_2O$ nanowires and their conversion to α-Fe_2O_3 nanowires for photoelectrochemical application. *Nano Lett.* **12,** 724-731 (2012).

42. Parkinson, M. F., et al., Effect of vertically structured porosity on electrochemical performance of FeF_2 films for lithium batteries. *Electrochim. Acta.* **125,** 71-82 (2014).

43. Chueh, W. C., et al., Intercalation pathway in many-particle $LiFePO_4$ electrode revealed by nanoscale state-of-charge mapping. *Nano Lett.* **13,** 866-872 (2013).

44. Li, Y., et al., Current-induced transition from particle-by-particle to concurrent intercalation in phase-separating battery electrodes. *Nature Mater.* **13,** 1149-1156 (2014).

45. Cosandey, F., et al., EELS spectroscopy of iron fluorides and FeF_x/C nanocomposite electrodes used in Li-ion batteries. *Microsc. Microanal.* **13,** 87-95 (2007).

46. Hua, X., et al., Comprehensive study of the CuF_2 conversion reaction mechanism in a lithium ion battery. *J. Phys. Chem. C* **118,** 15169-15184 (2014).

47. Li, L., Caban-Acevedo, M., Girard, S. N., Jin, S., High-purity iron pyrite (FeS_2) nanowires as high-capacity nanostructured cathodes for lithium-ion batteries. *Nanoscale* **6,** 2112-2118 (2014).

48. Shapiro, D. A., et al., Chemical composition mapping with nanometre resolution by soft X-ray microscopy. *Nature Photon.* **8,** 765-769 (2014).

CHAPTER 4

The Origin of Large Voltage Hysteresis in Metal Fluoride Lithium-Ion Battery Conversion Electrodes

4.1 Abstract

Conversion electrode materials can reversibly store multiple lithium-ions to enable high energy-density lithium-ion batteries. However, their progress towards practical applications is severely hindered by an usually large voltage hysteresis between the discharge and charge processes that leads to low energy efficiency. The physical origins of such large hysteresis are poorly understood but surprisingly under-studied. Here we investigate sources of the large hysteresis in prototypical conversion electrode material iron fluoride (FeF_3). We reveal the relationship between voltage profile of FeF_3 and phase evolution and spatial distribution in the electrode through integrated (*in situ*) experimental and theoretical simulation studies. Based on the comprehensive mechanistic understanding, we conclude that the hysteresis is caused by iR voltage drop, various kinetic overpotentials, and different spatial distributions of electrochemically relevant phases, which are all kinetic issues in nature and can be addressed by optimizing material transport properties and electrode architecture.

This CHAPTER is a manuscript to be submitted, in collaboration with R. Jacobs, P. Gao, L. Gan, F. Wang, D. Morgan, and S. Jin.

4.2 Introduction

Lithium-ion battery (LIB) technology has revolutionized portable electronics and been touted as promising solution to future energy challenges from large-scale applications, such as grid-level storage and electrical vehicles[1, 2]. Current LIBs function by processes of intercalation chemistry, which consists of topotactic insertion/removal of Li^+ into/from the host lattice of electrode materials, represented by $LiCoO_2$, $LiFePO_4$, $LiMn_2O_4$, and graphite[3]. Despite excellent rate capability and long cycle-life, the energy density achievable with intercalation (500–600 Wh $kg^{-1}_{\text{active material}}$) is inherently limited by number of interstitial sites in the host lattice (typically < 1 per formula)[1]. Clearly, transition from portable electronics to large-scale applications requires new battery materials and/or new chemistries with higher specific energy densities[1, 3-5]. The discovery of reversible multiple-lithium storage in metal fluorides and oxides in the early 2000s opens up promising opportunities for high energy-density storage[6-11], which does not necessarily depend on available interstitial sites. Instead, it is realized through a heterogeneous conversion reaction ($MF_x + xLi^+ + xe^- = M + xLiF$ or $M_xO_y + 2yLi^+ + 2ye^- = xM + yLi_2O$). The last decade has witnessed tremendous advances in preparation of nanostructured conversion electrode materials that exhibit high specific energy densities (and power capability)[4]. However, their practical applications have been deterred by an unusually large voltage hysteresis (voltage gap) between discharge and charge steps. This hysteresis ranges from several hundred mV to ~2 V[4], comparable to that of a Li-O_2 battery[5] but much higher than that of a Li-sulfur battery (200–300 mV)[5] or a typical intercalation electrode material (several tens mV)[12] at similar rates. It leads to a high degree of round-trip energy inefficiency that is unacceptable in practical applications. To overcome this challenge, it is necessary to understand its physical origins. However, efforts in

this direction have been surprisingly rare, as most work has focused on synthesis and electrochemical testing[4].

Iron fluorides (FeF_3 and FeF_2) are among the most studied conversion electrode materials owing to their very high specific energy densities (> 1000 Wh kg^{-1}) and improved reversibility as compared with other fluorides, especially after nanostructuring and /or mixing with conductive carbon[9-11, 13-26]. Notably, FeF_3 is one of the very few conversion electrode materials[27, 28] whose voltage hysteresis has been previously studied, both by density functional theory (DFT) calculations within the generalized gradient approximation with Hubbard *U* correction (GGA+*U*)[14] and electrochemical measurements[19, 20]. The current belief is that a large portion of the voltage hysteresis has its origin from the system progressing through fundamentally different reaction pathways during discharge and charge[14, 19, 20] and the existence of different intermediate phases results in the large split in electrochemical potential. According to the DFT/GGA+*U* calculations and associated models, FeF_3 is first lithiated to $Li_x[Fe^{3+}_{1-x}Fe^{2+}_x]F_3$ before full reduction of Fe to LiF/Fe during discharge, and a series of Fe^{3+}-containing compounds ($Li_{3-3x}Fe^{3+}_xF_3$) form sequentially during charge before formation of a defect trirutile FeF_3[14]. However, this understanding of the reaction pathways is not fully justified by results from *ex situ* solid nuclear-magnetic resonance (NMR)[15], pair distribution function analysis (PDF)[15], transmission electron microscopy (TEM)[13], *in situ* X-ray absorption spectroscopy[25], and in situ X-ray spectroimaging experiments[26], all of which suggest the existence of Fe^{2+}-containing intermediate phases during and/or after charge. Additionally, different interpretations of the intermediate phases that form during discharge exist between the *ex situ*[15] and *in situ* experimental works[25] (e.g., trirutile $Li_{0.5}FeF_3$ vs. rhombohedral $Li_{0.92}FeF_3$, respectively). These

discrepancies have constrained the understanding of voltage hysteresis and therefore need to be reconciled through systematic studies into both thermodynamic and kinetic aspects of the reaction mechanism.

Here we use *in situ* synchrotron X-ray absorption spectroscopy (XAS) to track changes in Fe oxidation states and local bonding structure during cycling of three iron fluoride model samples, FeF_2 nanowires (NWs), FeF_3 NWs, and FeF_3 microwires (MWs). Combining results from *in situ* TEM experiments and hybrid functional DFT calculations (HSE06), we propose that the reaction pathway of the FeF_3 cathode is as follows: rhombohedral $FeF_3 \rightarrow$ trirutile $Li_{0.25}FeF_3 \rightarrow$ trirutile $Li_{0.5}FeF_3 \rightarrow$ rutile $FeF_2 + LiF \rightarrow Fe + 3LiF$ during discharge, and $Fe + 3LiF \rightarrow$ rutile FeF_2-like phases + $LiF \rightarrow$ trirutile $Li_{0.5}FeF_3$ during charge. We find that reaction homogeneity (completeness and spatial distribution of each electrochemical reactions) strongly depends on reaction kinetics in these multiple-step reaction processes. Based on the new mechanistic understanding and results from galvanostatic intermittent titration technique (GITT) experiments, we show that the large voltage hysteresis observed in the FeF_3 cathode is due to a combination of iR (Ohmic) drop, kinetic overpotentials, and difference in apparent potentials which are result of different spatial distributions of electrochemically relevant phases. These results have general implications for understanding voltage hysteresis in other conversion electrode materials and suggest new strategies to minimize its adverse effect.

4.3 Results and Discussion

4.3.1 Model Samples

We prepared FeF_3 NWs[18] and MWs[26] according to previous work and synthesized the FeF_2 NWs for the first time via thermal reduction of FeF_3 NWs using a small amount of glucose at 450 °C under flowing argon (see Methods for synthetic details; see morphology in Figure A3.1a-c). The phase identities of these samples are confirmed using powder X-ray diffraction (PXRD, Supplementary Fig. 1d). Further TEM characterization reveals that all of these wire samples are polycrystalline and made of attached particle domains (Figure A3.2). We chose these materials as the model samples because of their higher electrochemical activity at room temperature compared with other iron fluoride samples[11, 15, 16]. They can all reach near theoretical capacity at a moderate current rate (Figure A3.3), which is critical for finishing the *in situ* experiments in a reasonable amount of beam time and collecting useful mechanistic information.

4.3.2 *In situ* XAS on an FeF_2 electrode

We first studied the reaction mechanism of an FeF_2 electrode using *in situ* XAS as a comparison to the FeF_3 electrode, because Li-FeF_2 is a simpler conversion/reconversion system (ideally only Fe^{2+} and Fe^0 are involved) than Li-FeF_3 (Fe^{3+}, Fe^{2+}, and Fe^0 are involved). Figure A4.1a shows the electrochemical profile of a Li/FeF_2 battery discharged at a current of C/12 (1 C = 571 mA g^{-1} for FeF_2) to ~1.2 V and then charged at a rate of C/6 to 4.2 V (the current was doubled due to limited time). After the constant-current charging step, a constant-voltage charging step was applied at 4.2 V until the current dropped to ~C/50. Fe *K*-edge XAS spectra were collected every 18 min during the electrochemical cycling so that the change in average

states of lithiation (x_{Li}) was +0.05 per spectrum during discharge and –0.1 per spectrum during charge (see x_{Li} for each spectrum in Table A3.1). The change in Fe oxidation state and local bonding structure were monitored, respectively, by X-ray absorption near-edge structure (XANES, Figure A4.1b) and extended X-ray absorption fine-structure spectroscopy (EXAFS, Figure A4.1c).

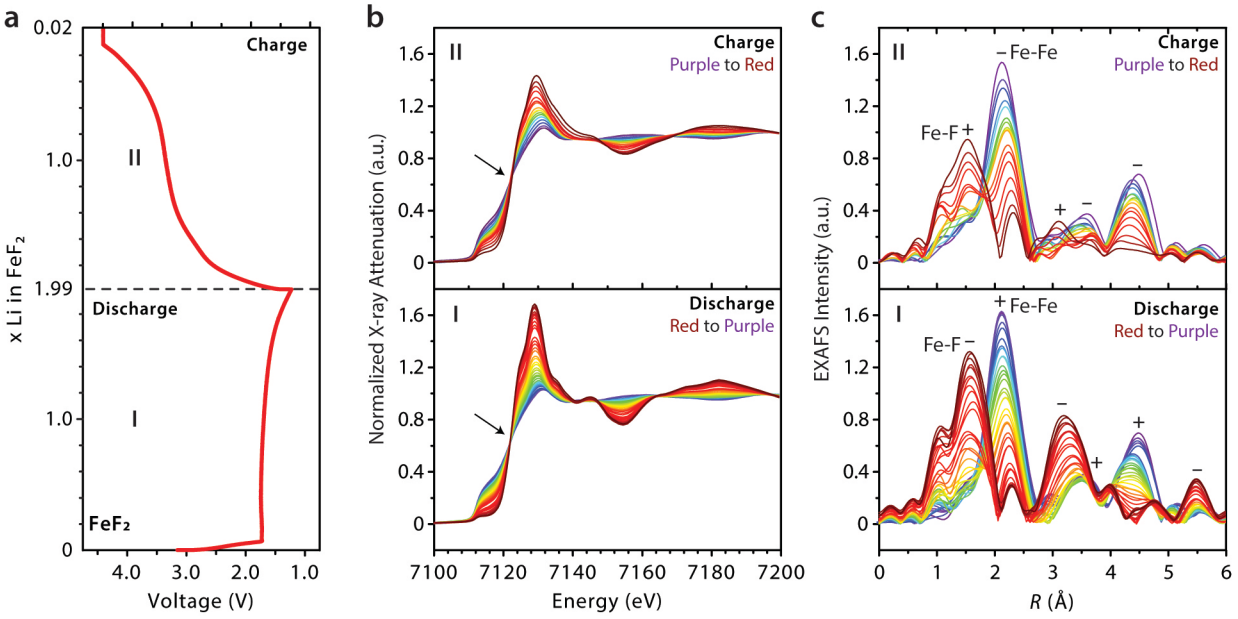

Figure A4.1 | In situ XAS results on an FeF_2 electrode. a. Voltage profile of an FeF_2 nanowire electrode discharged at a current rate of 1/12 C (1 C = 571 mA g^{-1} for FeF_2) and recharged at a current rate 1/6 C. **b.** and **c.** are XANES and EXAFS spectra taken at every 18 min during active discharge (+0.05 x_{Li} per spectrum) and charge (–0.10 x_{Li} per spectrum), respectively. The black arrows indicate the isosbestic points shared by the XANES spectra.

During discharge (x_{Li} = 0→1.99 Li per FeF_2, region **I** in Figure A4.1a-c), we observed that the absorption edge of the XANES spectra gradually shifted toward lower energies, the white line intensity concurrently decreased, and isosbestic points are shared by all the spectra

(indicated by the arrow), indicating a two-phase conversion reaction $FeF_2 + 2Li^+ + 2e^- \rightarrow Fe + 2LiF$. Accordingly, in the EXAFS patterns, the intensity of FeF_2-related peaks gradually decreases (marked with "–") as the intensity of Fe-related peaks increases (marked with "+"). Standard EXAFS patterns of FeF_2 and Fe are shown in Figure A3.4 for comparison. It appears that FeF_2 becomes lithium saturated quickly and starts to decompose into LiF and Fe, as we observed the metallic Fe-related EXAFS peaks as soon as the cell voltage hit the plateau at ~1.75 V (<0.05 Li insertion). Interestingly, we also observed continuous and progressive shifts in the EXAFS peaks during discharge. For example, the Fe-related peak shifted towards smaller *R* values as the discharge reaction proceeded, decreasing from ~2.3 Å (~ 0 Li insertion) to ~2.1 Å (~1.99 Li insertion). Further EXAFS fittings were performed (Figure A3.5) and revealed that the Fe-Fe bond length gradually decreases, which indicates that the Fe nanoparticles formed initially have a larger lattice constant than those formed later during discharge (conversion), consistent with results from the previous *in situ* TEM experiments on FeF_2 nanoparticles[17].

During charge (x_{Li} = 1.99→0.02 Li per FeF_2, region **II** in Figure A4.1a-c), we observed changes in both XANES spectra and EXAFS patterns that closely mirror what occurred during discharge, indicating that Fe and LiF are gradually reconverted into a rutile phase highly similar to FeF_2, at least in the local structure. This rutile phase most likely nucleates first at the interface between the electrolyte and the active particles (now made of LiF/Fe nanocomposites), where Li^+ ions are extracted and transferred into the electrolyte most easily. When the cell was charged to > ~3.3 V, we observed that some Fe in the electrode was over-charged to +3 oxidation state, as evidenced by the absorption edge of the XANES spectra shifting toward higher energy and the Fe-F related peaks in the EXAFS patterns shifting towards smaller *R* value than that of the

pristine $Fe^{2+}F_2$ electrode (0 Li per FeF_2). We also performed linear combination fitting analysis (LCA; See fitting examples in Figure A3.6a and fitting parameters in Table A3.1) to estimate the relative mole fraction of different Fe oxidations states (Figure A3.7). The results reveal that the electrode was charged back to a multiple phase mixture containing Fe, Fe^{2+}, and Fe^{3+}, not the pure rutile FeF_2 phase.

4.3.3 *In situ* XAS on FeF_3 electrodes

Next, we studied the reaction mechanism of an FeF_3 NW cathode. An Li/FeF_3 battery was discharged at a current of C/10 (1 C = 712 mA g^{-1}) to 1.0 V and then charged at a rate of C/10 to 4.5 V, after which a constant-voltage charging step was applied at 4.5 V until the current dropped to ~C/50. Fe *K*-edge XAS spectra were collected every 18 min during the electrochemical cycling so that the change in average states of lithiation (x_{Li}) was about +0.09 per spectrum during discharge and –0.09 per spectrum during charge (see x_{Li} for each spectrum in Table A3.2). The electrochemical profile (Figure A4.2a) is divided into four different regions based on features observed in the XANES spectra (Figure A4.2b) and EXAFS patterns (Figure A4.2c).

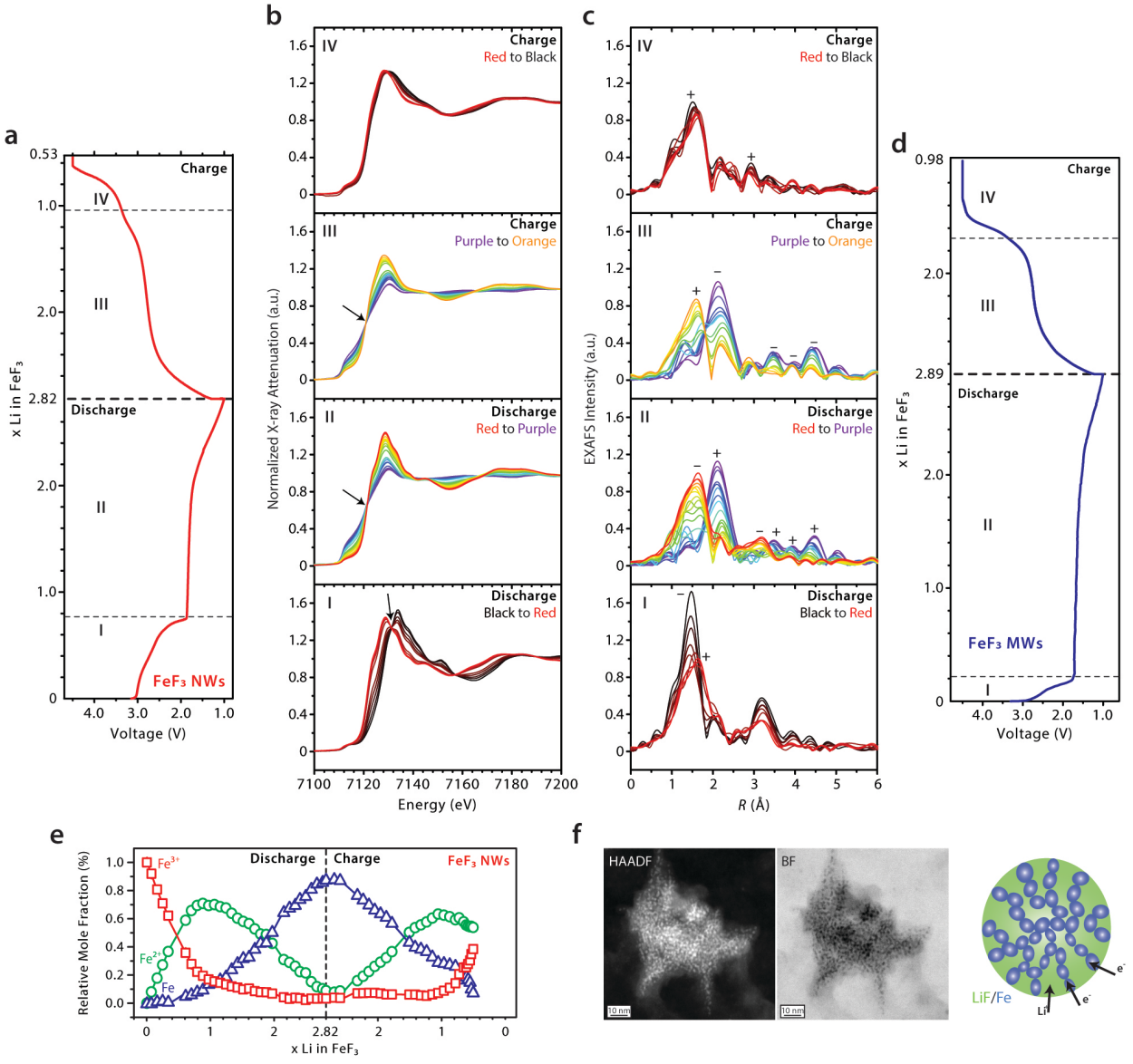

Figure A4.2 | In situ XAS and TEM on FeF_3 nanowire electrodes. a. Voltage profile of an FeF_3 nanowire electrode discharged and recharged at a current rate of 1/10 C (1 C = 712 mAh g^{-1}). **b.** and **c.** are XANES and EXAFS spectra taken every 18 min during active discharge (+0.09 x_{Li} per spectrum) and charge (–0.09 x_{Li} per spectrum). The black arrows indicate the isosbestic points. **d.** Voltage profile of an FeF_3 microwire electrode discharged and recharged at a current rate of 1/10 C, shown as a comparison to the nanowire electrode. **e.** Phase evolution

during the cycling of the FeF_3 nanowire electrodes, which is estimated by linear combinational fitting analysis of the XANES spectra. **f.** High-angle annular dark-field, bright-field STEM images and schematic illustration showing the microstructure of a bundle of fully lithiated FeF_3 NWs, which is made of interconnected Fe domains surrounded by LiF. The STEM images were recorded in the *in situ* TEM experiment.

In discharge region **I** in Figure A4.2 (x_{Li} = 0→0.78 Li per FeF_3), the Fe^{3+} in FeF_3 is gradually reduced to Fe^{2+} with Li uptake, as evidenced by the shift in absorption edge of the XANES spectra. Meanwhile, the change in EXAFS peak position and intensity indicates that the local structure deviates from that of the original rhombohedral FeF_3 and becomes increasingly rutile- like, which resembles rutile FeF_2 after 0.78 Li insertion (Figure A3.8). In another Li-FeF_3 NW battery discharged at a slower rate of 1/20 C, we observed two different isosbestic points in the XANES spectra (see Figure A3.9) in region **I**, which may be indicative of two different Li_yFeF_3 phases. No additional isosbestic points were observed afterwards. In the subsequent discharge region **II** in Figure A4.2 (x_{Li} = 0.78→2.82 Li per FeF_3)**,** we observed changes that are highly similar to those which occurred during the discharge of the FeF_2 NW electrode (Figure A4.1a-c, region **I**) in the changes of the absorption edge, white line intensity, and EXAFS peak position and intensity, indicating reduction of rutile Fe^{2+}-containing phase(s) to metallic Fe. We also studied the phase and microstructural evolution of the FeF_3 NW electrode by *in situ* TEM electron diffraction (ED, Figure A3.10 and Movie A3.1) and scanning transmission electron microscopy (STEM, Supplementary Movie A3.2), which show results consistent with the *in situ* XAS experiments. We observed that the lithiation reaction initiated from the surface and propagated toward the core of each electrochemically active domains (Movie A3.2). Notably,

after being fully lithiated the microstructure of the FeF_3 NW electrode is similar to that of the fully lithiated FeF_2 nanoparticles[16, 17]. Nanocomposites consisting of bicontinuous LiF/Fe networks were formed (Figure A4.2f). The average size of the Fe domains is 2–3 nm. This microstructure is also the key to understanding the phase evolution during recharge.

We performed LCA (See fitting examples in Figure A3.6b and fitting parameters in Table A3.2) to estimate the relative mole fraction of different Fe oxidations states (Figure A4.2e) during the discharge (and charge) of the FeF_3 electrode. We found that a noticeable amount of Fe (> 5%) already existed at x_{Li} = 0.61 and Fe^{3+}, Fe^{2+}, and Fe coexisted in the electrode between x_{Li} = 0.61 to 2.15 (<5 % Fe^{3+}, Table A3.2). This result indicates that the reduction of Fe^{2+} to Fe had already started on the outside (Fe^{2+}-containing region) before the first reduction (Fe^{3+} to Fe^{2+}) completed in the whole electrochemically active particle. One interesting question that can be asked is what Li composition in the Li-FeF_3 system is necessary for metallic Fe to begin forming, since different values x_{Li} = 0.75, 0.92, or 1.0 were previously reported in FeF_3/carbon nanocomposite samples[14, 15, 25]. In order to understand this issue, we studied the reaction mechanism of FeF_3 MWs for comparison (Figure A3.11), which consist of large particle domains that the NWs (Figure A3.2). The FeF_3 MW/Li cell was cycled at the same rate as the FeF_3 NW/Li cell, i.e. 1/10 C but its voltage profile (Figure A4.2d) shows different features. The first sloping plateau at higher voltages (region **I**) is much shorter but the second flat plateau (region **II**) is much longer than those of the FeF_3 NW/Li cell. The energy density of the Li-FeF_3 MW system is lower due to the loss of the high voltage plateau. Further LCA fittings (See fitting examples in Figure A3.6c and fitting parameters in Table A3.3) reveal that a noticeable amount

of metallic Fe started to exist at $x_{Li} = 0.31$ (> 5% mole fraction) and Fe^{3+}, Fe^{2+}, and Fe coexisted in the electrode until $x_{Li} = 2.41$ ($Fe^{3+} < 5\%$, Figure A3.11 and Table A3.3).

The comparison between the reaction behavior of FeF_3 NWs and MWs reveals how reaction homogeneity and the corresponding voltage profile are affected by the size of the active domains, which correlates with the reaction kinetics. As shown by the *in situ* STEM experiment (Movie A3.2), the lithiation reaction of FeF_3 proceeds from the surface to the core of each electrochemically active domain. In the MWs, which consist of larger active domains (and thus smaller surface area) than the NWs, the applied current (1/10 C) is more likely to exceed what the reaction kinetics (Li^+ and/or electron transport) can keep up with. Therefore, the Fe^{2+}-containing rutile phase produced in the initial reduction (lithiation) on the outside is further lithiated to produce LiF and Fe early at $x_{Li} = 0.31$ before the interior FeF_3 domains can begin to react. The occurrence of reduction of Fe^{2+} to Fe dictates the voltage profile so that the second flat plateau becomes much longer. By contrast, in the NWs, faster reaction kinetics (shorter distance for Li^+ and/or electron transport) allow the first reduction step ($Fe^{3+} \rightarrow Fe^{2+}$) to further complete before Fe formation (at $x_{Li} = 0.61$). Furthermore, in the FeF_3/carbon nanocomposite samples reported previously[14, 15, 25], even smaller particle size and better electrical contact afforded by the carbon matrix likely facilitate the first reduction even more, which explains the Fe initial formation approaching $x_{Li} = 1.0$. We note that x_{Li} is considered as a better measure of the state of lithiation averaged within the entire electrode. It does not necessarily reflect the stoichiometric information of the Li_yFeF_3 phase that readily extrudes Fe upon further lithiation, especially in the kinetically limited situations (such as the MWs). It is possible that in all cases Fe starts to form at $y = 1$, but the existence of unreacted FeF_3 phase at the core of the active

particles leads to $x_{Li} < 1$. These results illustrate the critical role of inhomogeneity in governing the conversion processes and voltage curves for FeF_3 materials.

During charge of the FeF_3 NW electrode (region **III** of Figure A4.2, $x_{Li} = 2.82 \rightarrow 1.03$ Li per FeF_3), the changes in XANES spectra and EXAFS patterns not only mirror what occurred in discharge (region **II** of Figure A4.2), but also highly similar to those observed during the charge of the FeF_2 electrode (region **II** of Figure A4.1). These results provide clear evidence that a rutile-FeF_2-like Fe^{2+}-containing phase is formed during charge of the FeF_3 electrode. These findings are actually consistent with previous results from *ex situ* NMR and PDF experiments[15] but in disagreement with the reaction mechanism calculated from past DFT-GGA+*U* simulations[14], which predicts the formation of Fe^{3+}-containing phases. In fact, we only observed oxidation of Fe^{2+} into Fe^{3+} when the cell voltage exceeded ~3.3 V in charge region **IV** ($1.04 \rightarrow 0.53$ Li per FeF_3), as evidenced by the absorption edge further shifting toward higher energies. Further, the local structure at the final state (0.53 Li per FeF_3) still resembles rutile FeF_2. According to EXAFS patterns, the Fe-F peak position is slightly smaller than that in rutile FeF_2 but larger than that in rhombohedral FeF_3 (Figure A4.2c) in *R* value. Therefore, the final product (0.53 Li per FeF_3) after charge could be trirutile $Li_{0.5}FeF_3$.

Additionally, we compared the electrochemical capacity with the capacity estimated from the LCA fittings for the FeF_2 and FeF_3 NW electrode and found reasonable matches (Figure A3.15). These results suggest that electrolyte decomposition (or any other non-metal-center side reaction) does not contribute significantly to the observed capacity in the iron fluoride conversion cathodes studied in this work (when low cut-off voltage ≥ 1 V is used). This reaction

behavior is different from metal oxide conversion electrodes that are discharged to lower voltages (< 1 V)[28-32].

4.3.4 DFT calculations and FeF_3 reaction pathway

To corroborate and help interpret the experimental findings, we performed a detailed multicomponent phase analysis using DFT calculations of materials in the Li-Fe-F ternary system. The DFT calculations were performed using hybrid HSE functions[33], which have been shown to more accurately reproduce experimental formation energies and Li insertion voltages for transition metal-containing compounds than GGA- or GGA+*U*-based DFT. Figure A4.3a is a plot of the relevant portion of the HSE-DFT ternary Li-Fe-F phase diagram where the FeF_3 and FeF_2 lithiation reactions occur. (The GGA and GGA+*U* Li-Fe-F phase diagrams are included in the Supplementary Fig.13 for comparison). The red dots represent stable phases (materials predicted to be on the convex hull), the black dots represent materials that were predicted to be unstable (above the convex hull), while the purple dots are important composition points where no lithiated FeF_2 or FeF_3 materials were calculated due to an insufficient number of interstitial sites for Li insertion. When examining the stable FeF_2 lithiation path (green dotted line in Figure A4.3), FeF_2 immediately begins to dissociate upon lithiation to precipitate metallic Fe and LiF. This three-phase region persists over the entire lithiation path until $x_{Li} = 2$, at which point the reduction from Fe^{2+} to metallic Fe is complete and produces a two phase mixture of metallic Fe and LiF. In delithiation of the Fe/LiF (1:2 in mole ratio), FeF_2 should be formed as the stable phase but $Li_{0.5}FeF_3$ may also be produced from FeF_2 if there is excess LiF, which is likely the case at the surface of the active particles and indeed observed by the *in situ* XAS experiment (Figure A4.1a-c, region **IV**).

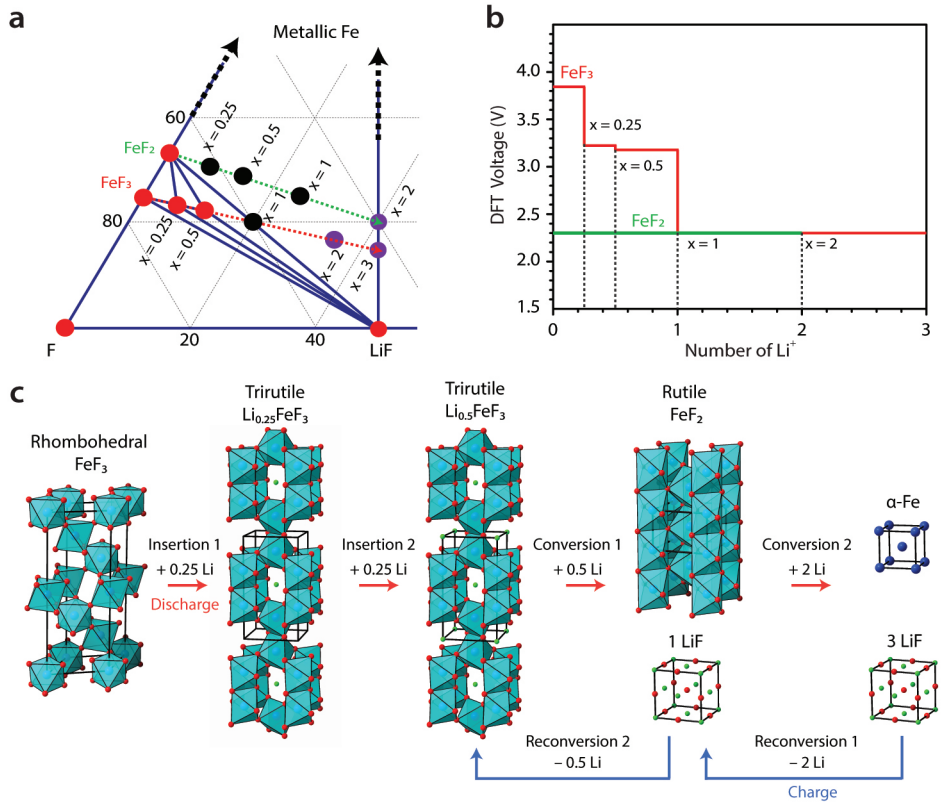

Figure 4.3 | DFT-HSE calculation results and FeF_3 reaction pathway. a. DFT calculated Fe-Li-F phase diagram using the HSE approach. The lithiation pathways for FeF_3 and FeF_2 are indicated by the red and green dashed arrows, respectively. Red dots represent stable phases, black dots represent unstable lithiated phases and purple dots indicate relevant compositions where no lithiated compound was calculated. The fraction of lithiation *x* for Li_xFeF_2 and Li_xFeF_3 are labeled for both pathways. **b.** Calculated DFT voltage curves for FeF_3 and FeF_2 at different states of lithiation. **c.** Discharge and charge reaction pathways of the FeF_3 electrode, which are derived from both the experimental and DFT calculation results. Li, Fe, and F atoms are represented by green, blue, and red spheres.

The stable lithiation path for FeF_3 (red dotted line in Figure A4.3) shows direct Li intercalation when $x \leq 0.5$. Upon lithiation to $x_{Li} = 0.25$, the pristine rhombohedral FeF_3 phase is no longer stable, and a phase change to the defected trirutile ($Li_{0.25}FeF_3$) structure occurs. This defected trirutile phase is stable up to $x_{Li} = 0.5$ ($Li_{0.5}FeF_3$), after which dissociation to FeF_2 and LiF occurs because no more interstitial sites for lithium insertion are available. When $x_{Li} = 1$, all Fe^{3+} has been reduced to Fe^{2+} and the system is a two-phase mixture of FeF_2 and LiF. Further lithiation promotes the reduction of Fe^{2+} to metallic Fe, which is exactly the same process as the lithiation of FeF_2. In delithiation of Fe/LiF (1:3 in mole ratio), FeF_2 should be formed as the stable phase first; $Li_{0.5}FeF_3$ can be produced later from the FeF_2 and the excess LiF. These DFT-HSE calculation results are in good agreement with the *in situ* XAS data (Figure A4.2a-c).

Figure A4.3b shows the calculated DFT lithiation voltages. Since they are representative of equilibrium voltages, in which case no polarization or kinetic overpotential is included, they are higher than those experimentally observed when a current was applied (Figure A4.1a and 2a). As the experimental battery was allowed to relax to approach equilibrium conditions, its voltages would become closer to the DFT calculated values. This trend is indeed seen from the GITT measurements after relaxation, which is discussed in more detail below.

Combining the results from the *in situ* XAS and HSE-DFT calculations, we can now propose complete and consistent reaction pathways for FeF_3 (and FeF_2) cathodes, as shown in Figure A4.3c. We note that kinetic limitations can cause one reaction not proceed completely over the entire particle domain before the subsequent one being forced to initiate in the pre-reacted region under galvanostatic condition. This new mechanistic understanding is clearly different from the one predicted previously by DFT-GGA+U calculations[14], which has been the

basis for understanding the large voltage hysteresis in FeF_3 as well as other conversion electrode materials. The previous model assumes that the electrochemical reaction is controlled by the slow diffusion of Fe so that Fe is oxidized to the highest oxidation state (Fe^{3+}) during charge in order to maximize lithium extraction. A series of Fe^{3+}-containing phases, such as spinel $Li_{15/8}Fe^{3+}{}_{3/8}F_3$, ilmenite $Li_{3/2}Fe^{3+}{}_{1/2}F_3$, and rutile $Li_{3/4}Fe^{3+}{}_{3/4}F_3$ are predicted to form sequentially during charge, which constituents a fundamentally different reaction pathway from that taken during discharge (reduction of rutile $Fe^{2+}F_2$ like phase to Fe)[14]. This model provides a seemingly reasonable explanation for the voltage hysteresis because the presence of different phases (and with Fe at different oxidation states) during discharge and charge would indeed lead to different potentials in the electrochemical system. However, our new mechanistic understanding are clearly suggesting that other mechanisms governs the voltage hysteresis.

4.3.5 Origins of the voltage hysteresis in the FeF_3 electrode

To better understand the possible causes of the large voltage hysteresis, we performed GITT experiments on the FeF_3 NW and MW electrodes, respectively. Figure A4.4a shows the GITT profiles of an FeF_3 NW/Li cell and an FeF_3 MW/Li cell cycled at 50 mA g^{-1}. The cells was allowed to relax for 4 h after every 1 h discharging/charging. The GITT profiles are also divided into four regions based on the understanding of the reaction mechanism. Figure A4.4b provides a close-up view of the GITT profiles collected from the FeF_3 NW electrode. In the discharge half-cycle (red curve), as soon as the current is removed, the voltage first suddenly increases a small value, and then gradually increases as the electrode approaches equilibrium condition[34]. The opposite occurs in the charge half-cycle (Figure A4.4b, blue curve,).

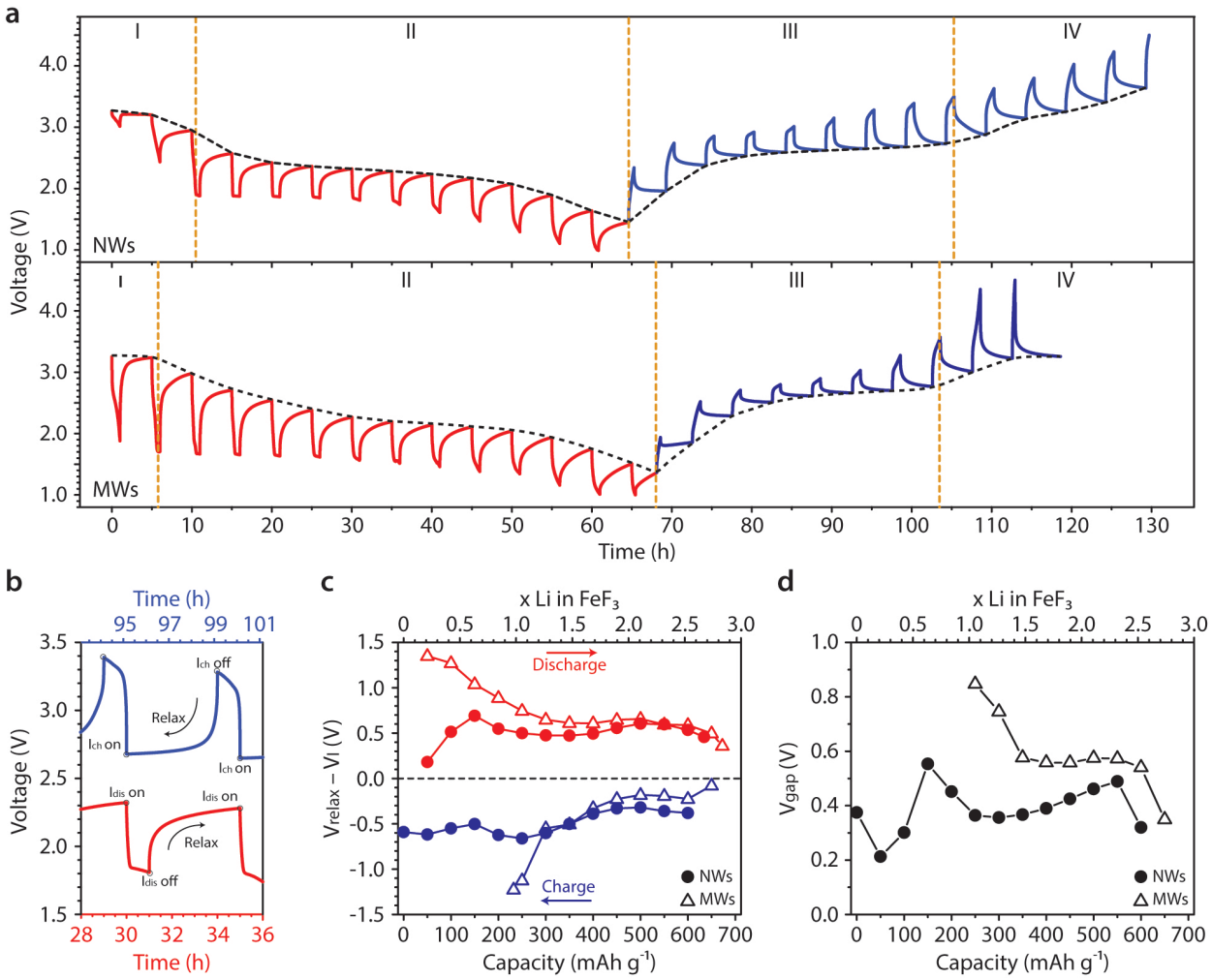

Figure 4.4 | GITT results and analysis. a. GITT profiles of a FeF_3 NW electrode and a MW electrode. The cells were discharged and charged at a rate of 50 mA g^{-1} for 1h and then allowed to relax 4 hours. **b.** Zoom-in view of the GITT curve for the NW electrode. **c.** Voltage change after the 4 h relaxation at different states of discharge and charge of the NW and MW electrodes, respectively. **d.** Voltage difference between discharge and charge steps after the 4 h relaxation at the same state of lithiation of the NW and MW electrodes, respectively.

We can identify the following components from the GITT that likely contribute to the large voltage hysteresis of FeF_3. The first one is the Ohmic iR voltage drop, which is the sudden voltage jump after the current is removed and typically <50 mV in our measurements. The second component consists of various kinetic overpotentials that are required to nucleate new phases, drive phase transformations, and overcome interfacial penalty for making nanophases. These kinetic overpotentials are manifested in the voltage "spikes" during the extended voltage relaxation. However, their magnitudes are not straightforward to quantify using the GITT results, because the active particles undergo significant phase transformations and cannot achieve truly a homogeneous composition over the entire particle simply through Li^+ diffusion during the relaxation. Reverse-step potentiostatic intermittent titration technique (PITT) may be a more suitable approach to quantitatively evaluate the kinetic overpotentials in conversion electrode materials[20]. The voltage after the 4 h relaxation (V_{relax}) in our measurements may be better considered as the quasi-equilibrium potential for a partially reacted system. We find that V_{relax} (black dashed lines in Figure A4.4a) largely correlates with the composition of the electrodes inferred from the *in situ* XAS results. For example, since the $Fe^{3+}F_3$ phase in the MW electrode is reacted more slowly than that in the NW electrode during discharge due to kinetic limitations, V_{relax} observed in the MW electrode is higher initially (black dashed lines in Figure A4.4a). As the $Fe^{3+}F_3$ phase is consumed, the two V_{relax} curves of the MW and NW electrodes become more comparable. Figure A4.4c shows how much the voltage relaxes after 4 h for the FeF_3 NW and MW electrodes, respectively, at different states of lithiation. During discharge, we observe that the voltage relaxes more in the MW electrode than the NW electrode (Figure A4.4c), which is a result of the reaction inhomogeneity: the intermediate phase $Fe^{2+}F_2$ is being further lithiated to

produce LiF and Fe on the outside despite the presence of unreacted FeF_3 at the bulk of the active particle. After all the FeF_3 is consumed, the magnitude of the voltage relaxation in the MW and the NW electrode becomes comparable (Figure A4.4c). Similar analysis based on reaction homogeneity can be made for the charging process. Figure A4.4d shows the voltage difference at the same state of lithiation between discharge and charge steps after the 4 h relaxation (V_{gap}) for both the MW and NW electrodes. V_{gap} can become slightly smaller based on its changing trend if the relaxation time is increased but should not become zero due to the difference in spatial distribution of the electrochemically relevant phases during discharge and charge steps and in the way these phases are connected in the electrochemical system (i.e. access to Li^+ and electron). For example, at states of lithiation close to $x_{Li} = 3$ per FeF_3, during discharge the intermediate phase FeF_2 is located at the interior of the active particles while Fe and LiF are on the outside and have contact with the electrolyte and current collector; by contrast, during charge the intermediate phase FeF_2 is formed on the outside while Fe is located inside and may be screened or even isolated from the electrochemical system, by the electrically and ionically insulating FeF_2 phase. Such a difference in phase distribution yields a difference in apparent potentials, which is another component contributing to the voltage hysteresis, in addition to the iR drop and kinetic overpotentials discussed above. This compositional inhomogeneity mechanism for driving hysteresis is likely to play a role in many kinetically limited conversion materials where during Li insertion (extraction) the most reduced (oxidized) phases are present at the active surface and drive the potential down (up) compared the theoretical OCV. Interesting comparisons may also be made with Li-sulfur and Li-oxygen batteries during discharging/charging: after voltage relaxation, a voltage gap remains in the Li-sulfur system[35]

possibly due to presence of different Li_2S_n (n= 8, 6, 4, 2, and 1) phases, but approaches zero in the Li-oxygen system because there is only Li_2O_2[36].

4.3.6 Improvement strategies

These new understandings suggest strategies to minimize the voltage hysteresis, which is important to improving the battery round-trip energy efficiency. One straightforward approach is to construct a composite electrode consisting of nanostructured active particles whose size must be comparable to the length scale of the conversion reaction (<10 nm for FeF_3) and directly connected to electrically conductive scaffolds. This is expected to minimize the voltage hysteresis caused by compositional inhomogeneity as well as iR drop. This approach seems quite promising because the beneficial effect has already been observed in the case of $FeCl_3$ conversion anode when ultra-small $FeCl_3$ nanoparticles are embedded between graphene layers to make a graphite intercalation compound (GIC)[37]. The $FeCl_3$-GIC electrode shows a moderate voltage gap (<200 mV) between discharge and charge steps and excellent reversibility when cycled at a current of 50 mA g^{-1}. Therefore, it is useful to develop new synthetic methods to make FeF_3 electrodes with similar microstructures. However, sufficient amount of FeF_3 material needs to be embedded so that the overall volumetric energy density is not severely compromised. Another approach that deserves further exploration is incorporating another cation or anion into the metal fluoride lattice to lower the kinetic overpotentials (similar to a "catalyst") by improving ionic and electronic transport properties and creating a more disordered microstructure. This approach may be more promising than the first one in terms of available energy density because no additional inactive components is introduced. One example is $Cu_yFe_{1-y}F_2$ solid-solution[38], in which case that Fe in FeF_2 is partially substituted by Cu. The ternary fluoride electrode exhibits

reversible Cu and Fe redox reactions with smaller hysteresis than the pure FeF_2 electrode. One remaining challenge that needs to be addressed is to preserve the beneficial effect in repeated cycling, as Cu is rapidly lost through Cu^+ dissolution into the liquid electrolyte[38, 39].

4.4 Summary and Outlooks

In summary, we have studied the electrochemical reaction mechanism of the FeF_3 (and FeF_2) conversion electrode through integrated experimental and theoretical studies. The phase evolution in the electrode is highly symmetrical (see Figure A4.2e) during discharge and charge but the spatial distribution of the electrochemically relevant phases, which is controlled by reaction kinetics, is very different. Such a difference changes the way the relevant phases are connected to electrolyte (Li^+) and current collector (electron) during discharge and charge, which consequently introduces a voltage gap. This gap, along with various kinetic overpotentials and the iR voltage drop, leads to the large voltage hysteresis observed in the FeF_3 conversion electrode. These understandings suggest that promising approaches, including but not limited to nanostructure engineering and incorporation of other ions, can help reduce the hysteresis to a reasonable level to eventually enable practical applications. These results provide the long-awaited conceptual breakthrough in understanding and tackling the large voltage hysteresis in conversion electrode materials[39-41] and may guide future efforts to improve their performance in lithium-ion batteries.

4.5 Methods.

4.5.1 Synthesis of FeF_3 samples

FeF_3 nanowires (NWs) and microwires (MWs) were synthesized by thermal dehydration of α-$FeF_3 \cdot 3H_2O$ NWs and MWs, respectively, at 350 °C for 2.5 h in argon atmosphere, based on previous work[18, 26]. Briefly, the precursor α-$FeF_3 \cdot 3H_2O$ NWs and MWs were first synthesized respectively by reacting different amounts of $Fe(NO_3)_3 \cdot 9H_2O$ and HF aqueous solution in ethanol at 60 °C for 18 h. The concentration ratio of $c(Fe^{3+})$: c(HF) : $c(H_2O)$ is 13.3 mM : 5560 mM : 6760 mM for the NW synthesis and 53.2 mM: 500 mM: 11575 mM for the MW synthesis. FeF_2 NWs were prepared by mixing FeF_3 NWs (90 wt%) with a small amount of glucose (10 wt%) and heating the mixture at 450 °C for 2.5 hour.

4.5.2 Material Characterization

Scanning electron microscopy (SEM) images were collected using a LEO 55 VP scanning electron microscope at 5 kV. Transmission electron microscopy (TEM) images and electron diffraction (ED) patterns were recorded using either a Philips FEI FM200 (200 kV) or a FEI Titan TEM (200 kV). We collected powder X-ray diffraction (PXRD) data on a Bruker D8 diffractometer using Cu Kα radiation. Conventional electrochemical measurements were performed on electrodes made of 70 wt% active material, 20 wt% carbon black and 10 wt% binder. The electrodes were packed into CR2032-type coin cells in an argon-filled glovebox, with Li metal as the counter/quasi-reference electrode, 1 M $LiPF_6$ in EC/DMC (1/1 by volume, BASF) as the electrolyte, and electrolyte-soaked polyethylene-polypropylene films as the separator. Galvanostatic cycling and galvanostatic intermittent titration technique (GITT)

experiments were performed using either a Biologic SP-200 or a VMP-3 Potentiostat/Galvanostat controlled by EC-Lab software.

4.5.3 *In situ* X-ray Absorption Spectroscopy (XAS)

We collected *in situ* X-ray absorption spectra at beamline X18A, NSLS, BNL, using a perforated 2032-type coin cell with holes on both sides sealed by Kapton tapes. The electrodes were made of 70 wt% active material, 20 wt% carbon black and 10 wt% binder and coated on Al foil (25 μm thickness). The measurements were performed in transmission mode using a Si (111) double-crystal monochromator, which was detuned to ~35% of its original maximum intensity to eliminate the high order harmonics in the beam. A reference X-ray absorption spectrum of metallic Fe (*K*-edge 7112 eV) was simultaneously collected using a standard Fe foil. Energy calibration was done using the first inflection point of the Fe *K*-edge spectrum as the reference point. The X-ray absorption data were processed and analyzed using IFEFFIT-ATHENA. Standard reference spectra from FeF_3, FeF_2, and Fe powders were collected to carry out spectrum fitting and estimate the ratio between different Fe oxidation states.

4.5.4 *In situ* transmission electron microscopy

In-situ STEM images, ED patterns were recorded at 200 kV in a JEOL2100F microscope. The *in situ* nano-battery consisting of a copper half-grid (current collector), FeF_3 NWs supported on the amorphous carbon film (cathode) and Li metal (anode) was fabricated in an argon-filled glove box and transferred into the TEM chamber by using an argon-filled plastic bag. A thin passivation layer of LiN_xO_y on the surface of the Li that was formed due to brief exposure to air before transferring to the TEM chamber, acted as the solid electrolyte. The biasing probe was

connected to the carbon membrane and the reaction was initiated by applying a negative bias typically at a value of 2 V.

4.5.5 Computational methods

We performed all calculations using Density Functional Theory (DFT) with the Vienna *ab initio s*imulation package (VASP)[42] and a plane wave basis set. The hybrid functional of Heyd, Scuseria and Ernzerhof (HSE06)[33] with Perdew-Burke-Ernzerhof (PBE)-type pseudopotentials[43] utilizing the projector augmented wave (PAW)[44] method was used for Fe, F and Li atoms. The valence electron configurations of Fe, F and Li atoms were Fe: $3p^6 3d^7 4s^1$, F: $2s^2 2p^5$, Li: $2s^1$. All calculations were performed with spin polarization enabled and with a plane wave cutoff energy set at least 30% larger than the maximum plane wave energy for the chosen set of pseudopotentials, equal to 520 eV. Reciprocal space integration in the Brillouin zone was performed with the Monkhorst-Pack scheme with k-point densities set for each material such that total energy errors were only 1 meV/cell[45].

Bulk Li, Fe, LiF, FeF_2 and FeF_3 materials were simulated within the $Im\bar{3}m$ (body centered cubic structure, Li and Fe), $Fm\bar{3}m$ (rocksalt structure), $P4_2/mnm$ (rutile structure) and $R\bar{3}c$ (rhombohedral structure) space groups, respectively. The lithiated FeF_2 structures, Li_xFeF_2 (x = 0.25, 0.5, 1), and lithiated FeF_3 structures, Li_xFeF_3 (x =0.25, 0.5, 1) were simulated as direct Li insertion into the interstitial sites of the rutile structure (Li_xFeF_2) and rhombohedral, monoclinic and defected trirutile structures (Li_xFeF_3). The monoclinic structure possesses the *Cc* space group while the defected trirutile structure is based on the $P4_2/mnm$ space group and the $ZnSb_2O_6$ structure with the 2*a* Wyckoff sites vacant. These vacant sites serve as interstitial

positions for direct Li insertion. The average voltage to insert Li $\bar{V}_{x_1 \to x_2}$ (in V/Li) from composition x_1 to composition x_2 in these structures is expressed as:

$$\bar{V}_{x_1 \to x_2} = -\frac{1}{(x_2 - x_1)}\left(E_{x_2}^{FeF_3/FeF_2} - E_{x_1}^{FeF_3/FeF_2} - (x_2 - x_1)E_{Li}\right) \quad (1)$$

where $E_{x_2}^{FeF_3/FeF_2}$ and $E_{x_1}^{FeF_3/FeF_2}$ are the calculated DFT energies of a lithiated FeF_2 or FeF_3 material with Li composition x_2 and x_1, respectively, and E_{Li} is the DFT energy of metallic Li.

The phase stability of the Li-Fe-F system was analyzed by plotting the formation energies (relative to the pure elements Li, Fe, F) of each calculated compound at their respective compositions. The phase diagram is constructed by calculating the convex hull from these formation energies. Specific material compositions that are thermodynamically stable lie on the convex hull, while those that are unstable are above the convex hull.

4.6 References

1. Armand, M., Tarascon, J. M., Building better batteries. *Nature* **451,** 652-657 (2008).

2. Bruce, P. G., Energy storage beyond the horizon: Rechargeable lithium batteries. *Solid State Ionics* **179,** 752-760 (2008).

3. Goodenough, J. B., Kim, Y., Challenges for Rechargeable Li Batteries. *Chem. Mater.* **22,** 587-603 (2009).

4. Cabana, J., Monconduit, L., Larcher, D., Palacín, M. R., Beyond Intercalation-Based Li-Ion Batteries: The State of the Art and Challenges of Electrode Materials Reacting Through Conversion Reactions. *Adv. Mater.* **22,** E170-E192 (2010).

5. Bruce, P. G., Freunberger, S. A., Hardwick, L. J., Tarascon, J.-M., Li-O_2 and Li-S batteries with high energy storage. *Nature Mater.* **11,** 19-29 (2012).

6. Poizot, P., et al., Nano-sized transition-metal oxides as negative-electrode materials for lithium-ion batteries. *Nature* **407,** 496-499 (2000).

7. Balaya, P., Li, H., Kienle, L., Maier, J., Fully Reversible Homogeneous and Heterogeneous Li Storage in RuO_2 with High Capacity. *Adv. Funct. Mater.* **13,** 621-625 (2003).

8. Morcrette, M., et al., A reversible copper extrusion-insertion electrode for rechargeable Li batteries. *Nature Mater.* **2,** 755-761 (2003).

9. Li, H., Richter, G., Maier, J., Reversible Formation and Decomposition of LiF Clusters Using Transition Metal Fluorides as Precursors and Their Application in Rechargeable Li Batteries. *Adv. Mater.* **15,** 736-739 (2003).

10. Badway, F., Cosandey, F., Pereira, N., Amatucci, G. G., Carbon Metal Fluoride Nanocomposites: High-Capacity Reversible Metal Fluoride Conversion Materials as Rechargeable Positive Electrodes for Li Batteries. *J. Electrochem. Soc.* **150,** A1318-A1327 (2003).

11. Badway, F., Pereira, N., Cosandey, F., Amatucci, G. G., Carbon-Metal Fluoride Nanocomposites: Structure and Electrochemistry of FeF_3:C. *J. Electrochem. Soc.* **150,** A1209-A1218 (2003).

12. Dreyer, W., et al., The thermodynamic origin of hysteresis in insertion batteries. *Nature Mater.* **9,** 448-453 (2010).

13. Cosandey, F., et al., EELS Spectroscopy of Iron Fluorides and FeF_x/C Nanocomposite Electrodes Used in Li-Ion Batteries. *Microsc. Microanal.* **13,** 87-95 (2007).

14. Doe, R. E., Persson, K. A., Meng, Y. S., Ceder, G., First-Principles Investigation of the Li−Fe−F Phase Diagram and Equilibrium and Nonequilibrium Conversion Reactions of Iron Fluorides with Lithium. *Chem. Mater.* **20,** 5274-5283 (2008).

15. Yamakawa, N., Jiang, M., Key, B., Grey, C. P., Identifying the Local Structures Formed during Lithiation of the Conversion Material, Iron Fluoride, in a Li Ion Battery: A Solid-State NMR, X-ray Diffraction, and Pair Distribution Function Analysis Study. *J. Am. Chem. Soc.* **131,** 10525-10536 (2009).

16. Wang, F., et al., Conversion Reaction Mechanisms in Lithium Ion Batteries: Study of the Binary Metal Fluoride Electrodes. *J. Am. Chem. Soc.* **133,** 18828-18836 (2011).

17. Wang, F., et al., Tracking lithium transport and electrochemical reactions in nanoparticles. *Nature Commun.* **3,** 1201 (2012).

18. Li, L., Meng, F., Jin, S., High-Capacity Lithium-Ion Battery Conversion Cathodes Based on Iron Fluoride Nanowires and Insights into the Conversion Mechanism. *Nano Lett.* **12,** 6030-6037 (2012).

19. Liu, P., et al., Thermodynamics and Kinetics of the Li/FeF_3 Reaction by Electrochemical Analysis. *J. Phys. Chem. C* **116,** 6467-6473 (2012).

20. Ko, J. K., et al., Transport, Phase Reactions, and Hysteresis of Iron Fluoride and Oxyfluoride Conversion Electrode Materials for Lithium Batteries. *ACS Appl. Mater. Interfaces* **6,** 10858-10869 (2014).

21. Parkinson, M. F., et al., Effect of Vertically Structured Porosity on Electrochemical Performance of FeF_2 Films for Lithium Batteries. *Electrochim. Acta.* **125,** 71-82 (2014).

22. Kim, S.-W., et al., Fabrication of FeF_3 Nanoflowers on CNT Branches and Their Application to High Power Lithium Rechargeable Batteries. *Adv. Mater.* **22,** 5260-5264 (2010).

23. Li, C., Mu, X., van Aken, P. A., Maier, J., A High-Capacity Cathode for Lithium Batteries Consisting of Porous Microspheres of Highly Amorphized Iron Fluoride Densified from Its Open Parent Phase. *Adv. Energy Mater.* **3,** 113-119 (2013).

24. Thorpe, R., et al., The solid state conversion reaction of epitaxial FeF_2(110) thin films with lithium studied by angle-resolved X-ray photoelectron spectroscopy. *Phys. Chem. Chem. Phys.* (2015).

25. Zhang, W., et al., In Situ Electrochemical XAFS Studies on an Iron Fluoride High-Capacity Cathode Material for Rechargeable Lithium Batteries. *J. Phys. Chem. C* **117,** 11498-11505 (2013).

26. Li, L., et al., Visualization of electrochemically driven solid-state phase transformations using operando hard X-ray spectro-imaging. *Nat. Commun.* **6,** 6883 (2015).

27. Khatib, R., et al., Origin of the Voltage Hysteresis in the CoP Conversion Material for Li-Ion Batteries. *J. Phys. Chem. C* **117,** 837-849 (2013).

28. Boesenberg, U., et al., Asymmetric pathways in the electrochemical conversion reaction of NiO as battery electrode with high storage capacity. *Sci. Rep.* **4,** (2014).

29. Laruelle, S., et al., On the Origin of the Extra Electrochemical Capacity Displayed by MO/Li Cells at Low Potential. *J. Electrochem. Soc.* **149,** A627-A634 (2002).

30. Hu, Y.-Y., et al., Origin of additional capacities in metal oxide lithium-ion battery electrodes. *Nature Mater.* **12,** 1130-1136 (2013).

31. Ponrouch, A., Taberna, P.-L., Simon, P., Palacín, M. R., On the origin of the extra capacity at low potential in materials for Li batteries reacting through conversion reaction. *Electrochim. Acta.* **61,** 13-18 (2012).

32. Lowe, M. A., Gao, J., Abruna, H. D., In operando X-ray studies of the conversion reaction in Mn_3O_4 lithium battery anodes. *J. Mater. Chem. A* **1,** 2094-2103 (2013).

33. Heyd, J., Scuseria, G. E., Ernzerhof, M., Hybrid functionals based on a screened Coulomb potential. *J. Chem. Phys.* **118,** 8207-8215 (2003).

34. Weppner, W., Huggins, R. A., Determination of the Kinetic Parameters of Mixed-Conducting Electrodes and Application to the System Li_3Sb. *J. Electrochem. Soc.* **124,** 1569-1578 (1977).

35. Cuisinier, M., et al., Unique behaviour of nonsolvents for polysulphides in lithium-sulphur batteries. *Energy Environ. Sci.* **7,** 2697-2705 (2014).

36. Cui, Z. H., Guo, X. X., Li, H., Equilibrium voltage and overpotential variation of nonaqueous Li-O_2 batteries using the galvanostatic intermittent titration technique. *Energy Environ. Sci.* **8,** 182-187 (2015).

37. Wang, F., et al., Graphite Intercalation Compounds (GICs): A New Type of Promising Anode Material for Lithium-Ion Batteries. *Adv. Energy Mater.* **4,** 1300600 (2014).

38. Wang, F., et al., Ternary metal fluorides as high-energy cathodes with low cycling hysteresis. *Nat. Commun.* **6,** 6668 (2015).

39. Hua, X., et al., Comprehensive Study of the CuF_2 Conversion Reaction Mechanism in a Lithium Ion Battery. *J. Phys. Chem. C* **118,** 15169-15184 (2014).

40. Wiaderek, K. M., et al., Comprehensive Insights into the Structural and Chemical Changes in Mixed-Anion FeOF Electrodes by Using Operando PDF and NMR Spectroscopy. *J. Am. Chem. Soc.* **135,** 4070-4078 (2013).

41. Lee, D. H., et al., Understanding improved electrochemical properties of NiO-doped NiF_2-C composite conversion materials by X-ray absorption spectroscopy and pair distribution function analysis. *Phys. Chem. Chem. Phys.* **16,** 3095-3102 (2014).

42. Kresse, G., Furthmüller, J., Efficient iterative schemes for *ab initio* total-energy calculations using a plane-wave basis set. *Phys. Rev. B* **54,** 11169-11186 (1996).

43. Perdew, J. P., Burke, K., Ernzerhof, M., Generalized Gradient Approximation Made Simple. *Phys. Rev. Lett.* **77,** 3865-3868 (1996).

44. Kresse, G., Joubert, D., From ultrasoft pseudopotentials to the projector augmented-wave method. *Phys. Rev. B* **59,** 1758-1775 (1999).

45. Monkhorst, H. J., Pack, J. D., Special points for Brillouin-zone integrations. *Phys. Rev. B* **13,** 5188-5192 (1976).

CHAPTER 5

High-Purity Iron Pyrite (FeS_2) Nanowires as High-Capacity Nanostructured Cathodes for Lithium-Ion Batteries

5.1 Abstracts

Iron pyrite is an earth-abundant and inexpensive material that has long been interesting for electrochemical energy storage and solar energy conversion. A large-scale conversion synthesis of phase-pure pyrite nanowires has been developed for the first time. Nano-pyrite cathodes exhibited high Li-storage capacity and excellent capacity retention in Li/pyrite batteries using a liquid electrolyte, which retained a discharge capacity of 350 mAh g^{-1} and a discharge energy density of 534 Wh kg^{-1} after 50 cycles at 0.1 C rate.

This chapter was published in *Nanoscale* **6**, 2112, (2014), in collaboration with M. Caban-Acevedo, S. N. Girard, and S. Jin.

5.2 Introduction

Iron pyrite (cubic FeS_2, fool's gold) has long been studied as an interesting material for solar energy conversion[1-4] and electrochemical energy storage[5-7]. Pyrite has a suitable band gap (E_g = 0.95 eV) and strong optical absorption ($\alpha > 6 \times 10^5$ cm^{-1} for $hv > 1.3$ eV), which stimulated the early research efforts in the 1980–1990s to investigate pyrite as a thin light absorber for photovoltaic (PV) and photoelectrochemical (PEC) applications.[1-4] Compared to other conventional leading solar materials such as Si and CdTe, pyrite stands out with its essentially limitless material abundance, low toxicity, and significantly lower raw material cost.[8] These attractive attributes justify the resurgent interest in this material, as high-performance energy conversion devices based on inexpensive earth-abundant materials are favorable to address energy challenges today and for the future. It is comparatively less well known that pyrite is also an excellent and inexpensive battery cathode material that exhibits a high theoretical capacity of 894 mAh g^{-1} by reacting with four Li^+ *via* electrochemical conversion reaction to form Fe and Li_2S.[5, 9] It is currently used in commercial primary batteries and shows remarkable power performance and significantly longer working life than equivalent-sized alkaline batteries.[10] Pyrite has also been investigated as a promising secondary battery cathode in Li-Al/FeS_2 batteries for potential transport applications.[11, 12] It shows good reversibility at 400 °C[12] but only limited rechargeability can be achieved at ambient temperature[5]. Such limited reversibility is due in large part to the conversion mechanism involved in the lithiation/delithiation of pyrite cathodes, which operates very differently from the commonly used intercalation cathode materials.[9] To date, most of the previous pyrite cathodes were prepared from micrometer-sized

natural[5, 6, 13-17] or synthetic[6, 13, 18] pyrite particles but the lithium-storage behavior of nanostructured phase-pure pyrite remains inadequately explored.

Nanostructuring has been shown as an effective approach to improve the capacity and rate capability of electrode materials by reducing the ion/electron diffusion distance, increasing electrode/electrolyte contact area, and better accommodating the strain associated with the lithium insertion/removal reaction.[19] This strategy has been much more prominently pursued for anode materials so far, such as Si[20-23] and Sn/SnO_2[24, 25], but it can be potentially more effective for conversion cathodes,[9, 26] such as pyrite, to address similar challenges including sluggish reaction kinetics and dramatic structural changes during lithiation and delithiation. However, the synthesis of phase-pure pyrite nanostructures has long been considered challenging. It is complicated by the existence of many sub-stoichiometric iron sulfide phases and the polymorph marcasite phase (orthorhombic FeS_2).[2] Important advances have been made recently: a number of synthetic approaches to pyrite nanostructures have been reported, including chemical vapor deposition,[27-29] thermal sulfidation of iron,[30] sulfidation of Fe_2O_3 (hematite) assisted by a H_2S plasma,[31] sulfidation reaction with $FeCl_2$ or $FeBr_2$,[32] and colloidal nanocrystal synthesis.[33, 34] While these methods yield pyrite samples suitable for thin-film solar device fabrication and/or investigation of fundamental physical properties, the scale of these preparations is not sufficient (usually < 1 mg)[26-31] to allow battery electrode preparation. Chemical transformation of existing nanostructures provides a versatile approach to preparing novel nanomaterials and may potentially circumvent the aforementioned challenge. This approach not only allows independent control over the shape, size, morphology, structure and chemical composition of target materials, but may also enable scalable nanomaterial synthesis.[35] α-$FeF_3 \cdot 3H_2O$ nanowires (NWs) can be

synthesized from solution in a large quantity[36] and they are versatile precursors to make NWs of iron-based materials, such as α-Fe_2O_3 (hematite)[36] and iron fluoride (FeF_3)[26]. Here we report for the first time a scalable synthesis of phase-pure pyrite NWs *via* thermal sulfidation of the precursor α-$FeF_3 \cdot 3H_2O$ NWs in bulk-like quantity. The phase purity of the converted pyrite NWs was confirmed by synchrotron-based high-resolution powder X-ray diffraction (HRPXRD), Raman spectroscopy, transmission electron microscopy (TEM), and electron diffraction (ED). Furthermore, we prepared composite electrodes comprised of pyrite NWs, carbon black, and polyvinylidene difluoride (PVDF) binder and performed galvanostatic cycling tests to show that the nano-pyrite cathodes exhibit high capacity and excellent capacity retention at room temperature.

5.3 Results and Discussion

To prepare the pyrite NWs, we first synthesized the precursor α-$FeF_3 \cdot 3H_2O$ NWs using a solution synthesis[36] that follows the design of dislocation-driven NW growth[37, 38] (see A4.1 for experimental details). The α-$FeF_3 \cdot 3H_2O$ NWs were made in bulk-like white powders and first dried and partially dehydrated under vacuum. The color of the powders changed from white to brownish/greenish after the partial water loss. The pyrite NWs (~5–10 mg scale) were prepared by sulfidation of the partially dehydrated NWs at 500 °C for 2 h under a sulfur atmosphere using a home-made tube reactor equipped with gas-flow and pressure controls (Figure 5.1a). The sulfur precursor was positioned at a temperature of ~415 °C throughout the reaction, which yields an estimated sulfur vapor pressure of ~480 Torr[39]. The sulfidation of α-$FeF_3 \cdot 3H_2O$ NWs has also been accomplished in a closed ampoule using excess sulfur, which yields more pyrite sample in a

single reaction batch (~50–80 mg scale). Representative scanning electron microscopy (SEM) images of the precursor α-$FeF_3 \cdot 3H_2O$ NWs (approximately 30–200 nm in diameter) and the as-converted pyrite NWs are shown in Figure 5.1b and 5.1c, respectively. The NWs became more tortuous after the sulfidation and tended to entangle and fuse to form mattes of NW networks (Figure 5.1c). The diameter of the pyrite NWs typically ranges from 15 nm to 200 nm.

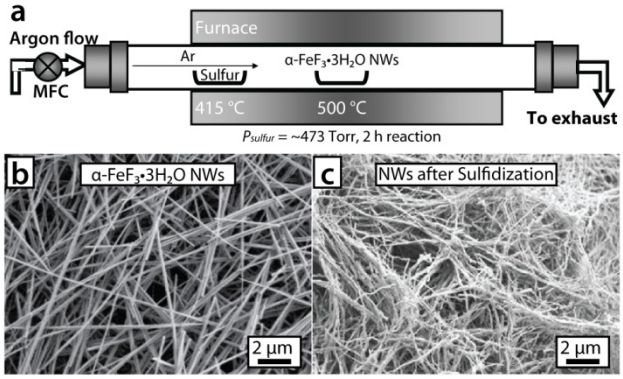

Figure 5.1 (a) Schematic illustration of the pyrite NW synthesis setup using a flow tube reactor; (b) and (c) are SEM images of the NWs before and after sulfidation.

The phase identity of the NWs after the sulfidation was confirmed to be pyrite (cubic FeS_2, JCPDS No. 65-3321, space group $Pa\bar{3}$, a = 5.419 Å) by synchrotron-based HRPXRD (Figure 5.2a) taken on beamline 11-BM at the Advanced Photon Source at Argonne National Laboratory. Even with the high 2θ range (25–155 °) and high sensitivity afforded by the HRPXRD, no other impurity phases such as marcasite (orthorhombic FeS_2, JCPDS No. 65-2567, space group *Pnnm*, a = 4.445 Å, b = 5.425 Å, c = 3.388 Å), pyrrhotite ($Fe_{1-x}S$, x = 0–0.17) , or troilite (FeS) were detectable. Furthermore, we have carried out confocal micro-Raman spectroscopy to provide additional evidence for the phase-purity of the converted NWs. A representative Raman

spectrum (Figure 5.2b) shows three peaks at 339 cm^{-1}, 376 cm^{-1}, and 429 cm^{-1}, corresponding to three different characteristic active modes of pyrite, namely the S_2 libration (E_g), S-S in-phase stretch (A_g), and coupled libration and stretch [triplydegenerate, specifically $T_{g(3)}$] modes, respectively.[40, 41] No Raman peaks from marcasite (386 and 323 cm^{-1}) were observed.

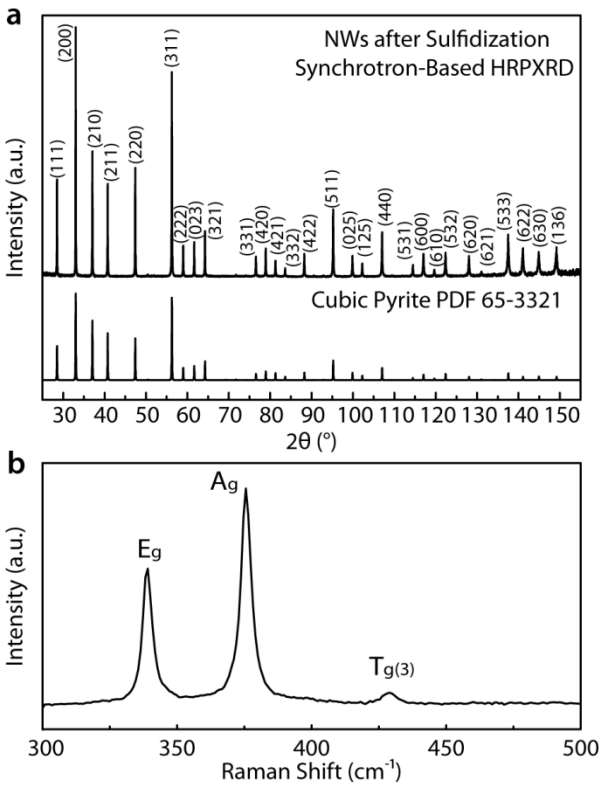

Figure 5.2. (a) HRPXRD of the NWs after sulfidation in comparison with reference diffractogram of cubic pyrite; (b) Confocal micro-Raman spectrum of the NWs after sulfidation.

The phase purity of the pyrite NWs was also investigated by TEM, ED, and fast Fourier transform (FFT) analysis. An ED ring pattern (Figure 5.3a) was obtained from an ensemble of NWs dropcasted on a TEM grid. The diffraction rings can be exclusively indexed to iron pyrite reflections. HRTEM was carefully performed and the representative HRTEM image (Figure 5.3b)

shows a lattice-resolved single-crystal pyrite NW oriented along the [110] zone axis (ZA), determined from the corresponding indexed FFT (Figure 5.3b inset). Note that the zone axis patterns (ZAPs) of cubic pyrite and its orthorhombic polymorph marcasite are nearly identical and often difficult to conclusively distinguish due to their highly similar crystal structures. As we have demonstrated previously,[30, 32] HRTEM and FFT analysis must be carried out along unique ZAs of pyrite, such as [110] ZA, to convincingly identify the pyrite crystal structure and rule out the existence of marcasite (see the comparison between the simulated [110] ZAP for pyrite and its most similar ZAP for marcasite in Figure A4.1).

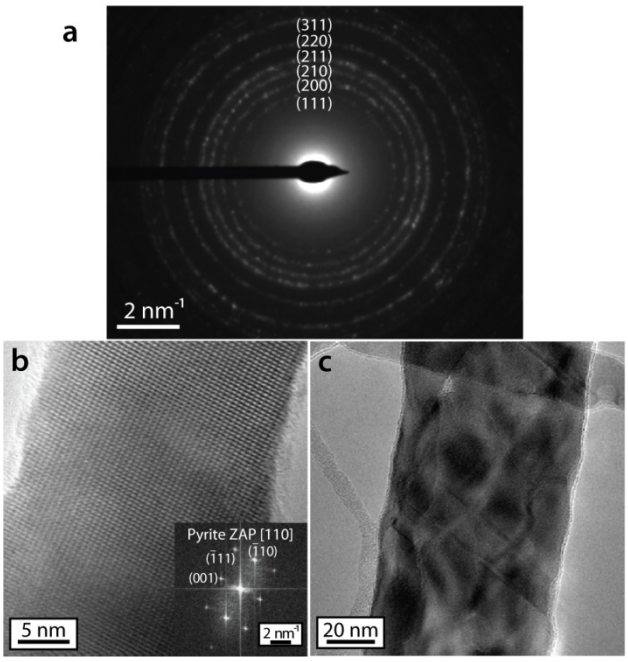

Figure 5.3. (a) Representative ED pattern for an ensemble of as-converted NWs revealing single-phase pyrite; (b) Lattice-resolved HRTEM image of a representative thin pyrite NW and the corresponding FFT showing its single crystallinity. Note that the [110] ZAP for pyrite is

unique and distinguishable from any ZAPs for marcasite; (c) TEM image of a representative thick polycrystalline pyrite NW.

We have also examined the microstructure of the converted pyrite NWs using TEM and observed two types of structural transformation behavior correlated with the diameter of the NWs. Thinner pyrite NWs (typically < 20 nm in diameter) usually contains large segments of single crystalline pyrite domains or even exhibit complete single-crystallinity. One representative example is shown in Figure 5.3b, in which a continuous single-crystal pyrite lattice can be clearly seen. On the other hand, NWs with large diameters (typically > 20 nm) tend to become polycrystalline. As shown in Figure 5.3c for a representative example, the NW is comprised of multiple polycrystalline domains, but the overall one-dimensional (1D) morphology after the sulfidation is preserved. The transformation behavior may be explained in terms of diffusion of reactant atoms/ions. For the thin NWs, smaller domain size and shorter diffusion distance may afford faster reaction kinetics. A single nucleation event of the pyrite phase likely occurs, which quickly propagates along the whole NW to achieve the homogeneous transformation with preserved single-crystallinity. Conversely, multiple nucleation events could occur in a thick NW and hence lead to the formation of polycrystalline pyrite domains. Similar chemical transforming behaviors have been observed in the conversion of α-$FeF_3 \cdot 3H_2O$ NWs to α-Fe_2O_3 NWs, though the critical diameter for the preservation of single-crystallinity is larger (~100 nm) in that case.[36] These two syntheses decouple the control over material morphology and chemical composition and produce iron-based functional nanomaterials in a large quantity, which further illustrates that the chemical transformation of existing nanostructures is a versatile method of nanomaterial

synthesis,[35] and specifically, α-$FeF_3 \cdot 3H_2O$ NWs are very useful precursors to NWs of other iron-based nanomaterials.

We suggest that the following chemical reactions may be responsible for the conversion of the NWs, in which partially dehydrated α-$FeF_3 \cdot 3H_2O$ ($FeF_3 \cdot xH_2O$) quickly loses the residual lattice water and reacts with sulfur vapor to produce pyrite and sulfur hexafluoride (SF_6) at 500 °C.

$$4FeF_3 \cdot xH_2O\ (s) + 5S_2\ (g) \rightarrow 4FeS_2\ (s) + 2SF_6\ (g) + 4xH_2O\ (g) \quad (1)$$

This is the first investigation of chemical transformation of iron fluoride to iron pyrite. The conversion is favorable because both pyrite and SF_6 are very stable (see estimated Gibbs free energy of formation in Table A4.1) in the sulfur-rich atmosphere at the reaction temperature (500 °C) and the volatile products (SF_6 and water vapor) are quickly carried away by the flowing argon gas, driving the equilibrium to favor the formation of pyrite based on Le Chatelier's principle. Furthermore, benefited from the metastability and nanoscale dimension of the precursor NWs, the kinetic energy barrier for atoms and ions to diffuse is significantly reduced. This effectively facilitates in the complete conversion from the iron fluoride precursor to pyrite without producing any other iron sulfide impurities, such as pyrrhotite $Fe_{1-x}S$ and marcasite FeS_2. Compared with previous pyrite synthesis, the facile conversion reported herein not only produces phase-pure pyrite, it is also significantly larger in reaction scale, which greatly facilitates our subsequent study on the lithium-storage capability of nanostructured pyrite cathodes.

We have also measured the optical absorption of the as-synthesized pyrite NWs using a UV-Vis-NIR spectrophotometer equipped with an integration sphere. The pyrite NW film (~500 nm

in thickness) deposited on a borosilicate glass substrate shows very strong optical absorption ($\alpha > 10^5$ cm^{-1} for $hv > 1.0$ eV) and an absorption onset of about ~0.8 eV. More precise determination of the optical bandgap is complicated by the existence of sub-band gap absorption, which is often observed on nanostructured pyrite samples[31, 42] but its origin is still controversial and requires further investigation. The strong light absorption of the pyrite NWs illustrates that they can be effective solar absorber. Therefore, we have prepared semiconducting pyrite thin-film electrodes by converting α-$FeF_3 \cdot 3H_2O$ NW films deposited on conductive substrates[43]. Investigation of their photoelectrochemical properties is underway.

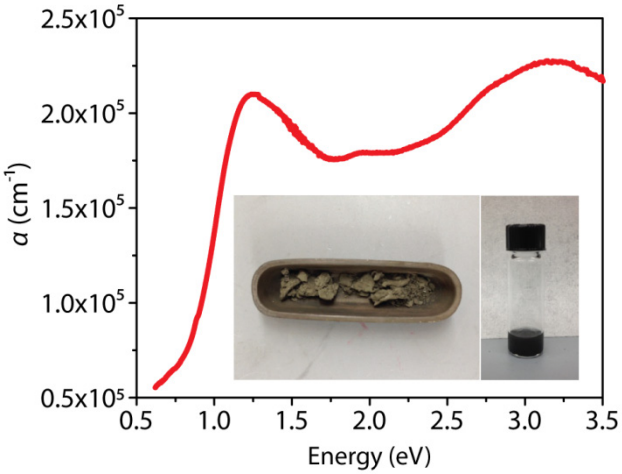

Figure 5.4. Absorption coefficient α of a pyrite NW film (~500 nm in thickness) deposited on a borosilicate glass substrate. α may be underestimated due to the void spaces within the NW film. Insets show the appearance of the converted pyrite NWs (about 45 mg in an alumina boat of 3 cm in length) and a NW/iso-propanol suspension, demonstrating that the pyrite NWs absorb light strongly.

We performed electrochemical tests on composite electrodes made of pyrite NWs, carbon black, and PVDF binder in a weight ratio of 7:2:1 packed into coin cells (see Supporting Information for details). As the highly entangled and fused pyrite NWs could be broken into shorter nanorods and small nanoparticles during the electrode preparation process, we refer to the as-prepared composite electrodes as nano-pyrite cathodes and do not judge how the NW morphology affects the electrochemical performance in this work. 1 M lithium bis(trifluoromethane)sulfonimide (LiTFSi) dissolved in tetra(ethylene glycol)dimethyl ether (TEGDME) was used as the battery electrolyte, because it was shown to improve the cycling performance of Li/FeS_2 batteries at room temperature as compared to the more common ethylene carbonate/dimethyl carbonate based electrolytes.[16] We will focus our discussion on the lithium storage behavior of nanostructured pyrite.

We first investigated the lithium storage behavior of the nano-pyrite cathode in the 1st discharge at different current densities. Four Li/nano-pyrite cells were discharged from open-circuit voltage to 1.1 V at 0.01 C, 0.05 C, 0.1 C, and 0.2 C (1 C = 894 mA g^{-1} for pyrite) rate respectively and their discharge profiles are shown in Figure 5.4a. The nano-pyrite cathode exhibited a high discharge capacity of 744 mAh g^{-1} at 0.01 C rate, which is equivalent to ~3.3 Li^+ storage per FeS_2 (Figure 5.5a). When we lower the cut-off voltage to 0.9 V, ~3.6 Li+ storage per FeS_2 (~800 mAh g^{-1}) can be achieved. This performance is comparable to those obtained on the best FeS_2 cathodes reported previously.[13, 14] According to previous work,[5] the lithiation of pyrite involves two reactions, which can occur at one or two voltage depending on the kinetics of the system.

$$FeS_2 + 2Li^+ + 2e^- \rightarrow Li_2FeS_2 \quad (2)$$

$$Li_2FeS_2 + 2Li^+ + 2e^- \rightarrow 2Li_2S + Fe^0 \qquad (3)$$

At ambient temperature (T ≤ 30 °C), the two reactions proceed simultaneously due to the slow diffusion of Li^+ into pyrite, which explains the single plateau at ~1.53 V observed in this work (Figure 5.5a) and other reports.[5, 6, 13-16] Using electrochemical impedance spectroscopy (see Figure A4.2 for details), we estimated that the diffusion coefficient of Li^+ of the nano-pyrite cathodes were on the order of 10^{-14}–10^{-15} cm^2 s^{-1}. Note that at higher temperatures (T > 55 °C) the rate of diffusion of Li^+ through the bulk pyrite increases and the first reaction could proceed at a higher voltage of ~1.7 V.[5] We also observed that the discharge capacity and voltage plateau of nano-pyrite cathode are rate dependent. When the discharge current density increases, the discharge capacity decreases and the plateau voltage drops slightly. For example, at a rate of 0.2 C, the nano-pyrite cathode yielded a lower capacity of 651 mAh g^{-1} with a lower voltage plateau of ~1.42 V (Figure 5.5a). At high current densities, this effect originates from the slow Li^+ diffusion within the electrode and/or across an electrode/electrolyte interface that hinders charge distribution to reach equilibrium.[44] The accumulated Li^+ and electrons at the electrode surface force the formation of most Li-rich phases (Li_2S and Fe). Hence the battery voltage drops faster and the discharge process is also terminated faster, even though the inner part of electrode material has not been fully utilized.

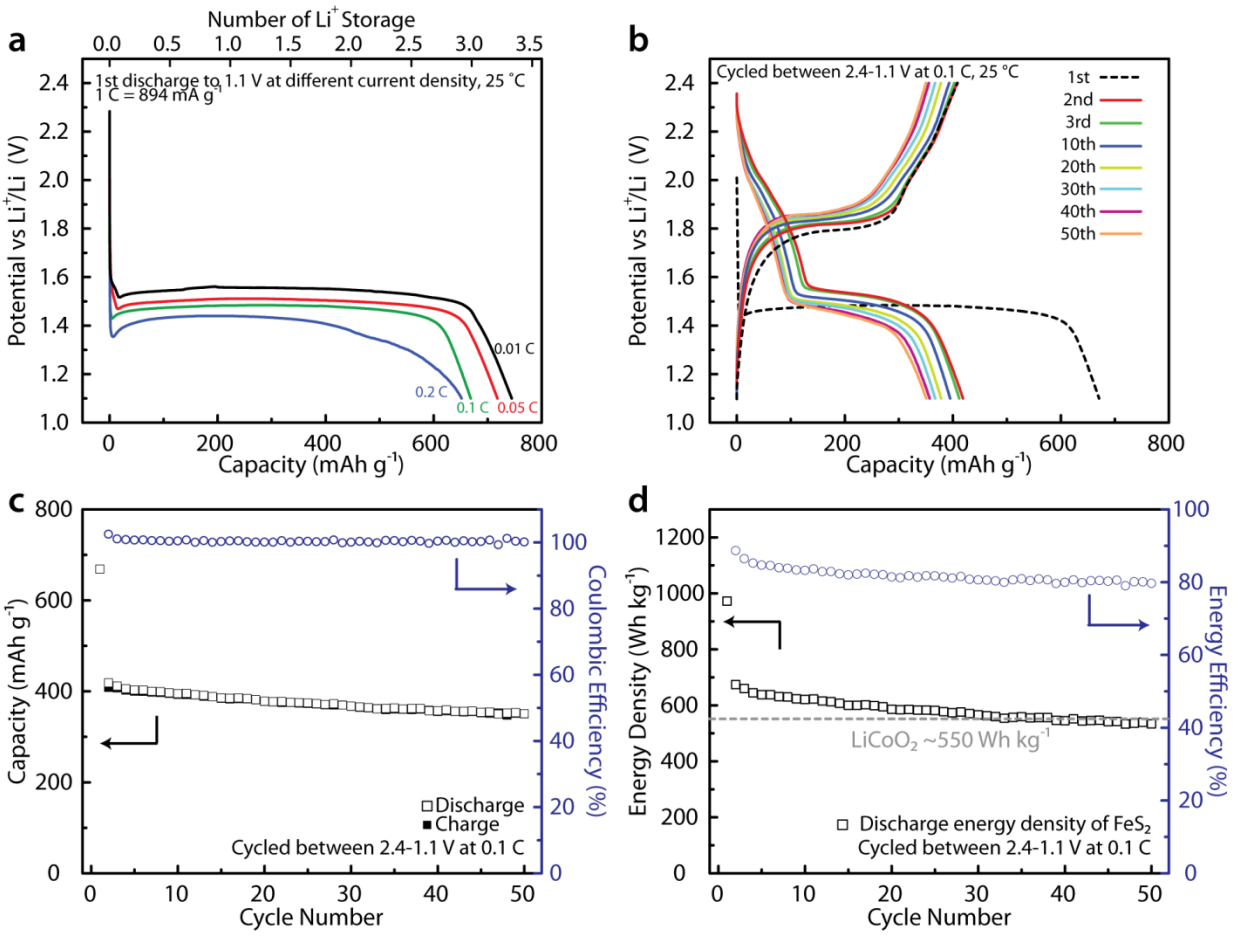

Figure 5.5. (a) Discharge profiles of four different Li/nano-pyrite cells discharge at different current densities at room temperature; (b) Voltage profiles for the 1st, 2nd, 3rd, 10th, 20th, 30th, 40th, and 50th discharge-charge cycles of a nano-pyrite cathode cycled between 2.4–1.1 V at 0.1 C rate at room temperature; (c) Discharge/charge capacity and Coulombic efficiency of the same nano-pyrite cathode in (b) vs cycle number. Note that the FeS_2 cathode is initially at charged state and undergoes discharging at the 1st cycle so that CE is only calculated from the 2nd cycle to the 50th cycle. The Coulombic efficiencies are slightly higher than 100%, which could be due to minor side reactions during discharge; (d) Discharge energy density and energy efficiency of the nano-pyrite cathode vs cycle number shown along with the theoretical discharge energy

density of $LiCoO_2$ cathode (550 Wh kg^{-1}), which is calculated using an average voltage of 3.9 V and a capacity of 140 mAh g^{-1}. Note that all the reported capacity performance in this paper was calculated based on the mass of the FeS_2.

We further investigated the reversible lithium storage capability of the nano-pyrite cathode using discharge/charge cycling tests. The Li/nano-pyrite cell was cycled over the voltage range of 2.4–1.1 V *vs* Li^+/Li at 0.1 C rate. The nano-pyrite cathode exhibited a discharge capacity of 668 mAh g^{-1} at the 1st discharge but only 409 mAh g^{-1} was recovered at the subsequent charge (Figure 5.5b, dashed curves). Despite this, the nano-pyrite cathode showed a very stable cycling performance after the first cycle (Figure 5.5c). It retained a discharge capacity of 350 mAh g^{-1} after 50 cycles and showed high averge Coulombic efficiency (100.4%, Figure 5.5c). The Li-storage capacity of the nano-pyrite cathode is much higher than that of the current $LiCoO_2$ intercalation cathode material (140 mAh g^{-1}). This enables the nano-pyrite cathode to have comparable discharge energy density to the theoretical energy density of $LiCoO_2$ cathode (Figure 5.5d) in spite of its lower potential. To the best of our knowledge, such good cycling performance of a Li/FeS_2 cell using a liquid electrolyte at room temperature has not been reported before. The good performance may be attributed to the nanoscale dimension of the nano-pyrite cathode, which affords a shorter Li^+ and electron transport pathway, improved conversion reaction kinetics, and better utilization of the active material upon discharge and charge.

Our results demonstrate that nanostructured pyrite can be a promising cathode material to enable high-capacity rechargeable batteries at lower material cost. However, since the charge

capacity is only ~61 % of the discharge capacity in the first cycle, it is clear that the pyrite phase is not recovered upon recharge to 2.4 V and the full capacity of pyrite cathode is not yet utilized in subsequent cycling. Previous reports[5, 18] suggest that the most probable phase formed in the charge reaction and also the most relevant electrochemically active phase in subsequent cycling could be $Li_{2-x}FeS_2$ ($0 < x < 0.8$):

Charge reactions:

$$Fe^0 + 2Li_2S \rightarrow Li_2FeS_2 + 2Li^+ + 2e^- \qquad (4)$$

$$Li_2FeS_2 \rightarrow Li_{2-x}FeS_2 + xLi^+ + xe^- \ (0 < x < 0.8) \qquad (5)$$

Subsequent cycling:

$$Li_{2-x}FeS_2 + (2+x)Li^+ + (2+x)\ e^- \rightleftarrows Fe^0 + 2Li_2S \ (0 < x < 0.8) \qquad (6)$$

As Fe^0 is involved in the discharge and charge reactions, the cycling behavior of such electrode is different from that of a pure Li_2S cathode, which shows different voltage profile and usually suffers rapid capacity loss.[45]

In order to recover the pyrite phase and obtain more capacity, we have tried to recharge the Li/nano-pyrite cell to a higher voltage (> 2.4 V), but such attempts resulted in fast capacity fading (Figure A4.3) in subsequent cycles. Previous *in situ* X-ray diffraction and *in situ* Mössbauer spectroscopy studies on micrometer-sized pyrite cathodes have shown that upon recharge to beyond 2.4 V, the hexagonal $Li_{2-x}FeS_2$ phase ($0 < x < 0.8$) formed in the charge reaction begins to decompose to form non-stoichiometric pyrrhotite (FeS_y) and elemental sulfur (S):[5]

$$Li_{2-x}FeS_2 \rightarrow FeS_y + (2-y)S + (2-x)Li^+ + (2-x)e^- \quad (7)$$

As these two phases (FeS_y and S) do not readily react to produce pyrite at temperatures below 265 °C,[5] lithiation of elemental sulfur occurs in the subsequent discharge (Figure A4.3) to produce a large amount of lithium sulfides likely isolated from the active Fe nanodomains formed in the discharge reaction. As the large amount of interfacial surface between lithium sulfide and Fe nanodomains is the key to the reversibility of their conversion reactions,[9, 18] isolated lithium sulfides are difficult to decompose during recharge and could dissolve more easily in the liquid electrolyte. This provides an possible explanation for the observed fast capacity fading (Figure A4.3). Therefore, we suggest that simply nanostructuring the pyrite cathode is not sufficient to fully address the challenge facing room-temperature Li/FeS_2 batteries using a liquid electrolyte. In order to fully utilize the charge-storage capability of pyrite, the incorporation of carefully designed catalysts may be necessary to alter the reaction pathway and suppress the formation of elemental sulfur during recharge.[9] *In situ* TEM[46] or *in situ* transmission X-ray microscopy[10, 47] studies on the electrochemical conversion reactions of single-crystal pyrite NWs[32] may also be a fruitful future direction to provide insights into the reaction mechanism at the microscopic level.

5.4 Summary and Outlooks

In summary, we have demonstrated the first example of large-scale synthesis of pyrite NWs *via* chemical transformation of iron fluoride NWs. As conclusively confirmed by various structural characterization techniques, high-purity pyrite NWs without other lower sulfides or marcasite polymorph impurities can be readily produced by this conversion synthesis. The nanostructured pyrite cathode prepared from the pyrite NWs exhibited excellent cycling performance at room temperature over the voltage range of 2.4–1.1 V in a Li/FeS_2 cell using a 1 M LiTFSi/TEGDME electrolyte, which retained a discharge capacity of 350 mAh g^{-1} after 50 cycles at 0.1 C rate. Furthermore, we revealed that nanostructuring did improve the reaction kinetics by shortening the Li^+ and electron transport path but it likely has not altered the delithiation reaction pathway. This work establishes nanostructured pyrite as a promising high-capacity cathode materials for rechargeable Li-ion batteries. In order to fully utilize the charge storage capability of pyrite, more in-depth understanding of the electrochemical conversion mechanism *via in situ* microscopy studies and additional strategies to control the conversion reactions such as incorporating carefully designed catalysts are needed. We hope that this work can serve as an impetus for further research efforts aiming to utilize earth-abundant Fe-based conversion cathode materials to increase the energy storage of Li-ion batteries.

5.5 References

1. Ennaoui, A., Tributsch, H., Iron sulphide solar cells. *Solar Cells* **13,** 197-200 (1984).

2. Ennaoui, A., et al., Iron disulfide for solar energy conversion. *Sol. Energy Mater. Sol. Cells* **29,** 289-370 (1993).

3. Ennaoui, A., Fiechter, S., Goslowsky, H., Tributsch, H., Photoactive Synthetic Polycrystalline Pyrite (FeS_2). *J. Electrochem. Soc.* **132,** 1579-1582 (1985).

4. Ennaoui, A., Tributsch, H., Energetic Characterization of the Photoactive FeS_2 (Pyrite) Interface. *Sol. Energy Mater.* **14,** 461-474 (1986).

5. Fong, R., Dahn, J. R., Jones, C. H. W., Electrochemistry of Pyrite-Based Cathodes for Ambient-Temperature Lithium Batteries. *J. Electrochem. Soc.* **136,** 3206-3210 (1989).

6. Shao-Horn, Y., Horn, Q. C., Chemical, Structural and Electrochemical Comparison of Natural and Synthetic FeS_2 Pyrite in Lithium Cells. *Electrochim. Acta* **46,** 2613-2621 (2001).

7. Peled, E., et al., Li/CPE/FeS_2 rechargeable battery. *Electrochim. Acta* **43,** 1593-1599 (1998).

8. Wadia, C., Alivisatos, A. P., Kammen, D. M., Materials Availability Expands the Opportunity for Large-Scale Photovoltaics Deployment. *Environ. Sci. & Technol.* **43,** 2072-2077 (2009).

9. Cabana, J., Monconduit, L., Larcher, D., Palacin, M. R., Beyond Intercalation-Based Li-Ion Batteries: The State of the Art and Challenges of Electrode Materials Reacting Through Conversion Reactions. *Adv. Mater.* **22,** E170-E192 (2010).

10. Meirer, F., et al., Three-dimensional imaging of chemical phase transformations at the nanoscale with full-field transmission X-ray microscopy. *J. Synchrotron. Radiat.* **18,** 773-781 (2011).

11. Tomczuk, Z., et al., Phase Relationships in Positive Electrodes of High Temperature Li-Al / LiCl-KCl / FeS_2 Cells. *J. Electrochem. Soc.* **129,** 925-931 (1982).

12. Preto, S. K., Tomczuk, Z., Winbush, S. v., Roche, M. F., Reactions of FeS_2, CoS_2, and NiS_2 Electrodes in Molten LiCl - KCl Electrolytes. *J. Electrochem. Soc.* **130,** 264-273 (1983).

13. Shao-Horn, Y., Osmialowski, S., Horn, Q. C., Nano-FeS_2 for Commercial Li / FeS_2 Primary Batteries. *J. Electrochem. Soc.* **149,** A1499-A1502 (2002).

14. Shao-Horn, Y., Osmialowski, S., Horn, Q. C., Reinvestigation of lithium reaction mechanisms in FeS_2 pyrite at ambient temperature. *J. Electrochem. Soc.* **149,** A1547-A1555 (2002).

15. Choi, Y. J., et al., Electrochemical properties of nickel-precipitated pyrite as cathode active material for lithium/pyrite cell. *J. Alloy. Compd.* **485,** 462-466 (2009).

16. Choi, J. W., et al., Electrochemical characteristics of room temperature Li/FeS_2 batteries with natural pyrite cathode. *J. Power Sources* **163,** 158-165 (2006).

17. Montoro, L. A., Rosolen, J. M., Shin, J. H., Passerini, S., Investigations of natural pyrite in solvent-free polymer electrolyte, lithium metal batteries. *Electrochim. Acta* **49,** 3419-3427 (2004).

18. Yersak, T. A., et al., Solid State Enabled Reversible Four Electron Storage. *Adv. Energy Mater.* **3,** 120-127 (2012).

19. Bruce, P. G., Scrosati, B., Tarascon, J.-M., Nanomaterials for rechargeable lithium batteries. *Angew. Chemie. Int. Ed.* **47,** 2930-2946 (2008).

20. Chan, C. K., et al., High-performance lithium battery anodes using silicon nanowires. *Nature Nanotech.* **3,** 31-35 (2008).

21. Wu, H., et al., Stable cycling of double-walled silicon nanotube battery anodes through solid-electrolyte interphase control. *Nature Nanotech.* **7,** 310-315 (2012).

22. Wu, H., et al., Stable Li-ion battery anodes by in-situ polymerization of conducting hydrogel to conformally coat silicon nanoparticles. *Nature Commun.* **4,** 1943 (2013).

23. Szczech, J. R., Jin, S., Nanostructured silicon for high capacity lithium battery anodes. *Energy Environ. Sci.* **4,** 56-72 (2011).

24. Lou, X. W., Li, C. M., Archer, L. A., Designed Synthesis of Coaxial SnO_2@carbon Hollow Nanospheres for Highly Reversible Lithium Storage. *Adv. Mater.* **21,** 2536-2539 (2009).

25. Lou, X. W., et al., Template-free synthesis of SnO_2 hollow nanostructures with high lithium storage capacity. *Adv. Mater.* **18,** 2325-2329 (2006).

26. Li, L., Meng, F., Jin, S., High-Capacity Lithium-Ion Battery Conversion Cathodes Based on Iron Fluoride Nanowires and Insights into the Conversion Mechanism. *Nano Lett.* **12,** 6030-6037 (2012).

27. Meester, B., Reijnen, L., Goossens, A., Schoonman, J., Synthesis of Pyrite (FeS_2) Thin Films by Low-Pressure MOCVD. *Chem. Vap. Deposition* **6,** 121-128 (2000).

28. Höpfner, C., et al., Stoichiometry-, phase- and orientation-controlled growth of polycrystalline pyrite (FeS_2) thin films by MOCVD. *J. Cryst. Growth* **151,** 325-334 (1995).

29. Berry, N., et al., Atmospheric-Pressure Chemical Vapor Deposition of Iron Pyrite Thin Films. *Adv. Energy Mater.* **2,** 1124-1135 (2012).

30. Cabán-Acevedo, M., et al., Synthesis and Properties of Semiconducting Iron Pyrite (FeS2) Nanowires. *Nano Lett.* **12,** 1977-1982 (2012).

31. Morrish, R., Silverstein, R., Wolden, C. A., Synthesis of Stoichiometric FeS_2 through Plasma-Assisted Sulfurization of Fe_2O_3 Nanorods. *J. Am. Chem. Soc.* **134,** 17854-17857 (2012).

32. Cabán-Acevedo, M., et al., Synthesis, Characterization, and Variable Range Hopping Transport of Pyrite (FeS_2) Nanorods, Nanobelts and Nanoplates. *ACS Nano* **7,** 1731-1739 (2013).

33. Wadia, C., et al., Surfactant-Assisted Hydrothermal Synthesis of Single phase Pyrite FeS_2 Nanocrystals. *Chem. Mater.* **21,** 2568-2570 (2009).

34. Puthussery, J., et al., Colloidal Iron Pyrite (FeS_2) Nanocrystal Inks for Thin-Film Photovoltaics. *J. Am. Chem. Soc.* **133,** 716-719 (2010).

35. Moon, G. D., et al., Chemical transformations of nanostructured materials. *Nano Today* **6,** 186-203 (2011).

36. Li, L., et al., Facile Solution Synthesis of α-$FeF_3 \cdot 3H_2O$ Nanowires and Their Conversion to α-Fe_2O_3 Nanowires for Photoelectrochemical Application. *Nano Lett.* **12,** 724-731 (2012).

37. Jin, S., Bierman, M. J., Morin, S. A., A New Twist on Nanowire Formation: Screw-Dislocation-Driven Growth of Nanowires and Nanotubes. *J. Phys. Chem. Lett.* **1,** 1472-1480 (2010).

38. Morin, S. A., Bierman, M. J., Tong, J., Jin, S., Mechanism and Kinetics of Spontaneous Nanotube Growth Driven by Screw Dislocations. *Science* **328,** 476-480 (2010).

39. Peng, D.-Y., Zhao, J., Representation of the vapour pressures of sulfur. *J. Chem. Thermodyn.* **33,** 1121-1131 (2001).

40. Kleppe, A. K., Jephcoat, A. P., High-pressure Raman spectroscopic studies of FeS_2 pyrite. *Mineralogical Magazine* **68,** 433-441 (2004).

41. Vogt, H., Chattopadhyay, T., Stolz, H. J., Complete first-order Raman spectra of the pyrite structure compounds FeS_2, MnS_2 and SiP_2. *J. Phys. Chem. Solids* **44,** 869-873 (1983).

42. Bi, Y., et al., Air Stable, Photosensitive, Phase Pure Iron Pyrite Nanocrystal Thin Films for Photovoltaic Application. *Nano Lett.* **11,** 4953-4957 (2011).

43. Faber, M. S., et al., Earth-Abundant Cobalt Pyrite (CoS_2) Thin Film on Glass as a Robust, High-Performance Counter Electrode for Quantum Dot-Sensitized Solar Cells. *J. Phys. Chem. Lett.* **4,** 1843-1849 (2013).

44. Goodenough, J. B., Kim, Y., Challenges for Rechargeable Li Batteries†. *Chem. Mater.* **22,** 587-603 (2009).

45. Cai, K., Song, M.-K., Cairns, E. J., Zhang, Y., Nanostructured Li_2S–C Composites as Cathode Material for High-Energy Lithium/Sulfur Batteries. *Nano Lett.* **12,** 6474-6479 (2012).

46. Wang, F., et al., Tracking lithium transport and electrochemical reactions in nanoparticles. *Nature Commun.* **3,** 1201 (2012).

47. Nelson, J., et al., In Operando X-ray Diffraction and Transmission X-ray Microscopy of Lithium Sulfur Batteries. *J. Am. Chem. Soc.* **134,** 6337-6343 (2012).

APPENDIX 1

Supporting Information for CHAPTER 2:

High-Capacity Lithium-Ion Battery Conversion Cathodes Based on Iron Fluoride Nanowires and Insights into the Conversion Mechanism

---

This Appendix was originally made available online as supporting information for *Nano Lett.* **12,** 6030-6037 (2012), in collaboration with F. Meng and S. Jin.

A1.1 Experimental details

Materials. All chemicals were used as received without further purification. Hydrofluoric acid (aqueous HF solution, 48 wt%, CAS # 7664-39-3. *Warning: HF solution is highly corrosive and must be handled with care and proper protection. Please see safety information.*[1]), iron (III) nitrate nonahydrate [$Fe(NO_3)_3 \cdot 9H_2O$, ≥98.0%, CAS # 7782-61-8] and acetonitrile (Chromasolv® Plus, for HPLC, ≥99.9, CAS #75-05-8) and commercial iron trifluoride powder (FeF_3, ≥98.0%, CAS # 7783-50-8) were purchased from Sigma Aldrich. Ethanol (200 proof, CAS #64-17-5) was purchased from Decon Laboratories Inc. N-methyl-2-pyrrolidone (NMP, ≥99.5%, CAS # 872-50-4), 1 M lithium hexafluorophosphate ($LiPF_6$) dissolved in 1:1 (v:v) ethyl carbonate (EC)/dimethyl carbonate (DMC), polyethylene separator membranes, polyvinylidene difluoride (PVDF, ≥99.5%, CAS # 24937-79-9) binder, lithium foils (15.6 mm in diameter × 0.45 mm in thickness, >99%, CAS #7439-93-2) and 2032-type coin cell cases were purchased from MTI Corporation. Carbon black [Super P® conductive, ≥99% (metal basis), CAS # 1333-86-4] and aluminum foils [0.025 mm in thickness, ≥99.45% (metal basis), CAS # 7429-90-5] were purchased from Alfa Aesar.

NW Synthesis. α-$FeF_3 \cdot 3H_2O$ NWs were prepared *via* an improved synthesis based on our previous work.[2] Briefly, 7.5 mL ethanol and 2.0 mL HF aqueous solution (48 wt%) were carefully added into a 15 mL plastic centrifuge tube in sequence. The centrifuge tube was sealed and gently shaken by hand with great caution to allow the two liquids to mix. An Fe^{3+} solution in ethanol with a concentration of 266 mM was made by dissolving 1.616 g $Fe(NO_3)_3 \cdot 9H_2O$ in 15.0 mL ethanol. 0.500 mL of this Fe^{3+}/ethanol solution was then quickly injected into the HF/ethanol mixture using an Eppendorf pipet. The resulting colorless solution with a concentration ratio of

$c(Fe^{3+})$: $c(HF)$: $c(H_2O)$ ≈ 13.3 mM: 5560 mM: 6760 mM was gently mixed by shaking and kept in an oven at 60 °C for 24 h. No substrate was used during the reaction and aggressive agitation was avoided to suppress the formation of large β-$FeF_3 \cdot 3H_2O$ crystals. The white cloudy precipitate that appeared over time was collected by centrifugation at 5000 rpm for 5 min, washed with dry ethanol twice and vacuum-dried at room temperature. Typically, 6.6–7.7 mg NWs can be acquired from a 10 mL-scale reaction, corresponding to a yield of 30–35% (*vs* the 12–24% in our previous work[2]) based on the limiting agent of Fe.

FeF_3 NWs were prepared by thermal dehydration of the as-synthesized α-$FeF_3 \cdot 3H_2O$ NWs in an inert atmosphere using a tube furnace (Lindberg/Blue M) equipped with pressure and gas flow controls. Briefly, a large alumina boat containing ~150 mg α-$FeF_3 \cdot 3H_2O$ NWs (white solid) were placed at the center of the tube furnace. The tube was first slowly evacuated and flushed three times with argon gas and then the NWs were kept under vacuum (~40 mTorr) at 50 °C to for 20 min to dry completely. Then under a flowing argon gas at a rate of 200 sccm and a pressure of 760 Torr, the furnace temperature was slowly ramped from 50 °C to 350 °C in 150 min (~2 °C min^{-1}) and held at 350 °C for 30 min before naturally cooling down to produce a pale greenish/brownish product.

Material Characterization. Scanning electron microscopy (SEM) images were acquired using a LEO 55 VP field emission scanning electron microscope at a working voltage of 5 kV. As-synthesized α-$FeF_3 \cdot 3H_2O$ NWs, FeF_3 NWs and the commercial FeF_3 powder were dispersed in ethanol and dropcasted onto Si/SiO_2 substrates mounted on metallic pucks using double-sided carbon tapes for SEM characterization. The FeF_3 NW electrodes (nanocomposite films of FeF_3

NWs, carbon black and PVDF binder on aluminum foils) were directly mounted on metallic pucks using double-sided carbon tape and examined by SEM. Transmission electron microscopy (TEM) images and electron diffraction (ED) patterns were acquired using either a Philips CM200 transmission electron microscope or a FEI Titan transmission electron microscope at an accelerating voltage of 200 kV. The TEM samples were prepared by dropcasting FeF_3 NWs in ethanol onto lacey-carbon grids (Ted Pella Inc. lacey carbon type-A, 300 Mesh). The FeF_3 NW electrodes after the galvanostatic cycling tests were recovered from disassembled coin cells and first soaked in dry acetonitrile for 30 min in order to remove surface-absorbed species. The electrodes were then blown dry with a gentle stream of N_2. The electrode film was scratched using a pair of clean tweezers and the resulting powder (a mixture of tested NWs, carbon black and PVDF binder) was transferred to a small centrifuge tube, to which a small amount of fresh ethanol was added to create a suspension with the help of a brief sonication at 100 W for 1 min. The suspension was drop-casted onto the lacey-carbon TEM grids and dried to make the TEM samples. All the TEM grids were checked for appropriate NW density using an optical microscope before TEM characterization. Air/moisture-exposure was minimized as much as possible for the cycled FeF_3 NW TEM samples and oxide layer formation at the surface of the NWs has not been observed so far. Powder X-ray diffraction (PXRD) data was collected on a Siements STOE diffractometer using Cu Kα radiation. The PXRD samples were prepared by drop-casting the ethanol suspensions of α-$FeF_3 \cdot 3H_2O$ NWs and FeF_3 NWs onto glass substrates and air-dried.

FeF_3 Cathode Processing and Electrochemical Measurements. Electrochemical measurements were performed on electrodes pasted on aluminum foils, which were prepared

from slurries containing 70 wt% FeF_3 NWs, 20 wt% conductive carbon black and 10 wt% PVDF binder using NMP as the solvent. The mass loading of active material (FeF_3 NWs) was around 2 mg cm^{-2}. The FeF_3 cathodes based on the commercial FeF_3 powder were prepared in the same fashion. CR2032-type coin cells were assembled in an argon-fill glovebox, using Li metal as the counter/quasi-reference electrode, 1 M $LiPF_6$ in EC/DMC (1/1 by volume) as the electrolyte, polyethylene films as the separator. All the cells were aged overnight before any tests. Cyclic voltammetry (CV) and electrochemical impedance spectroscopy (EIS) were performed using a Biologic SP-200 Potentiostat operated using EC-Lab software. CV scans were taken in a voltage window of 4.5–1.0 V *vs* Li^+/Li at a scan speed of 0.5 mV s^{-1}. EIS measurements were carried out over a frequency range from 200 kHz to 50 mHz with a perturbation voltage of 10 mV. The cells were rest for 1 h before taking the EIS measurements. Discharge/charge cycling tests were done on a multi-channel battery analyzer (MTI BST8-WA) operated using Neware software at room temperature (~25 °C) in a voltage window of 4.5–1.5 V *vs* Li^+/Li under a constant current of 50 mA g^{-1} and 200 mA g^{-1} (relative to the mass of FeF_3 NWs). After constant-current charging to 4.5 V, an additional constant-voltage charging step was performed at 4.5 V until the current drops to 1/10 of its original value. This protocol for battery charging was used unless noted otherwise. All reported performance was calculated based on the mass of the active material (FeF_3 NWs).

A1.2 Additional figures and tables

Table A1.1 Different dehydration conditions and the product compositions.

Dehydration conditions	Major phases present in the products
200 °C, 8h	Residual α-$FeF_3 \cdot 3H_2O$ + β-$FeF_3 \cdot 3H_2O$ + cubic FeF_3
ramping to 300 °C at 2 °C min^{-1} and hold at 300 °C for 30 min	Cubic FeF_3 + Rhombohedral FeF_3 + FeF_2
ramping to 350 °C at 2 °C min^{-1} and hold at 350 °C for 30 min	Rhombohedral FeF_3 + FeF_2
ramping to 600 °C at 2 °C min^{-1} and hold at 650 °C for 30 min	Rhombohedral FeF_3 + FeF_2

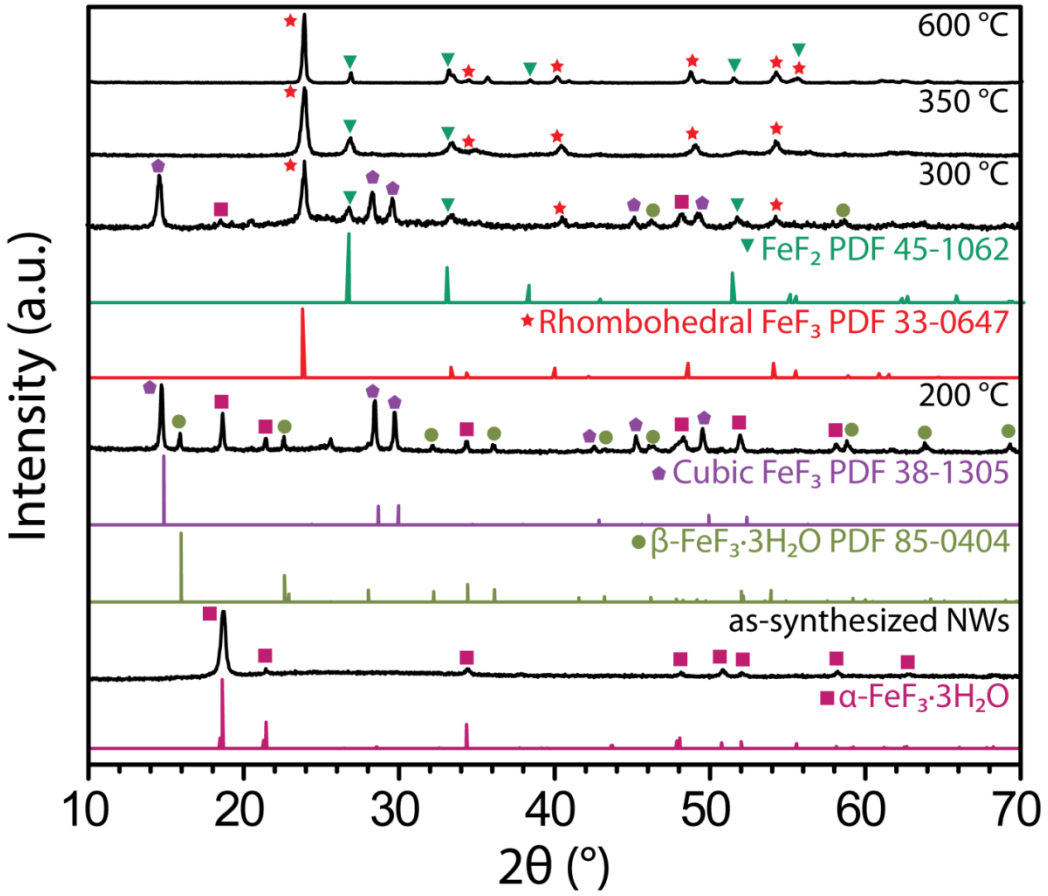

Figure A1.1 | PXRD of dehydration products obtained at different conditions. Experimental patterns are all in black and reference diffractograms are displayed in different colors. The dehydration conditions and the resulting product phases were summarized in **Table A1.1** below. All the dehydration experiments were carried out under a flow of 200 sccm argon gas and a pressure of 760 Torr.

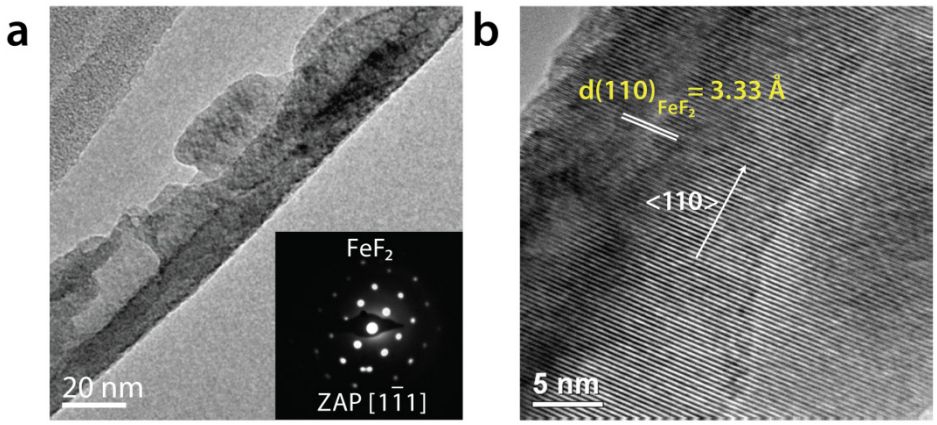

Figure A1.2 (a) TEM image of a single-crystalline FeF_2 nanowire (NW). Inset is the corresponding SAED pattern indexed to the [1$\bar{1}$1] zone axis of tetragonal FeF_2. The one extra spot in the SAED pattern is likely caused by the minor imperfection of the crystal; (b) HRTEM image of the NW in (a) showing continuous lattice fringes and a NW axial direction of <110>.

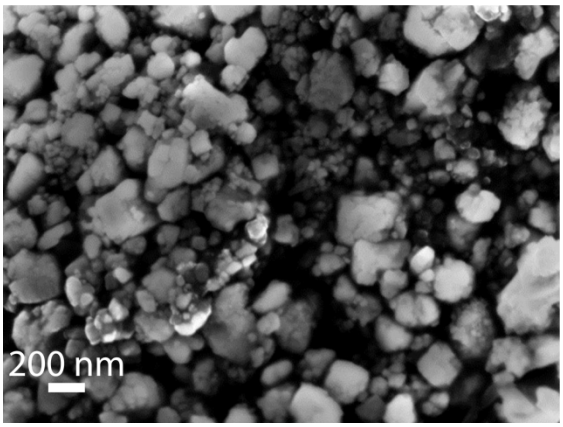

Figure A1.3 A SEM image of the commercial FeF_3 powder clearly showing an average grain size > 200 nm.

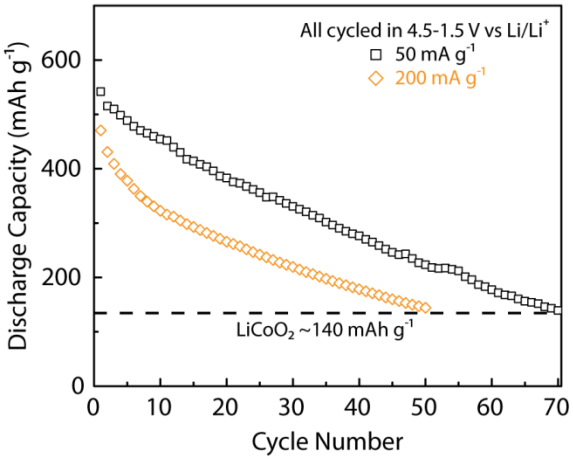

Figure A1.4 The typical cycling performance of a FeF_3 NW cathode cycled at a current of 200 mA g^{-1} (open yellow squares, up to 50 cycles). No additional constant-voltage charging was used in this cycling test. The cycling performance of the FeF_3 NW cathode measured at 50 mA g^{-1} current obtained from the same cell presented in Figure 3c in the main text is also shown as a comparison. The cycling test was stopped at 70 cycles for this cell

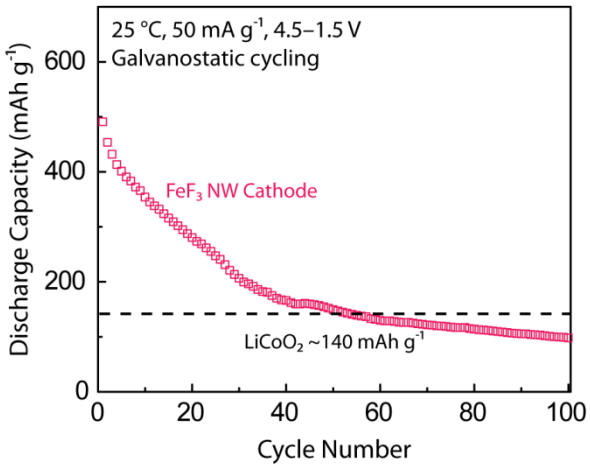

Figure A1.5. Discharge capacity of the FeF_3 NW electrode *vs* cycle number (up to 100 cycles) in comparison the practical capacity of $LiCoO_2$ (~140 mAh g^{-1}, the dashed line); No additional

constant-voltage charging was used in this cycling test and this data is acquired from a different battery cell from the one shown in Figure 3 of the main text.

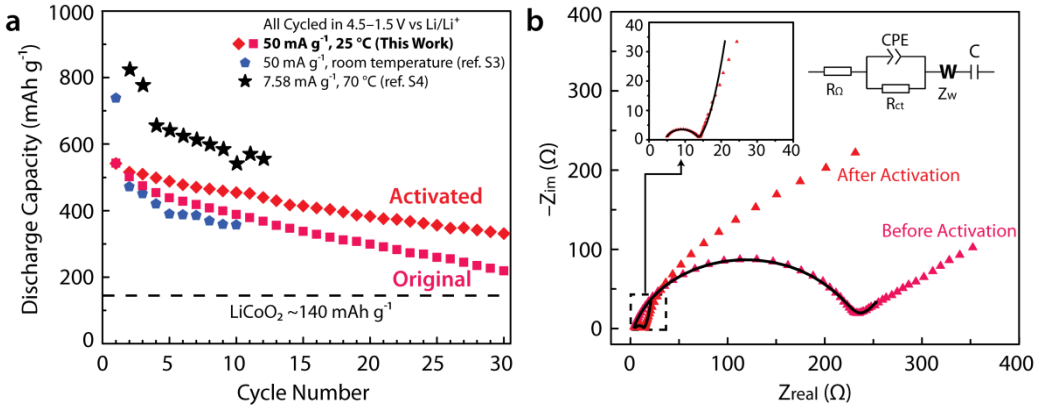

Figure A1.6. (a) A comparison of the typical cycling performance of a CV-activated battery cell and a non-activated cell. The previous record-performance (the light-blue pentagons) achieved at room temperature on a FeF_3 nanoparticle/carbon nanotube nanocomposite cathode[3] is shown as a comparison to demonstrate the improved electrochemical properties of our FeF_3 NW cathode. The cycling performance of a FeF_3 nanoparticle (*with average crystallite size ~25 nm*)/carbon black nanocomposite cathode tested *at 70 °C and under a small current of 7.58 mA* g^{-1} is also shown as the black stars,[4] in which case the high capacity benefited from improved reaction kinetics at the elevated temperature and a small current. All the discharge capacity was calculated based on the mass of the active materials (FeF_3); (b) Electrochemical impedance spectroscopy of the FeF_3 NW electrode at the charged state measured before and after one cycle of CV scan. Symbols represent experimental spectra and continuous lines are the fitted data using the equivalent circuit shown in the inset on the right. The inset on the left is a magnified

view of the data shown in the dashed box. The charge-transfer resistance (diameter of the semicircle) was significantly reduced after one cycle of CV scan.

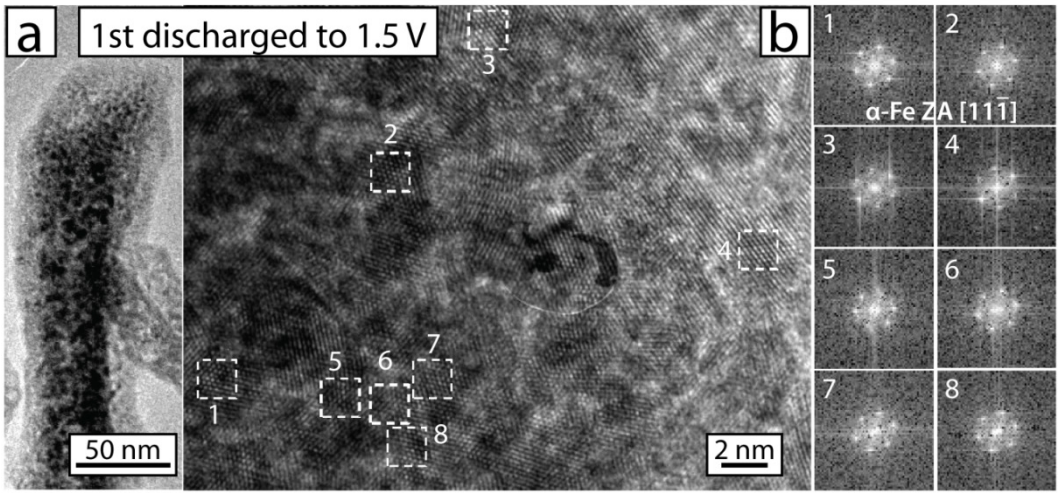

Figure A1.7. (a) TEM image of a single lithiated FeF_3 NWs with many small dark nanodomains (3–5 nm) clearly visible; (b) HRTEM image and FFT analysis that confirm that the dark nanodomains are single-crystal α-Fe oriented along the direction of $[11\bar{1}]$ zone axis. The adjacent α-Fe nanodomains [domain 5, 6, 7, and 8 in (b)] were interconnected through the common {110} family planes. The α-Fe nanodomains not close to each other could have different orientations, such as the case for domains 1, 2, 3, and 4. The feature in the center of (b) is a known defect in the camera of the TEM at the time of the experiment.

A1.3 References

[1] Safety Information of Hydrofluoric Acid.

http://www.sigmaaldrich.com/catalog/ProductDetail.do?lang=en&N4=30107|SIAL&N5=SEARCH_CONCAT_PNO|BRAND_KEY&F=SPEC

[2] Li, L.; Yu, Y.; Meng, F.; Tan, Y.; Hamers, R. J.; Jin, S. *Nano Lett.* **2012,** 12, 724-731.

[3] Kim, S.-W.; Seo, D.-H; Gwon, H.; Kim, J.; Kang, K. *Adv. Mater.* **2010,** 22, 5260-5264

[4] Badway, F.; Cosandey, F.; Pereira, N.; Amatucci, G. G. *J. Electrochem. Soc.* **2003,** 150, A1318-A1327.

APPENDIX 2

Supporting Information for CHAPTER 3:

Visualization of Electrochemically-Driven Solid-State Phase Transformations Using *Operando* Hard X-ray Spectro-Imaging

This Appendix was originally made available online as supporting information for *Nature Commun.* **6**, 6883, (2015), in collaboration with Y.-c. K. Chen-Wiegart, J. Wang, P. Gao, Q. Ding, Y.-S. Yu, F. Wang, J. Cabana, J. Wang, and S. Jin.

A2.1 Supplementary Methods

Materials: All chemicals were used as received without further purification. Hydrofluoric acid (aqueous HF solution, 48 wt%, CAS # 7664-39-3. *Warning: HF solution is highly corrosive and must be handled with care and proper protection. Please see the MSDS document in Sigma-Aldrich website*), iron (III) nitrate nonahydrate [$Fe(NO_3)_3 \cdot 9H_2O$, ≥98.0%, CAS # 7782-61-8], commercial iron trifluoride powder (FeF_3, ≥98.0%, CAS # 7783-50-8), iron difluoride powder (FeF_2, ≥98.0%, CAS # 7789-28-8), metallic iron particles (Fe, >99.0%, CAS # 7439-89-6), lithium ribbon (0.75 mm in thickness, >99.9%, CAS #7439-93-2) were purchased from Sigma Aldrich. Ethanol (200 proof, CAS #64-17-5) was purchased from Decon Laboratories Inc. N-methyl-2-pyrrolidone (NMP, ≥99.5%, CAS # 872-50-4), polyethylene separator membranes, polyvinylidene difluoride (PVDF, ≥99.5%, CAS # 24937-79-9) binder, lithium foils (15.6 mm in diameter × 0.45 mm in thickness, >99%, CAS #7439-93-2) and 2032-type coin cell cases were purchased from MTI Corporation. 1 M lithium hexafluorophosphate ($LiPF_6$) dissolved in 1:1 (v:v) ethyl carbonate (EC)/dimethyl carbonate (DMC) electrolyte was purchased from BASF. Carbon black [Super P® conductive, ≥99% (metal basis), CAS # 1333-86-4] and aluminum foils [0.025 mm in thickness, ≥99.45% (metal basis), CAS # 7429-90-5] were purchased from Alfa Aesar. Carbon Papers (Toray Paper 030 TGPH030-1005, 110 μm in thickness) were purchased from Fuel Cell Earth LLC.

Synthesis of FeF_3 Microwires and Polyhedra: We developed the syntheses of two new FeF_3 (rhombohedral structure, $R\bar{3}c$) samples with different morphologies and microstructures by rationally controlling the supersaturation of growth solution[1–3]. In both syntheses, ethanol was

used as the solvent, $Fe(NO_3)_3 \cdot 9H_2O$ as the Fe^{3+} source, and HF as the F^- source. Both F^- and H_2O act as ligands in complex with Fe^{3+} to control the supersaturation.

FeF_3 microwires (MWs) were prepared by thermal dehydration of α-$FeF_3 \cdot 3H_2O$ MWs in argon atmosphere. The precursor α-$FeF_3 \cdot 3H_2O$ MWs were synthesized *via* a new synthesis developed based on our previous work[1]. A diluted HF/ethanol solution (~5 M HF) was first prepared by mixing 1.812 mL HF aqueous solution (48 wt%) with 8.3 mL ethanol in a plastic centrifuge tube. Then, 7.0 mL ethanol, 1.0 mL diluted HF (~5 M), 1.0 mL deionized water were sequentially added into a 15 mL plastic centrifuge tube with caution. The centrifuge tube was sealed and gently shaken by hand with great caution to allow the liquids to mix. An Fe^{3+} solution in ethanol with a concentration of 532 mM was made by dissolving 1.616 g $Fe(NO_3)_3 \cdot 9H_2O$ in 7.5 mL ethanol. 1.000 mL of this Fe^{3+}/ethanol solution was then quickly injected into the HF/ethanol mixture using an Eppendorf pipet. The resulting colorless solution with a concentration ratio of $c(Fe^{3+})$: $c(HF)$: $c(H_2O)$ $\approx$ 53.2 mM: 500 mM: 11575 mM was gently mixed by shaking and kept in an oven at 60 °C for 18 h. No substrate was used during the reaction and aggressive agitation was avoided to suppress the formation of large β-$FeF_3 \cdot 3H_2O$ crystals. The white cloudy precipitate that appeared over time was collected by centrifugation at 5000 rpm for 5 min, washed with dry ethanol twice and vacuum-dried at room temperature. Typically, ~15 mg product of α-$FeF_3 \cdot 3H_2O$ MWs could be obtained from a 10 mL scale synthesis, corresponding to a reaction yield of ~17 % based on the limiting reagent of Fe. In order to make the anhydrous FeF_3 MWs, the as-synthesized white precipitate of α-$FeF_3 \cdot 3H_2O$ MWs was dehydrated in an inert atmosphere using a quartz tube reactor equipped with pressure and gas flow controls and placed a tube furnace (Lindberg/Blue M). Briefly, a large alumina boat

containing ~150 mg α-$FeF_3 \cdot 3H_2O$ MWs were placed at the center of the tube furnace. The tube reactor was first slowly evacuated and flushed three times with argon gas and then the MWs were kept under vacuum (~40 mTorr) at 50 °C to for 20 min to dry completely. Then under a flowing argon gas at a flow rate of 100 sccm and a pressure of 770 Torr, the furnace temperature was slowly ramped from 50 °C to 350 °C in 150 min (~2 °C min^{-1}) and held at 350 °C for 30 min before naturally cooling down to produce a pale greenish/brownish product (~100 % reaction yield).

Rhombohedral phase FeF_3 polyhedra were prepared by thermal conversion of metastable cubic phase FeF_3 polyhedra, which were synthesized in ethanol solution. Briefly, a diluted HF/ethanol solution (~1 M HF) was first prepared by mixing 0.719 mL HF aqueous solution (48 wt%) with 19.3 mL ethanol in a plastic centrifuge tube. Then, 7.5 mL ethanol, 1.0 mL diluted HF (~1 M), 0.5 mL deionized water were sequentially added into a 15 mL plastic centrifuge tube with caution. The centrifuge tube was sealed and gently shaken by hand with great caution to allow the liquids to mix. An Fe^{3+} solution in ethanol with a concentration of 200 mM was made by dissolving 0.808 g $Fe(NO_3)_3 \cdot 9H_2O$ in 10.0 mL ethanol. 1.000 mL of this Fe^{3+}/ethanol solution was then quickly injected into the HF/ethanol mixture using an Eppendorf pipet. The resulting colorless solution with a concentration ratio of $c(Fe^{3+})$: c(HF) : $c(H_2O)$ ≈ 20 mM: 100 mM: 4670 mM was gently mixed by shaking and kept in an oven at 60 °C for 24 h. No substrate was used during the reaction and aggressive agitation was avoided to suppress the formation of large β-$FeF_3 \cdot 3H_2O$ crystals. The light yellow precipitate that appeared over time was collected by centrifugation at 5000 rpm for 5 min, washed with dry ethanol twice and vacuum-dried at room temperature. Typically, 5−6 mg product of the cubic phase FeF_3 polyhedra could be obtained

from a 10 mL scale synthesis, corresponding to a reaction yield of 22–27 % based on the limiting reagent of Fe. The as-synthesized cubic phase FeF_3 polyhedra were thermally annealed in an argon atmosphere at 350 °C for 30 min in the same quartz tube reactor described above to produce the rhombohedral phase FeF_3 polyhedra (~100 % reaction yield).

Material Characterization: Scanning electron microscopy (SEM) images were acquired using a LEO 55 VP field emission scanning electron microscope at a working voltage of 5 kV. Transmission electron microscopy (TEM) images and electron diffraction (ED) patterns were acquired using either a Tecnai T-12 transmission electron microscope (120 kV) or a FEI Titan transmission electron microscope (200 kV). The TEM samples were prepared by dropcasting FeF_3 samples in ethanol onto lacey-carbon grids (Ted Pella Inc. lacey carbon type-A, 300 Mesh). Air/moisture-exposure was minimized as much as possible. Powder X-ray diffraction (PXRD) data were collected on a Bruker D8 diffractometer using Cu Kα radiation and corrected for background. The PXRD samples were prepared by drop-casting the ethanol suspensions of the samples onto glass substrates and dried. The Brunauer–Emmet–Teller (BET) specific surface area and pore size distribution of the FeF_3 MWs were obtained from nitrogen adsorption–desorption isotherms measured by a Quantachrome Autosorb-1 gas sorption analyzer.

Processing of FeF_3 Cathode and Electrochemical Measurements: Electrochemical measurements were performed on electrodes pasted on aluminum foils (~25 μm thickness), which were prepared from slurries containing 70 wt% active material, 20 wt% conductive carbon black and 10 wt% PVDF binder using NMP as the solvent. The mass loading of the active material (FeF_3) is around 2 mg cm^{-2}. CR2032-type coin cells were assembled in an argon-filled glovebox, using

Li metal as the counter/quasi-reference electrode, 1 M $LiPF_6$ in EC/DMC (1/1 by volume) as the electrolyte, and electrolyte-soaked polyethylene films as the separator. All cells were aged a few hours before any tests. Electrochemical impedance spectroscopy (EIS) was performed using a Biologic SP-200 Potentiostat operated using EC-Lab software. EIS measurements were carried out over a frequency range from 200 kHz to 50 mHz with a perturbation voltage of 10 mV. Constant current discharge/charge tests were carried out using a Biologic VMP-3 potentiostat/galvanostat in a voltage window of 4.5–1.0 V at different current rates. All reported performance was calculated based on the mass of the active material.

Fabrication of Batteries for *Operando* Studies: The *operando* experiments were performed using perforated 2032-type coin cells with ~4 mm holes on both sides of the cell cases. The holes were sealed using Kapton tapes. The holes need to be small to ensure a small cell impedance. The FeF_3 samples (polyhedra and MWs 1:1 by weight) were mixed with carbon black and PVDF binder in a weight ratio of 3:5:2 in NMP. The resulting slurry was pasted onto thin aluminum foils (~8 μm thickness) or carbon papers (~110 μm thickness) and then dried in vacuum to make electrodes. The thin aluminum foils and thin carbon papers are quite transparent to hard X-rays but still robust enough for handling, which is critical to the *operando* experiment. The density of samples on the electrodes was checked using an optical microscope or a scanning electron microscope before packing into coin cells. The *operando* cells were assembled in an argon-filled glovebox using Li metal as the counter/quasi-reference electrode and polyethylene films soaked with 1 M $LiPF_6$ EC/DMC (1/1 by volume) electrolyte as the separator. No additional electrolyte was added during the cell packing in order to minimize the X-ray attenuation caused by the electrolyte liquid. The as-made cells were aged for a few hours and checked using

electrochemical impedance spectroscopy before being used in the *operando* experiments, during which the cell was held by a custom-modified coin cell holder and discharged and charged at rate of ~1/15 C (1 C = 712 mA/g). The coin cell holder was purchased from MTI Corporation and attached to a stainless steel rod standing on the motorized stage. The positive lead of the cell holder was modified to make contact with the coin cell from the side so that the X-ray was not blocked. We also put a piece of perforated stainless steel foil between the positive lead and the coin cell to apply a gentle pressure to make better electrical contact.

Operando Hard X-ray Spectro-Imaging: The *operando* hard X-ray spectro-imaging experiments were performed using the full-field transmission X-ray microscope (FFTXM) at beamline X8c, National Synchrotron Light Source (NSLS), Brookhaven National Laboratory (BNL). The TXM operates using a bending magnetic source and a Si (111) double-crystal monochromator. It routinely operates in absorption contrast mode over a wide energy range from 5 to 11 keV with spatial and energy resolutions of ~25 nm and $\Delta E/E = 10^{-4}$, respectively.

In the *operando* experiment, the *operando* coin cell was mounted on an motorized *X, Y, Z, θ* stage and aligned so that the X-ray beam could transmit through the two holes in the cell. A field of view of $40 \times 40\ \mu m^2$ with a 2048 × 2048 CCD camera was used. The cell was continuously cycled in galvanostatic or potentiostatic mode and the X-ray absorption-contrast images (X-ray transmitted through the sample) and reference background images (X-ray passing through air) were collected in sequence under dynamic conditions. To track the phase transformations in the electrode, a full series of TXM images were collected at each states of discharge and charge. Each TXM image series was collected by scanning across the Fe *K*-edge (7112 eV) from 7091 to 7285 eV, with a step size of 2 eV, and taking one TXM image at each energy step, which

generated 1024 × 1024 XANES spectra with 2 × 2 binned pixels or 512 × 512 XANES spectra with 4 × 4 binned pixels depending on the choice of camera binning. The exposure time for each image was chosen depending on the intensity of the beam and was typically 8–10 seconds for 2 × 2 camera binning and 4–5 seconds for 4 × 4 camera binning during our experiments. Each chemical phase map took ~8 minutes to finish when using 4 × 4 camera binning and the output pixel size is ~80 nm.

Data Processing and Chemical Map Construction: Each set of TXM images was first aligned using the Xradia Controller Software to correct the positioning errors of the motor stage, X-ray optics, or sample. Then all data were analyzed using a customized program developed in house using Matlab R2011b.

We first carried out background normalization for all TXM images using the unique reference background images (X-ray passing through air) collected at each energy to get the absorption-contrast images. One example is shown in Figure A2.1a, which is a field-of-view taken from an *operando* cell discharged to ~2.0 V. Then we could extract the XANES spectrum (X-ray attenuation versus energy raw data) at each pixel (1024 × 1024 pixels for binning 2, 512 × 512 pixels for binning 4). Here we used the single pixel spectrum (red open circles in Figure A2.1b) extracted from point S1 in Figure A2.1a to explain the data normalization procedures and compare the effectiveness of our methods with previously reported methods[4–7].

XANES spectra need to be normalized and scaled in order to be directly compared with each other and correctly fitted using standard reference spectra. The normalization is done using the data points in the pre-edge and post-edge regions[4–7], which involves five major steps: 1) Fit the pre-edge spectrum to a linear function and subtract it from the spectrum over the entire range of

energy; 2) Identify the threshold energy E_0, which is the maximum of the 1st derivative of the spectrum; 3) Fit the post-edge spectrum to a linear function; 4) Determine the edge-jump value, which is the difference between the pre-edge function and post-edge function at the threshold energy E_0; 5) Normalize the spectrum using the edge-jump value to make the pre-edge become ~0 and the post-edge become ~1.

The normalized spectrum can then be fitted to standard reference spectra to determine the ratio between different phases. This is because that based on Beer's Law, the total X-ray attenuation at each pixel can be considered as the sum of X-ray attenuation from each constituent phase with attenuation coefficient $\boldsymbol{\mu}$ and thickness $\boldsymbol{t}$, which can be written as:

$$-\ln(\boldsymbol{I_t}/\boldsymbol{I_0}) = \boldsymbol{\mu}(\mathrm{FeF_3}) \cdot \boldsymbol{t}(\mathrm{FeF_3}) + \boldsymbol{\mu}(\mathrm{FeF_2}) \cdot \boldsymbol{t}(\mathrm{FeF_2}) + \boldsymbol{\mu}(\mathrm{Fe}) \cdot \boldsymbol{t}(\mathrm{Fe}) \qquad (1)$$

where $\boldsymbol{I_0}$ is the incident X-ray intensity and $\boldsymbol{I_t}$ is the X-ray intensity after it passes through the sample. Note that attenuation coefficient $\boldsymbol{\mu}$ and $-\ln(\boldsymbol{I_t}/\boldsymbol{I_0})$ are energy dependent [as the $-\ln(\boldsymbol{I_t}/\boldsymbol{I_0})$ versus *energy* plot is the XANES spectrum] and the rutile FeF_2 phase was used to represent all the possible rutile related Fe^{2+}-containing phases. This is a reasonable approximation because it was reported that the Li_xFeF_3 (when $x \approx 1.0$) phase contains structural features that are found in the rutile FeF_2 structure (*23*). As other battery components in the pathway of the beam (such as electrolyte, carbon, PVDF binder, and separator) also attenuate the X-ray during the *operando* experiment, their contribution (denoted by $\boldsymbol{A_{bkg}}$) is non-trivial and should also be taken into consideration. The modified equation can be written as:

$$-\ln(\boldsymbol{I_t}/\boldsymbol{I_0}) = \boldsymbol{\mu}(\mathrm{FeF_3}) \cdot \boldsymbol{t}(\mathrm{FeF_3}) + \boldsymbol{\mu}(\mathrm{FeF_2}) \cdot \boldsymbol{t}(\mathrm{FeF_2}) + \boldsymbol{\mu}(\mathrm{Fe}) \cdot \boldsymbol{t}(\mathrm{Fe}) + \boldsymbol{A_{bkg}} \qquad (2)$$

Previous methods depend heavily upon the strong X-ray absorption of large-sized samples (10–20 μm) and considered the X-ray absorption of the materials under study approximately equal to the total X-ray absorption[4–7]. This approximation is no longer valid for the smaller and weakly absorbing samples investigated herein. As a result, those methods failed to correctly normalize the XANES spectra for smaller and less X-ray absorbing samples, such as the porous FeF_3 MWs examined herein (Figure A2.1a). An example of such improperly normalized spectra is shown in Figure A2.1e, which is clearly off the scale compared with the standard reference spectra (Figure A2.2). When the fitting was carried out using these improperly normalized spectra at all the pixels, the quality of the resulting chemical phase map is unsatisfactory (see Figure A2.1b), because very few pixels could be fitted correctly to pass the *R-value* filter (misfit filter).

We solved this normalization problem by approximating the internal background X-ray absorption (A_{bkg}, black circles in Figure A2.1d) using the X-ray attenuating information readily available from the area that does not contain the FeF_3 sample but all the other components in the *operando* cell, such as electrolyte, polymeric binder, carbon black, current collector, and separator (the black box in Figure A2.1a). We first subtracted the internal background spectrum (black circles in Figure A2.1d) from the total X-ray attenuation (red circles in Figure A2.1d) and then carried out the data normalization following the aforementioned five-step procedure, which yielded correctly normalized spectrum as shown in Figure A2.1f. Using our custom-developed program, this normalization procedure could be conveniently applied to the spectra at all pixels.

The correctly normalized spectrum at each pixel was then fitted with the linear combination of three μt values. The ratio of the weighing factor is an analogue of the thickness fraction and

therefore represents the volume fractions of solid state phases containing different Fe oxidation states. The fitting was carried out by minimizing the $\boldsymbol{R}$ value (a measure of misfit) for each spectrum at each pixel, which is defined as:

$$\boldsymbol{R} = \sum_{\boldsymbol{Ei}}^{\boldsymbol{Ef}} (\boldsymbol{dataE} - \boldsymbol{refE})^2 / \sum_{\boldsymbol{Ei}}^{\boldsymbol{Ef}} \boldsymbol{dataE}^2 \qquad (3)$$

where $\boldsymbol{Ei}$ is 7091 eV, $\boldsymbol{Ef}$ is 7285 eV, $\boldsymbol{dataE}$ is the normalized spectrum at each pixel for the given energy $\boldsymbol{E}$, and $\boldsymbol{refE}$ is the possible fitting reference value that is a linear combination of X-ray attenuation of FeF_3, FeF_2, and Fe. The standard reference XANES spectra were collected from commercial FeF_3, FeF_2, and Fe powders under the same conditions using TXM and verified using a standard spectroscopy beamline X18A at NSLS, BNL. During the fitting, we considered all possible combinations with FeF_3, FeF_2, and Fe with 2 vol% resolution, which was a total of 1326 possible combinations. *R values* were minimized at each pixel to find the best-matched phase combination of different Fe oxidation states so that Red-Green-Blue (Red: Fe^{3+}, Green: Fe^{2+}, Blue: Fe) colors can be assigned accordingly to generate the chemical phase map (Supplementary Figure1c). We applied an *R-value* filter (misfit filter) to the resulting phase map and only pixels with $R < 0.08$ were displayed in order to give the most accurate chemical phase information. The comparison between Figure A2.1c and Figure A2.1b clearly show that our new data processing procedures could generate a higher quality chemical phase map compared with the previously reported methods. These new data processing procedures were consistently employed to yield the chemical phase maps shown in Figure 3.2 and 3.3 in the manuscript text and Figure A2.6 and A2.7 in this Appendix.

Operando X-ray Absorption Spectroscopy Experiment on FeF_3 Microwires*:* The *operando* X-ray absorption experiments were performed at beamline X18A, National Synchrotron Light Source,

Brookhaven National Laboratory. The measurements were performed in transmission mode using a Si (111) double-crystal monochromator, which was detuned to ~35% of its original maximum intensity to eliminate the high order harmonics in the beam. A reference X-ray absorption spectrum of Fe (*K*-edge 7112 eV) was simultaneously collected using a standard Fe foil. Energy calibration was done using the first inflection point of the Fe *K*-edge spectrum as the reference point. The X-ray absorption data were processed and analyzed using IFEFFIT-ATHENA. Standard reference spectra from commercial FeF_3, FeF_2, and Fe powders were also collected in order to carry out linear combination analysis to determine the ratio between different Fe oxidation states. The rutile FeF_2 phase was used to represent all the possible rutile related Fe^{2+}-containing phases. This is a reasonable approximation because it was reported that the Li_xFeF_3 (when $x \approx 1.0$) phase contains structural features that are found in the rutile FeF_2 structure[S8].

The *operando* experiments were performed using perforated 2032-type coin cells with holes on both sides of the cell cases. The holes were sealed using Kapton tapes. The FeF_3 MWs were mixed with carbon black and PVDF binder in a weight ratio of 7:2:1 in NMP. The resulting slurry was pasted onto thin aluminum foils (~25 μm thickness) to make electrodes. The *operando* cells were assembled in an argon-filled glovebox using Li metal as the counter/quasi-reference electrode and polyethylene films soaked with 1 M $LiPF_6$ EC/DMC (1/1 by volume) electrolyte as the separator. The as-made cells were aged for a few hours and checked using electrochemical impedance spectroscopy before being used in the *operando* experiments, during which the cell was discharged and charged at rate of ~1/12 C (1 C = 712 mA/g).

A2.2 Supplementary Figures

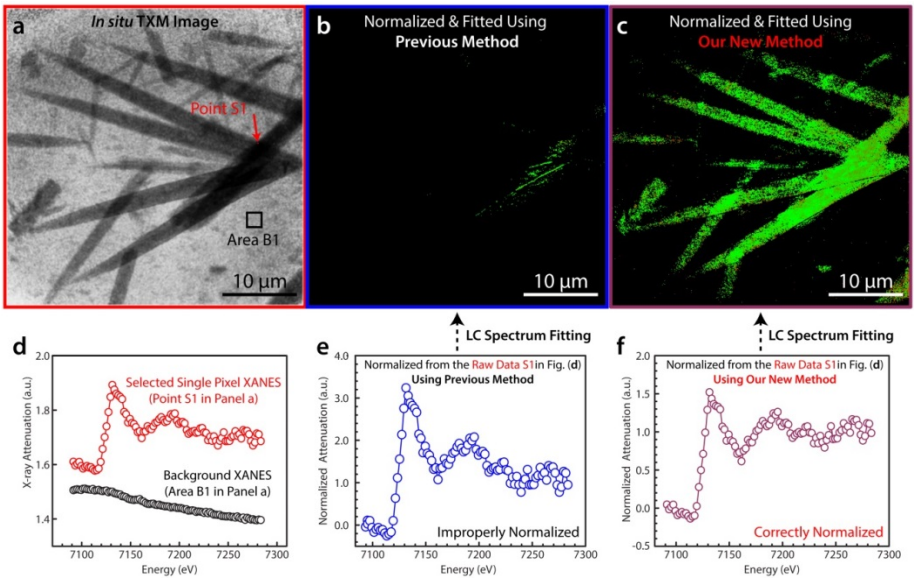

Figure A2.1 | Construction of chemical phase maps using improved data processing method. (**a**) Absorption-contrast image shown along with the chemical phase maps constructed using different data process approaches (**b**, **c**) for the same region in a FeF_3 MW electrode. We took XANES spectra from the areas with and without the FeF_3 MWs respectively and used them as examples to demonstrate the difference of data processing approaches in generating chemical phase maps. The randomly selected single pixel XANES spectrum from the sample-containing area and the background spectrum are shown in (**d**). The background spectrum contains information on X-ray attenuation by all the other components in the *operando* cell, such as electrolyte, polymeric binder, carbon black, current collector, and separator. (**e**) shows the spectrum directly normalized using previously reported methods[4–7], which is clearly off the normal scale (typically 0–2 in the y-axis) compared with the reference standard spectra in **Figure A2.2**. When all the other spectra at other pixels were treated the same way and fitted, only very few of them could be preserved to generate the unsatisfactory phase map in (**b**). In contrast, (**f**)

shows the spectrum correctly normalized and scaled using our new approach. The background X-ray attenuation was subtracted first before the normalization. High-quality chemical phase maps, such as that shown in (**c**), can then be generated by fitting the background subtracted normalized spectra at each pixel.

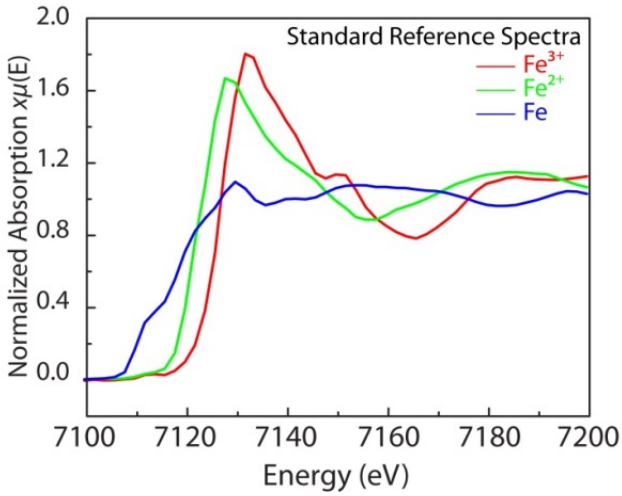

Figure A2.2 | Reference spectra used for fitting to generate chemical phase maps. XANES spectra were collected from commercial $Fe^{3+}F_3$, $Fe^{2+}F_2$, and metallic Fe powders using TXM-XANES.

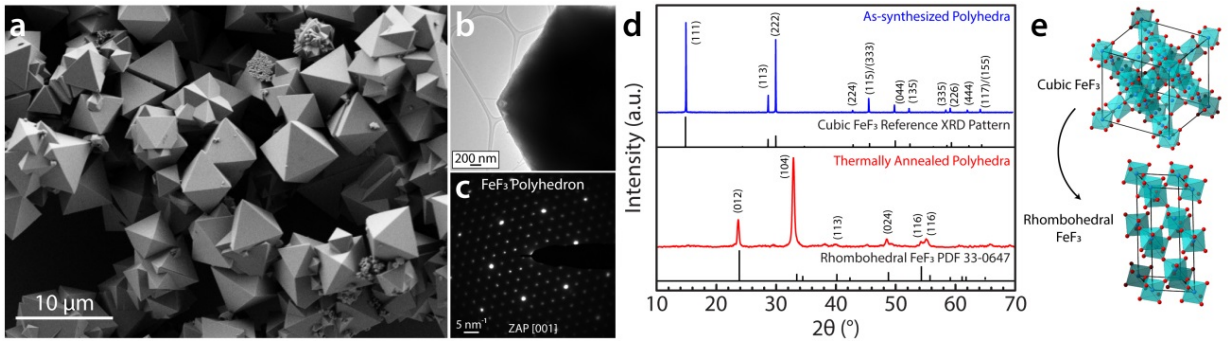

Figure A2.3 | Complete structural characterizations of the FeF_3 polyhedra. (**a**) SEM image of the FeF_3 polyhedra with rhombohedral crystal structure. (**b**) Representative TEM image of a polyhedron. (**c**) Selected-area electron diffraction pattern taken from the same polyhedron in (**b**), showing that the polyhedron is single-crystalline. (**d**) Powder X-ray diffractograms of the polyhedra before and after thermal treatment in comparison with the reference standard PDF cards. The as-made polyhedra are phase-pure cubic FeF_3 and they are fully converted to rhombohedral FeF_3 after the thermal treatment in argon at 350 °C for 30 min. (**e**) shows the crystal structures of cubic and rhombohedral FeF_3. The conversion from the cubic phase to the rhombohedral phase involves rotation and distortion of the corner-sharing FeF_6 octahedra. The crystallographic information of cubic FeF_3 was obtained from the Inorganic Crystal Structure Database (ICSD). Note that rhombohedral FeF_3 is the thermodynamically stable phase.

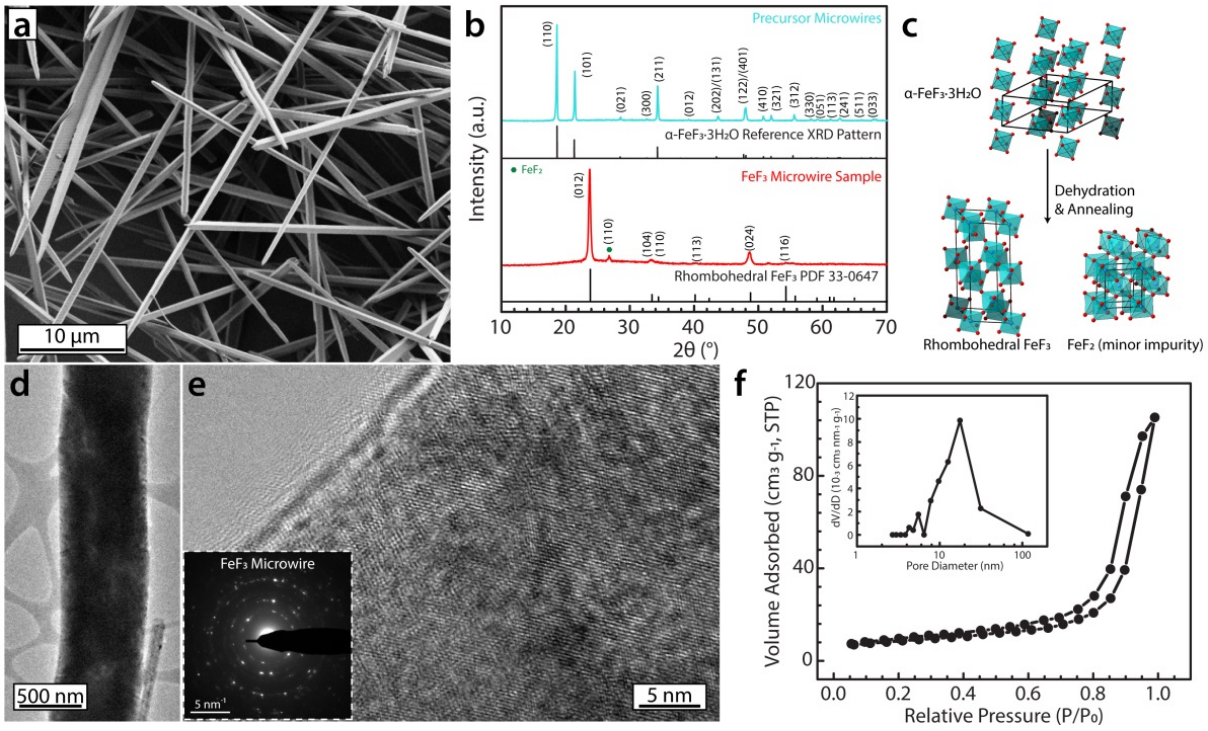

Figure A2.4 | Complete structural characterizations of the FeF_3 MWs. (**a**) SEM image of the FeF_3 MWs. (**b**) Powder X-ray diffractograms of the MWs before and after thermal conversion in comparison with the reference standard PDF cards. The thermal dehydration of α-$FeF_3{\cdot}3H_2O$ MWs led to the formation of MWs of rhombohedral FeF_3. FeF_2 was also produced as a minor impurity phase during the dehydration. (**c**) shows the crystal structures of α-$FeF_3{\cdot}3H_2O$, FeF_3, and FeF_2. α-$FeF_3{\cdot}3H_2O$ is made of separate $FeF_3(H_2O)_3$ octahedra with F^- and H_2O randomly distributed. FeF_3 and FeF_2 are made of FeF_6 octahedra connected by sharing corners or edges. The dehydration and conversion of α-$FeF_3{\cdot}3H_2O$ involves the loss of H_2O and reorganization of the octahedra. (**d**) Low-magnification TEM image of a FeF_3 wire, suggesting porosity. (**e**) High-resolution TEM image of the FeF_3 wire shown in (**d**) showing that the wire is polycrystalline and contains many grain boundaries. The inset is a selected-area electron diffraction pattern taken from the wire in (**d**). The diffraction ring pattern can be indexed to rhombohedral FeF_3 and

confirms the polycrystallinity of the wire. (**f**) Nitrogen adsorption/desorption profile of the FeF_3 MWs, revealing that the MWs are mesoporous. The inset shows the pore size distribution. The BET surface area is ~30 m^2/g and the mode (most frequent value) of the pore size is ~17 nm.

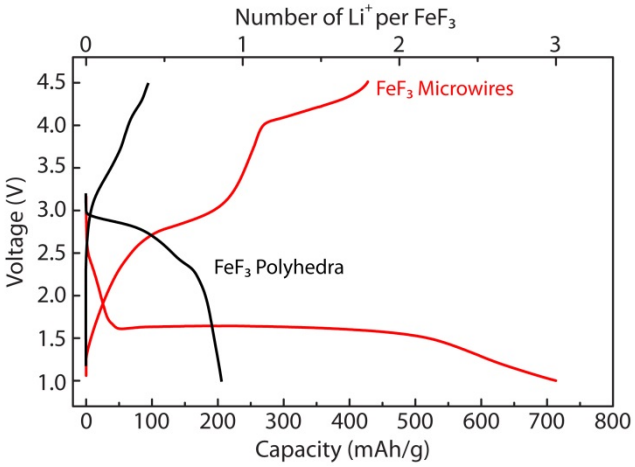

Figure A2.5 | Electrochemical capacity tests of the FeF_3 polyhedra and MWs packed in coin-cell batteries. The FeF_3 polyhedra and MWs were mixed with carbon black and polymeric binder in a 7:2:1 weight ratio and packed into two different 2032-type coin cells for testing. The discharge/charge current was set at 50 mA/g (~1/14.2 C, 1C = 712 mA/g).

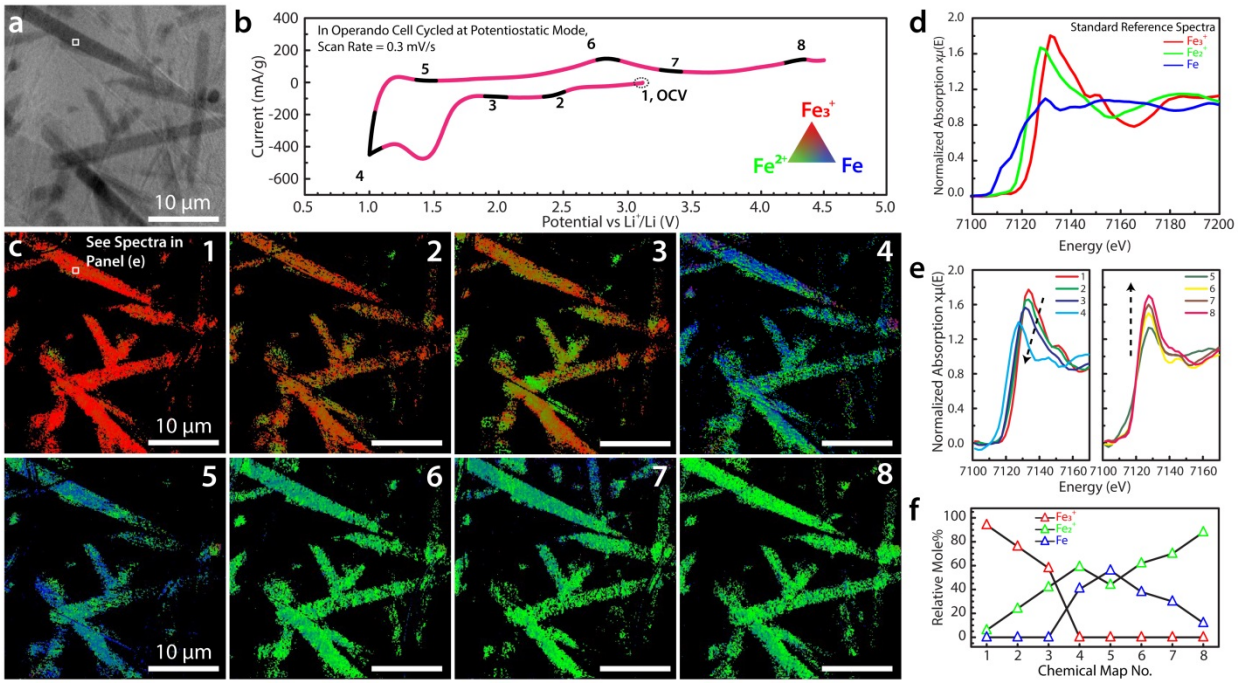

Figure A2.6 | TXM-XANES visualization of the electrochemical reaction of FeF_3 microwire electrode in potentiostatic mode. (**a**) Absorption-contrast image of the area of analysis. (**b**) Voltammogram of the *operando* cell at voltage scan rate of 0.3 mV/s. The black segments on the voltammogram indicate the time periods when the XANES data were collected. (**c**) Reference standard spectra collected from commercial FeF_3, FeF_2, and Fe powders. (**d**) Chemical phase maps at different states of discharge/charge. Conversion from Fe^{3+} to Fe^{2+} and Fe can be clearly seen in (Panel **c** 1–4). Reconversion from Fe went through Fe^{2+}-containing phases and did not go back to Fe^{3+} (Panel **c** 5–8). (**e**) Selected-area XANES spectra to show the changes during the electrochemical conversion/reconversion. The white squares in (**a**) and (**c**) mark the area used to generate the XANES spectra. (**f**) The mole percentage of the Fe species in different oxidation states in map c1 to c8.

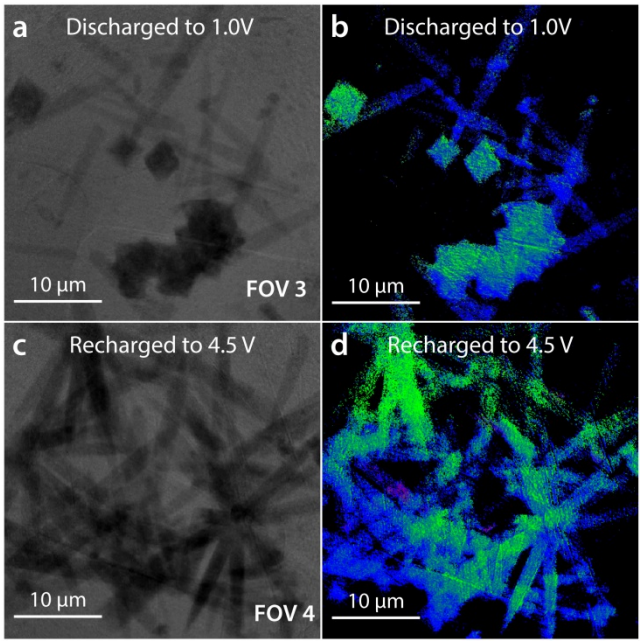

Figure A2.7. Chemical phase maps generated from other areas of the same *operando* FeF_3 electrode (made of a mixture of MWs and polyhedra) at the end of discharge and charge. (**a**) and (**b**) are absorption-contrast image and the resulting chemical phase map, respectively, taken at the end of discharge. It is clear that the MWs reacted more completely than the polyhedra. (**c**) and (**d**) are absorption-contrast image and the resulting chemical phase map, respectively, taken at the end of charge. The recharge reaction was not complete. Metallic Fe and Fe^{2+} were found to co-exist at the end of recharge, indicating the reconversion must go through Fe^{2+}-containing intermediate(s) during recharge.

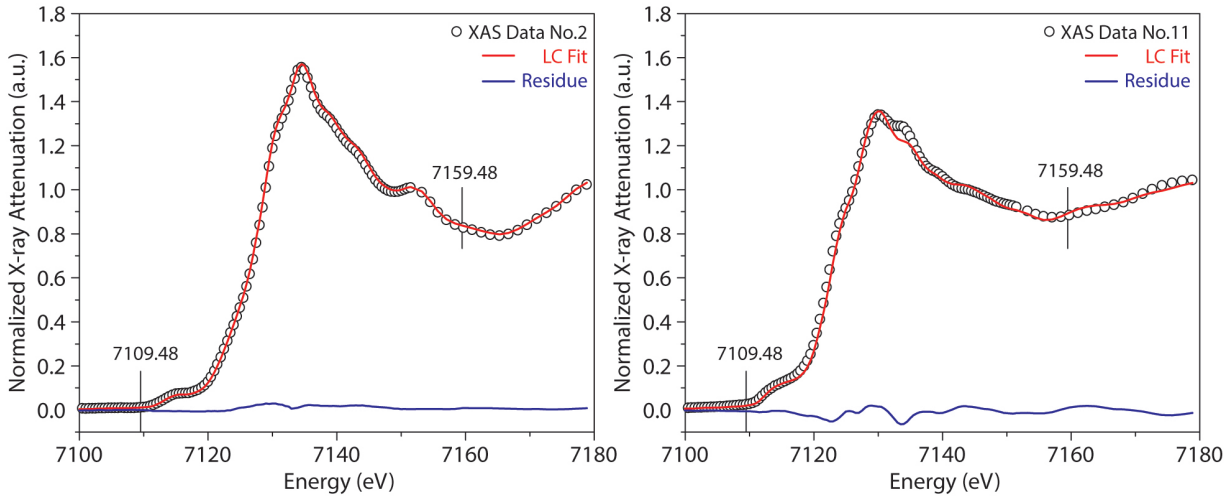

Figure A2.8 | Two representative best fits of XAS spectra. The linear combinational fitting was performed in the energy range from 7109.48 to 7159.48 eV. The X-ray absorption data were processed and analyzed using IFEFFIT-ATHENA.

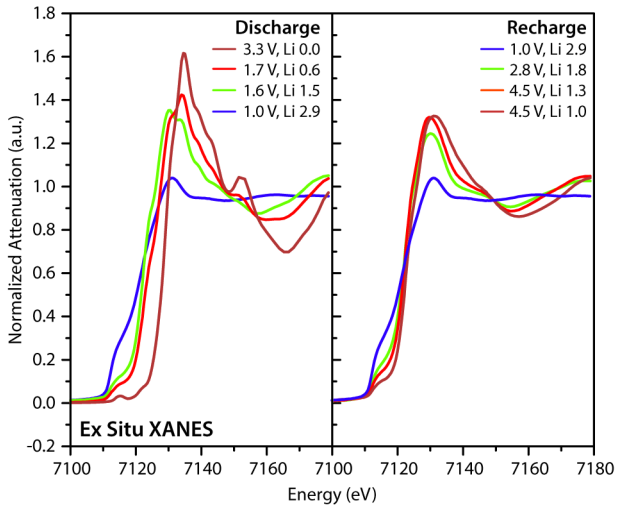

Figure A2.9 | *Ex Situ* XAS on electrodes cycled to different states of discharge and charge. The electrodes were recovered from coin cells dissembled inside a glovebox and sealed between Kapton tapes.

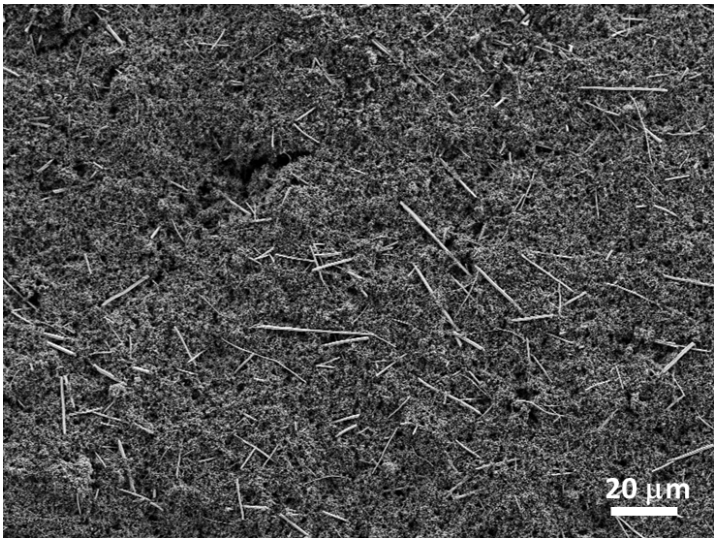

Figure A2.10 | Representative SEM image of FeF_3 microwire electrode with binders and carbon black.

A2.3 Supplementary Table

Supplementary A2.1 Details for the linear combinational fitting results in Figure 3.4d

XAS Data No.	R-factor	χ^2	$Fe^{3+}F_3$		$Fe^{2+}F_2$		Fe	
			Weight	**Error**	**Weight**	**Error**	**Weight**	**Error**
1	Did not fit. Pristine FeF_3 electrde							
2	0.0008	0.0184	0.8939	*0.0068*	0.1061	*0.0038*	NA, 2-standard fit	
3	0.0001	0.0013	0.7688	*0.0023*	0.1779	*0.0018*	0.0533	*0.0029*
4	0.0001	0.0024	0.6722	*0.0032*	0.2464	*0.0024*	0.0814	*0.0040*
5	0.0005	0.0065	0.6277	*0.0052*	0.2964	*0.0040*	0.0759	*0.0065*
6	0.0003	0.0058	0.4634	*0.0049*	0.3820	*0.0038*	0.1546	*0.0062*
7	0.0004	0.0086	0.4010	*0.0060*	0.4235	*0.0046*	0.1755	*0.0075*
8	0.0008	0.0140	0.3766	*0.0076*	0.4691	*0.0058*	0.1543	*0.0096*
9	0.0013	0.0295	0.2772	*0.0111*	0.5236	*0.0085*	0.1991	*0.0139*
10	0.0026	0.0614	0.2111	*0.0160*	0.6020	*0.0122*	0.1870	*0.0201*
11	0.0006	0.0127	0.2175	*0.0073*	0.5056	*0.0056*	0.2769	*0.0091*
12	0.0006	0.0081	0.2007	*0.0058*	0.4835	*0.0044*	0.3158	*0.0073*
13	0.0005	0.0108	0.1601	*0.0067*	0.5086	*0.0051*	0.3314	*0.0084*
14	0.0009	0.0186	0.1090	*0.0088*	0.5284	*0.0067*	0.3626	*0.0110*
15	0.0008	0.0164	0.0731	*0.0082*	0.5137	*0.0063*	0.4132	*0.0104*
16	0.0008	0.0156	0.0166	*0.0080*	0.4873	*0.0062*	0.4961	*0.0101*
17	0.0030	0.0396	0.0000	*0.0128*	0.4035	*0.0098*	0.5965	*0.0161*
18	0.0030	0.0330	0.0000	*0.0117*	0.2668	*0.0089*	0.7332	*0.0147*
19	0.0029	0.0276	0.0000	*0.0107*	0.1719	*0.0082*	0.8281	*0.0135*
20	0.0044	0.0387	0.0000	*0.0127*	0.1260	*0.0097*	0.8740	*0.0160*
21	0.0042	0.0361	0.0000	*0.0122*	0.1137	*0.0094*	0.8863	*0.0154*
22	0.0012	0.0113	0.0000	*0.0068*	0.1467	*0.0052*	0.8533	*0.0086*
23	0.0017	0.0168	0.0000	*0.0084*	0.1636	*0.0064*	0.8364	*0.0105*
24	0.0013	0.0134	0.0059	*0.0074*	0.1778	*0.0057*	0.8163	*0.0094*
25	0.0015	0.0201	0.0000	*0.0091*	0.2829	*0.0070*	0.7171	*0.0115*
26	0.0011	0.0181	0.0011	*0.0086*	0.3581	*0.0066*	0.6408	*0.0109*
27	0.0018	0.0333	0.0000	*0.0117*	0.4650	*0.0090*	0.5350	*0.0148*
28	0.0016	0.0316	0.0000	*0.0115*	0.5052	*0.0088*	0.4948	*0.0144*
29	0.0014	0.0312	0.0000	*0.0114*	0.5431	*0.0087*	0.4569	*0.0143*
30	0.0013	0.0275	0.0292	*0.0107*	0.5578	*0.0082*	0.4130	*0.0135*
31	0.0013	0.0291	0.0959	*0.0110*	0.6083	*0.0084*	0.2958	*0.0138*
32	0.0013	0.0312	0.1370	*0.0114*	0.6297	*0.0087*	0.2333	*0.0143*
33	0.0014	0.0253	0.1976	*0.0102*	0.5778	*0.0078*	0.2246	*0.0129*
34	0.0013	0.0249	0.2280	*0.0102*	0.5706	*0.0078*	0.2014	*0.0128*
35	0.0013	0.0234	0.2515	*0.0098*	0.5508	*0.0075*	0.1977	*0.0124*
36	0.0013	0.0219	0.2890	*0.0095*	0.5249	*0.0073*	0.1861	*0.0120*
37	0.0012	0.0227	0.3034	*0.0097*	0.5358	*0.0074*	0.1608	*0.0122*

- The linear combinational fitting was performed in the energy range from 7109.48 to 7159.48 eV.
- The rutile FeF_2 phase was used to represent all the possible rutile related Fe^{2+}-containing

A2.4 References

1. Li, L., Meng, F., Jin, S., High-capacity lithium-ion battery conversion cathodes based on iron fluoride nanowires and insights into the conversion mechanism. *Nano Lett.* **12,** 6030-6037 (2012).

2. Morin, S. A., Bierman, M. J., Tong, J., Jin, S., Mechanism and kinetics of spontaneous nanotube growth driven by screw dislocations. *Science* **328,** 476-480 (2010).

3. Meng, F., Morin, S. A., Forticaux, A., Jin, S., Screw dislocation driven growth of nanomaterials. *Acc. Chem. Res.* **46,** 1616-1626 (2013).

4. Wang, J., Chen-Wiegart, Y.-c. K., Wang, J., In Situ chemical mapping of a lithium-ion battery using full-field hard X-ray spectroscopic imaging. *Chem. Commun.* **49,** 6480-6482 (2013).

5. Yang, F., et al., Nanoscale morphological and chemical changes of high voltage lithium–manganese rich NMC composite cathodes with cycling. *Nano Lett.* **14,** 4334-4341 (2014).

6. Wang, J., Chen-Wiegart, Y.-c. K., Wang, J., In operando tracking phase transformation evolution of lithium iron phosphate with hard X-ray microscopy. *Nature Commun.* **5,** 4570 (2014).

7. Yu, Y.-S., et al., Nonequilibrium pathways during electrochemical phase transformations in single crystals revealed by dynamic chemical imaging at nanoscale resolution. *Adv. Energy Mater.* Early View, **5,** 1402040 (2014).

8. Yamakawa, N., Jiang, M., Key, B., Grey, C. P., Identifying the local structures formed during lithiation of the conversion material, iron fluoride, in a Li-ion battery: A solid-state NMR, X-ray

diffraction, and pair distribution function analysis study. *J. Am. Chem. Soc.* **131,** 10525-10536 (2009).

APPENDIX 3

Supplementary Information for CHAPTER 4:

The Origin of Large Voltage Hysteresis in Metal Fluoride Lithium-Ion Battery Conversion Electrodes

---

This Appendix is the supporting information for CHAPTER 4, a manuscript to be submitted, in collaboration with R. Jacobs, P. Gao, L. Gan, F. Wang, D. Morgan, and S. Jin.

A3.1 Supplementary figures

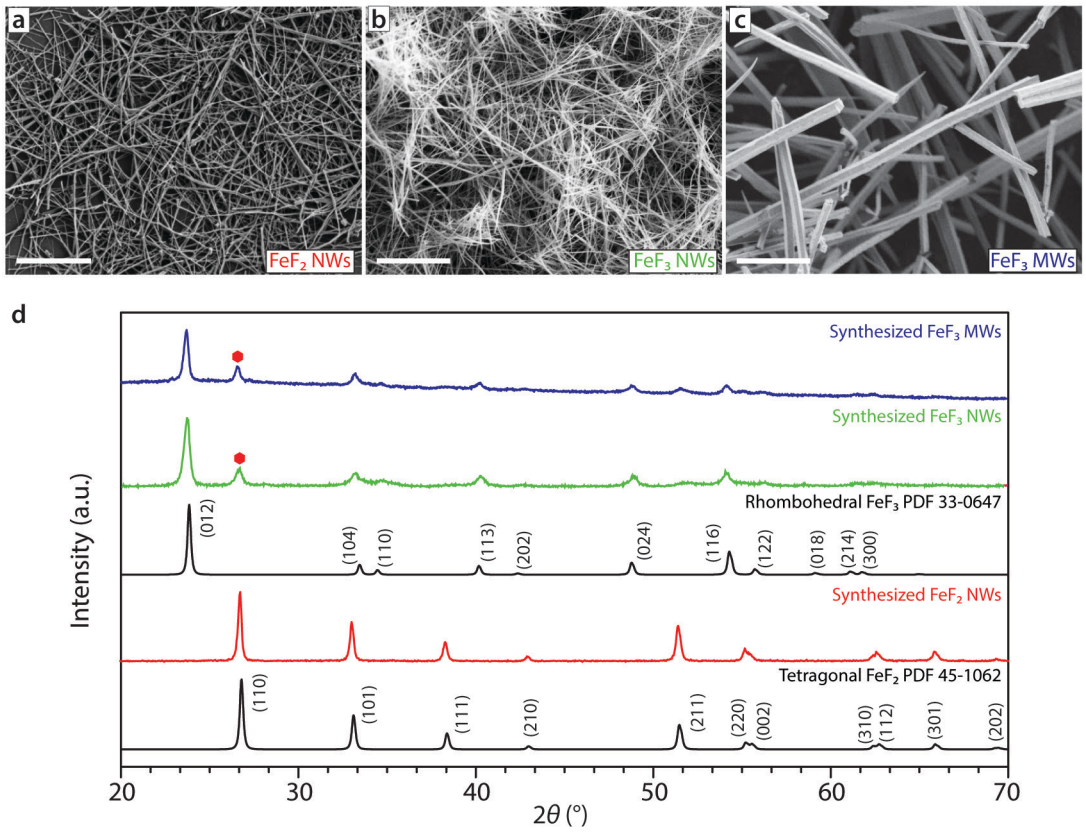

Figure A3.1 | Characterization of study materials. a, b and **c** are SEM images of FeF_2 nanowires, FeF_3 nanowires, and FeF_3 microwires, respectively. Scale Bars are 5 μm, 10 μm, and 10 μm, respectively. **d.** Powder XRD patterns of as-synthesized FeF_2 nanowires, FeF_3 nanowires, and FeF_3 microwires in comparison with standard JCPDS PDF cards. Note that both the FeF_3 nanowire and microwire samples contain a small amount of FeF_2. The impurity FeF_2 (110) peak is denoted by red hexagons.

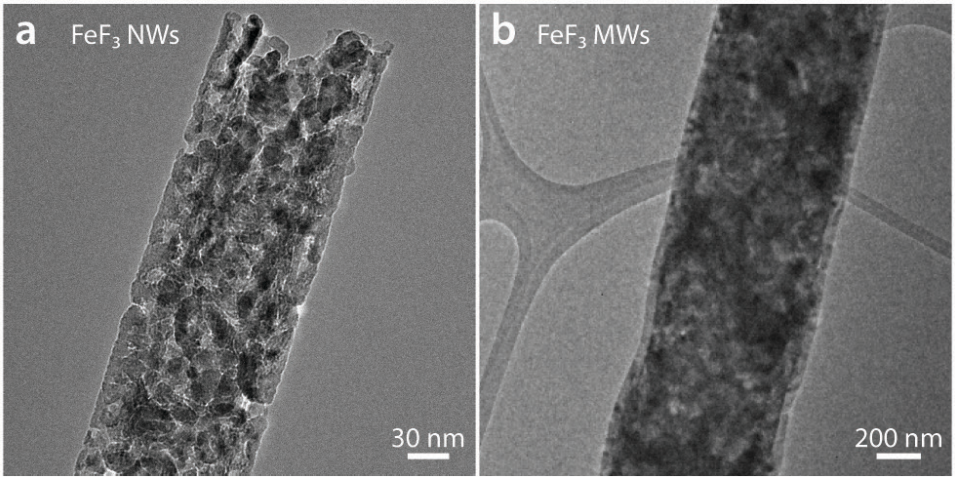

Figure A3.2 | Microstructure of FeF_3 nanowires and microwires. a and **b** are TEM images of FeF_3 nanowires and FeF_3 microwires, respectively. Both samples are porous. The FeF_3 domain size is smaller in nanowires than microwires.

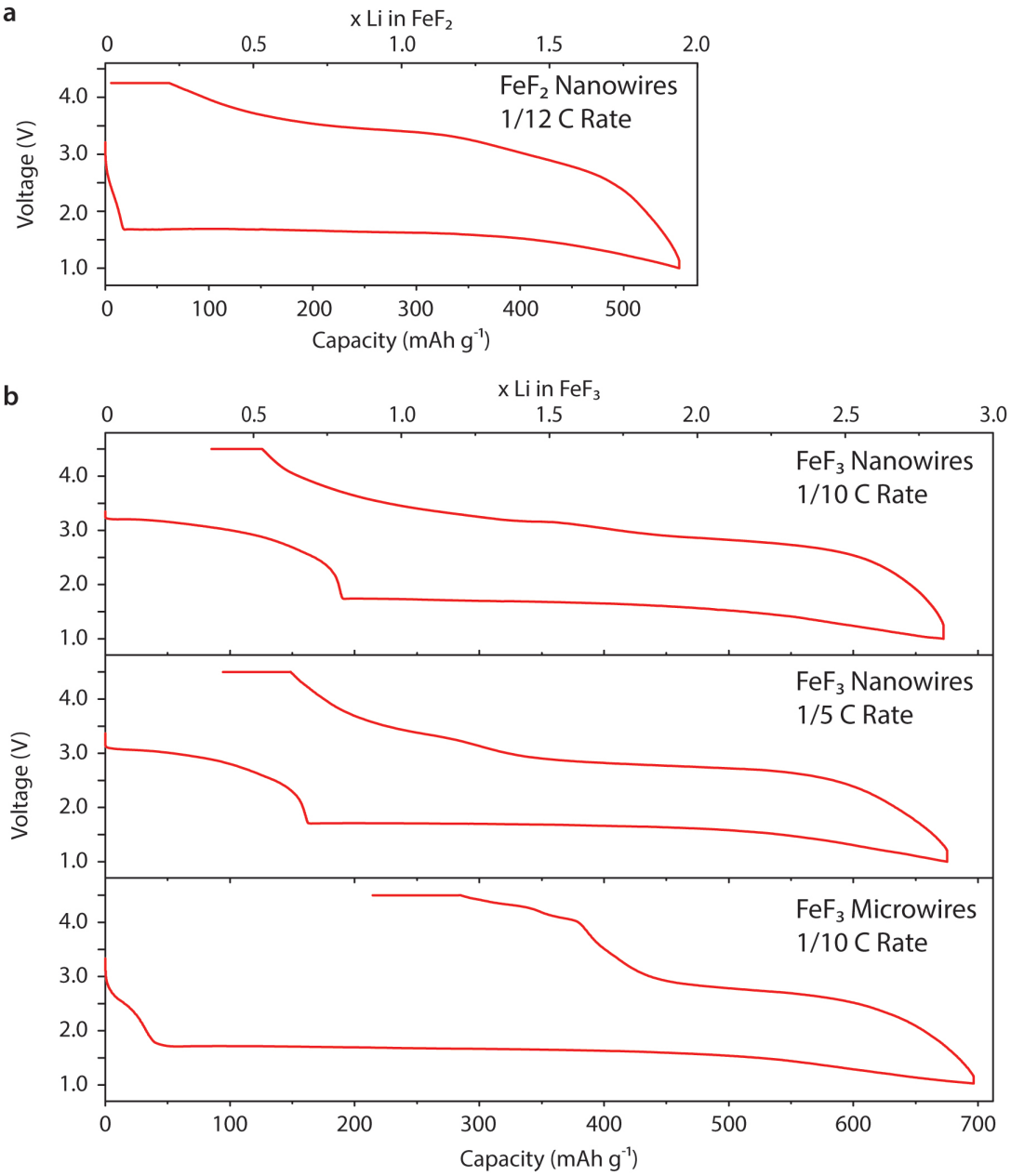

Figure A3.3 | Electrochemical cycling profile of the iron fluoride samples. a. 1st cycle discharge/charge profile of a FeF_2 nanowire electrode cycled at 1/12 C (1 C = 571 mA g^{-1} for FeF_2) . **b.** 1st cycle discharge/charge profiles of a FeF_3 nanowire electrode cycled at 1/10 C, 1/5

C, and a FeF_3 microwire electrode cycled at 1/10 C (1 C = 712 mA g^{-1} for FeF_3). Note that an additional constant-voltage charging step was applied after the constant-current charging step.

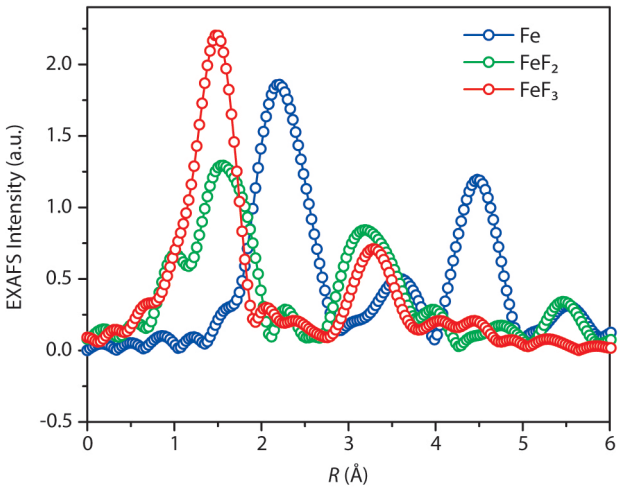

Figure A3.4 | Reference standard EXAFS patterns. EXAFS patterns collected from commercial FeF_3, FeF_2, and Fe samples.

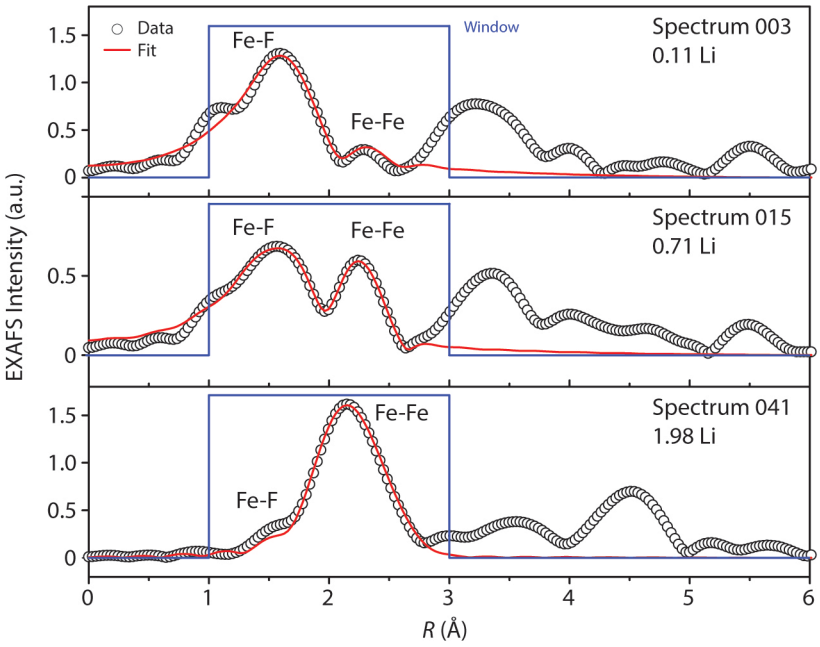

Figure A3.5 | EXAFS patterns and fittings. The EXAFS patterns taken during the lithiation of the FeF_2 nanowire electrode and fitted to estimate the Fe-Fe distance, which is larger at initial lithiation (~2.49 Å at 0.11 Li) but getting smaller as the lithiation proceeds (~2.45 Å at 0.71 Li and ~2.44 Å at 1.98 Li).

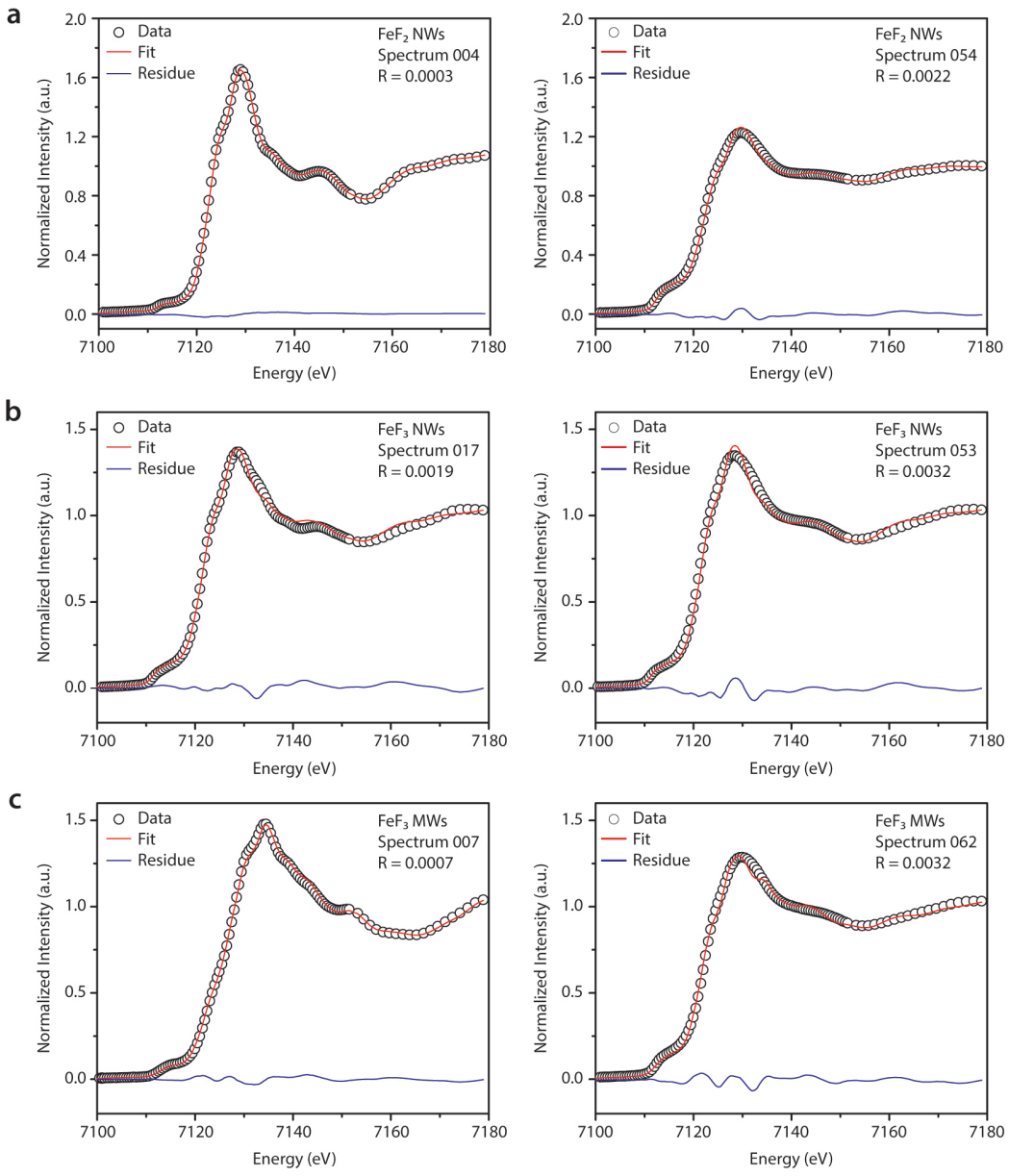

Figure A3.6 | Representative best fits of *in situ* XAS spectra. a, b and **c** are examples of linear combination fitting analysis performed on the spectra collected from the FeF_2, FeF_3 nanowire, and FeF_3 microwire experiments, respectively. The fittings were performed in the energy range from –20 eV to +30 eV across the absorption edge, using FeF_3, FeF_2 and Fe spectra collected

from commercial powder samples as reference standards. Fitting details can be found in Supplementary Table 1-3.

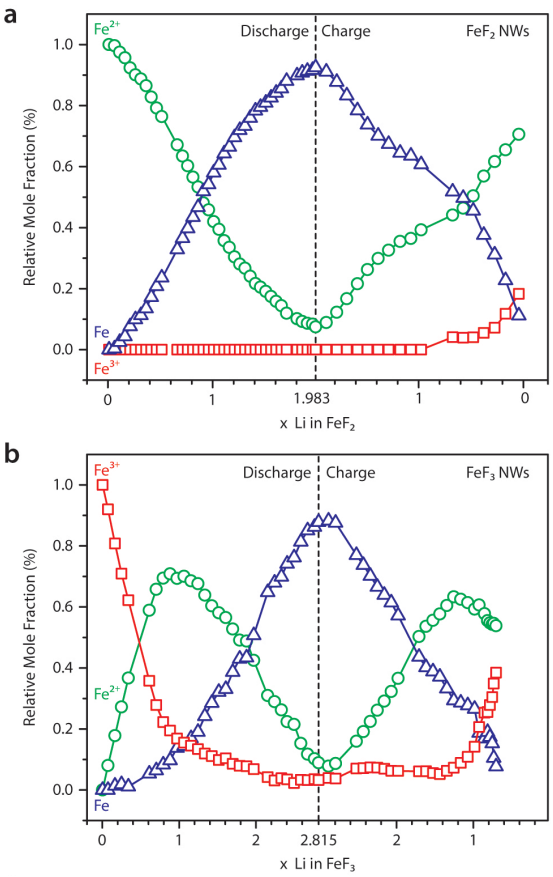

Figure A3.7 | Phase evolution during the cycling of FeF_2 and FeF_3 nanowire electrodes. The mole fraction of the Fe species in different oxidation states at different states of lithiation during discharge and charge of FeF_2 (**a**) and FeF_3 nanowire (**b**) electrodes, which is estimated by linear combinational fitting analysis of the XANES spectra.

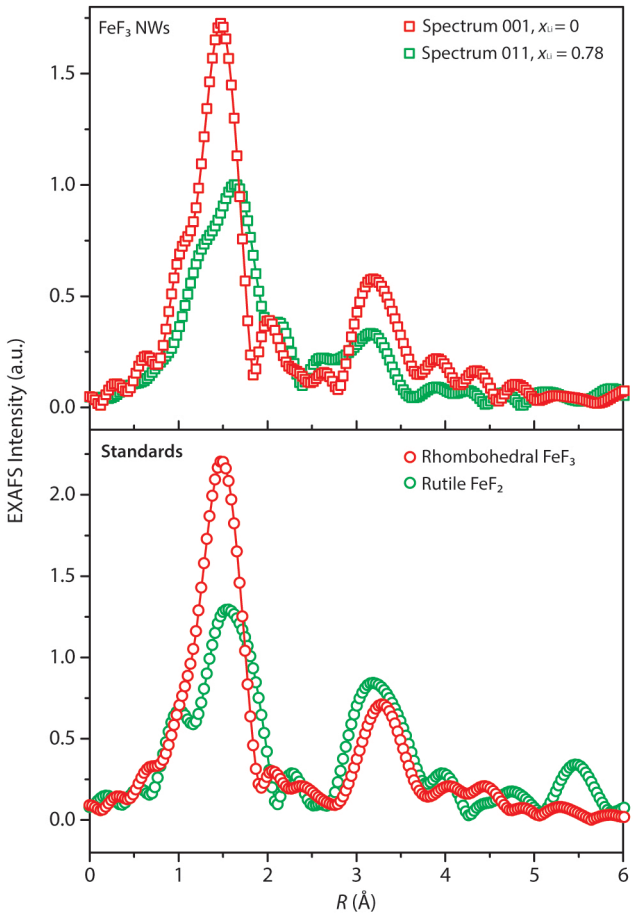

Figure A3.8 | EXAFS patterns of a partially lithiated FeF_3 electrode in comparison with the standards. The FeF_3 electrode was lithiated to x_{Li} ~0.78 Li. Standard reference patterns were collected from commercial FeF_3 and FeF_2 powders.

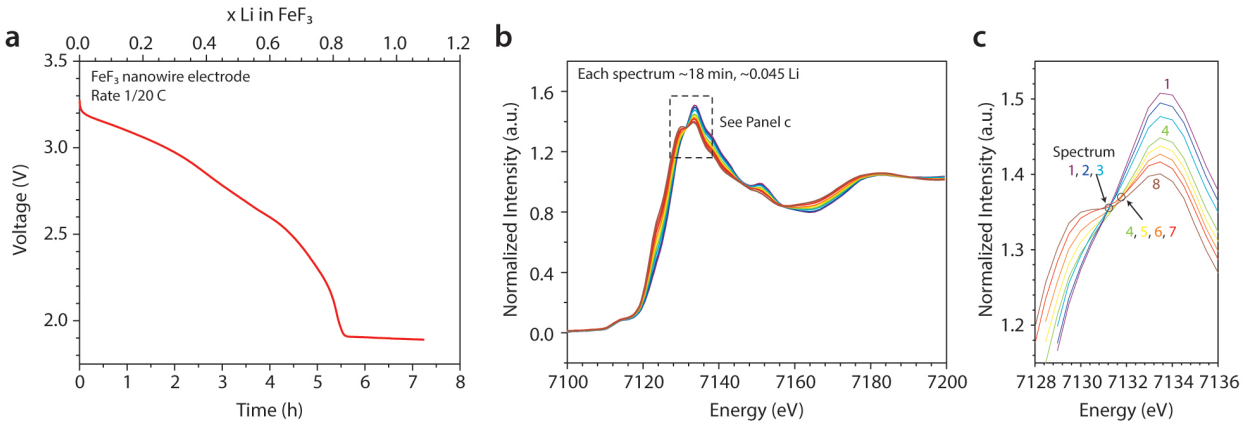

Figure A3.9 | *In situ* XAS results on FeF_3 nanowires discharged at 1/20 C. a. Discharge and charge voltage profile of a FeF_3 nanowire cathode discharged at a current rate of 1/20 C. **b.** XANES spectra taken at every 18 min (~0.045 Li change per 18 min). **c.** Zoom-in view of the XANES spectra showing two different isosbestic points shared by spectrum 1-3 and 4-7, respectively. No additional isosbestic point was observed since spectrum 8.

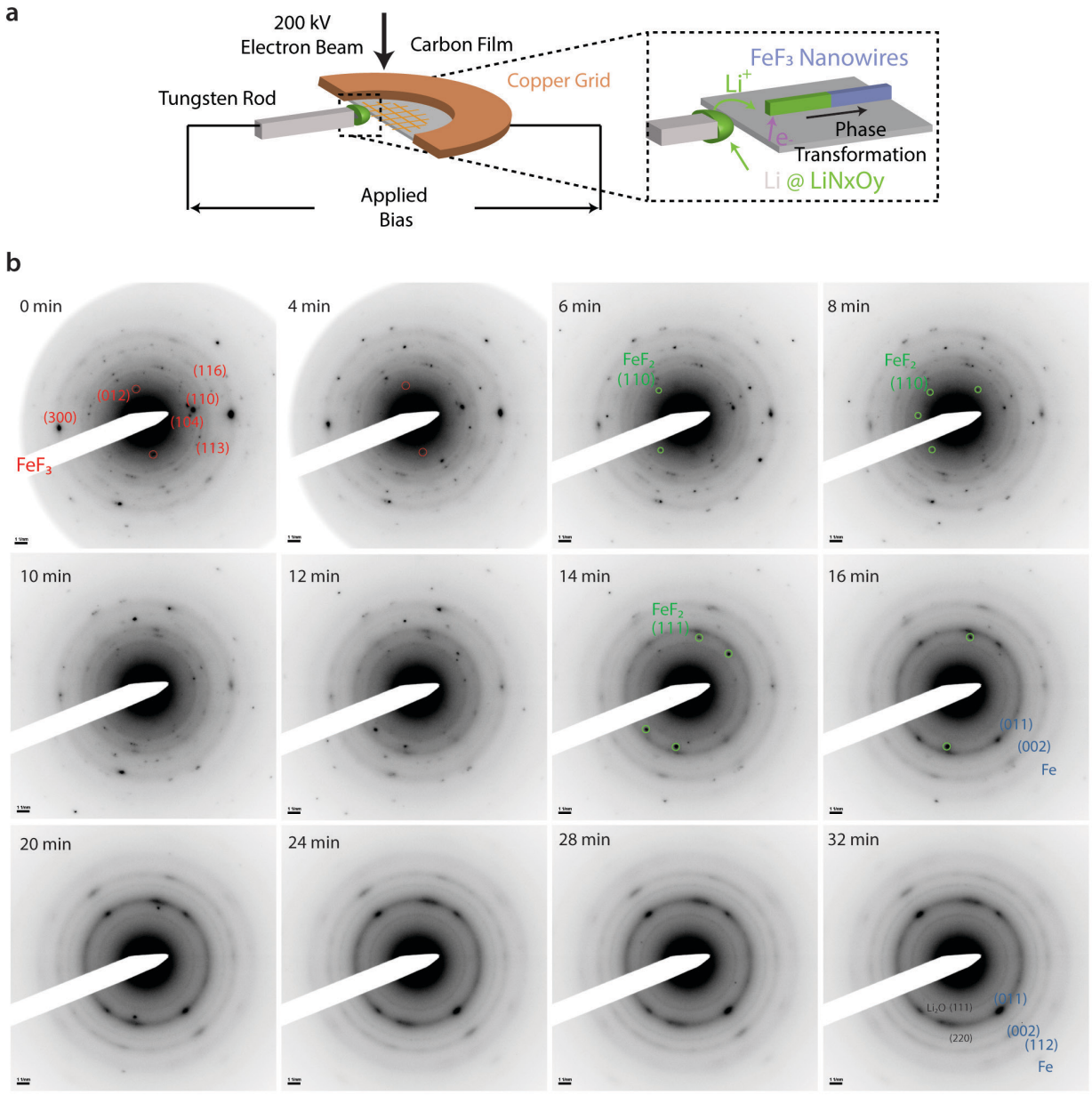

Figure A3.10 | In situ TEM electron diffraction during lithiation of FeF_3 nanowires. a. Schematic illustration of *in-situ* TEM measurements. **b.** Electron diffraction patterns taken during the lithiation of FeF_3 nanowires, which were reduced to metallic Fe after 32 min. All scale bars are 1 μm.

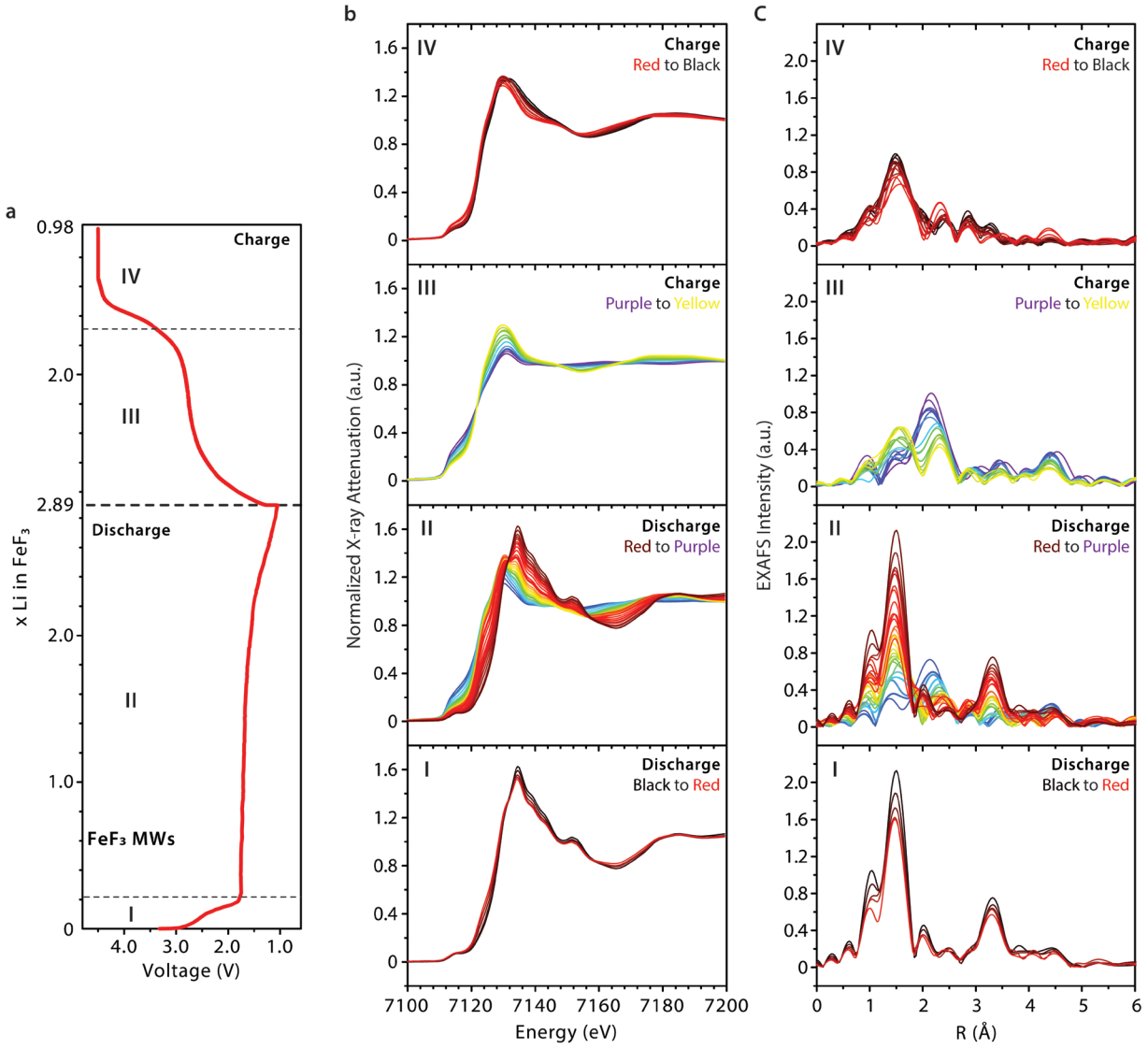

Figure A3.11 | In situ XAS results on FeF_3 microwires. a. Voltage profile of an FeF_3 microwire cathode discharged and recharged at a current rate of 1/10 C. **b.** and **c.** are XANES and EXAFS spectra taken at every 18 min during active discharge (+0.09 x_{Li} per spectrum) and charge (–0.09 x_{Li} per spectrum).

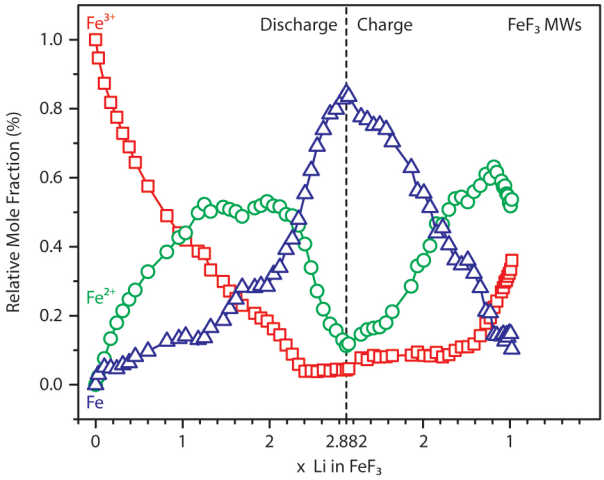

Figure A3.12 | Phase evolution during cycling of the FeF_3 microwire electrode. The mole fraction of the Fe species in different oxidation states at different states of lithiation during discharge and charge of the FeF_3 microwire electrode, which is estimated by linear combinational fitting analysis of the XANES spectra.

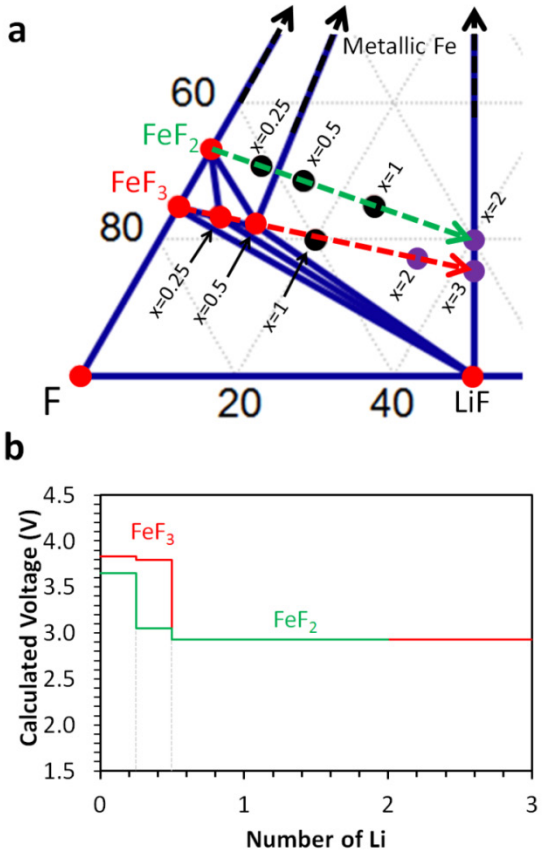

Figure A3.13 | DFT-GGA calculated phase diagram and voltage curves. a. DFT calculated Fe-Li-F phase diagram using the GGA approach. The lithiation pathways for FeF_3 and FeF_2 are indicated by the red and green dashed arrows, respectively. Red dots represent stable phases, black dots represent unstable lithiated phases and purple dots indicate relevant compositions where no lithiated compound was calculated. The fraction of lithiation x for Li_xFeF_2 and Li_xFeF_3 are labeled for both pathways. **b.** Calculated voltage curves for FeF_3 and FeF_2 based on the lithiation pathways indicated in **a**.

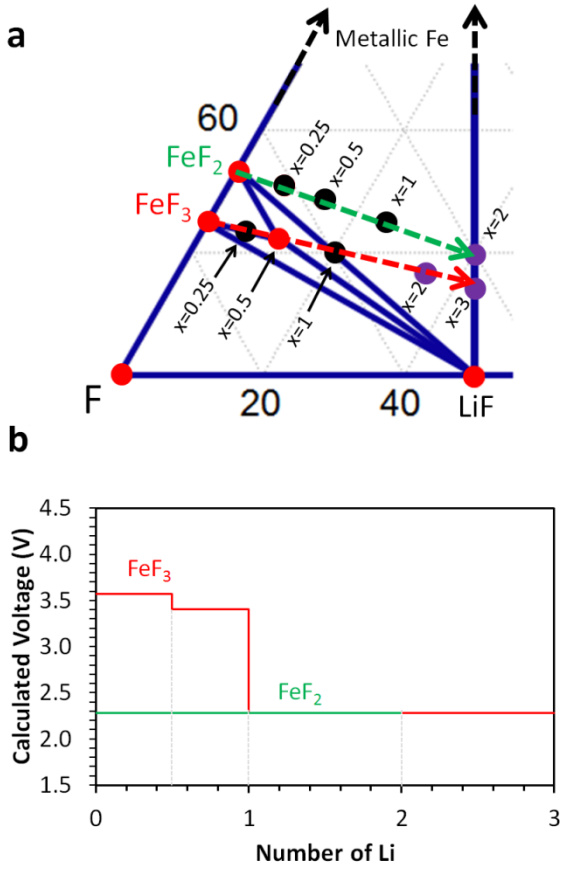

Figure A3.14 | DFT-GGA+U calculated phase diagram and voltage curves. a. DFT calculated Fe-Li-F phase diagram using the GGA+*U* approach (*U* = 5.3 eV for Fe, *J* = 0 eV). The lithiation pathways for FeF_3 and FeF_2 are indicated by the red and green dashed arrows, respectively. Red dots represent stable phases, black dots represent unstable lithiated phases and purple dots indicate relevant compositions where no lithiated compound was calculated. The fraction of lithiation *x* for Li_xFeF_2 and Li_xFeF_3 are labeled for both pathways. **b.** Calculated voltage curves for FeF_3 and FeF_2 based on the lithiation pathways indicated in **a**. Note that for calculations which involve mixing of GGA and GGA+U calculations (e.g. FeF_2 and metallic Fe), an energy shift of -2.73 eV/Fe is added to the computed DFT-GGA+U energy of the appropriate compounds following the methodology of Ref. [1].

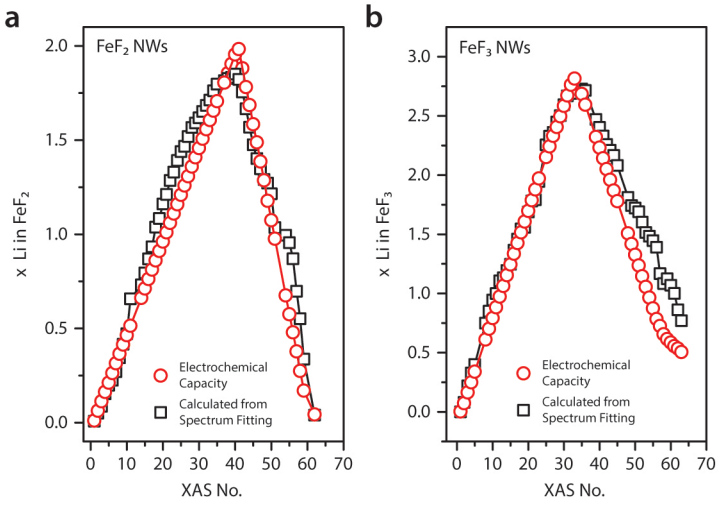

Figure A3.15 | Capacity comparison. Electrochemical capacity measured by the potentiostat/galvanostat in comparison with the capacity estimated from spectrum fitting for the FeF_2 (**a**) and FeF_3 nanowire (**b**) electrodes. Note that the electrochemical capacity is measured from the whole electrode (~1.26 cm^2) while the XAS spectrum is collected from a small area (<0.01 cm^2) where X-ray transmits through. The difference between the two capacities may be caused by fitting errors, reaction inhomogeneity (i.e. materials in other areas react faster or slower), and/or a minor amount of electrolyte reduction (during discharge) or oxidation (during recharge).

A3.2 Supplementary Tables

Table A3.1 | Details for the linear combinational fitting results (FeF_2 electrode)

			Fe		FeF_2		FeF_3			
XAS No.	R	χ^2	weight	error	weight	error	weight	error	x_{Li} (spectrum)	x_{Li} (echem)
1	0.0000	0.0000	0.0000	0.0000	1.0000	0.0000	0.0000	NA	0.007	0.011
2	0.0005	0.0133	0.0036	0.0042	0.9964	0.0042	0.0000	NA	0.050	0.063
3	0.0004	0.0106	0.0249	0.0038	0.9751	0.0038	0.0000	NA	0.087	0.113
4	0.0003	0.0086	0.0434	0.0034	0.9566	0.0034	0.0000	NA	0.153	0.163
5	0.0005	0.0137	0.0764	0.0043	0.9236	0.0043	0.0000	NA	0.199	0.212
6	0.0004	0.0105	0.0993	0.0037	0.9007	0.0037	0.0000	NA	0.225	0.263
7	0.0003	0.0074	0.1127	0.0031	0.8873	0.0031	0.0000	NA	0.270	0.315
8	0.0004	0.0098	0.1350	0.0036	0.8650	0.0036	0.0000	NA	0.344	0.365
9	0.0003	0.0075	0.1722	0.0032	0.8278	0.0032	0.0000	NA	0.416	0.414
10	0.0003	0.0073	0.2080	0.0031	0.7920	0.0031	0.0000	NA	0.472	0.464
11	0.0004	0.0083	0.2362	0.0033	0.7638	0.0033	0.0000	NA	0.657	0.514
14	0.0005	0.0117	0.3286	0.0040	0.6714	0.0040	0.0000	NA	0.731	0.662
15	0.0006	0.0125	0.3655	0.0041	0.6345	0.0041	0.0000	NA	0.795	0.712
16	0.0008	0.0155	0.3973	0.0046	0.6027	0.0046	0.0000	NA	0.869	0.762
17	0.0008	0.0165	0.4347	0.0047	0.5653	0.0047	0.0000	NA	0.934	0.812
18	0.0009	0.0178	0.4669	0.0049	0.5331	0.0049	0.0000	NA	1.038	0.861
19	0.0006	0.0107	0.5189	0.0038	0.4811	0.0038	0.0000	NA	1.083	0.911
20	0.0007	0.0128	0.5417	0.0041	0.4583	0.0041	0.0000	NA	1.161	0.961
21	0.0007	0.0119	0.5805	0.0040	0.4195	0.0040	0.0000	NA	1.212	1.01
22	0.0012	0.0201	0.6058	0.0052	0.3942	0.0052	0.0000	NA	1.285	1.06
23	0.0011	0.0180	0.6427	0.0049	0.3573	0.0049	0.0000	NA	1.330	1.11
24	0.0012	0.0201	0.6648	0.0052	0.3352	0.0052	0.0000	NA	1.392	1.159
25	0.0010	0.0167	0.6959	0.0047	0.3041	0.0047	0.0000	NA	1.439	1.209
26	0.0011	0.0179	0.7195	0.0049	0.2805	0.0049	0.0000	NA	1.466	1.259
27	0.0015	0.0226	0.7332	0.0055	0.2668	0.0055	0.0000	NA	1.519	1.308
28	0.0020	0.0299	0.7595	0.0063	0.2405	0.0063	0.0000	NA	1.567	1.359
29	0.0015	0.0219	0.7833	0.0054	0.2167	0.0054	0.0000	NA	1.591	1.408
30	0.0018	0.0261	0.7954	0.0059	0.2046	0.0059	0.0000	NA	1.618	1.457
31	0.0017	0.0252	0.8090	0.0058	0.1910	0.0058	0.0000	NA	1.652	1.507
32	0.0023	0.0335	0.8258	0.0067	0.1742	0.0067	0.0000	NA	1.684	1.557
33	0.0019	0.0276	0.8418	0.0061	0.1582	0.0061	0.0000	NA	1.712	1.606
34	0.0022	0.0323	0.8561	0.0066	0.1439	0.0066	0.0000	NA	1.761	1.656
35	0.0019	0.0267	0.8806	0.0060	0.1194	0.0060	0.0000	NA	1.797	1.706
37	0.0029	0.0400	0.8986	0.0073	0.1014	0.0073	0.0000	NA	1.815	1.805
38	0.0032	0.0440	0.9077	0.0077	0.0923	0.0077	0.0000	NA	1.827	1.855
39	0.0034	0.0482	0.9135	0.0080	0.0865	0.0080	0.0000	NA	1.833	1.904
40	0.0035	0.0482	0.9164	0.0080	0.0836	0.0080	0.0000	NA	1.851	1.954
41	0.0033	0.0446	0.9254	0.0077	0.0746	0.0077	0.0000	NA	1.822	1.983

42	0.0037	0.0509	0.9111	0.0082	0.0889	0.0082	0.0000	NA	1.755	1.881
43	0.0030	0.0443	0.8776	0.0077	0.1224	0.0077	0.0000	NA	1.666	1.781
44	0.0026	0.0384	0.8331	0.0072	0.1669	0.0072	0.0000	NA	1.568	1.686
45	0.0024	0.0372	0.7840	0.0071	0.2160	0.0071	0.0000	NA	1.475	1.584
46	0.0025	0.0396	0.7375	0.0073	0.2625	0.0073	0.0000	NA	1.402	1.488
47	0.0025	0.0408	0.7011	0.0074	0.2989	0.0074	0.0000	NA	1.348	1.386
48	0.0023	0.0381	0.6740	0.0071	0.3260	0.0071	0.0000	NA	1.291	1.286
49	0.0026	0.0445	0.6453	0.0077	0.3547	0.0077	0.0000	NA	1.271	1.177
50	0.0020	0.0361	0.6356	0.0070	0.3644	0.0070	0.0000	NA	1.215	1.074
51	0.0024	0.0427	0.6073	0.0076	0.3927	0.0076	0.0000	NA	1.035	0.976
54	0.0022	0.0265	0.5177	0.0074	0.4413	0.0063	0.0410	0.0098	0.994	0.675
55	0.0020	0.0247	0.4972	0.0072	0.4636	0.0061	0.0392	0.0094	0.955	0.575
56	0.0020	0.0258	0.4553	0.0073	0.5041	0.0063	0.0406	0.0096	0.870	0.479
57	0.0020	0.0282	0.3760	0.0077	0.5690	0.0065	0.0549	0.0101	0.697	0.378
58	0.0018	0.0270	0.3116	0.0075	0.6165	0.0064	0.0719	0.0099	0.551	0.274
59	0.0015	0.0246	0.2274	0.0072	0.6549	0.0061	0.1176	0.0094	0.337	0.17
62	0.0013	0.0238	0.1116	0.0070	0.7056	0.0060	0.1828	0.0093	0.040	0.043

- X-ray beam was not available at the time that spectrum 12, 13, 36, 52, and 53 was collected.
- FeF_3 was introduced as a reference standard spectrum from 54 to yield more accurate fitting.
- x_{Li}(spectrum) is the capacity estimated from spectrum fitting, based on the mole fraction of different Fe oxidation states. x_{Li}(echem) is the average capacity during the 18 min spectrum collection measured by the potentiostat/galvanostat Their comparison is plotted in Figure A3.15a.

Table A3.2 | Details for the linear combinational fitting results (FeF_3 nanowire electrode)

			FeF_2		Fe		FeF_3			
XAS No.	**R**	χ^2	**weight**	**error**	**weight**	**error**	**weight**	**error**	**xLi (spectrum)**	**xLi (echem)**
1	0.0000	0.0000	0.0000	0.0000	0.0000	0.0000	1.0000	0.0169	0.000	0.000
2	0.0000	0.0014	0.0800	0.0014	0.0000	0.0017	0.9200	0.0170	0.080	0.073
3	0.0002	0.0060	0.1780	0.0029	0.0138	0.0036	0.8082	0.0175	0.219	0.164
4	0.0005	0.0123	0.2721	0.0041	0.0186	0.0052	0.7093	0.0181	0.328	0.250
5	0.0007	0.0181	0.3669	0.0050	0.0112	0.0063	0.6220	0.0187	0.400	0.339
8	0.0018	0.0452	0.5889	0.0079	0.0534	0.0100	0.3577	0.0212	0.749	0.611
9	0.0022	0.0530	0.6576	0.0086	0.0641	0.0108	0.2782	0.0218	0.850	0.702
10	0.0026	0.0613	0.6941	0.0092	0.0834	0.0117	0.2225	0.0225	0.944	0.792
11	0.0025	0.0593	0.7083	0.0091	0.0971	0.0115	0.1946	0.0223	1.000	0.883
12	0.0025	0.0589	0.6934	0.0091	0.1378	0.0114	0.1688	0.0223	1.107	0.973
13	0.0023	0.0545	0.7006	0.0087	0.1441	0.0110	0.1552	0.0219	1.133	1.064
14	0.0022	0.0509	0.6856	0.0084	0.1694	0.0106	0.1450	0.0217	1.194	1.154
15	0.0022	0.0495	0.6760	0.0083	0.1902	0.0105	0.1338	0.0215	1.247	1.245
16	0.0020	0.0447	0.6386	0.0079	0.2420	0.0100	0.1194	0.0211	1.365	1.335
17	0.0019	0.0400	0.6036	0.0075	0.2852	0.0094	0.1112	0.0207	1.459	1.426
18	0.0017	0.0351	0.5805	0.0070	0.3214	0.0088	0.0981	0.0203	1.545	1.516
19	0.0014	0.0292	0.5653	0.0064	0.3309	0.0080	0.1039	0.0198	1.558	1.607
20	0.0012	0.0245	0.5277	0.0058	0.3867	0.0074	0.0857	0.0193	1.688	1.697
21	0.0013	0.0234	0.4911	0.0057	0.4299	0.0072	0.0790	0.0192	1.781	1.788
22	0.0013	0.0255	0.4881	0.0060	0.4343	0.0075	0.0776	0.0194	1.791	1.878
23	0.0009	0.0158	0.4247	0.0047	0.5071	0.0059	0.0682	0.0185	1.946	1.971
25	0.0012	0.0207	0.3096	0.0054	0.6484	0.0068	0.0419	0.0190	2.255	2.152
26	0.0018	0.0275	0.2895	0.0062	0.6794	0.0078	0.0311	0.0196	2.328	2.242
27	0.0013	0.0206	0.2624	0.0053	0.6992	0.0068	0.0384	0.0190	2.360	2.331
28	0.0015	0.0224	0.2240	0.0056	0.7413	0.0071	0.0347	0.0191	2.448	2.406
29	0.0034	0.0492	0.2148	0.0083	0.7624	0.0104	0.0229	0.0215	2.502	2.496
30	0.0022	0.0303	0.1528	0.0065	0.8137	0.0082	0.0335	0.0199	2.594	2.584
31	0.0024	0.0327	0.1172	0.0067	0.8507	0.0085	0.0321	0.0201	2.669	2.672
32	0.0028	0.0380	0.1023	0.0073	0.8623	0.0092	0.0354	0.0205	2.689	2.762
33	0.0029	0.0392	0.0890	0.0074	0.8783	0.0093	0.0326	0.0207	2.724	2.815
35	0.0022	0.0296	0.0782	0.0064	0.8828	0.0081	0.0391	0.0198	2.726	2.685
36	0.0026	0.0354	0.0867	0.0070	0.8758	0.0089	0.0375	0.0203	2.714	2.594
39	0.0017	0.0244	0.1596	0.0058	0.7699	0.0074	0.0705	0.0193	2.469	2.322
40	0.0015	0.0225	0.1913	0.0056	0.7372	0.0071	0.0715	0.0191	2.403	2.232
41	0.0015	0.0236	0.2244	0.0057	0.7016	0.0072	0.0740	0.0192	2.329	2.141

42	0.0016	0.0253	0.2612	0.0059	0.6656	0.0075	0.0732	0.0194	2.258	2.051
43	0.0016	0.0254	0.2914	0.0059	0.6392	0.0075	0.0694	0.0194	2.209	1.960
44	0.0015	0.0251	0.3226	0.0059	0.6144	0.0075	0.0629	0.0194	2.166	1.870
45	0.0018	0.0308	0.3660	0.0065	0.5716	0.0083	0.0625	0.0199	2.081	1.779
48	0.0029	0.0557	0.5028	0.0088	0.4362	0.0111	0.0610	0.0220	1.811	1.508
49	0.0029	0.0570	0.5363	0.0089	0.4022	0.0112	0.0616	0.0222	1.743	1.417
50	0.0027	0.0532	0.5560	0.0086	0.3885	0.0109	0.0555	0.0218	1.721	1.327
51	0.0027	0.0540	0.5769	0.0087	0.3710	0.0109	0.0520	0.0219	1.690	1.236
52	0.0029	0.0597	0.6046	0.0091	0.3326	0.0115	0.0628	0.0224	1.602	1.146
53	0.0032	0.0682	0.6333	0.0097	0.2937	0.0123	0.0730	0.0230	1.514	1.055
54	0.0026	0.0559	0.6251	0.0088	0.2859	0.0111	0.0890	0.0221	1.483	0.965
55	0.0022	0.0487	0.6142	0.0082	0.2772	0.0104	0.1086	0.0215	1.446	0.874
56	0.0020	0.0424	0.5928	0.0077	0.2658	0.0097	0.1414	0.0209	1.390	0.784
57	0.0027	0.0621	0.6063	0.0093	0.1872	0.0117	0.2066	0.0226	1.168	0.725
58	0.0023	0.0544	0.5779	0.0087	0.1686	0.0110	0.2535	0.0219	1.084	0.655
59	0.0017	0.0371	0.5549	0.0072	0.1898	0.0091	0.2553	0.0205	1.124	0.615
60	0.0015	0.0340	0.5477	0.0069	0.1738	0.0087	0.2785	0.0202	1.069	0.585
61	0.0015	0.0338	0.5430	0.0069	0.1526	0.0087	0.3044	0.0202	1.001	0.555
62	0.0015	0.0369	0.5461	0.0072	0.1051	0.0090	0.3488	0.0205	0.861	0.535
63	0.0018	0.0425	0.5385	0.0077	0.0769	0.0097	0.3846	0.0209	0.769	0.505

- X-ray beam was not available or unstable at the time that spectrum 6, 7, 24, 37, 38, 46, and 47 was collected.
- x_{Li}(spectrum) is the capacity estimated from spectrum fitting, based on the mole fraction of different Fe oxidation states. x_{Li}(echem) is the average capacity during the 18 min spectrum collection measured by the potentiostat/galvanostat. Their comparison is plotted in Figure A3.15b.

Table A3.3 | Details for the linear combinational fitting results (FeF_3 microwire electrode)

			Fe		FeF2		FeF3			
XAS No.	**R**	χ^2	**weight**	**error**	**weight**	**error**	**weight**	**error**	**xLi (spectrum)**	**xLi (echem)**
1	NA	NA	0	NA	0	NA	1 (Pristine)	NA	0.000	0.000
2	0.0002	0.0054	0.0300	0.0037	0.0231	0.0028	0.9469	0.0024	0.113	0.032
3	0.0001	0.0045	0.0508	0.0033	0.0755	0.0025	0.8737	0.0022	0.228	0.099
4	0.0002	0.0064	0.0483	0.0040	0.1334	0.0030	0.8183	0.0026	0.278	0.172
5	0.0002	0.0046	0.0459	0.0034	0.1791	0.0026	0.7750	0.0022	0.317	0.242
6	0.0002	0.0057	0.0576	0.0038	0.2137	0.0029	0.7287	0.0025	0.386	0.311
7	0.0003	0.0087	0.0636	0.0046	0.2472	0.0035	0.6892	0.0030	0.438	0.384
8	0.0003	0.0090	0.0817	0.0047	0.2743	0.0036	0.6441	0.0031	0.519	0.456
10	0.0005	0.0139	0.0973	0.0059	0.3272	0.0045	0.5754	0.0038	0.619	0.601
13	0.0008	0.0199	0.1257	0.0070	0.3846	0.0053	0.4898	0.0046	0.762	0.818
15	0.0012	0.0295	0.1336	0.0085	0.4263	0.0065	0.4402	0.0056	0.827	0.956
16	0.0013	0.0314	0.1408	0.0088	0.4397	0.0067	0.4194	0.0057	0.862	1.035
18	0.0031	0.0799	0.1155	0.0141	0.4977	0.0107	0.3868	0.0091	0.844	1.180
19	0.0049	0.1240	0.0970	0.0175	0.5227	0.0133	0.3802	0.0114	0.814	1.251
20	0.0027	0.0649	0.1654	0.0127	0.5020	0.0096	0.3326	0.0082	0.998	1.323
22	0.0023	0.0545	0.1865	0.0116	0.5143	0.0088	0.2993	0.0076	1.074	1.468
23	0.0019	0.0439	0.2204	0.0104	0.5081	0.0079	0.2715	0.0068	1.169	1.541
24	0.0017	0.0372	0.2479	0.0096	0.5021	0.0073	0.2501	0.0062	1.246	1.613
25	0.0013	0.0296	0.2822	0.0086	0.4876	0.0065	0.2302	0.0056	1.334	1.685
27	0.0016	0.0368	0.2814	0.0095	0.5119	0.0072	0.2068	0.0062	1.356	1.830
28	0.0019	0.0414	0.2875	0.0101	0.5191	0.0077	0.1935	0.0066	1.381	1.901
29	0.0030	0.0648	0.2851	0.0127	0.5307	0.0096	0.1842	0.0082	1.386	1.973
30	0.0020	0.0440	0.3198	0.0104	0.5181	0.0079	0.1622	0.0068	1.477	2.045
31	0.0027	0.0571	0.3397	0.0119	0.5158	0.0090	0.1444	0.0077	1.535	2.118
32	0.0024	0.0482	0.3918	0.0109	0.4935	0.0083	0.1147	0.0071	1.669	2.190
33	0.0027	0.0531	0.4220	0.0115	0.4896	0.0087	0.0884	0.0075	1.756	2.262
34	0.0034	0.0655	0.4793	0.0127	0.4617	0.0097	0.0590	0.0083	1.900	2.334
35	0.0047	0.0844	0.5536	0.0145	0.4075	0.0110	0.0389	0.0094	2.068	2.407
36	0.0039	0.0662	0.6208	0.0128	0.3391	0.0097	0.0400	0.0083	2.202	2.479
37	0.0042	0.0673	0.6912	0.0129	0.2710	0.0098	0.0378	0.0084	2.345	2.547
38	0.0042	0.0673	0.7392	0.0129	0.2186	0.0098	0.0422	0.0084	2.436	2.619
39	0.0040	0.0597	0.7847	0.0122	0.1758	0.0092	0.0394	0.0079	2.530	2.695
40	0.0053	0.0806	0.7985	0.0141	0.1567	0.0107	0.0448	0.0092	2.552	2.767

41	0.0056	0.0800	0.8280	0.0141	0.1297	0.0107	0.0423	0.0091	2.614	2.839
42	0.0051	0.0712	0.8451	0.0133	0.1126	0.0101	0.0422	0.0086	2.648	2.882
43	0.0054	0.0768	0.8356	0.0138	0.1183	0.0105	0.0461	0.0090	2.625	2.855
45	0.0037	0.0566	0.7765	0.0118	0.1458	0.0090	0.0777	0.0077	2.475	2.713
46	0.0040	0.0632	0.7682	0.0125	0.1594	0.0095	0.0724	0.0081	2.464	2.641
47	0.0041	0.0636	0.7516	0.0125	0.1638	0.0095	0.0846	0.0082	2.419	2.569
48	0.0034	0.0528	0.7529	0.0114	0.1671	0.0087	0.0800	0.0074	2.426	2.496
49	0.0028	0.0438	0.7397	0.0104	0.1793	0.0079	0.0810	0.0068	2.398	2.424
50	0.0036	0.0593	0.7041	0.0121	0.2115	0.0092	0.0844	0.0079	2.324	2.352
53	0.0042	0.0713	0.6291	0.0133	0.2851	0.0101	0.0858	0.0086	2.172	2.135
54	0.0067	0.1196	0.5617	0.0172	0.3440	0.0131	0.0942	0.0112	2.029	2.063
55	0.0033	0.0596	0.5553	0.0121	0.3601	0.0092	0.0846	0.0079	2.026	1.991
56	0.0038	0.0696	0.5138	0.0131	0.4028	0.0100	0.0834	0.0085	1.944	1.919
57	0.0061	0.1213	0.4399	0.0173	0.4665	0.0132	0.0935	0.0113	1.786	1.847
58	0.0037	0.0723	0.4544	0.0134	0.4651	0.0102	0.0805	0.0087	1.828	1.774
59	0.0053	0.1077	0.4055	0.0163	0.5075	0.0124	0.0870	0.0106	1.724	1.702
60	0.0062	0.1298	0.3617	0.0179	0.5391	0.0136	0.0993	0.0117	1.624	1.630
61	0.0055	0.1163	0.3470	0.0170	0.5438	0.0129	0.1092	0.0110	1.585	1.558
62	0.0032	0.0665	0.3607	0.0128	0.5292	0.0097	0.1102	0.0083	1.611	1.485
63	0.0039	0.0836	0.3227	0.0144	0.5593	0.0109	0.1181	0.0094	1.527	1.413
64	0.0039	0.0869	0.2812	0.0147	0.5769	0.0111	0.1419	0.0095	1.420	1.341
65	0.0034	0.0802	0.2123	0.0141	0.6098	0.0107	0.1779	0.0092	1.247	1.277
66	0.0028	0.0646	0.2082	0.0126	0.5978	0.0096	0.1940	0.0082	1.222	1.226
67	0.0037	0.0911	0.1446	0.0150	0.6310	0.0114	0.2244	0.0098	1.065	1.184
68	0.0028	0.0677	0.1422	0.0129	0.6156	0.0098	0.2421	0.0084	1.042	1.150
70	0.0022	0.0543	0.1409	0.0116	0.5901	0.0088	0.2691	0.0075	1.013	1.097
71	0.0020	0.0494	0.1460	0.0111	0.5727	0.0084	0.2813	0.0072	1.011	1.076
72	0.0022	0.0552	0.1264	0.0117	0.5761	0.0089	0.2975	0.0076	0.955	1.057
73	0.0019	0.0465	0.1444	0.0107	0.5533	0.0081	0.3024	0.0070	0.986	1.040
74	0.0019	0.0460	0.1379	0.0107	0.5478	0.0081	0.3143	0.0069	0.962	1.024
75	0.0015	0.0366	0.1493	0.0095	0.5279	0.0072	0.3228	0.0062	0.976	1.008
76	0.0015	0.0367	0.1480	0.0095	0.5179	0.0072	0.3341	0.0062	0.962	0.993
77	0.0021	0.0515	0.1029	0.0113	0.5368	0.0086	0.3603	0.0073	0.846	0.979

- X-ray beam was not available or unstable at the time that spectrum 9, 11, 12, 26, 51, 52 was collected.
- x_{Li} (spectrum) is the capacity estimated from spectrum fitting, based on the mole fraction of different Fe oxidation states. x_{Li} (echem) is the average capacity during the 18 min spectrum collection measured by the potentiostat/galvanostat

A3.3 Supplementary Movies

These movies are available upon request at linsen@chem.wisc.edu or jin@chem.wisc.edu.

Movie A3.1 | In situ TEM electron diffraction during the lithiation of FeF_3 nanowires.

Movie A3.2 | In situ STEM during the lithiation of a bundle of FeF_3 nanowires.

A3.4 References

(1) A. Jain, G. Hautier, S. P. Ong, C. J. Moore, C. C. Fischer, K. A. Persson and G. Ceder. Formation enthalpies by mixing GGA and GGA+*U* calculations, *Phys. Rev. B*, 2011, **84**, 045115.

APPENDIX 4

Supplementary Information for CHAPTER 5:

High-Purity Iron Pyrite (FeS_2) Nanowires as High-Capacity Nanostructured Cathodes for Lithium-Ion Batteries

---

This Appendix was made available online as supporting information for *Nanoscale* **6**, 2112, (2014), in collaboration with M. Caban-Acevedo, S. N. Girard, and S. Jin.

A4.1 Experimental methods

Materials. All chemicals were used as received without further purification. Hydrofluoric acid (aqueous HF solution, 48 wt%, CAS # 7664-39-3. *Warning: HF solution is highly corrosive and must be handled with care and proper protection. Please see safety information*[1]), iron (III) nitrate nonahydrate [$Fe(NO_3)_3{\cdot}9H_2O$, ≥98.0%, CAS # 7782-61-8], elemental sulfur (S, 99.5–100.5%, CAS # 7704-34-9), lithium bis(trifluoromethane)sulfonimide (LiTFSi, 99.95% trace metal basis, CAS # 90076-65-6), and tetraethylene glycol dimethyl ether (TEGDME, ≥99.0%, CAS # 143-24-8) were purchased from Sigma Aldrich. Ethanol (200 proof, CAS # 64-17-5) was purchased from Decon Laboratories Inc. N-methyl-2-pyrrolidone (NMP, ≥99.5%, CAS # 872-50-4), polyethylene separator membranes, polyvinylidene difluoride (PVDF, ≥99.5%, CAS # 24937-79-9) binder, lithium foils (15.6 mm in diameter × 0.45 mm in thickness, >99%, CAS # 7439-93-2) and 2032-type coin cell cases were purchased from MTI Corporation. Carbon black [Super P® conductive, ≥99% (metal basis), CAS # 1333-86-4] and aluminum foils [0.025 mm in thickness, ≥99.45% metal basis, CAS # 7429-90-5] were purchased from Alfa Aesar.

Nanowire Synthesis. The α-$FeF_3{\cdot}3H_2O$ nanowires (NWs) were prepared *via* an improved synthesis based on our previous work.[2] Briefly, 7.5 mL ethanol and 2.0 mL HF aqueous solution (48 wt%) were carefully added into a 15 mL plastic centrifuge tube in sequence. The centrifuge tube was sealed and gently shaken by hand with great caution to allow the two liquids to mix. An Fe^{3+} solution in ethanol with a concentration of 266 mM was made by dissolving 1.616 g $Fe(NO_3)_3{\cdot}9H_2O$ in 15.0 mL ethanol. 0.500 mL of this Fe^{3+}/ethanol solution was then quickly injected into the HF/ethanol mixture using an Eppendorf pipet. The resulting colorless

solution with a concentration ratio of $c(Fe^{3+})$: $c(HF)$: $c(H_2O)$ ≈ 13.3 mM: 5560 mM: 6760 mM was gently mixed by shaking and kept in an oven at 60 °C for 24 h. No substrate was used during the reaction and aggressive agitation was avoided to suppress the formation of large *β*-$FeF_3{\cdot}3H_2O$ crystals. The white cloudy precipitate that appeared over time was collected by centrifugation at 5000 rpm for 5 min, washed with dry ethanol twice and vacuum-dried at room temperature. Typically, 6.6–7.7 mg NWs can be acquired from a 10 mL-scale reaction, corresponding to a yield of 30–35% based on the limiting agent of Fe.

The $FeF_3{\cdot}3H_2O$ NWs (~10 mg) were transferred to an alumina boat, which was loaded at the center of a home-made flow tube reactor setup with flow and pressure control. The $FeF_3{\cdot}3H_2O$ NWs were first dehydrated under vacuum by slowly heating to a 100 °C at a rate of ~2 °C/min, then to 200 °C at a rate of ~ 0.5 °C min^{-1}. The powder color changed from white to green/brown. Then the sulfidation reaction was carried out at 500 °C for 2 h under a sulfur atmosphere. An alumina boat containing ~3 g elemental sulfur was introduced and positioned at a temperature of ~415 °C throughout the reaction, which yields an estimated sulfur vapor pressure of ~480 Torr.[3] After 2 h of reaction the reactor was evacuated and the tube furnace was open to allow the reactor to cool down naturally to room temperature. Larger scale of conversion (~80 mg) could also be readily carried out in a closed ampule using sufficient amount of sulfur to ensure a saturated sulfur atmosphere at 500 °C.

Material Characterization. Scanning electron microscopy (SEM) images were acquired using a LEO 55 VP field emission scanning electron microscope at a working voltage of 2 kV. Transmission electron microscopy (TEM) images and electron diffraction (ED) patterns were

acquired using a Philips CM200 transmission electron microscope at an accelerating voltage of 200 kV. The TEM samples were prepared by dropcasting FeS_2 NWs suspended in ethanol onto lacey-carbon grids (Ted Pella Inc. lacey carbon type-A, 300 Mesh). All the TEM grids were checked for appropriate NW density using an optical microscope before TEM characterization. High-resolution X-ray diffraction was performed by synchrotron radiation at Argonne National Laboratory on the Advanced Photon Source (APS), beamline 11-BM using a 12-analyzer Si detector and calibrated radiation wavelength of 0.412455 Å.[4, 5] The samples were hand ground using a mortar and pestle and passed through a 40 μm steel mesh sieve. The resulting fine powders were packed into 0.5 mm quartz capillaries and evacuated to a residual vacuum of ~10^{-3} Torr and flame-sealed using a high temperature torch. The capillaries were placed in a double-tilt goniometer in transmission geometry (Debye-Scherrer method) and rotated at 500 rpm. The confocal micro-Raman spectra of an as-synthesized sample on borosilicate substrate were collected with a Horiba Jobin Yvan LabRAM ARAMIS confocal microscope using a 100 μm aperture and a 532 nm laser source. Optical measurements were performed using a Cary-5000 UV-Vis-NIR spectrophotometer equipped with an integration sphere (Agilent Technologies).

Nano-pyrite Cathode Processing and Electrochemical Measurements. Electrochemical measurements were performed on nanocomposite electrodes pasted on aluminum foils, which were prepared from slurries containing 70 wt% FeS_2 NWs, 20 wt% conductive carbon black, and 10 wt% PVDF binder using NMP as the solvent. The mass loading of active material (FeS_2) was about 2 mg cm^{-2}. CR2032-type coin cells were assembled in an argon-fill glovebox, using Li metal as the counter/quasi-reference electrode, 1 M LiTFSi in TEGDME as the electrolyte, polyethylene films as the separator. All cells were aged overnight before electrochemical tests.

Discharge/charge cycling tests were performed with a multi-channel battery analyzer (MTI BST8-WA) operated using Neware software at room temperature (~25 °C) over different voltage windows at different current densities from 0.01 C to 0.2 C (1 C = 894 mA g^{-1}). All reported performance was calculated based on the mass of the active material (FeS_2). Electrochemical impedance spectroscopy (EIS) were performed using a Biologic SP-200 Potentiostat operated using EC-Lab software over a frequency range from 200 kHz to 50 mHz with a perturbation voltage of 10 mV. The cells were rest for 0.5 h before taking the EIS measurements.

A4.2 Additional tables and figures

Table A4.1. List of the free energy of formation ($\Delta_f G$, in kJ mol^{-1}) for FeS_2 and SF_6.

Chemical Species	Free Energy of Formation ($\Delta_f G$) / kJ mol^{-1}				
	600 K	700 K	**773 K**	800 K	900 K
FeS_2 (*s*)	–143.86	–137.074	**–131.035**	–129.946	–120.367
SF_6 (*g*)	–1008.204	–971.804	**–944.911**	–935.416	–897.998

Notes: 1) Values for 600 K, 700 K, 800 K, and 900 K are taken from the NIST-JANAF Thermochemical Tables (http://kinetics.nist.gov/janaf/). The values for 773 K were linearly extrapolated from the tabulated values.

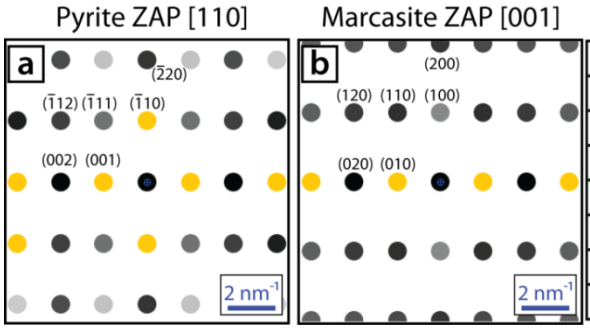

Pyrite [110]		Marcasite [001]	
(hkl)	d^{-1} / nm^{-1}	(hkl)	d^{-1}/ nm^{-1}
(001)	1.84	(010)	1.84
(002)	3.69	(020)	3.69
(1̄10)	2.61	(100)	2.25
(1̄11)	3.20	(110)	2.91
(1̄12)	4.52	(120)	4.32
(2̄20)	5.22	(200)	4.50

Figure A4.1 Simulated ZAPs for the pyrite [110] (a) in comparison with the ZAP for the marcasite [001] (b). Tables of the respective lattice spacings for the individual zone axis patterns are provided for numerical comparison. Double diffraction spots are included. The scalar bars in (a) and (b) have the same length and both correspond to 2 nm^{-1}. Simulated pattern are generated using JEMS electron microscopy software.

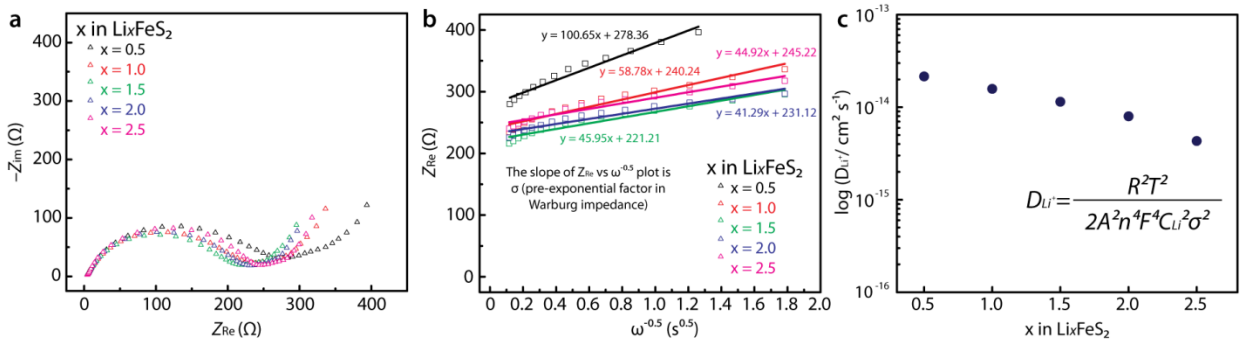

Figure A4.2 (a) EIS spectra ($-Z_{im}$ vs Z_{Re} plot) measured at different states of lithiation. The measurements were done on the same coin cell in the frequency range from 200 kHz to 50 mHz with a perturbation voltage of 10 mV. The battery cell was discharged at 0.1 C rate (89.4 mA g^{-1}) to certain states of lithiation and allowed to rest 0.5 h before each EIS measurement; (b) Z_{Re} vs $\omega^{-1/2}$ plots at different states of lithiation (only the data in diffusion-controlled regime were plotted, where f = 11.7–0.05 Hz.) ω is the radial frequency. Note that the slope of the Z_{Re} vs

$\omega^{-1/2}$ plot is σ (pre-exponential factor in Warburg impedance);[6, 7] (c) Chemical diffusion coefficient D_{Li} at different states of lithiation. D_{Li} is calculated using the equation $D_{Li} = \frac{R^2T^2}{2A^2n^4F^4C_{Li}^2\sigma^2}$ [6, 7], where R is the gas constant (8.314 J K^{-1} mol^{-1}), T is the temperature (298.15 K), A is the surface area of the electrode (1.27 cm^2), n is the charge carried by Li^+ (n = 1), F is the Faraday constant (96485 C mol^{-1}), σ is the pre-exponential factor in Warburg impedance decided from the slope of Z_{Re} vs $\omega^{-1/2}$ plot in (b), and C_{Li} is the concentration of Li^+ in the solids (mol cm^{-3}). We used the volume of Li_2FeS_2 (intermediate phase during lithiation of FeS_2) crystal lattice to estimate C_{Li}.

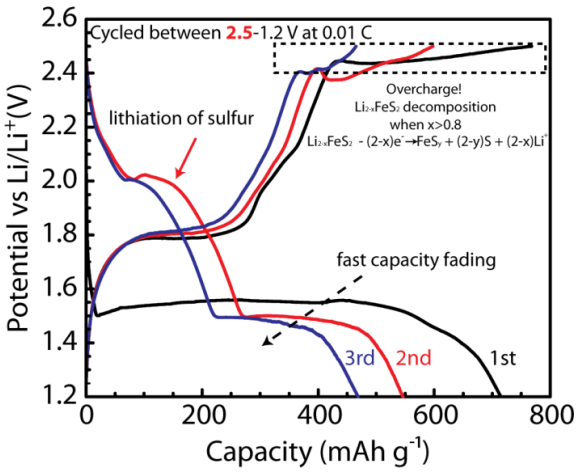

Figure A4.3 Voltage profile of a Li/nano-pyrite cell cycled in 2.5–1.1 V voltage range showing the voltage plateau originated from $Li_{2-x}FeS_2$ decomposition upon recharge beyond 2.4 V (highlighted in the dashed box in the upper right corner) and fast capacity fading in subsequent cycles.

A4.3 References

[1] Safety Information of Hydrofluoric Acid.

http://www.sigmaaldrich.com/catalog/ProductDetail.do?lang=en&N4=30107|SIAL&N5=SEARCH_CONCAT_PNO|BRAND_KEY&F=SPEC

[2] L. Li; Y. Yu; F. Meng; Y. Tan; R. J. Hamers; S. Jin. *Nano Lett.* **2012,** *12*, 724.

[3] D.-Y. Peng; J. Zhao. *J. Chem. Thermodyn.* **2001,** *33*, 1121.

[4] P. L. Lee, D. Shu, M. Ramanathan, C. Preissner, J. Wang, M. A. Beno, R. B. Von Dreele, L. Ribaud, C. Kurtz, S. M. Antao, X. Jiao, B. H. Toby, *J. Synchrotron Rad.* **2008,** 15, 427.

[5] J. Wang, B. H. Toby, P. L. Lee, L. Ribaud, S. M. Antao, C. Kurtz, M. Ramanathan, R. B. V. Dreele, M. A. Beno, *Rev. Sci. Instrum.* **2008,** 79, 085105.

[6] C. Ho, I. D. Raistrick and R. A. Huggins, *J. Electrochem. Soc.*, **1980,** 127, 8.

[7] N. Takami; A. Satoh; M. Hara; T. Ohsaki. *J. Electrochem. Soc.* **1995,** *142*, 9.

APPENDIX 5

Facile Solution Synthesis of α-$FeF_3 \cdot 3H_2O$ Nanowires and Their Conversion to α-Fe_2O_3 Nanowires for Photoelectrochemical Application

---

This Appendix was originally published in Nano Lett. **12,** 724-731 (2012), in collaboration with Y. Yu, F. Meng, Y. Tan, R. J. Hamers, and S. Jin.

A5.1 Abstract

We report for the first time the facile solution growth of α-$FeF_3 \cdot 3H_2O$ nanowires (NWs) in large quantity at a low supersaturation level and their scalable conversion to porous semiconducting α-Fe_2O_3 (hematite) NWs of high aspect-ratio via a simple thermal treatment in air. The structural characterization by transmission electron microscopy shows that thin α-$FeF_3 \cdot 3H_2O$ NWs (typically <100 nm in diameter) are converted to single-crystal α-Fe_2O_3 NWs with internal pores, while thick ones (typically >100 nm in diameter) become polycrystalline porous α-Fe_2O_3 NWs. We further demonstrated the photoelectrochemical (PEC) application of the nanostructured photoelectrodes prepared from these converted hematite NWs. The optimized photoelectrode with a ~400 nm thick hematite NW film yielded a photocurrent density of 0.54 mA/cm^2 at 1.23 V vs. reversible hydrogen electrode potential after modification with cobalt catalyst under standard conditions (AM 1.5 G, 100 mW/cm^2, pH = 13.6, 1M NaOH). The low cost, large quantity, and high aspect-ratio of the converted hematite NWs, together with the resulting simpler photoelectrode preparation, can be of great benefit for hematite-based PEC water splitting. Furthermore, the ease and scalability of the conversion from hydrated fluoride NWs to oxide NWs suggest a potentially versatile and low-cost strategy to make NWs of other useful iron-based compounds that may enable their large-scale renewable energy applications.

A5.2 Introduction

The scale and significance of the energy challenges demand inexpensive earth-abundant materials to be developed as the semiconductors, catalysts, or conducting electrodes for renewable energy technologies.[1-3] However, most abundant materials have inferior properties and performance in comparison with their more conventional peers and suffer from many shortcomings in applications. A case in point is iron-based compounds: since iron (Fe) is the fourth most abundant element in the Earth's crust, Fe-based semiconductors such as α-Fe_2O_3 (hematite, bandgap 2.1 eV)[4, 5] and β-FeS_2 (pyrite, bandgap 0.95 eV)[6] have the capacity to meet or exceed the annual worldwide energy consumption and the potential for a significant material cost reduction over conventional or leading solar materials.[1] However, they (especially hematite) are poor semiconductors whose mobility and minority carrier diffusion length are unsuitable for solar energy applications.[4, 5] In addition, iron fluoride (FeF_3) is a promising high-capacity Li-ion battery cathode material that is much cheaper than the current lithium cobalt oxide ($LiCoO_2$) cathode material.[7] However, such promise has been held back by the slow ionic diffusion and low conductivity of FeF_3. For many of these unconventional abundant materials, new design concepts based on nanoscale materials such as NWs may enhance their utility because the nanoscale dimensions may circumvent their shortcomings or make them much more tolerable for applications.[4, 8-11]

In particular, nanostructures of hematite have been exploited in the last few years to significantly enhance its photoelectrochemical (PEC) water oxidation performance for solar water splitting.[4, 5, 12-18] Despite having the advantages of favorable bandgap, excellent stability, abundance and low cost,[4] hematite has poor absorptivity near the bandgap ($\alpha^{-1} \sim 0.12$ □m at □=

550 nm),[19] low mobility (< 1 $cm^2 V^{-1} s^{-1}$),[20] short excited carrier lifetime (about 10 ps),[21] and short carrier (hole) diffusion length (2–4 nm).[22] Therefore, most of the carriers generated far away from the semiconductor-electrolyte interface cannot be collected, resulting in only small photocurrent.[22] In properly engineered nanostructures, most active absorbing hematite nano-domains should be within nanometer (~10 nm) distance from the semiconductor-electrolyte interface, yet sufficient effective thickness of materials is retained to absorb much of the solar light. Following this strategy of tuning the nano-morphologies, "cauliflower" nanostructures[12] or core-shell nanostructures grown via chemical vapor deposition and/or atomic layer deposition,[15] in combination with improved doping[16, 17] and surface modification with more efficient oxygen evolution catalysts,[12, 23-26] have led to significantly improved performance and made the nanostructured hematite a much more promising photoanode material. The hematite nanostructures made via solution processing have also been significantly improved following similar strategies,[13, 14, 16-18] even though their absolute performance still lags behind that of vapor phase synthesized hematite, they enjoy much simpler processing and lower cost. Such nanoparticle or mesoporous hematite films often suffer from recombination and poor transport across grain boundaries between particles. In this regard, 1D NWs with high aspect ratio and large surface area could improve the charge carrier collection by minimizing hopping transport. Furthermore, 1D materials are advantageous in solar applications[10, 27-31] because they have a long axis to absorb incident sunlight effectively (especially when they are aligned vertically) yet with a short radial distance for the photo-excited carriers to diffuse to semiconductor-electrolyte interface. It is thus valuable to develop low cost solution-based synthetic strategies to prepare high quality hematite NWs.

Moreover, for large scale applications in solar energy conversion and energy storage, the nanomaterials of abundant iron compounds should ideally be prepared in scalable processes that are much less energy-intensive and costly than those currently employed in the semiconductor industry. Even though NW synthesis in high temperature/vacuum vapor phase processes is useful for understanding the fundamental science and to establish the proof-of-concept for applications,[29, 31] solution growth would be more attractive in the long term due to the intrinsic low-cost and scalability advantages. Herein we report a facile solution synthesis of alpha iron fluoride trihydrate (α-$FeF_3 \cdot 3H_2O$) NWs for the first time, and also their subsequent conversion to semiconducting hematite NWs. These high aspect-ratio NWs of iron fluoride and hematite that can be readily prepared in bulk quantity could enable their applications in energy storage and solar energy conversion. To this end, we further demonstrate their application in PEC water splitting using the nanostructured photoelectrodes prepared from the converted hematite NWs.

A5.3 Results and Discussion

We intentionally designed and achieved the solution growth of α-$FeF_3 \cdot 3H_2O$ NWs under low supersaturation condition without the use of surfactants, following the guidelines illustrated by rational solution synthesis of ZnO and α-FeOOH NWs driven by screw dislocations.[32, 33] Due to the high solubility of $FeF_3 \cdot 3H_2O$ in water (5.92 g/100 g H_2O at 25 °C), we chose ethanol as the solvent, in which $FeF_3 \cdot 3H_2O$ dissolves very little.[34] Hydrofluoric acid (aqueous HF solution, 48 w.t. %) and iron (III) nitrate nonahydrate [$Fe(NO_3)_3 \cdot 9H_2O$] were used as the fluorine (F^-) and iron (Fe^{3+}) sources in our synthesis, respectively. Both of them disperse well in ethanol. It is also worth mentioning that F^- is a good complexing ligand for Fe^{3+} to make the stable FeF_6^{3-} complex ($K_f = 10^{15.04}$),[35] which effectively maintains the low supersaturation environment to favor NW

growth. For a typical α-$FeF_3 \cdot 3H_2O$ NW synthesis, 2.0 mL of HF aqueous solution (48 w.t. %) and 7.5 mL of ethanol were mixed in a sealed 15 mL plastic centrifuge tube, to which 0.5 mL of freshly prepared bright orange Fe^{3+}/ethanol solution (200 mM) was quickly added (Warning: HF solution is highly corrosive and must be handled with care and proper protection). The resulting colorless solution [$c(Fe^{3+})$: c(HF) : $c(H_2O) \approx$ 10 mM : 5560 mM : 6700 mM] was shaken by hand and then heated in an oven at 60 °C for 24h. The white cloudy precipitate that appeared over time was collected by centrifugation, washed with ethanol twice and then air-dried at room temperature. Typically, 2.0–4.0 mg NWs can be acquired from the 10 mL-scale reaction, corresponding to a yield of 12–24% based on the limiting reagent of Fe. The reaction can also be readily scaled up to meet the demand for a larger quantity of NW products.

The collected NWs were re-dispersed in ethanol and dropcasted onto a Si/SiO_2 substrate for scanning electron microscopy (SEM) examination. Representative SEM images (Figure A5.1a and 1b) reveal NWs of about 20–170 nm in diameter and 2–20 μm in length produced in high density by this simple approach. Powder X-ray diffraction (PXRD, Figure A5.1c) shows that the NWs can be well indexed to rhombohedral α-$FeF_3 \cdot 3H_2O$ (space group $R\bar{3}m$, a = 9.5135 Å, c = 4.7882 Å),[36] which is the metastable phase for $FeF_3 \cdot 3H_2O$.[36-38] No impurity phase in NWs was observed. Therefore, we suggest that the following two reactions are responsible for NW growth:

$$Fe^{3+} + 6F^- \rightarrow FeF_6^{3-} \qquad (1)$$

$$FeF_6^{3-} + 3H_2O \rightleftarrows FeF_3(H_2O)_3 + 3F^- \qquad (2)$$

Due to the high stability of FeF_6^{3-} ($K_f = 10^{15.04}$),[35] the first reaction is very favorable, as indicated by the rapid color change from bright-orange (Fe^{3+} dissolved in ethanol) to colorless (FeF_6^{3-}) upon mixing the Fe^{3+}/ethanol and the HF/ethanol solutions. The second reaction is slow and reversible, in which F^- and H_2O should be considered as both reactants and ligands to metal ions. The water molecules come from the 48 w.t. % HF aqueous solution and the water of hydration in $Fe(NO_3)_3 \cdot 9H_2O$. This equilibrium likely helps maintain a constant and low supersaturation of $FeF_3(H_2O)_3$, which is considered to be the precursor of crystal growth for both α- and β-$FeF_3 \cdot 3H_2O$.[37, 38] We suspect that the growth of α-$FeF_3 \cdot 3H_2O$ NWs is driven by screw dislocations,[32, 39, 40] but the as-grown NW samples are not electron-beam stable due to the easy loss of lattice water and thus it is impossible to either confirm or disprove this hypothesis. A typical TEM (Figure A5.1d) image shows the voids in the NWs caused by the high-energy electron beam during the observation. NWs quickly lose their lattice water and become amorphous according to the selected area electron diffraction (SAED, Figure A5.1d inset).

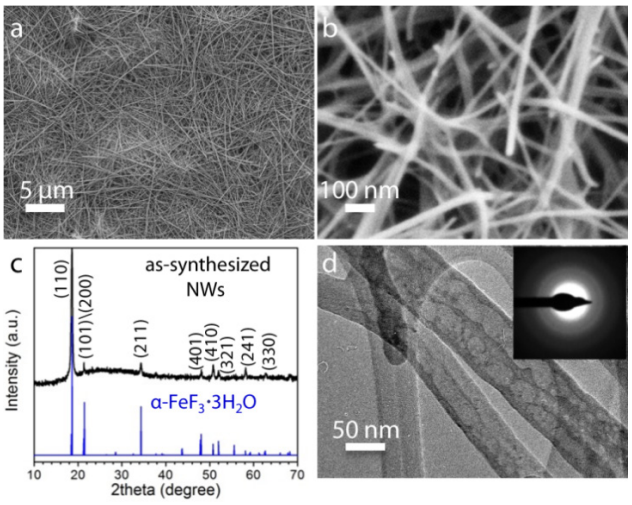

Figure A5.1 | Structural characterization of the α-$FeF_3 \cdot 3H_2O$ NWs. (a, b) Representative SEM images of as-synthesized NWs in high density collected on a Si/SiO_2 substrate; (c) PXRD of as-synthesized NWs collected on a glass substrate in comparison with the reference diffractogram for α-$FeF_3 \cdot 3H_2O$; (d) TEM images showing voids in NWs caused by the high-energy electron beam; Inset is the corresponding SAED pattern that shows NWs becoming amorphous during/after TEM observation.

These α-$FeF_3 \cdot 3H_2O$ NWs can be readily converted to semiconducting α-Fe_2O_3 (hematite) NWs by heating in air at 450 °C for 4h in a furnace housed in a fume hood.

$$4\ \alpha\text{-}FeF_3 \cdot 3H_2O \rightarrow 2\ \alpha\text{-}Fe_2O_3 + 12\ HF\uparrow + 6\ H_2O\uparrow$$

This conversion is thermodynamically favorable because hematite is very stable in air at high temperature, and the reaction generates volatile products further driving the equilibrium to the right-hand side. Furthermore, the metastablity and nanoscale dimension of α-$FeF_3 \cdot 3H_2O$ NWs reduces kinetic energy barrier for atoms and ions to diffuse. This facilitates the complete transformation from α-$FeF_3 \cdot 3H_2O$ to α-Fe_2O_3.[41] Typical SEM images (Figure A5.2a) shows that the 1D morphology of NWs is well preserved during the conversion. PXRD (Figure A5.2b) confirms that the air-annealed NWs are rhombohedral α-Fe_2O_3 (hematite, JCPDS No. 33-0664, space group $R\bar{3}c$, a = 5.036 Å, c = 13.75 Å) with no other detectable impurity phases. Even though hematite NWs/nanorods have been made via solution synthesis before,[17, 33, 42] these converted hematite NWs are significantly longer and larger in aspect ratio. 150 independent measurements on the length and diameter of α-Fe_2O_3 NWs yield an average length of 6.5 ± 2.3

μm, an average diameter of 84 ± 38 nm, and an average aspect ratio of 99 ± 70. While the uniformity of the dimensions and aspect ratio can still be improved, it is clear that such length and aspect ratio has not been achieved and/or reported before on the α-Fe_2O_3 NWs prepared via solution synthesis.[17, 33, 42] On the other hand, long hematite NWs can also be made by thermal oxidation of Fe foils,[43] but the scale of those preparations is small and the NWs are difficult to harvest. The NWs herein are made in a bulk quantity compared to previously reported hematite NWs made via vapor synthesis[43] or hydrolysis,[33, 42] and are more like entangled networks of NW mats. Thus the ways to utilize them in applications will be different.

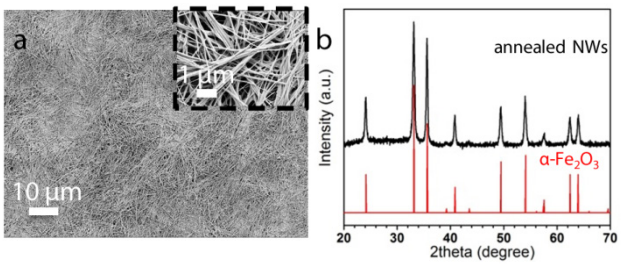

Figure A5.2. (a) Representative SEM images of α-Fe_2O_3 NWs in high density converted from α-$FeF_3 \cdot 3H_2O$ NWs by annealing in air at 450 °C for 4h; (b) PXRD of as-converted NWs collected on a glass substrate in comparison with the reference diffractogram for α-Fe_2O_3.

TEM characterization of these converted α-Fe_2O_3 NWs reveals that two types of structural transformation behavior are correlated with the diameter of the precursor α-$FeF_3 \cdot 3H_2O$ NWs: i) NWs with smaller diameters (typically <100 nm) are usually converted to single-crystal α-Fe_2O_3 NWs (10 thin single-crystal α-Fe_2O_3 NWs were examined). A representative example is shown

in Figure A5.3a, in which an SAED (Figure A5.3b) covering the whole object clearly shows that it is a single crystal despite some minor contrast variations seen in the low resolution TEM (LRTEM). Furthermore, a high resolution TEM (HRTEM) image of this thin NW shows continuous, single-crystal α-Fe_2O_3 lattice (Figure A5.3c). All of the thin α-Fe_2O_3 NWs examined exhibit the <110> growth direction, which is conducive to effective charge transport due to the higher electron and hole mobility along this direction.[4, 43, 44] ii) NWs with larger diameters (typically >100 nm) tend to become porous polycrystalline α-Fe_2O_3 (10 thick polycrystalline α-Fe_2O_3 NWs were examined), even though the overall 1D morphology of the NWs is maintained. It is clear that the object becomes multiple polycrystalline aggregates with void space between grains (Figure A5.3f). An HRTEM image highlights two attached nano-domains with indexed (113) and (104) crystal planes of α-Fe_2O_3 (Figure A5.3e).

We suggest that the different transforming behaviors may be explained in terms of diffusion of reactant atoms/ions in NWs with different thickness. Smaller domain size, shorter diffusion distance, and faster kinetics in thin NWs (<100 nm in diameter) give rise to a single nucleation event of the new solid phase and allow homogeneous transformation without disturbing their single crystallinity. Although chemical transformations of NWs with preserved single crystallinity have been reported before,[33, 41] the conversion from thin fluoride NWs to single-crystal oxide NWs, which involves the substitution of anions in the crystalline lattice, has not been observed. The ease and scalability of this conversion suggest a potentially versatile strategy to make single-crystal NWs of many useful Fe-based compounds en masse via the readily synthesized fluoride NWs.

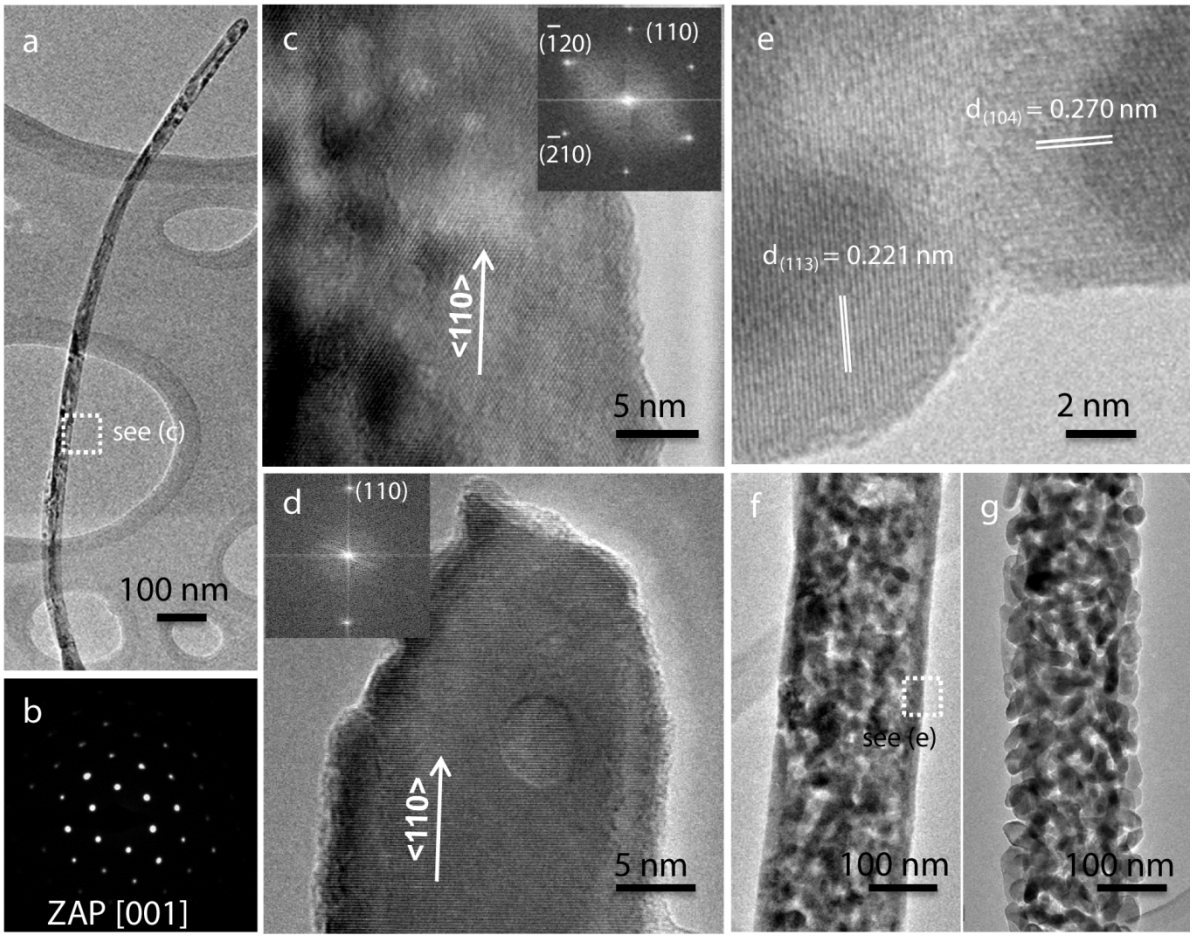

Figure A5.3. TEM characterization of the converted α-Fe_2O_3 NWs. (a) LRTEM image of a thin NW; (b) The SAED pattern corresponding to (a); (c) HRTEM image of the NW in (a) showing <110> growth direction and internal porosity, where the area of analysis is indicated by the white box in (a); Inset is the corresponding indexed fast Fourier transform pattern; (d) HRTEM image of another thin NW after additional annealing at 800 °C for 10 min, showing improved crystallinity, clear porosity, and confirming growth along <110>; Inset is the corresponding fast Fourier transform pattern; (e) and (f) Representative HRTEM and LRTEM images of a thick porous polycrystalline α-Fe_2O_3 NW after 450 °C conversion; (g) LRTEM image of a thick

polycrystalline α-Fe_2O_3 NW after additional annealing at 800 °C for 10 min, showing the preserved 1D morphology and grain growth behavior during high temperature annealing treatment.

Figure A5.3d and 3g show representative TEM images of thin and thick NWs respectively that have gone through additional annealing at 800 °C for 10 min, which is the same condition used later for activation of the photoelectrodes. We have noticed the preserved single crystallinity of thin NWs (Figure A5.3d) and the grain growth behavior for thick NWs (Figure A5.3g) after this thermal treatment.

Interestingly, internal porosity is also introduced to the converted thin hematite NWs with single crystallinity preserved (Figure A5.3c,d), which has been observed in other metal hydroxides/oxides systems.[33, 45-47] This can be explained by loss of water molecules and fluorine ions in the lattice that leads to a large increase in crystal density [ρ(α-$FeF_3 \cdot 3H_2O$) = 2.20 g/cm^3,[36, 48] while ρ(α-Fe_2O_3) = 5.25 g/cm^3].[34] In fact, porous hematite NWs may have better photocatalytic efficiency due to their increased surface area and small domain size that further reduce the carrier diffusion distance to the electrolyte.

The hematite NW photoelectrode samples for PEC measurements were prepared via the thermal conversion of α-$FeF_3 \cdot 3H_2O$ NWs as schematically illustrated in Figure A5.4a. The as-prepared α-$FeF_3 \cdot 3H_2O$ NWs can form uniform semi-transparent suspension in ethanol. Such suspension mixture with a concentration of 5 mg/mL was coated on fluorine-doped tin oxide (FTO) glass substrates (Hartford, TEC 15) via multiple cycles of doctor-blading using a 40 μm thick scotch tape (3M) as the spacer. The concentration of 5 mg/mL is suitable for making

uniform films without forming NW aggregates. For conversion to hematite NW films, these α-$FeF_3 \cdot 3H_2O$ NW films on FTO substrates were annealed in air (5 °C min^{-1} heating rate, 450 °C for 4h). Furthermore, an additional annealing step at 800 °C for 10 min was carried out on these hematite photoelectrodes. This is because the high temperature (800 °C) annealing has been reported to be important for yielding pronounced PEC oxidation current by solution-processed hematite photoelectrodes.[13, 17] It has been suggested that this enhanced photoactivity of hematite photoelectrodes can be attributed to the diffusion and doping of tin (Sn^{4+}) from FTO substrates into hematite nanostructures.[4, 13] We have not specifically acquired evidences to support or disprove this suggestion of Sn-doping. Furthermore, it is also possible that the high temperature annealing simply improves the crystallinity of the hematite and their electrical contact to the underlying FTO electrode. Without the 800 °C annealing, the photoelectrode shows little photoresponse.

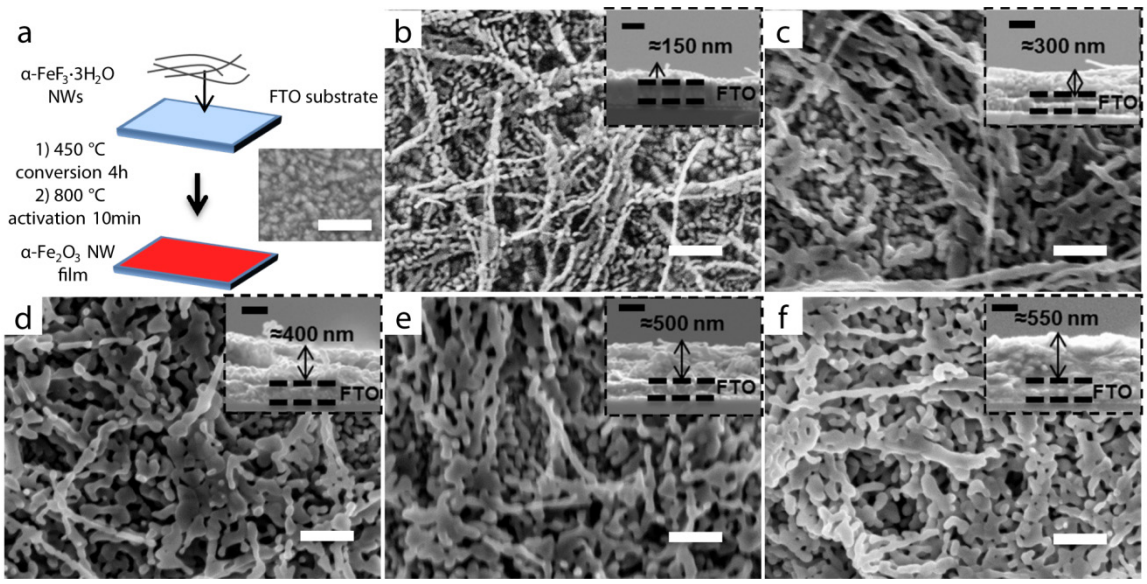

Figure A5.4 | SEM Images of Photoelectrodes Made from the Converted α-Fe_2O_3 NWs . (a) A schematic showing the preparation of nanostructured hematite photoelectrodes by conversion of the α-Fe_2O_3 NW films on FTO glass substrates (the SEM image shows a bare FTO substrate); (b–f) Top-view SEM images of the α-Fe_2O_3 NW films on FTO with increasing thickness and coverage. Scale bars are 1 μm. Insets are the corresponding cross-section images with shared 200 nm scale bar.

We prepared a series of photoelectrodes under otherwise identical conditions but varying the number of blading cycles and therefore the thickness of hematite NW films, and evaluated their morphologies and photocurrent responses (see later). The resulting films (Figure A5.4b–4f) are made of interconnected networks of hematite NWs with plenty of porous void space. Sintering and grain growth clearly occur after the annealing at 800 $^{\circ}$C, which is consistent with the TEM investigation (Figure A5.3g), but the NW connectivity is still mostly preserved. As shown in the cross-section SEM images of the NW photoelectrodes (insets of Figure A5.4b–4f), the thickness of the annealed hematite NW films increases from 150 nm to 300, 400, 500, and 550 nm as the number of blading operations increases from 8 to 18, 30, 40, and 55, respectively. Top-down view SEM images of Figure A5.4b–4f also reveal different coverage of hematite NW films on FTO substrate for different film thicknesses. The photoelectrode with 150 nm film thickness (Figure A5.4b) is not completely covered by NWs; some FTO surface is clearly exposed in comparison with the SEM image of the bare FTO substrate shown in Figure A5.4a. As more

NWs are added, the coverage increases and NWs start to pile up on top of each other when film thickness exceeds ~400 nm.

We measured the water oxidation photocurrent density as a function of the applied bias voltage for these hematite NW photoanodes with different thicknesses and coverage. Photocurrent measurements were conducted in a custom-built three-arm PEC cell with hematite NW films on FTO substrates as the working electrodes, Ag/AgCl electrode (with 3 M NaCl aqueous solution, E = 0.2094 V vs. reversible hydrogen electrode potential, RHE) as the reference electrode and a platinum mesh as the counter electrode in 1 M NaOH aqueous electrolyte (pH = 13.6). The samples were illuminated from the back side (the glass side) with simulated sunlight from a Xenon lamp solar simulator (1000 W, Newport) equipped with an AM 1.5G filter resulting in a power intensity of 100 mW/cm^2 and an excitation area of 0.13 cm^2. A potentiosat (SP-200, Biologic) was used to sweep the bias potential between –0.5 V and 0.7 V vs. Ag/AgCl at a scan rate of 10 mV/s while the corresponding photocurrents were measured. The photocurrent densities (J) for all photoelectrodes are plotted against the potential vs. RHE and displayed in Figure A5.5a. The photocurrent steadily increases as the film thickness increases, until it reaches 400 nm, after which further increase of the hematite NW loading results in the reduction of photocurrent density. This trend is more clearly seen in Figure A5.5b, where the photocurrent density at 1.23 V vs. RHE is plotted against the thickness of the NW films. For photoelectrode with a film thickness of 150 nm, a significant portion of FTO substrate was exposed without the coverage of NWs (Figure A5.4b). This incomplete coverage results in poor light harvesting and thus limits the photocurrent. In addition, because the absorption coefficient of hematite is not very high (1.41×10^5 cm^{-1} at λ = 550 nm, after 800 °C annealing),[13] thin films

cannot absorb the light completely, as evidenced by the semi-transparent lightly colored photoelectrode seen in the inset photograph in Figure A5.5a. Further NW deposition significantly increases the photocurrent density (at 1.23 V vs. RHE) from 0.04 mA/cm^2 for the photoelectrode with 150 nm thickness to 0.26 mA/cm^2 for the one with 400 nm thickness, when most of the substrate was covered by the NWs. However, as the film thickness exceeds 400 nm, the NWs piling atop the other NWs do not have intimate electrical contact with the conductive FTO substrate and the photoexcited carriers have to hop through the entangled NW networks to reach the FTO electrode and thus cannot be effectively collected. Especially, because hematite is known to be a poor semiconductor with low conductivity, low mobility, fast carrier recombination, and small carrier diffusion length, excited carriers from the hematite nanostructures far away from the FTO electrode could quickly recombine before they can be effectively collected to generate photocurrent.[4, 5] In addition, stacking NWs might also prevent the NWs underneath from accessing electrolyte. Because of these factors, hematite photoelectrodes thicker than ~500 nm have lower PEC performance compared to the photoelectrode with intermediate 400 nm thickness. Similar challenges/dilemma in designing nanostructured hematite photoelectrodes have also been identified in previous reports.[4, 13, 16] We believe that to solve such conflicting design requirements (the need to fully absorb the light vs. the effective collection of the carriers), using NW electrodes that are more vertically aligned[10, 27, 28, 30] and/or 3D (heterostructured) nanostructure electrodes[5, 31] would be fruitful directions. Furthermore, the hematite NWs herein were not intentionally doped; intentionally doping the hematite NWs[16, 17, 43] is expected to further improve their properties. Research is underway on integrating these hematite NWs in such improved designs.

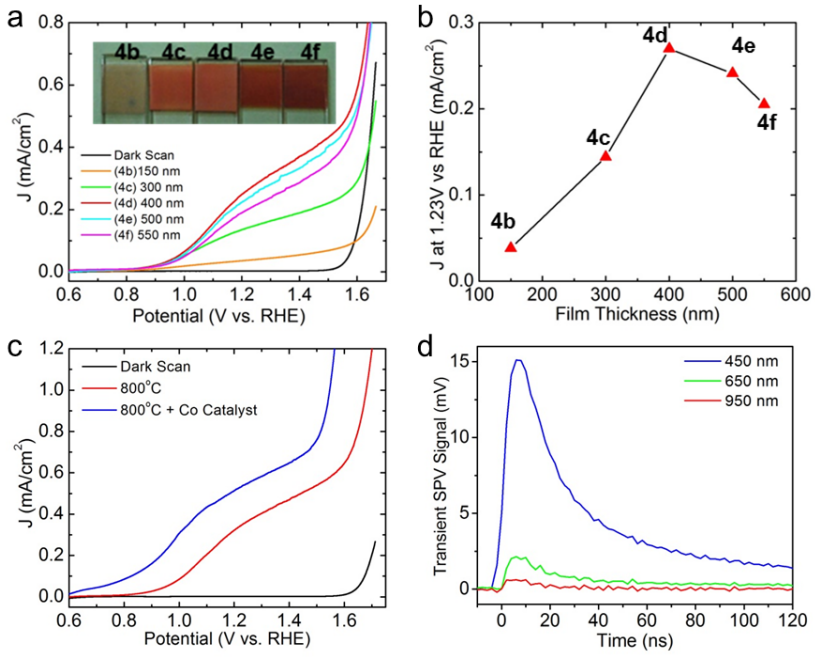

Figure A5.5 | Photoelectrochemical and surface-photovoltage measurements. (a) Photocurrent densities (J) vs. bias voltage (V vs. RHE) under AM 1.5G simulated solar light at 100 mW/cm^2 for hematite NW photoelectrodes with various thickness (corresponding SEM images shown in Figure A5.4b–4f). The inset shows the photographs of these photoelectrodes with increasingly darker red color and decreasing transparency; (b) Photocurrent densities at 1.23 V vs. RHE observed with the hematite NW photoelectrodes in (4b–4f) as a function of the film thickness; (c) The effect of Co catalyst treatment on the photocurrent densities of hematite NW photoelectrodes; (d) TR-SPV signals of the hematite NW photoelectrode measured at three different incident light wavelengths.

With the optimized hematite film thickness, the photoelectrode with the best performance displayed a photocurrent of 0.36 mA/cm^2 at 1.23 V vs. RHE, as shown in Figure A5.5c. The water oxidation onset potential for this and other hematite NW photoelectrodes is around 0.9 V, which is similar to the typical values observed in hematite photoelectrodes without catalysts.[12, 13] The large onset voltage is due to the sluggish oxygen evolution kinetics directly on hematite photoanodes.[4, 24] The kinetics can be improved by modifying the hematite with oxygen evolution catalysts, among which cobalt (Co) catalyst is commonly used and readily prepared.[12] Following the procedure described in the literature,[12] the electrode measured in Figure A5.5c was impregnated with cobalt catalyst. Briefly, the hematite electrode after photoelectrochemical measurement was first rinsed thoroughly with deionized (DI) water to remove NaOH and dried in a stream of nitrogen. An aqueous solution of $Co(NO_3)_2$ (10 mM) was dropcasted on the surface of hematite NW photoelectrodes with the amount equal to 10 μL per 1 cm^2 of the surface area. The photoelectrode was rinsed with DI water again after a few seconds. The photoelectrode was treated by Co catalyst twice and measured again. Figure A5.5c shows that the photocurrent onset potential shifts about 130 mV to the negative, which is slightly higher than the 80 mV cathodic shift previously reported for other nanostructures.[4, 12] As a result of this cathodic shift, the photocurrent density at 1.23 V vs. RHE increases to 0.54 mA/cm^2, which is comparable to previously reported values obtained on solution-processed hematite photoelectrodes that are not intentionally doped.[13, 17] Further cobalt treatments led to a slight decrease in performance.

The hematite NW photoelectrodes were further studied by time-resolved surface photovoltage (TR-SPV) technique (see experimental details in the Supporting Information). SPV

is a contactless technique that can reveal information on charge separation at the surface of a material.[49] In TR-SPV, the sample is illuminated with brief pulses of light from a pulsed laser; charge separation at the interface generates a change in surface potential that can be sensed using a pickup electrode located in close proximity. The measurements were performed under ambient conditions in a capacitor-like arrangement that has been described previously.[50] The recorded transient TR-SPV signals of the hematite electrode sample measured in air using three different incident light wavelengths (Figure A5.5d) show a rise of the signal followed by a decay that can be fit to a multiple exponential. When the SPV measurement was performed at a series of wavelengths, the peak amplitude of the transients matched the UV/Vis absorption spectrum of the film. The sign of the SPV signal indicates an accumulation of positive charges at the surface of the electrode.[51-53] Most semiconductors have their surface Fermi levels pinned approximately near the middle of the bandgap; for an n-type semiconductor, this leads to upward band-bending near the surface, and an accumulation of holes near the surface upon excitation with above-bandgap light. Thus, the sign of the signal observed in the TR-SPV measurements confirms that the converted hematite NWs are n-type. A biexponential fit using $SPV(t) = A_1e^{-k_1t} + A_2e^{-k_2t}$ yielded time constants of ~12 ns and ~80 ns. Since SPV studies on α-Fe_2O_3 photoelectrodes have rarely been reported before[54] to our knowledge, little is known about the time scale for surface charge trapping and/or other charge-transfer events at the surface. However, the SPV data clearly demonstrate that upon illumination there is a net transfer of electron density from the surface to the bulk.

A5.4 Summary and outlooks

In summary, we have designed and achieved the facile solution growth of α-$FeF_3 \cdot 3H_2O$ NWs on a large scale by following the approach of dislocation-driven NW growth. The as-synthesized α-$FeF_3 \cdot 3H_2O$ NWs can be readily converted into porous semiconducting α-Fe_2O_3 (hematite) NWs. The converted thinner α-Fe_2O_3 NWs (typically <100 nm in diameter) preserve their single crystallinity, while thicker ones (typically >100 nm in diameter) become multiple polycrystalline aggregates yet with their 1D morphology maintained. Furthermore, we have demonstrated the application of nanostructured photoelectrodes prepared from the converted hematite NWs in PEC water splitting. To fully address the conflicting requirements to fully absorb the light vs. the effective collection of carriers, we believe that further research efforts in designing NW hematite photoelectrodes should be focused on using more vertically aligned NW electrodes, 3D/heterostructured nanostructured electrodes, and developing strategies to intentionally dope the hematite NWs to improve their photocatalytic efficiency. The converted hematite NWs enjoy the advantages of low cost, large quantity, and high aspect-ratio, all of which make photoelectrode preparation easier and cheaper, and could greatly benefit applications using hematite-based materials for PEC water splitting. More broadly, the convenient and scalable conversion from metastable hydrated fluoride NWs to oxide NWs demonstrates a potentially versatile and low-cost strategy to make NWs of other useful Fe-based materials in large quantity with their single crystallinity preserved, which may enable the large scale renewable energy applications of these unconventional abundant materials.

A5.5 References

1. Wadia, C., Alivisatos, A. P., Kammen, D. M., Materials Availability Expands the Opportunity for Large-Scale Photovoltaics Deployment. Environ. Sci. Technol. **43,** 2072-2077 (2009).

2. Lewis, N. S., Nocera, D. G., Powering the planet: Chemical challenges in solar energy utilization. Proc. Natl. Acad. Sci. USA **103,** 15729-15735 (2006).

3. Lewis, N. S., Toward cost-effective solar energy use. Science **315,** 798-801 (2007).

4. Sivula, K., Le Formal, F., Grätzel, M., Solar Water Splitting: Progress Using Hematite (α-Fe2O3) Photoelectrodes. ChemSusChem **4,** 432-449 (2011).

5. Lin, Y., et al., Hematite-based solar water splitting: challenges and opportunities. Energy Environ. Sci. (2011).

6. Ennaoui, A., et al., Iron disulfide for solar energy conversion. Solar Energy Materials and Solar Cells **29,** 289-370 (1993).

7. Badway, F., Pereira, N., Cosandey, F., Amatucci, G. G., Carbon-Metal Fluoride Nanocomposites. Structure and electrochemistry of FeF_3:C. J. Electrochem. Soc. **150,** A1209-A1218 (2003).

8. Baxter, J., et al., Nanoscale design to enable the revolution in renewable energy. Energy Environ. Sci. **2,** 559-588 (2009).

9. Nozik, A. J., Nanoscience and Nanostructures for Photovoltaics and Solar Fuels. Nano Lett. **10,** 2735-2741 (2010).

10. Hochbaum, A. I., Yang, P. D., Semiconductor Nanowires for Energy Conversion. Chem. Rev. **110,** 527-546 (2010).

11. Szczech, J. R., Jin, S., Nanostructured silicon for high capacity lithium battery anodes. Energy Environ. Sci. **4,** 56-72 (2011).

12. Kay, A., Cesar, I., Grätzel, M., New Benchmark for Water Photooxidation by Nanostructured α-Fe2O3 Films. J. Am. Chem. Soc. **128,** 15714-15721 (2006).

13. Sivula, K., et al., Photoelectrochemical Water Splitting with Mesoporous Hematite Prepared by a Solution-Based Colloidal Approach. J. Am. Chem. Soc. **132,** 7436-7444 (2010).

14. Brillet, J., Grätzel, M., Sivula, K., Decoupling Feature Size and Functionality in Solution-Processed, Porous Hematite Electrodes for Solar Water Splitting. Nano Lett. **10,** 4155-4160 (2010).

15. Lin, Y., Zhou, S., Sheehan, S. W., Wang, D., Nanonet-Based Hematite Heteronanostructures for Efficient Solar Water Splitting. J. Am. Chem. Soc. **133,** 2398-2401 (2011).

16. Wang, G., et al., Facile Synthesis of Highly Photoactive α-Fe_2O_3-Based Films for Water Oxidation. Nano Lett. **11,** 3503-3509 (2011).

17. Ling, Y., et al., Sn-Doped Hematite Nanostructures for Photoelectrochemical Water Splitting. Nano Lett. **11,** 2119-2125 (2011).

18. Gonçalves, R. H., Lima, B. H. R., Leite, E. R., Magnetite Colloidal Nanocrystals: A Facile Pathway To Prepare Mesoporous Hematite Thin Films for Photoelectrochemical Water Splitting. J. Am. Chem. Soc. **133,** 6012-6019 (2011).

19. Itoh, K., Bockris, J. O. M., Thin Film Photoelectrochemistry: Iron Oxide. J. Electrochem. Soc. **131,** 1266-1271 (1984).

20. Bosman, A. J., Vandaal, H. J., Small-Polaron Versus Band Conduction in Some Transition-Metal Oxides. Adv. Phys. **19,** 1-117 (1970).

21. Cherepy, N. J., et al., Ultrafast Studies of Photoexcited Electron Dynamics in γ- and α-Fe_2O_3 Semiconductor Nanoparticles. J. Phys. Chem. B **102,** 770-776 (1998).

22. Kennedy, J. H., Frese, J. K. W., Photooxidation of Water at alpha-Fe_2O_3 Electrodes. J. Electrochem. Soc. **125,** 709-714 (1978).

23. Barroso, M., et al., The Role of Cobalt Phosphate in Enhancing the Photocatalytic Activity of α-Fe_2O_3 toward Water Oxidation. J. Am. Chem. Soc. **133,** 14868-14871 (2011).

24. Zhong, D. K., Gamelin, D. R., Photoelectrochemical Water Oxidation by Cobalt Catalyst ("Co−Pi")/ α-Fe_2O_3 Composite Photoanodes: Oxygen Evolution and Resolution of a Kinetic Bottleneck. J. Am. Chem. Soc. **132,** 4202-4207 (2010).

25. Zhong, D. K., et al., Photo-assisted electrodeposition of cobalt-phosphate (Co-Pi) catalyst on hematite photoanodes for solar water oxidation. Energy Environ. Sci. **4,** 1759-1764 (2011).

26. Tilley, S. D., Cornuz, M., Sivula, K., Grätzel, M., Light-Induced Water Splitting with Hematite: Improved Nanostructure and Iridium Oxide Catalysis. Angew. Chem. Int. Ed. **49,** 6405-6408 (2010).

27. Boettcher, S. W., et al., Energy-Conversion Properties of Vapor-Liquid-Solid-Grown Silicon Wire-Array Photocathodes. Science **327,** 185-187 (2010).

28. Boettcher, S. W., et al., Photoelectrochemical Hydrogen Evolution Using Si Microwire Arrays. J. Am. Chem. Soc. **133,** 1216-1219 (2011).

29. Tian, B., Kempa, T. J., Lieber, C. M., Single nanowire photovoltaics. Chem. Soc. Rev. **38,** 16-24 (2009).

30. Kayes, B. M., Atwater, H. A., Lewis, N. S., Comparison of the device physics principles of planar and radial p-n junction nanorod solar cells. J. Appl. Phys. **97,** (2005).

31. Bierman, M. J., Jin, S., Potential applications of hierarchical branching nanowires in solar energy conversion. Energy Environ. Sci. **2,** 1050-1059 (2009).

32. Morin, S. A., Bierman, M. J., Tong, J., Jin, S., Mechanism and Kinetics of Spontaneous Nanotube Growth Driven by Screw Dislocations. Science **328,** 476-480 (2010).

33. Meng, F., Morin, S. A., Jin, S., Rational Solution Growth of α-FeOOH Nanowires Driven by Screw Dislocations and Their Conversion to α-Fe_2O_3 Nanowires. J. Am. Chem. Soc. **133,** 8408-8411 (2011).

34. Haynes, W. M., Physcial Constants of Inorganic compounds, CRC Handbook of Chemistry and Physics. 91st ed. 2010).

35. Hocking, R. K., et al., Fe L-Edge X-ray Absorption Spectroscopy Determination of Differential Orbital Covalency of Siderophore Model Compounds: Electronic Structure Contributions to High Stability Constants. J. Am. Chem. Soc. **132,** 4006-4015 (2010).

36. Karraker, D. G., Smith, P. K., .alpha.- and .beta.-ferric fluoride trihydrate revisited: crystal structure and iron-57 Moessbauer spectra. Inorg. Chem. **31,** 1118-1120 (1992).

37. Forsberg, K. M., Rasmuson, A. C., Crystal growth kinetics of iron fluoride trihydrate. J. Cryst. Growth **296,** 213-220 (2006).

38. Forsberg, K. M., Rasmuson, A. C., Crystallization of metal fluoride hydrates from mixed hydrofluoric and nitric acid solutions, Part I, Iron (III) and Chromium (III). J. Cryst. Growth **312,** 2351-2357 (2010).

39. Jin, S., Bierman, M. J., Morin, S. A., A New Twist on Nanowire Formation: Screw-Dislocation-Driven Growth of Nanowires and Nanotubes. J. Phys. Chem. Lett. **1,** 1472-1480 (2010).

40. Bierman, M. J., et al., Dislocation-Driven Nanowire Growth and Eshelby Twist. Science **320,** 1060-1063 (2008).

41. Moon, G. D., et al., Chemical transformations of nanostructured materials. Nano Today **6,** 186-203 (2011).

42. Vayssieres, L., Beermann, N., Lindquist, S.-E., Hagfeldt, A., Controlled Aqueous Chemical Growth of Oriented Three-Dimensional Crystalline Nanorod Arrays: Application to Iron(III) Oxides. Chem. Mater. **13,** 233-235 (2001).

43. Lukowski, M. A., Jin, S., Improved Synthesis and Electrical Properties of Si-Doped α-Fe_2O_3 Nanowires. J. Phys. Chem. C **115,** 12388-12395 (2011).

44. Benjelloun, D., et al., Anisotropy of the Electrical-Properties of Iron-Oxide α-Fe_2O_3. Mater. Chem. Phys. **10,** 503-518 (1984).

45. Li, Y. G., Tan, B., Wu, Y. Y., Freestanding mesoporous quasi-single-crystalline Co_3O_4 nanowire arrays. J. Am. Chem. Soc. **128,** 14258-14259 (2006).

46. Li, Y. G., Wu, Y. Y., Critical Role of Screw Dislocation in the Growth of $Co(OH)_2$ Nanowires as Intermediates for Co_3O_4 Nanowire Growth. Chem. Mater. **22,** 5537-5542 (2010).

47. Tian, Z. R., et al., Manganese oxide mesoporous structures: Mixed-valent semiconducting catalysts. Science **276,** 926-930 (1997).

48. Penfold, B. R., Taylor, M. R., The crystal structure of a disordered form of iron(II) fluoride tetrahydrate. Acta Crystallogr. **13,** 953-956 (1960).

49. Kronik, L., Shapira, Y., Surface photovoltage phenomena: theory, experiment, and applications. Surf. Sci. Rep. **37,** 1-206 (1999).

50. Benson, M. C., et al., Modular “Click” Chemistry for Electrochemically and Photoelectrochemically Active Molecular Interfaces to Tin Oxide Surfaces. ACS Appli. Mater. Interfaces **3,** 3110-3119 (2011).

51. Peng, L., et al., Synthesis, photoelectric properties and photocatalytic activity of the Fe_2O_3/TiO_2 heterogeneous photocatalysts. Phys. Chem. Chem. Phys. **12,** 8033-8041 (2010).

52. Wei, X., et al., A study of the dynamic properties of photo-induced charge carriers at nanoporous TiO_2/conductive substrate interfaces by the transient photovoltage technique. Nanotechnology **19,** (2008).

53. Mahrov, B., et al., Photovoltage study of charge injection from dye molecules into transparent hole and electron conductors. Appl. Phys. Lett. **84,** 5455-5457 (2004).

54. Peng, L., et al., Surface photovoltage characterization of an oriented α-Fe_2O_3 nanorod array. Chem. Phys. Lett. **459,** 159-163 (2008).

APPENDIX 6

Facile Post-Growth Doping of Nanostructured Hematite Photoanodes for Enhanced Photoelectrochemical Water Oxidation

---

This Appendix was originally published in *Energy Environ. Sci.* **6,** 500-512 (2013), in collaboration with R. Franking, M. A. Lukowski, F. Meng, Y. Tan, R. J. Hamers, and S. Jin.

A6.1 Abstract

We report a facile approach to perform post-growth doping of hematite (α-Fe_2O_3) nanostructures by depositing titanium (Ti) precursor solution and subsequent annealing in air. Using hematite nanowire photoanodes on fluorine doped tin oxide (FTO) glass substrates as a model system, the doping conditions were carefully optimized and highly photoactive hematite photoanodes were prepared at a more practically acceptable temperature of 650–700 °C than the ≥800 °C commonly used in previous works. A combination of microstructural characterization, elemental analysis, photoelectrochemical (PEC) measurements, and electrochemical impedance spectroscopy (EIS) analysis were employed to confirm the distribution of Ti atoms in hematite nanostructures and the role of Ti dopants in enhancing the photocurrent of hematite photoanodes. It was found that the Ti-treatment increases the donor concentration of hematite by about 10 fold and facilitates majority carrier transport and collection, which may account for the performance enhancement. Moreover, EIS measurements under illumination and Mott-Schottky analysis clearly showed that Ti dopants interact with the surface trap states of hematite, suggesting that surface passivation may also contribute to the improved PEC performance. This facile post-growth doping method can be applied to other hematite nanostructures such as electrochemically deposited hematite films and expanded to other dopants such as zirconium (Zr).

A6.2 Broader Context

Photoelectrochemical (PEC) water splitting based on earth-abundant semiconductor materials is a promising approach to harvest and store solar energy and may potentially supply the world's energy demand with a clean and sustainable chemical fuel (H_2). Hematite (rust) is an

attractive photoanode material due to its high theoretical solar-to-hydrogen efficiency (16.8% under AM 1.5 G illumination), a suitable valence band position for water oxidation, excellent stability, and low material cost. However, hematite severely suffers from its non-optimal physical and surface properties. Even though nanostructures and doping during hematite material growth have been commonly used to improve the PEC performance of hematite photoanodes, facile post-growth doping of hematite and its impact on the electrical and surface properties and thus the PEC performance of hematite have been rarely investigated. Herein a simple doping strategy via dopant precursor solution soaking followed by thermal annealing has been demonstrated. This strategy could be generally applicable to various existing hematite nanostructures. Furthermore, electrochemical studies lead to new insights into the PEC water oxidation reaction at the surface of doped hematite, which suggest future research directions for further improving the overall PEC performance of hematite photoanodes.

A6.3 Introduction

Efficient utilization of solar energy requires the development of technologies that can effectively harvest and store solar energy in a cost-effective fashion using earth-abundant materials.[1, 2] Photoelectrochemical (PEC) water splitting is a promising approach to convert solar energy and store it in the form of chemical energy in H_2 and O_2.[2, 3] High performance PEC systems based on single-crystalline III-V semiconductors have been demonstrated in laboratories,[4, 5] but they are neither chemically stable nor economically viable to be utilized in practical applications. Earth-abundant metal oxides with intermediate bandgaps such as α-Fe_2O_3 (hematite)[6-25] and WO_3[26, 27] have therefore been intensively investigated as alternative photoelectrode materials in recent years with the hope of enabling cost-effective PEC devices

with reasonable efficiency. Specifically, hematite has a favorable bandgap of about 2.2 eV allowing a maximum theoretical solar-to-hydrogen efficiency of 16.8% under AM 1.5G illumination.[18] Other advantages of hematite include its suitable valence band edge position for water oxidation reaction, excellent stability against photocorrosion and chemical corrosion in alkaline electrolytes, and low toxicity.[6] These attributes make hematite a promising photoanode material. However, hematite suffers from low absorptivity near the bandgap ($\alpha^{-1} \sim 0.12$ μm at λ = 550 nm),[28] low carrier mobility (< 1 $cm^2\ V^{-1}\ s^{-1}$),[29] short minority carrier life time (~10 ps)[30] and diffusion length (~2–4 nm),[31] a large requisite external bias,[6] and complex surface chemistry,[19] which has so far limited its PEC performance. Nanostructuring has been commonly used to enhance the PEC performance of hematite photoanodes, which benefits from the decoupled light absorption and photo-generated carrier collection.[6, 18, 32, 33] Significantly improved photocurrents have been reported on nanostructured hematite photoanodes,[8, 10, 13, 14, 17] even though the enhancement in photovoltage (or potential at the photocurrent onset) remains relatively small. We have developed a simple thermal treatment procedure for converting solution-synthesized α-$FeF_3 \cdot 3H_2O$ nanowires (NWs) to three-dimensional (3D) photoanodes made of networks of hematite NWs on fluorine-doped tin oxide (FTO) substrates (Figure A6.1a).[23] Respectable photocurrent densities comparable to previously reported values[9, 24] for solution-processed nanostructured hematite photoelectrodes without intentional doping have been demonstrated after an indispensable thermal annealing step at 800 °C (Figure A6.1a). It was suggested that such high temperature annealing induces Sn doping of hematite from FTO substrates. However, not only is this high temperature treatment detrimental to glass substrates but also further enhancement of the PEC performance would be desirable.

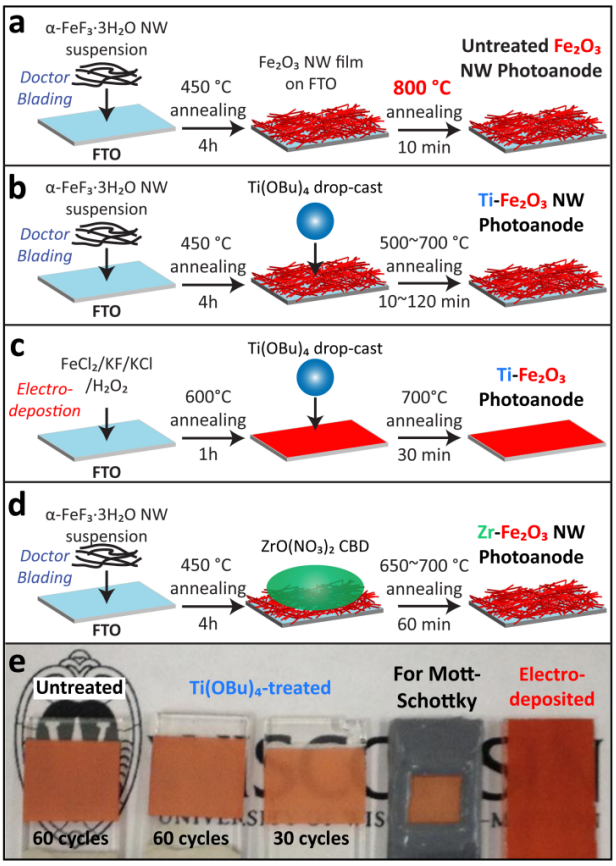

Figure A6.1. Preparation schemes for: a) an untreated hematite NW photoanode, b) a Ti-treated hematite NW photoanode, c) a Ti-treated electrodeposited hematite film photoanode, and d) a Zr-treated hematite NW photoanode; and e) a photograph showing typical photoanodes. Films shown from left to right include untreated and Ti-treated NW films with 60 cycles of doctor blading, a Ti-treated NW film with 30 cycles of doctor blading, a typical NW film after epoxy encapsulation for Mott-Schottky measurements, and a Ti-treated electrodeposited hematite film.

Elemental doping also plays critical role in improving the PEC properties of hematite photoanodes. Dopants such as Si,[8, 34-36] Ge,[37, 38] Ti,[13, 39] Sn,[9, 40] Mg,[16, 37, 41] Mo,[42] Cr,[42] Zr,[43] Pt,[44]

Al,[45] Zn,[46] Nb,[47] and co-doping of Ti and Mg[48] have been investigated for hematite thin films or nanostructures synthesized through a variety of methods, such as hydrothermal growth, electrodeposition, chemical vapor deposition, atomic layer deposition, and other vapor deposition methods. While most of the dopants lead to modest improvement in the PEC performance of hematite photoanodes, Si,[8, 34, 49] Ti[13] and Sn[14] doping has been shown to greatly increase the photocurrent and lead to better onset potential of photoresponse. In most of these reports, the dopants are incorporated into (nanostructured) hematite during the process of material growth, which typically allows a certain degree of control over the doping level and sometimes unintentionally alter the material growth to induce favorable characteristics such as small feature sizes,[8, 14] increased surface area,[8] and preferential orientation of the hematite nanostructure along the more conductive [110] axis[50] vertical to the underlying substrate.[8] In contrast, very few post-growth doping methods have been explored.[35] Post-growth doping is interesting as a simple and complementary doping strategy that does not depend on the methods of hematite synthesis, and may be conveniently applied to any arbitrary hematite nanostructures to further improve their PEC performance.

We herein report a facile method for post-growth doping of hematite nanostructures *via* a brief exposure to titanium (Ti) or zirconium (Zr) dopant precursor solutions and subsequent annealing at 650–700 °C in air (Figure A6.1b-d). Application of this surprisingly simple strategy to our previously developed hematite NW photoanodes[23] as a model system enabled hematite photoelectrodes (Figure A6.1b,d) with greatly improved photocurrents without the need of the high temperature (≥800 °C) annealing commonly used in previous work.[9, 14, 24] Furthermore, we performed microstructural characterization, elemental analysis, and electrochemical impedance

spectroscopy (EIS) on the treated hematite photoanodes to confirm the elemental doping and understand the correlation with the improved PEC performance and surface chemistry of hematite. We also showed that this simple method can be generally applicable to other hematite nanostructures by doping electrochemically deposited nanostructured hematite films with Ti (Figure A6.1c). The combined PEC and EIS results obtained from the hematite photoanodes with different nanostructures and/or different dopants also suggest that future research should be focused on understanding the surface trap states and developing effective passivation approach to further improve the overall PEC performance of hematite.

A6.4 Experimental section

Unless otherwise specified, all reagents were purchased from Sigma-Aldrich and used as received. General schemes for the preparations of various hematite photoelectrodes are shown in Figure A6.1 along with a photograph of the resulting films.

Nanowire synthesis and 3D nanostructured hematite photoelectrode preparation

Nanowire films of hematite were prepared based on a procedure published previously that uses the conversion of α-$FeF_3 \cdot 3H_2O$ NWs to hematite through thermal oxidation in air (Figure A6.1a).[23] First, α-$FeF_3 \cdot 3H_2O$ NWs were synthesized by first mixing 7.5 mL of ethanol and 2.0 mL of 48% HF in a 15 mL plastic centrifuge tube. *Caution! HF is highly corrosive and proper safety precautions must be followed.* Using an Eppendorf pipet, 0.5 mL of a freshly prepared 266 mM $Fe(NO_3)_3 \cdot 9H_2O$ ethanol solution was quickly added to the centrifuge tube at room temperature. After sealing the centrifuge tube, the resulting colorless solution was then gently mixed by hand and heated in an oven at 60 °C for 24 h. The white cloudy precipitates were

collected by centrifugation, washed twice with dry ethanol and dried under vacuum at room temperature.

The clumps of dried NWs were gently broken up with a pipet tip and mixed in ethanol at a concentration of 5 mg mL^{-1}. The mixture was sonicated for approximately 2 min until a uniform suspension was made. Excess sonication can lead to breaking and dissolution of the NWs. The resulting dispersion was deposited onto fluorine doped tin oxide (FTO) glass (Hartford, TEC 15) via 30 cycles of doctor blading using 40 μm thick Scotch magic tape (3M) as a spacer. During each cycle, 10 μL of suspension was applied over an area 1 cm wide by 10 cm long. After blading, the FTO substrate was cut into 10 pieces, each with a 1 cm by 1 cm NW film area. This pooled sample preparation and splitting scheme ensures the consistency of the performance comparison made in this work. The white films were heated in air at 450 °C for 4 h in a box furnace to result in films with rustic red color, as shown in Figure A6.1e. For the highest performing devices, thicker films were prepared by performing a second round of 30 blading cycles and oxidation at 450 °C, giving 60 cycles total. The two separate oxidation steps were needed to prevent macroscopic cracking of these thicker films during oxidation.

Electrodeposition of hematite films

Electrodeposited hematite films were prepared following the procedures reported by Schrebler et al.[51] Briefly, films were deposited onto an FTO glass working electrode using a Biologic SP–200 potentiostat cycling from –0.52 to +0.41 V at 100 mV sec^{-1} for a total of 100 cycles from an aqueous solution containing 5 mM $FeCl_3 \cdot 6H_2O$, 5 mM KF, 1 M H_2O_2 and 0.1 M KCl. Platinum mesh and a Ag/AgCl electrode (1 M KCl) were used as the counter and reference

electrodes, respectively. After electrodeposition the films were rinsed with deionized water, blown dry and heated to 600 °C for 4 h with a ramp rate of 2 °C min^{-1}.

Ti and Zr doping treatment and annealing

In a typical procedure, we used a simple drop–casting method to treat the hematite films with a Ti precursor solution. A 3 μL drop of titanium n-butoxide [$Ti(OBu)_4$] solution in ethanol (100 mM) was placed in the center of the hematite film (1 cm^2) and allowed to dry in air (Figure A6.1b, c). The films were then annealed with no further rinsing or treatment. For the Zr treatment by chemical bath deposition, the hematite films were placed in a 100 mM $ZrO(NO_3)_2$ solution in ethanol for 10 min at 60 °C (Figure A6.1d). After deposition, the Zr-treated samples were rinsed thoroughly with ethanol and blown dry. For annealing after the doping treatment, all hematite samples were placed on a ceramic plate in a preheated box furnace in air at the desired temperatures for 10 min to 2 h (typically 700 °C for 1 h). Then the samples were removed from the furnace still on the hot ceramic plate and allowed to cool quickly to room temperature.

Structural characterization

X–ray photoelectron spectroscopy (XPS) was carried out using a monochromatic Al Kα source (nominally 1486.6 eV photo energy) with an analyzer resolution of 0.2 eV and electron take off angle of 45°. Peak positions were calculated after shifting the carbon (1s) peak to 284.8 eV and fitting the raw data to Voigt functions after a background subtraction. Scanning electron microscopy (SEM) was performed using a LEO Supra55 VP microscope on the nanostructured hematite films on FTO. Energy dispersive x–ray spectroscopy (EDS) measurements were taken on a LEO 1530 SEM with an accelerating voltage of 15 kV. High resolution transmission

electron microscopy (HRTEM) was taken using an aberration–corrected FEI Titan scanning transmission electron microscope (STEM) in the TEM mode. Samples for both EDS measurements and TEM were dry transferred to a 300 mesh lacey carbon TEM sample grid (Ted Pella) by dragging the grid across the surface of the entangled NW films. Raman spectroscopy is performed using a Horiba Jobin Yvon Labram Aramis Raman confocal microscope.

Photoelectrochemical measurements and electrochemical analysis

All photoelectrochemical measurements were carried out in a 1 M KOH (pH = 13.6) electrolyte using a BioLogic SP–200 potentiostat with a platinum mesh counter electrode and a Ag/AgCl (1 M KCl) reference electrode. Current–Voltage (IV) curves were swept at 50 mV s^{-1} from –0.5 to +0.6 V *vs* Ag/AgCl/3M NaCl. Curves were first swept in the dark to insure no oxidative side reactions then under solar AM 1.5G illumination (100 mW cm^{-2}) using a Xenon lamp solar simulator (1000 W, Newport). The illumination spot size was set by an aperture to 0.125 cm^2. Separate measurements were taken for illuminating the front and back side of the working electrodes. In order to improve the consistency of the data, only electrodes doctor bladed at the same time (from the same set of ten substrates) are directly compared and plotted together. Incident photon-to-current efficiency (IPCE) measurements were performed using a QTH Lamp (250 W, Newport) coupled with a monochromator (SpectroPro®-275, Acton Research Corporation).

For electrode fabrication for EIS and Mott–Schottky analysis, the bare FTO above the hematite films was coated with a silver paint (Ted Pella, Pelco® Conductive Silver) to improve the conductivity and electrical contact with the potentiostat alligator clips. The electrodes were

then encapsulated in epoxy (Loctite, 9460F) to prevent electrolyte contact with any bare FTO or silver paint, as shown in Figure A6.1e (4^{th} photographs from the left). An open area of approximately 0.25 cm^2 in the center of the hematite film was defined by the epoxy. Mott–Schottky calculations were derived from impedance measurements in the dark sweeping from –1.0 to +0.5 V *vs* Ag/AgCl with 50 mV increments. The resulting impedance data were well fit using Randles circuit models between 1–1500 Hz to determine the space charge capacitance at each potential. In order to calculate donor concentrations, a dielectric constant of 32 for hematite[52] was used and the active electrode areas were estimated using the adsorption of the azo dye Orange II.[8, 53] Unfortunately since the dye adsorbed strongly to the epoxy, area estimates had to be derived from parallel films prepared in a similar manner without epoxy encapsulation. We must caution that there may be a systematic error in the absolute values for carrier concentration due to the uncertainties in the dielectric constant and true active electrode areas. However relative trends compared within this work are highly repeatable and consistent. The surface state capacitances were calculated following a method described by Klahr et al.[19] Impedance data was taken using a voltage sweep from –0.5 to 0.5 V *vs* Ag/AgCl under AM 1.5G illumination (through the FTO side of the electrode) between 100 mHz and 1500 Hz. Higher frequencies appeared to show significant capacitive response from the exposed FTO under the NWs or morphological effects, and more consistent fits were achieved by excluding this region from the fitting.

A6.5 Results

Physical and Structural Analysis of the $Ti(OBu)_4$ Treated Hematite Nanowire Films

We first studied the morphological and chemical effects of the $Ti(OBu)_4$ drop-casting treatment and subsequent annealing on the hematite NW films. The $Ti(OBu)_4$ treated films were prepared following the scheme depicted in Figure A6.1b with 30 cycles of doctor blading. Representative SEM images comparing an untreated NW film annealed at 700 °C (Figure A6.2a) with a film treated with 100 mM $Ti(OBu)_4$ and annealed at 700 °C for 1 h (Figure A6.2b) show very similar morphologies. In both images the underlying NW networks can clearly be identified and no additional deposits or differences in morphology can be distinguished by SEM after $Ti(OBu)_4$ treatment. We conclude that the treatment process does not significantly alter the morphology of the nanostructures.

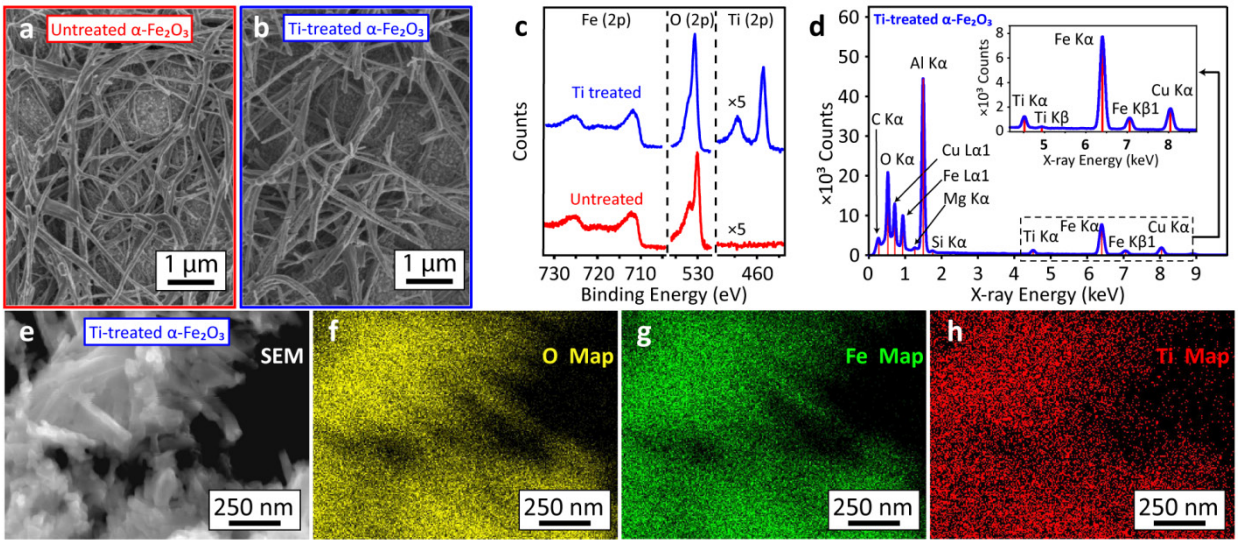

Figure A6.2. SEM micrographs of the a) untreated and b) $Ti(OBu)_4$ treated films. c) XPS comparing the Fe (2p), O (2p) and Ti (2p) binding energies of untreated (red) and treated (blue)

samples. d) representative SEM-EDS spectrum and e) SEM-EDS mapping of $Ti(OBu)_4$ treated NW aggregates to show the spatial distribution of O, Fe and Ti, respectively (f-g).

In order to confirm the presence of the Ti dopant atoms after treatment, we performed XPS, EDS, and EDS mapping experiments on similar untreated and treated hematite NW films. XPS spectra (Figure A6.2c) for the untreated and treated samples show Fe(2p) peaks at 710.9 ± 0.2 and 711.3 ± 0.2 eV, respectively. These peaks are consistent with Fe^{3+} ions in hematite.[54] The major O(1s) peak appears at 530.1 ± 0.2 eV for the untreated sample and 530.6 ± 0.2 eV for the $Ti(OBu)_4$ treated sample, also consistent with hematite. However, more detailed analysis of the O(1s) peak and Fe to O ratios is complicated by the presence of the underlying FTO. The untreated sample does not show any Ti within the detection limit of the measurement taken. The treated sample shows a clear Ti(2p) peak at 458.6 ± 0.2 eV. The position of this peak is consistent with Ti in a fully oxidized Ti^{4+} state.[55] Atomic ratios between Ti and Fe are difficult to interpret since some Ti may also be deposited directly onto the FTO.

Furthermore, we used EDS (Figure A6.2d) measurements to overcome the spatial limitations of XPS. We found the Ti to Fe ratios ranging from 0.02 to 0.1 scanning across five different areas in the Ti-treated sample; no Ti was detected in the untreated sample. SEM-EDS mapping (Figure A6.2e–h) shows a Ti signal that spatially correlates with the Fe and O from the hematite NWs. Similar results were achieved using STEM-EDS mapping on a single NW. Since the Ti signal can been seen from all NWs and we do not see significant Ti signal from objects without

Fe, we conclude that while the concentration of the Ti may not be perfectly uniform, it is distributed over the entire NW film and not as discrete particles.

We further analyzed the microstructure of the $Ti(OBu)_4$ treated NWs under HRTEM. TEM of a representative NW (Figure A6.3a) shows a multi-grain structure similar to what we reported previously for hematite NWs annealed at 800 °C.[23] All grains were single-crystalline α-Fe_2O_3. We could tilt to the same high-symmetry $[\bar{1}\bar{2}1]$ zone axis (Figure A6.3b) to take HRTEM images (Figure A6.3c-d), in which continuous lattice fringes matched with α-Fe_2O_3 (hematite, space group $R\bar{3}c$, a = 5.0356 Å, c = 13.7489 Å). Since no additional morphologies or phases were observed over many TEM examinations, we conclude that the NW samples maintained a hematite structure and no (or at least very few) particles of TiO_2 were formed on the surface after the Ti-treatment. This is also supported by the Raman spectroscopy data collected from the untreated and Ti-treated samples, in which only Raman bands of hematite were .

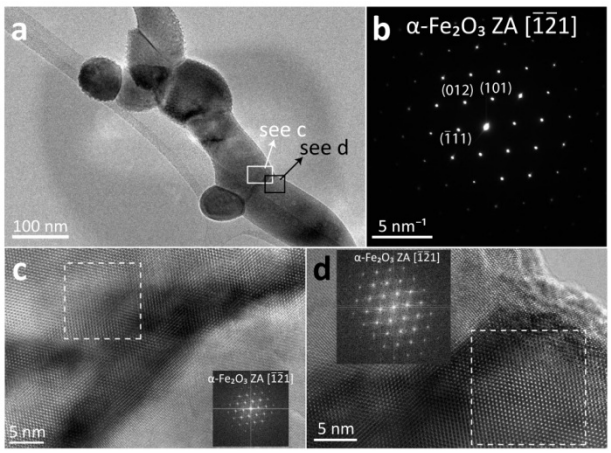

Figure A6.3. a) A representative TEM image of annealed (at 700 °C) hematite NWs dry-transferred from a Ti-doped hematite photoelectrodes; b) a select area electron diffraction

(SAED) pattern showing all NW grains were tilted to $[\bar{1}\bar{2}1]$ zone axis for HRTEM imaging; c) and d) HRTEM images showing lattice fringes of the NW grains labeled in a). The insets are FFT patterns obtained from the area circled by the white box, which match with the SAED pattern in b).

Photocurrent Density Measurements

In order to understand the effect of the Ti-treatment, we compared the water oxidation photocurrent density *vs* potential of thick (60 cycles of doctor blading) hematite NW electrodes with and without $Ti(OBu)_4$ treatment (Figure A6.4a). We measured the photocurrent illuminating from both the FTO side (solid lines) and NW film side (dashed lines). Two untreated samples were measured as controls, one annealed at 650 °C for 1 h (purple) and one annealed at 800 °C for 10 min (green). The Ti-treated sample (blue) was drop cast with 100 mM $Ti(OBu)_4$ and annealed at 650 °C for 1 h. Afterwards, the Ti treated sample was also soaked in a 10 mM $Co(NO_3)_2$ catalyst solution for 10 min and measured again (red), to further improve the photocurrent. The 650 °C control sample shows essentially no photocurrent at 1.23 V *vs* RHE, consistent with our previous work that showed that an 800 °C anneal is necessary for activation.[23] After annealing at 800 °C the sample shows a photocurrent density of 0.12 mA cm^{-2} at 1.23 V *vs* RHE when illuminated through the FTO side while illumination through the NW film side shows only 0.02 mA cm^{-2}. These values are less than those reported previously (0.36 mA cm^{-2})[23] because these films are too thick and not optimized for the 800 °C activation. The drop off in current when illuminating from the film side (the green dash line that overlaps with

the purple lines) may indicate that the electrical connection to the NWs far from the FTO is poor and majority carrier collection is not possible. In contrast, the Ti-treated sample shows a much larger photocurrent density of 0.37 mA cm^{-2} at 1.23 V *vs* RHE when illuminated from the FTO side and it increases to 0.48 mA cm^{-2} when illuminated from the NW film side. The film side current may be greater than the FTO side since it does not suffer from reflective losses at the FTO interface and diffusion of reactants in the electrolyte is more limited deeper in the NW film. The improvement in film side versus FTO side photocurrent after Ti treatment also indicates greatly increased activity of the electrolyte side NWs compared to those from untreated samples. The increased activity of Ti-treated films is also confirmed by the IPCE data, which is mostly consistent with the previous report for Ti-doped hematite prepared via magnetron co-sputtering.[39] These results may suggest improved electrical connection to and majority carrier collection from these outer NWs following doping treatment. After the application of cobalt catalyst, the potential onset shifts approximately 200 mV towards reducing potentials and the film side photocurrent density increases to 0.67 mA cm^{-2} at 1.23 V *vs* RHE. This photocurrent density is a new record for hematite films made from $FeF_3 \cdot 3H_2O$ NWs and these values are highly repeatable—five separate electrodes prepared in similar manner all achieved values between 0.63 and 0.67 mA cm^{-2} after the Ti treatment and $Co(NO_3)_2$ soaking. Overall, we conclude that the $Ti(OBu)_4$ treatment greatly enhances the water oxidation photocurrent density over untreated films and reduces the annealing temperature necessary for activation. Furthermore, the comparison of FTO side versus film side illumination suggests that the treatment improves the majority carrier collection from NWs far from the FTO back contact.

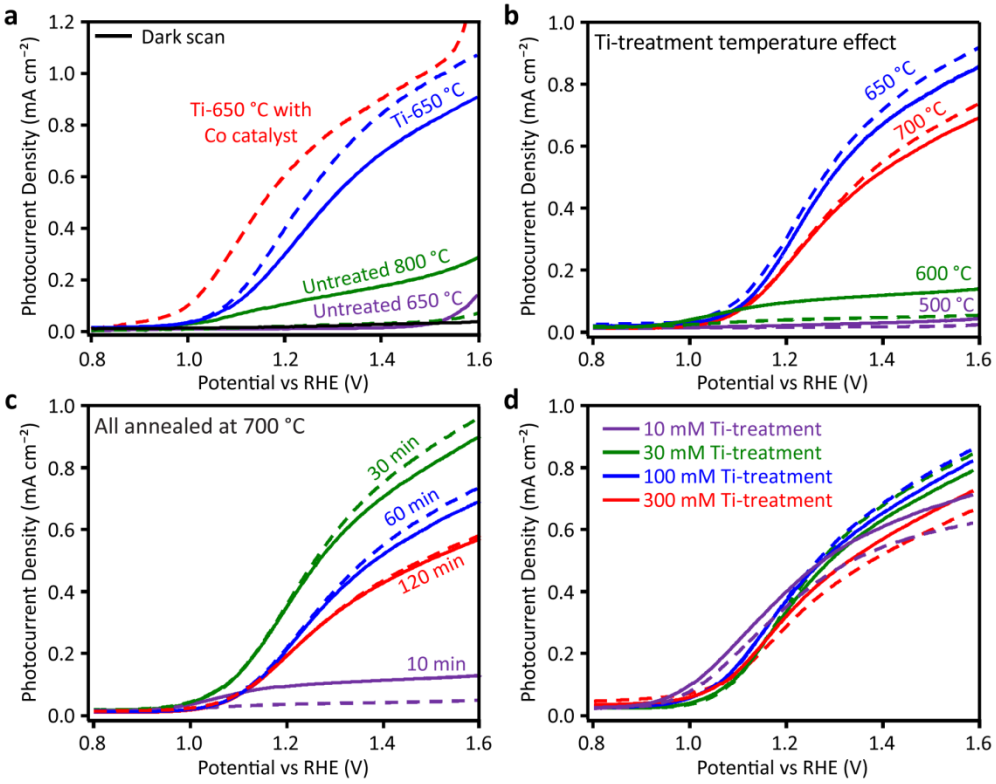

Figure A6.4. Photocurrent densities of hematite NW films measured under AM 1.5 G illumination at a light intensity of 100 mW cm^{-2} and a sweep rate of 50 mV sec^{-1}. Solid lines represent illumination through the FTO side of the samples and dashed lines represent illumination through the NW film side. Data are shown for hematite films: a) treated with 100 mM $Ti(OBu)_4$ and annealed at 650 °C for 1 h (blue), the same film subsequently soaked in 10 mM $Co(NO_3)_2$ for 10 min (red), an untreated film annealed at 650 °C (purple) and at 800 °C for 10 min (green); b) treated with 100 mM $Ti(OBu)_4$ and annealed for 1 h at 500 °C (purple), 600 °C (green), 650 °C (blue), and 700 °C (red); c) treated with 100 mM $Ti(OBu)_4$ and annealed at 700 °C for 10 (purple), 30 (green), 60 (blue), and 120 min (red); and d) annealed at 700 °C for 60 min after treatment with 10 (purple), 30 (green), 100 (blue), and 300 mM (red) $Ti(OBu)_4$.

Since the lower annealing temperature for activation is a key benefit of the Ti treatment, we examined the photocurrent density response curves as a function of annealing temperature for hematite NW films (30 cycles of doctor blading) treated with 100 mM $Ti(OBu)_4$ (Figure A6.4b). The separate films were annealed at 500 °C, 600 °C , 650 °C, and 700 °C for 1 h and again were measured illuminating from both the FTO side (solid lines) and NW film side (dashed lines). The sample annealed at 500 °C shows almost no photocurrent at 0.02 mA cm^{-1} at 1.23 V *vs* RHE from the FTO side and even less from the film side. After annealing at 600 °C the FTO side current increase to 0.10 mA cm^{-2} with the film side still less at 0.04 mA cm^{-2}. If improvement in majority carrier collection is the main source of the increase in photocurrent after Ti treatment, the results at 600 °C are consistent with a slight improvement in overall collection but not enough to allow easy transport of carriers from the electrolyte side NWs. For these films, annealing at 650 °C produced a photocurrent density of 0.35 mA cm^{-2} from the FTO side and 0.39 mA cm^{-2} for the NW side at 1.23 V *vs* RHE. These values are only slightly less than the thicker 60 cycle doctor blade film shown in Figure A6.4a. After annealing at 700 °C for 1h, the current decreases to 0.27 and 0.28 mA cm^{-2} from the FTO and film sides respectively. This decrease in current may result from either a degradation of the FTO glass at these higher temperatures or loss of active area due to sintering of the NW films.[23] The total area measured using an orange II dye adsorption method[8, 53] for representative samples decreases from 10 cm^2 after 650 °C annealing to 3.7 cm^2 after 700 °C annealing. In general, however, our data indicate that after Ti treatment, annealing at temperatures at or above 650 °C for 1 h is sufficient to activate the hematite films for photoelectrochemical water oxidation and 650 °C appears to

balance the need for achieving activation while avoiding negative effects of high temperature annealing.

In order to further zero in on the optimal conditions for the Ti treatment we also explored the effect of annealing time at 700 °C (Figure A6.4c) and the concentrations of the Ti precursor solutions (Figure A6.4d) for 30 cycle NW films. The samples annealed at 700 °C were all treated with 100 mM $Ti(OBu)_4$ and separately annealed for 10, 30, 60, and 120 min. The 10 min annealing time appears to have a similar effect on performance to annealing at a lower temperature. The FTO side photocurrent density is limited to 0.10 mA cm^{-2} with a film side current of 0.04 mA cm^{-2} at 1.23 V *vs* RHE. Annealing for 30 min shows much higher photocurrent densities at 0.42 and 0.43 mA cm^{-2}, illuminating from the FTO and film side respectively. These photocurrent densities are similar to those achieved with a 650 °C anneal for 1 h, suggesting that the shorter anneal time significantly reduces the negative effects of annealing at higher temperatures while still allowing complete activation of hematite. The longer annealing times of 60 and 120 min show gradually decreasing photocurrent with increasing annealing time. Again the decreasing photocurrent is likely due to either the degradation of the FTO glass and/or loss of hematite surface area through sintering. In all cases however, the film side photocurrent is similar to the FTO side suggesting that the majority carrier collection efficiency is similar between the front and back sides of the NW film and that the degradation processes at longer annealing times affect both the front and back sides equally.

We tested 4 different $Ti(OBu)_4$ precursor concentrations: 10 mM, 30 mM, 100 mM, and 300 mM (Figure A6.4d) followed by annealing at 700 °C for 1 h. At 1.23 V *vs* RHE, the 10 mM, 30 mM, and 100 mM treated samples all show fairly similar photocurrent densities ranging from

0.43 to 0.38 mA cm^{-2} including illuminating from either side of the electrodes. At more oxidizing potentials the 10 mM-treated sample shows smaller photocurrent densities than the other samples by as much as 0.25 mA cm^{-2}. However it does appear to have a slightly more reducing photocurrent onset by approximately 80 mV. The film side illumination produces a slightly reduced photocurrent versus the FTO side for the 10 mM treated sample as well, suggesting that the film may not be fully activated by the 10 mM treatment and anneal. Both the 30 mM and 100 mM treated samples show similar photocurrent over the entire potential range measured from both FTO side and film side illumination. This indicates both treatments fully activate the films to similar maximum photocurrent densities. The 300 mM treated sample shows smaller photocurrents above 1 V *vs* RHE compared to the other samples with 0.35 and 0.32 mA cm^{-2} (1.23 V *vs* RHE) illuminating from the FTO and film sides, respectively. Interestingly, the sample shows a photoresponse under film side illumination of almost 0.03 mA cm^{-2} at potentials as low as 0.8 V *vs* RHE, well below the approximately 0.9 V onset of the other samples. TiO_2 is a well-known photooxidation catalyst that shows response at lower potentials.[56, 57] Therefore, even though we do not see evidence for TiO_2 at lower concentrations, this low onset at high concentration of $Ti(OBu)_4$ may suggest the presence of photoactive TiO_2 within the hematite NW film after annealing. The presence of TiO_2 may also explain the reduced photocurrent at higher potentials after 300 mM treatment if the TiO_2 is insulating or otherwise passivating the active hematite surface. We conclude that while the treatment does not appear to be very sensitive to the concentration of $Ti(OBu)_4$, concentration between 30 to 100 mM achieve both high photocurrents and the most complete activation of the hematite films.

Mott–Schottky Analysis of Doped Hematite Films

In order to understand why the Ti treatment enhances the PEC properties, we performed Mott–Schottky analysis in the dark on hematite samples with and without $Ti(OBu)_4$ treatment (Figure A6.5). The control sample without any Ti treatment was annealed at 700 °C for 1 h. Two hematite NW film samples were treated with 100 mM $Ti(OBu)_4$ and annealed at 650 °C or at 700 °C for 1 h. We used a simple Randles circuit model (Figure A6.5a) to fit the impedance data between 1 and 1500 Hz and extract the space-charge capacitance. We then used the Mott–Schottky relationship to determine the donor concentration (N_D) and flat-band potential (V_{fb}):

$$\frac{1}{{C_{sc}}^2} = \frac{2}{q\varepsilon\varepsilon_0 N_D}\left(V - V_{fb} - \frac{kT}{q}\right)$$

where C_{sc} is the space charge capacitance, q is the elementary charge, ε_0 is the permittivity of free space, ε is the dielectric constant of hematite (32),[52] V is the applied potential across the space charge region, k is Boltzmann's constant, and T is the absolute temperature. Plotting $1/{C_{sc}}^2$ *vs* potential (V) should produce linear data with an x–intercept determining the flat-band potential (V_{fb}) and the slope inversely proportional to the donor concentration (N_D).[58]

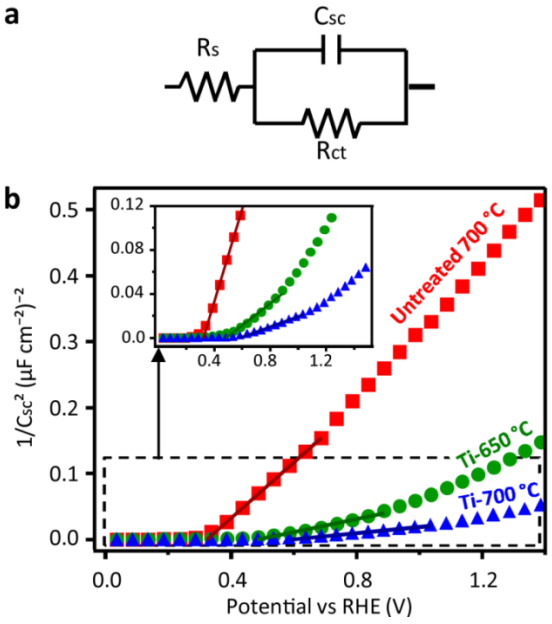

Figure A6.5. a) A diagram of the Randles circuit model used to fit the impedance data between 1 and 1500 Hz and extract the space charge capacitance (C_{sc}). b) Mott-Schottky plots of hematite NW films untreated and annealed at 700 °C (red) and treated with 100 mM $Ti(OBu)_4$ precursor and annealed at 650 °C (green) and 700 °C (blue). Solid lines are the linear fits used to calculate *x*-intercept and slope. The inset shows an expanded region around the treated samples.

Note that the Mott–Schottky relationship is derived assuming a perfectly flat electrode surface; therefore care must be taken when analyzing and interpreting data from rough surfaces or nanostructures with features on the scale of the depletion width.[49, 58] For ZnO nanorods, curvature in a Mott–Schottky plot has been shown to arise as the depletion width approached the radius.[59] In cases of porous TiO_2 films that are highly resistive, a transmission line circuit model

has been used to get accurate fitting of impedance data.[60] However, our data appear well fit between 1 and 1500Hz by a simpler Randles model with a single capacitive element.

The control sample annealed at 700 °C shows a highly linear Mott–Schottky plot between 0.4 and 1.4 V *vs* RHE (Figure A6.5b). The highly linear nature of this plot suggests that a transmission line model is indeed not necessary for determining the space charge region in our case and that the radius of the sintered NWs is sufficiently large to avoid curvature of the plot under these conditions. Performing a linear fit to the data from 0.4 to 0.8 V *vs* RHE and using electrode areas determined by orange II dye adsorption[8, 53] leads to an estimation of the flat-band potential at 0.32 V *vs* RHE and a donor concentration of 1.0×10^{19} cm^{-3}. In order to estimate the potential error in N_D caused by the NW morphology we also fitted the Mott–Schottky data to the equations suggested by Mora–Sero et al. for cylindrical nanorods.[59] Estimating the radius as 80 nm from SEM images, this more complex fitting gives a donor concentration of 1.6×10^{19} cm^{-3}. While our NWs are not perfectly cylindrical or uniform in diameter as the above model assumes, the calculated result suggests that effects from the NW morphology likely cause the linear fitting to underestimate the donor concentration by less than a factor of 2.

In contrast, both Mott–Schottky plots from the Ti-treated hematite NW films have much smaller slopes than the untreated sample indicating higher donor concentrations in the treated samples. However, unlike the untreated sample, they show noticeable curvature above the flat-band potential (Figure A6.5b inset). This curvature might be expected to come from the nanostructured morphology given the discussion above; however, by SEM we do not observe any changes in the morphology or NW radius after treatment (Figure A6.2a,b). Furthermore, since the treated samples have a higher donor concentration and therefore smaller depletion

width, we expect the treated samples to be overall less sensitive to morphology than the untreated sample which already shows no curvature. We therefore conclude that the curvature must come from non-morphological effects such as a non-uniform donor concentration or possible new surface states. These effects can make the extrapolation of an exact donor concentration and flat-band potential ambiguous;[58] however we estimate the values with a linear fit near the flat-band. The treated sample annealed at 650 °C shows a flat-band potential at approximately 0.48 V *vs* RHE with a donor concentration of 4.5×10^{19} cm^{-3} and the sample annealed at 700 °C shows a flat-band potential of 0.58 V *vs* RHE and a donor concentration of 9.5×10^{19} cm^{-3}. These donor concentrations before and after Ti-doping are comparable to those previously reported.[39] These results also suggest that the Ti-treatment shifts the flat-band potential to be more oxidizing by up to 260 mV. Interestingly this is consistent with the small oxidative peak shift seen for the Fe(1s) and O(1s) XPS data between the treated and untreated samples (Figure A6.2c). Finally, from the donor concentrations summarized in Table 1, we conclude that the $Ti(OBu)_4$ treatment coupled with annealing dopes the hematite NWs with Ti, resulting in a large increase in the carrier concentration up to almost 10 folds for the 700 °C annealed sample and almost 5 folds for the 650 °C annealed sample.

Table A6.1 Summary of Mott–Schottky fitting results for all hematite photoelectrodes.

Hematite Photoelectrodes	V_{fb} (*vs* RHE)	N_D (cm^{-3})
Untreated NW film, 700° C	0.32 V	1.0×10^{19}
Ti-treated NW film, 650 °C	0.48 V	4.5×10^{19}
Ti-treated NW film, 700 °C	0.58 V	9.5×10^{19}
Untreated electrodeposited Film, 700 °C	0.54 V*	1.1×10^{19}
Ti-treated Electrodeposited film, 700 °C	0.53 V	17×10^{19}
Zr-treated NW film, 650 °C	0.31 V	1.2×10^{19}
Zr-treated NW film, 700 °C	0.32 V	9.3×10^{19}

*Fermi level pinned by surface states

Surface State Capacitance

We sought to further examine the water oxidation reaction after the $Ti(OBu)_4$ treatment by taking impedance spectroscopy under illumination as a function of potential. Klahr et al. showed that under these conditions surface state capacitances could be measured which they attributed to the formation of metal–hydroxyl ($M–OH_x$) intermediate states implicated in water oxidation reactions.[19] The surface state capacitances (C_{trap}) are extracted from the impedance data by fitting to the circuit shown in Figure A6.6a. We measured the capacitance for two hematite NW films annealed at 700 °C for 1 h, one was untreated as a control and the other was treated with 30 mM $Ti(OBu)_4$. As shown in Figure A6.6b, the surface state capacitance for untreated sample shows a Gaussian peak at 0.82 V *vs* RHE. This peak position is slightly before the onset of the photocurrent (as seen in the dashed plot overlaid in Figure A6.6b), consistent with the formation

of the intermediate states. The surface-state capacitance for the treated sample shows a peak centered at 1.09 V *vs* RHE. This gives a peak shift of 270 mV towards oxidizing potentials after the Ti treatment, similar to the flat-band shift revealed by the Mott–Schottky measurements (see Table 1). The shift also correlates with the oxidative shift in the treated film's photocurrent onset. Integrating the capacitive peaks yields an approximately 1.8 times larger peak area for the treated film than the untreated film, which allows a comparison of the total charge stored. This suggests that the Ti treatment may help to increase the accessible oxidation sites within the film. However, since the surface states appear at the same potential after adjusting for the flat-band shift, we conclude that the energetics of the oxidation reaction remain largely unaltered by the Ti treatment.

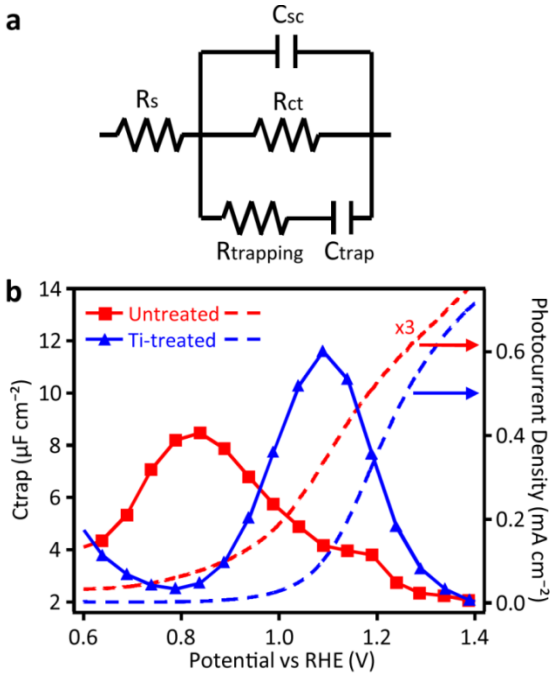

Figure A6.6. a) A diagram of the circuit model used to fit the impedance data between 1 and 1500 Hz and extract the surface trap capacitance (C_{trap}). b) Solid lines and markers represent the surface trap capacitance calculated from impedance data taken under illumination for untreated hematite NW films (red) and film treated with 30 mM $Ti(OBu)_4$ (blue), both annealed at 700 °C for 1 h. Dashed lines show the corresponding photocurrent densities for these films.

Doping Treatment of Electrodeposited Hematite Films

In order to explore the generality of the doping treatment in other hematite nanostructures, we investigated the effect of similar $Ti(OBu)_4$ treatment on electrodeposited nanocrystalline hematite film on FTO glass substrates prepared by following previously reported procedures.[42, 51] SEM images of the electrodeposited film show a highly porous structure with particles approximately 100 nm in diameter (Figure A6.7a inset). Photoelectrochemical and EIS measurements were carried out on untreated electrodeposited film and a film treated with 30 mM $Ti(OBu)_4$, both annealed at 700 °C for 30 min. The $Ti(OBu)_4$ treated hematite film displays a significantly larger photoresponse than the as-deposited film (Figure A6.7a). At 1.4 V *vs* RHE, the untreated film measures 0.14 mA cm^{-2} and 0.10 mA cm^{-2} illuminated from the FTO and films sides respectively. The Ti-treated film measures 0.34 mA cm^{-2} and 0.39 mA cm^{-2} for the FTO and film sides respectively. Similar to the NW hematite films, not only does the absolute photocurrent density increase after treatment but the current under film side illumination becomes slightly larger than the FTO side, suggesting better carrier collection.

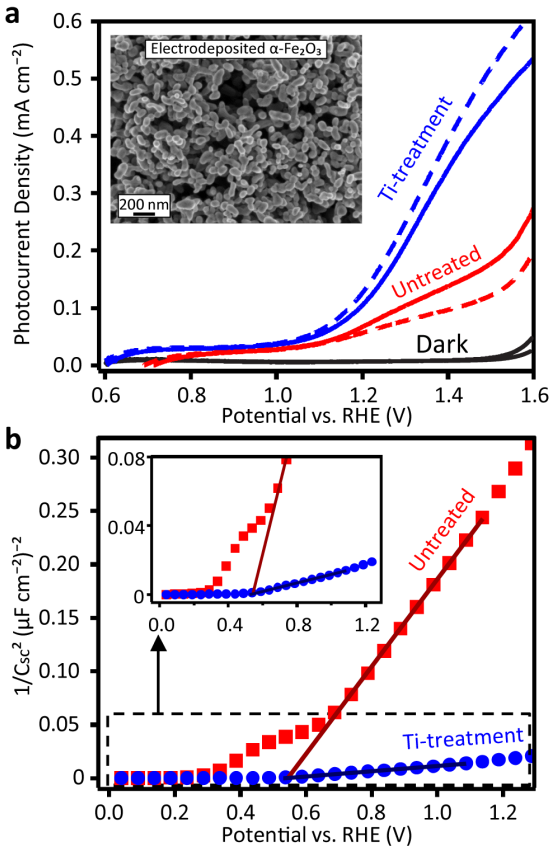

Figure A6.7. a) Photocurrent density measurements of the untreated (red) and Ti-treated (blue) electrodeposited films, both after 700 °C annealing for 30 min. Solid lines represent FTO side illumination and dashed lines represent hematite film side illumination. Inset is the SEM image of the electrodeposited film after Ti-treatment and annealing; b) Mott-Schottky plots of the same films in the dark. Solid lines represent linear fitting of the data and the inset shows an expanded view near the flat-band potential.

The Mott–Schottky plot of the untreated sample are in line with what has been observed before for electrodeposited hematite films.[61, 62] Using a Randles circuit with a single capacitive

element to fit the impedance data, curvature is observed in the data near the flat-band potential. At frequencies below 10 kHz, this curvature has been attributed to surface states and Fermi level pinning.[61] These states are centered at 0.54 V *vs* RHE and we have explored more complex fitting for them and discussed in detail in the electronic Supporting Information online. Fitting the linear region above the surface state effects, we estimate a donor concentration of 1.1×10^{19} cm^{-3}. In contrast, the Ti-treated sample shows a much more linear Mott–Schottky plot with no evidence of surface states, from which a flat-band potential of 0.53 V *vs* RHE and a donor concentration of 1.7×10^{20} cm^{-3} are calculated. Since the morphology of the electrodeposited hematite films is vastly different from the NW films, direct comparisons of the donor concentrations estimated from the Mott–Schottky plots (see Table 1) may be unreliable. However, since the relative donor concentration increases after the $Ti(OBu)_4$ treatment, we conclude that our simple $Ti(OBu)_4$ treatment can also effectively dope the electrodeposited hematite films with an increase in the donor concentration by approximately 10 times after 700 °C annealing.

Zr doping treatment

We explored the generality of this treatment and annealing method on hematite using other dopants by testing chemical bath deposition with a Zr precursor solution. We placed two hematite NW films (30 cycles) in a 100 mM $ZrO(NO_3)_2$ ethanol solution at 60 °C for 10 min followed by annealing one film at 650 °C and the other at 700 °C for 1 h. This chemical bath deposition method was more effective to improve the photocurrent of the treated hematite NW photoanodes compared to the dropcasting method. The SEM image of the Zr-treated NW sample after 700 °C annealing (Figure A6.8a) shows little charge in morphology from the untreated

NWs (Figure A6.2a). XPS measurements of the Zr-treated and 700 °C annealed film (Figure A6.8b) show clear peaks for Fe (2p) at 711.3 ± 0.2 eV, O (1s) at 530.6 ± 0.2 eV and Zr (3p) at 182.6 ± 0.2 eV. The Fe (1s) and O (1s) peaks are very similar to the peaks observed for the untreated sample annealed at 700 °C (see the discussion of Figure A6.2b for details) and consistent with hematite. The Zr (3p) peak position is consistent with Zr in the 4+ oxidation state. Since no Zr (3p) is observed for the untreated sample, we conclude that Zr is being deposited on the surface by the chemical bath deposition.

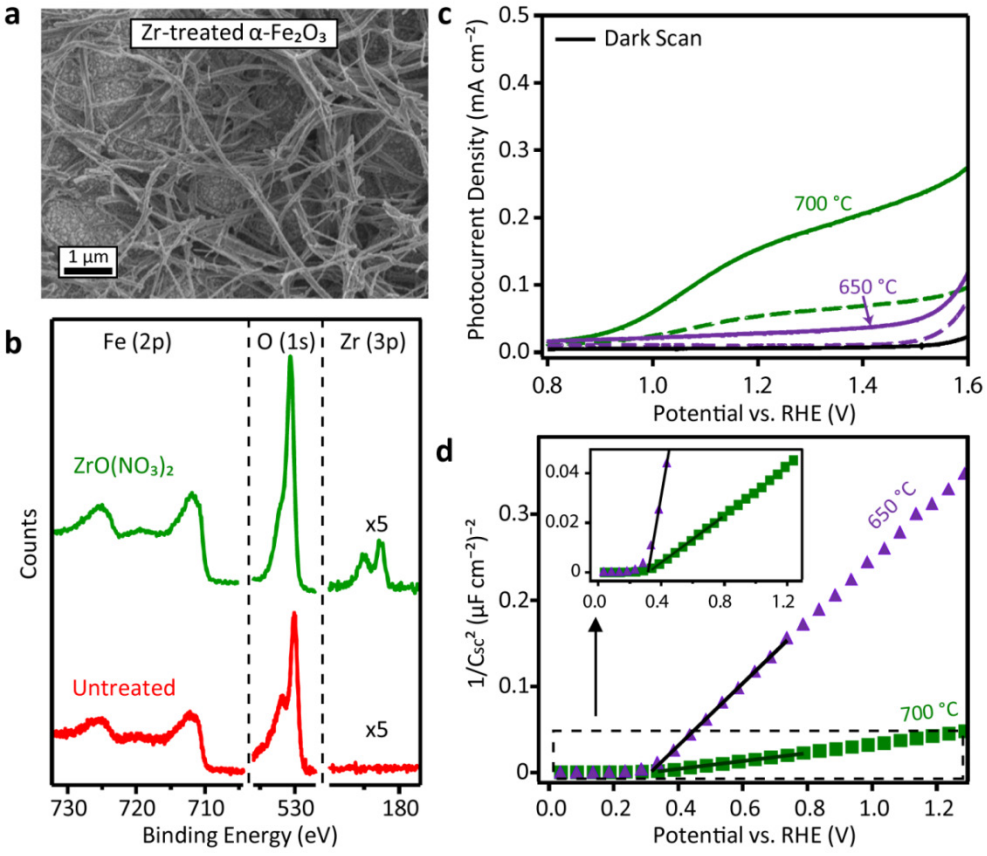

Figure A6.8. a) SEM of a hematite NW film after chemical bath deposition in a 100 mM $ZrO(NO_3)_2$ solution and annealing at 700 °C for 1 h. b) XPS of the Fe (2p), O (1s), and Zr (3p) binding energy regions for an untreated (red) and Zr-treated (green) sample. c) Photocurrent densities of Zr-treated hematite NW films annealed at 650 °C (purple) and 700 °C (green) for 1 h. Solid lines represent FTO side illumination and dashed lines represent NW film side illumination. d) Mott-Schottky plots for the above samples. Solid lines represent linear fits to the data. The inset shows an expanded view.

We measured the photocurrent density of the Zr-treated hematite NW films (Figure A6.8c). The film annealed at 700 °C shows photocurrent densities of 0.16 and 0.06 mA cm^{-2} illuminating from the FTO and film sides, respectively. While these photocurrents are much smaller than those observed for the Ti-treated films, the Zr-treated sample shows a small photocurrent density of 0.03 mA cm^{-2} where the untreated film (both annealed at 650 °C) shows no photocurrent response (see Figure A6.2a). For both Zr-treated samples, film side illumination yields a much smaller photocurrent than FTO side illumination suggesting the carrier collection from the electrolyte side of the films is still poor after treatment. Furthermore, Mott–Schottky analysis on both Zr-treated samples (Figure A6.8d) show that the 650 °C annealed sample has a flat-band potential of 0.31 V *vs* RHE with a donor concentration of 1.2×10^{19} cm^{-3}. The 700 °C annealed film shows a flat-band potential of 0.32 V *vs* RHE with a donor concentration of 9.3×10^{19} cm^{-3}. Both of these flat-band potentials are equivalent to that observed for the untreated film (Table 1). The donor concentration for the sample annealed at 650 °C is also very similar to the untreated sample. However, annealing at 700 °C increases the donor concentration dramatically. Therefore

we conclude that the $ZrO(NO_3)_2$ treatment appears to increase the carrier concentration and dope the hematite sample after annealing at 700 °C.

In addition, we have also explored 5 other metal precursors, $Sb(OCH_2CH_3)_3$, $Si(OCH_3)_3CH_2NH_2$, $NbCl_5$, $Cd(CH_3COO)_2$, and $Fe(NO_3)_3$ for doping the hematite NW films and some (Sb and Fe) were found to be effective. However, in our preliminary efforts none of these precursor treatment led to photocurrent densities larger than those observed for $Ti(OBu)_4$ treatment.

A6.6 Discussion

By combining all of our observations, we can address the question of why the $Ti(OBu)_4$ treatment leads to an improvement in the measured photocurrent density. We can imagine four possible mechanisms that can improve the photocurrent due to Ti species: First, photocurrent may come from TiO_2 deposits directly; second, Ti species may act as a catalyst for water oxidation; third, Ti may dope the hematite and improve majority carrier collection; and finally, Ti may act to passivate or favorably alter the surface states to reduce recombination and charge trapping.

TiO_2 is a well-known photocatalyst that can generate photocurrents down to nearly the hydrogen reduction potential.[56, 57] If the Ti-treatment led to the formation of significant TiO_2 deposits, new photocurrent could be generated at these deposits. However, we do not observe any new particle formation by SEM or see any TiO_2 lattice fringes under HRTEM. Furthermore we would expect any photocurrent directly from TiO_2 to be observed at potentials significantly

more reducing than the onset of about 0.9 V *vs* RHE we see for the majority of our samples. Indeed we may be measuring some currents from TiO_2 at more reducing potentials when treating the samples with high concentrations (300 mM) of the $Ti(OBu)_4$ solution (Figure A6.4d), where TiO_2 formation may be more likely. However, for the majority of our samples, we are confident that very little to no additional photocurrent is coming from TiO_2 deposits if they exist at all.

Similarly, one may imagine that Ti species on the surface could simply act as a catalyst towards water oxidation, improving the photocurrent by lowering the energy barriers of the reaction intermediates and accelerating the reaction kinetics. Cobalt species of various complexities are often applied to the surface of Fe_2O_3 exactly for this purpose as we have done in Figure A6.1a.[8, 63-65] Similarly, Ti complexes have been used on mesoporous structures to catalyze oxidation reactions.[66] However, we do not see a shift in the photocurrent onset towards reducing potentials that would indicate a lowed potential barrier after Ti treatment (Figure A6.4). More telling are measurements of the surface hydroxyl intermediate states (Figure A6.6) which only show an oxidative shift after treatment that tracks the shift in the flat-band potential. This indicates little change in the overpotential needed to form the intermediate species. With this direct measurement of the intermediate energy level we can be fairly certain that Ti species are not directly reducing the barriers towards water oxidation or catalyzing the reaction.

After excluding the reaction occurring directly on Ti sites, we might expect doping of the hematite by Ti to increase the photocurrent by improving the electrical conductivity of the nanostructures and therefore reducing resistive losses and improving the majority carrier collection. Indeed as discussed in the introduction, hematite nanostructures have been doped with a variety of elements in order to improve carrier collection and boost performance. Particularly,

Ti doping has been recently shown to improve the performance of hematite NWs grown through co-growth during a hydrothermal synthesis.[13] In our case, the dopant species are only added after the hematite growth, but doping may be expected since at temperatures above 500 °C, Ti is soluble in hematite up to at least several atomic percent.[67, 68] Therefore during the annealing steps at 650 and 700 °C, Ti should be able to diffuse into the crystal lattice of the hematite nanostructures. The presence of Ti throughout the hematite NWs is confirmed by EDS mapping (Figure A6.2). More importantly, Mott–Schottky analysis of Ti-treated hematite NWs and electrodeposited films shows a dramatic increase in the carrier concentration by almost a factor of 10 (Figure A6.5 and Figure A6.7). While the absolute values of the donor concentrations may have some systematic error due to the uncertainty in the true active electrode area and dielectric constant,[52] the calculated donor concentrations of approximately 1×10^{20} Ti atoms per cm^3 are less than 1% of the Fe concentration in hematite (3.9×10^{22} atoms cm^{-3}) and therefore reasonable based on the reported Ti solubility. Furthermore, the largest increase in photocurrent was observed when illuminating from the film side of the samples (Figure A6.4). This suggests that the majority carrier transport and collection must be greatly improved since the film side NWs are farthest from the FTO back contact. Our results therefore are consistent with Ti doping of hematite nanostructures improving the carrier collection and overall photocurrent density.

Finally, the Ti treatment may be improving the PEC performance by passivating surface and/or other mid–gap trap states. Recombination at surface states in hematite has been suggested as a major limiting factor in the performance of hematite electrodes.[69-71] Passivation of these states can reduce recombination and improve charge transport and collection. Both Sn and Al ions have been shown to passivate these states and improve the photocurrent density of hematite

electrodes.[72, 73] In these cases, changes in the doping and conductivity of the hematite were ruled out and the improvement in performance was attributed to a reduction in recombination at the surface sites. Similarly Al_2O_3, Ga_2O_3 and In_2O_3 over layers deposited by chemical bath deposition or atomic layer deposition have also been shown to passivate surface states, though primarily leading to an improvement in photocurrent onset rather than increasing photocurrent.[74] Finally, surface passivation by TiO_2 overlayers was also investigated previously and demonstrated no improvement in photocurrent.[73] However, the hematite electrodes in that report were only annealed at 500 °C, at which temperature we also do not see photoactivation. While our data do not directly confirm or deny the passivation of surface states after the $Ti(OBu)_4$ treatment and higher temperature annealing, we do see evidence that the surface chemistry of the hematite is significantly altered. From the Mott–Schottky analysis, the shifts in the surface state capacitance, and even XPS, we observe a change in the flat-band potential of approximately 260 mV towards oxidizing potentials. Since Ti is an n-type dopant for hematite, from the doping change alone, we would have expected a small shift in flat-band potential towards reducing potentials instead of oxidizing. The reversal of this shift suggests the $Ti(OBu)_4$ treatment is altering the surface electronic structure and possibly changing the pinning of the Fermi level at the surface. We can also see the Ti interacting with surface states more clearly with the electrochemically deposited hematite (Figure A6.7). In this case, the Mott–Schottky analysis clearly shows the presence of surface states in the untreated sample but none are visible after the Ti-treatment. Additionally, the Fermi level of the untreated electrodeposited hematite film appears pinned by the surface states to the same potential (0.54 V *vs* RHE) as the flat-band after Ti treatment, leading us to further speculate that there is interaction between these surface states

and the Ti dopants. Interestingly, the Zr treatment (Figure A6.8), which does not lead to as much of an improvement in the photocurrent especially under film side illumination, does not show a significant flat-band shift. This correlation between improved photocurrent density and a shift in flat-band potential and altered surface states within our data suggests surface passivation by some Ti species is at least plausible. Further studies will be needed to fully understand the surface state changes caused by the $Ti(OBu)_4$ treatment before firmer conclusions can be drawn. However, overall our results suggest that the improvement in photocurrent from the $Ti(OBu)_4$ treatment is likely coming from doping effects, or a combination of the doping and surface passivation.

A6.7 Summary and outlooks

A simple approach of solution-based treatment followed by thermal annealing around 650 °C has been developed to dope hematite nanostructures after growth and greatly enhance its photoactivity for PEC water splitting. A combination of microstructural characterization, elemental analysis, PEC measurements and EIS studies ruled out other possibilities and attributed the improved PEC performance mainly to the improved charge carrier transport and collection enabled by Ti doping. Ti atoms are shown to be distributed throughout the hematite nanostructures and its introduction led to about 10 fold increase in donor concentrations in hematite. Furthermore, the observed shifts in the flat-band potential and the peak potential of the surface trap state capacitance suggested that the Ti dopants also altered the surface electronic structure of hematite, which likely also contributed to the improved PEC performance by passivating the surface trap states. This facile post-growth doping method can be generally applied to other nanostructured hematite photoanodes such as electrochemically deposited

hematite films, or using other dopants such as Zr. Because this simple doping method does not depend on the growth method and history of the hematite samples, it may be conveniently applied to many previously reported undoped hematite nanostructures to enhance the PEC performance. The combined PEC and EIS results obtained from different doped hematite photoelectrodes demonstrated the importance of investigating the surface trap states and developing effective passivation strategies to further improve overall PEC performance of hematite in the future.

A6.8 References

1. Lewis, N. S., Nocera, D. G., Powering the planet: Chemical challenges in solar energy utilization. *Proc. Natl. Acad. Sci. U.S.A* **103,** 15729-15735 (2006).

2. Walter, M. G., et al., Solar Water Splitting Cells. *Chem. Rev.* **110,** 6446-6473 (2010).

3. Gratzel, M., Photoelectrochemical cells. *Nature* **414,** 338-344 (2001).

4. Khaselev, O., Turner, J. A., A Monolithic Photovoltaic-Photoelectrochemical Device for Hydrogen Production via Water Splitting. *Science* **280,** 425-427 (1998).

5. Licht, S., et al., Over 18% Solar Energy Conversion to Generation of Hydrogen Fuel; Theory and Experiment for Efficient Solar Water Splitting. *Int. J. Hydrog. Energy* **26,** 653-659 (2001).

6. Sivula, K., Le Formal, F., Grätzel, M., Solar Water Splitting: Progress Using Hematite (α-Fe_2O_3) Photoelectrodes. *ChemSusChem* **4,** 432-449 (2011).

7. Wheeler, D. A., et al., Nanostructured Hematite: Synthesis, Characterization, Charge Carrier Dynamics, and Photoelectrochemical Properties. *Energy Environ. Sci.* **5,** 6682-6702 (2012).

8. Kay, A., Cesar, I., Grätzel, M., New Benchmark for Water Photooxidation by Nanostructured α-Fe_2O_3 Films. *J. Am. Chem. Soc.* **128,** 15714-15721 (2006).

9. Sivula, K., et al., Photoelectrochemical Water Splitting with Mesoporous Hematite Prepared by a Solution-Based Colloidal Approach. *J. Am. Chem. Soc.* **132,** 7436-7444 (2010).

10. Tilley, S. D., Cornuz, M., Sivula, K., Grätzel, M., Light-Induced Water Splitting with Hematite: Improved Nanostructure and Iridium Oxide Catalysis. *Angew. Chem. Int. Ed.* **49,** 6405-6408 (2010).

11. Hisatomi, T., et al., Enhancement in the Performance of Ultrathin Hematite Photoanode for Water Splitting by an Oxide Underlayer. *Adv. Mater.* **24,** 2699-2702 (2012).

12. Ling, Y., et al., The Influence of Oxygen Content on the Thermal Activation of Hematite Nanowires. *Angew. Chem. Int. Ed.* **51,** 4074-4079 (2012).

13. Wang, G., et al., Facile Synthesis of Highly Photoactive α-Fe_2O_3-Based Films for Water Oxidation. *Nano Lett.* **11,** 3503-3509 (2011).

14. Ling, Y., et al., Sn-Doped Hematite Nanostructures for Photoelectrochemical Water Splitting. *Nano Lett.* **11,** 2119-2125 (2011).

15. Mayer, M. T., Du, C., Wang, D., Hematite/Si Nanowire Dual-Absorber System for Photoelectrochemical Water Splitting at Low Applied Potentials. *J. Am. Chem. Soc.* **134,** 12406-12409 (2012).

16. Lin, Y., et al., Growth of p-Type Hematite by Atomic Layer Deposition and Its Utilization for Improved Solar Water Splitting. *J. Am. Chem. Soc.* **134,** 5508-5511 (2012).

17. Lin, Y., Zhou, S., Sheehan, S. W., Wang, D., Nanonet-Based Hematite Heteronanostructures for Efficient Solar Water Splitting. *J. Am. Chem. Soc.* **133,** 2398-2401 (2011).

18. Lin, Y., et al., Hematite-based Solar Water Splitting: Challenges and Opportunities. *Energy Environ. Sci.* **4,** 4862-4869 (2011).

19. Klahr, B., et al., Water Oxidation at Hematite Photoelectrodes: The Role of Surface States. *J. Am. Chem. Soc.* **134,** 4294-4302 (2012).

20. Klahr, B., et al., Photoelectrochemical and Impedance Spectroscopic Investigation of Water Oxidation with "Co–Pi"-Coated Hematite Electrodes. *J. Am. Chem. Soc.* **134,** 16693-16700 (2012).

21. Klahr, B., et al., Electrochemical and Photoelectrochemical Investigation of Water Oxidation with Hematite Electrodes. *Energy Environ. Sci.* **5,** 7626-7636 (2012).

22. Hamann, T. W., Splitting Water with Rust: Hematite Photoelectrochemistry. *Dalton Trans.* **41,** 7830-7834 (2012).

23. Li, L., et al., Facile Solution Synthesis of α-$FeF_3 \cdot 3H_2O$ Nanowires and Their Conversion to α-Fe_2O_3 Nanowires for Photoelectrochemical Application. *Nano Lett.* **12,** 724-731 (2012).

24. Gonçalves, R. H., Lima, B. H. R., Leite, E. R., Magnetite Colloidal Nanocrystals: A Facile Pathway to Prepare Mesoporous Hematite Thin Films for Photoelectrochemical Water Splitting. *J. Am. Chem. Soc.* **133,** 6012-6019 (2011).

25. Chernomordik, B. D., et al., Photoelectrochemical Activity of As-Grown, α-Fe_2O_3 Nanowire Array Electrodes For Water Splitting. *Nanotechnology* **23,** 194009 (2012).

26. Su, J., et al., Vertically Aligned WO_3 Nanowire Arrays Grown Directly on Transparent Conducting Oxide Coated Glass: Synthesis and Photoelectrochemical Properties. *Nano Lett.* **11,** 203-208 (2010).

27. Santato, C., Ulmann, M., Augustynski, J., Photoelectrochemical Properties of Nanostructured Tungsten Trioxide Films. *J. Phys. Chem. B* **105,** 936-940 (2001).

28. Itoh, K., Bockris, J. O. M., Thin Film Photoelectrochemistry: Iron Oxide. *J. Electrochem. Soc.* **131,** 1266-1271 (1984).

29. Bosman, A. J., Vandaal, H. J., Small-Polaron Versus Band Conduction in Some Transition-Metal Oxides. *Adv. Phys.* **19,** 1-117 (1970).

30. Cherepy, N. J., et al., Ultrafast Studies of Photoexcited Electron Dynamics in γ- and α-Fe_2O_3 Semiconductor Nanoparticles. *J. Phys. Chem. B* **102,** 770-776 (1998).

31. Kennedy, J. H., Frese, J. K. W., Photooxidation of Water at α-Fe_2O_3 Electrodes. *J. Electrochem. Soc.* **125,** 709-714 (1978).

32. Van de Krol, R., Liang, Y., Schoonman, J., Solar Hydrogen Production with Nanostructured Metal Oxides. *J. Mater. Chem.* **18,** 2311-2320 (2008).

33. Bierman, M. J., Jin, S., Potential Applications of Hierarchical Branching Nanowires in Solar Energy Conversion. *Energy Environ. Sci.* **2,** 1050-1059 (2009).

34. Cesar, I., Kay, A., Gonzalez Martinez, J. A., Grätzel, M., Translucent Thin Film Fe_2O_3 Photoanodes for Efficient Water Splitting by Sunlight: Nanostructure-Directing Effect of Si-Doping. *J. Am. Chem. Soc.* **128,** 4582-4583 (2006).

35. Lukowski, M. A., Jin, S., Improved Synthesis and Electrical Properties of Si-Doped α-Fe_2O_3 Nanowires. *J. Phys. Chem. C* **115,** 12388-12395 (2011).

36. Chemelewski, W. D., Hahn, N. T., Mullins, C. B., Effect of Si Doping and Porosity on Hematite's (α-Fe_2O_3) Photoelectrochemical Water Oxidation Performance. *J. Phys. Chem. C* **116,** 5255-5261 (2012).

37. Sanchez, H. L., Steinfink, H., White, H. S., Solid solubility of Ge, Si, and Mg in Fe_2O_3 and photoelectric behavior. *J. Solid State Chem.* **41,** 90-96 (1982).

38. Sieber, K. D., Sanchez, C., Turner, J. E., Somorjai, G. A., Preparation, characterization and photoelectronic properties of germanium-substituted Fe_2O_3 single crystals. *J. Chem. Soc., Faraday Trans. 1: Physical Chemistry in Condensed Phases* **81,** 1263-1274 (1985).

39. Glasscock, J. A., Barnes, P. R. F., Plumb, I. C., Savvides, N., Enhancement of Photoelectrochemical Hydrogen Production from Hematite Thin Films by the Introduction of Ti and Si. *J. Phys. Chem. C* **111,** 16477-16488 (2007).

40. Hahn, N. T., Mullins, C. B., Photoelectrochemical Performance of Nanostructured Ti- and Sn-Doped α-Fe_2O_3 Photoanodes. *Chem. Mater.* **22,** 6474-6482 (2010).

41. Leygraf, C., Hendewerk, M., Somorjai, G. A., Photocatalytic Production of Hydrogen From Water by a p- And n-Type Polycrystalline Iron Oxide Assembly. *J. Phys. Chem.* **86,** 4484-4485 (1982).

42. Kleiman-Shwarsctein, A., et al., Electrodeposition of α-Fe_2O_3 Doped with Mo or Cr as Photoanodes for Photocatalytic Water Splitting. *J. Phys. Chem. C* **112,** 15900-15907 (2008).

43. Horowitz, G., Capacitance-Voltage Measurements and Flat-Band Potential Determination on Zr-Doped α-Fe_2O_3 Single-Crystal Electrodes. *J. Electroanal. Chem. Interf. Electrochem.* **159,** 421-436 (1983).

44. Hu, Y.-S., et al., Pt-Doped α-Fe_2O_3 Thin Films Active for Photoelectrochemical Water Splitting. *Chem. Mater.* **20,** 3803-3805 (2008).

45. Kleiman-Shwarsctein, A., et al., Electrodeposited Aluminum-Doped α-Fe_2O_3 Photoelectrodes: Experiment and Theory. *Chem. Mater.* **22,** 510-517 (2009).

46. Ingler, Baltrus, J. P., Khan, S. U. M., Photoresponse of p-Type Zinc-Doped Iron(III) Oxide Thin Films. *J. Am. Chem. Soc.* **126,** 10238-10239 (2004).

47. Sanchez, C., Sieber, K. D., Somorjai, G. A., The Photoelectrochemistry of Niobium Doped α-Fe_2O_3. *J. Electroanal. Chem. Interf. Electrochem.* **252,** 269-290 (1988).

48. Tang, H., et al., Titanium and Magnesium Co-Alloyed Hematite Thin Films for Photoelectrochemical Water Splitting. *J. Appl. Phys.* **111,** (2012).

49. Cesar, I., et al., Influence of Feature Size, Film Thickness, and Silicon Doping on the Performance of Nanostructured Hematite Photoanodes for Solar Water Splitting. *J. Phys. Chem. C* **113,** 772-782 (2009).

50. Rosso, K. M., Smith, D. M. A., Dupuis, M., An Ab Initio Model of Electron Transport in Hematite (α-Fe_2O_3) Basal Planes. *J. Chem. Phys* **118,** 6455-6466 (2003).

51. Schrebler, R., et al., An Electrochemical Deposition Route for Obtaining α-Fe_2O_3 Thin Films. *Electrochem. Solid State Lett.* **9,** C110-C113 (2006).

52. Glasscock, J. A., et al., Structural, Optical and Electrical Properties of Undoped Polycrystalline Hematite Thin Films Produced Using Filtered Arc Deposition. *Thin Solid Films* **516,** 1716-1724 (2008).

53. Bandara, J., Mielczarski, J. A., Kiwi, J., 1. Molecular Mechanism of Surface Recognition. Azo Dyes Degradation on Fe, Ti, and Al Oxides through Metal Sulfonate Complexes. *Langmuir* **15,** 7670-7679 (1999).

54. McIntyre, N. S., Zetaruk, D. G., X-Ray Photoelectron Spectroscopic Studies of Iron-Oxides. *Anal. Chem.* **49,** 1521-1529 (1977).

55. Carley, A. F., Chalker, P. R., Riviere, J. C., Roberts, M. W., The Identification and Characterization of Mixed Oxidation-States at Oxidized Titanium Surfaces by Analysis of X-Ray Photoelectron-Spectra. *J. Chem. Soc. Farady Trans. 1* **83,** 351-370 (1987).

56. Chen, X., Mao, S. S., Titanium Dioxide Nanomaterials: Synthesis, Properties, Modifications, and Applications. *Chem. Rev.* **107,** 2891-2959 (2007).

57. Linsebigler, A. L., Lu, G. Q., Yates, J. T., Photocatalysis on TiO_2 Surfaces - Principles, Mechanisms, and Selected Results. *Chem. Rev.* **95,** 735-758 (1995).

58. Gomes, W. P., Cardon, F., Electron-Energy Levels in Semiconductor Electrochemistry. *Prog. Surf. Sci.* **12,** 155-215 (1982).

59. Mora-Sero, I., et al., Determination of Carrier Density of Zno Nanowires by Electrochemical Techniques. *Appl. Phys. Lett.* **89,** 203117 (2006).

60. Fabregat-Santiago, F., et al., Decoupling of Transport, Charge Storage, and Interfacial Charge Transfer in The Nanocrystalline TiO_2/Electrolyte System by Impedance Methods. *J. Phys. Chem. B* **106,** 334-339 (2002).

61. Schrebler, R., et al., An Electrochemical Deposition Route for Obtaining α-Fe_2O_3 Thin Films - II. EQCM Study and Semiconductor Properties. *Electrochem. Solid State Lett.* **10,** D95-D99 (2007).

62. Schrebler, R. S., et al., The Influence of Different Electrodeposition E/T Programs Photoelectrochemical Properties of α-Fe_2O_3 Thin Films. *Thin Solid Films* **518,** 6844-6852 (2010).

63. Zhong, D. K., et al., Photo-Assisted Electrodeposition of Cobalt-Phosphate (Co-Pi) Catalyst on Hematite Photoanodes for Solar Water Oxidation. *Energy Environ. Sci.* **4,** 1759-1764 (2011).

64. Zhong, D. K., Gamelin, D. R., Photoelectrochemical Water Oxidation by Cobalt Catalyst ("Co−Pi")/α-Fe_2O_3 Composite Photoanodes: Oxygen Evolution and Resolution of a Kinetic Bottleneck. *J. Am. Chem. Soc.* **132,** 4202-4207 (2010).

65. Zhong, D. K., Sun, J., Inumaru, H., Gamelin, D. R., Solar Water Oxidation by Composite Catalyst/α-Fe_2O_3 Photoanodes. *J. Am. Chem. Soc.* **131,** 6086-6087 (2009).

66. Blasco, T., Corma, A., Navarro, M. T., Pariente, J. P., Synthesis, Characterization, and Catalytic Activity of Ti-MCM-41 Structures. *J. Catal.* **156,** 65-74 (1995).

67. Kikuchi, R., Burton, B. P., Calculation Of Phase-Diagrams of Some Oxide Systems Using the Cluster Variation Method. *Physica B & C* **150,** 132-141 (1988).

68. Nord, G. L., Lawson, C. A., Order-Disorder Transition Induced Twin Domains and Magnetic-Properties in Ilmenite-Hematite. *Am. Miner.* **74,** 160-176 (1989).

69. Le Formal, F., Gratzel, M., Sivula, K., Controlling Photoactivity in Ultrathin Hematite Films for Solar Water-Splitting. *Adv. Funct. Mater.* **20,** 1099-1107 (2010).

70. Fredlein, R. A., Bard, A. J., Semiconductor Electrodes .21. Characterization and Behavior of n-Type Fe_2O_3 Electrodes in Acetonitrile Solutions. *J. Electrochem. Soc.* **126,** 1892-1898 (1979).

71. Dareedwards, M. P., Goodenough, J. B., Hamnett, A., Trevellick, P. R., Electrochemistry and Photoelectrochemistry of Iron(III) Oxide. *J. Chem. Soc. Farady Trans. 1* **79,** 2027-2041 (1983).

72. Spray, R. L., McDonald, K. J., Choi, K. S., Enhancing Photoresponse of Nanoparticulate alpha-Fe2O3 Electrodes by Surface Composition Tuning. *J. Phys. Chem. C* **115,** 3497-3506 (2011).

73. Le Formal, F., et al., Passivating Surface States on Water Splitting Hematite Photoanodes with Alumina Overlayers. *Chem. Sci.* **2,** 737-743 (2011).

74. Hisatomi, T., et al., Cathodic Shift in Onset Potential of Solar Oxygen Evolution on Hematite by 13-Group Oxide Overlayers. *Energy Environ. Sci.* **4,** 2512-2515 (2011).

APPENDIX 7

Inhomogeneous Phase Transformation during the Electrochemical Delithiation of $LiFePO_4$ Microrods

---

This is an on-going work in collaboration with Dr. Hong Liang and Professor Ming Tang at Rice University.

A7.1 Introduction

$LiFePO_4$ is technologically important cathode material for lithium-ion batteries[1-3]. It has drawn heavy interest from battery industry due to its advantage in power capability, safety, environmental impact, and cost compared with other leading cathode materials, such as $LiCoO_2$. $LiFePO_4$ also provides an interesting platform to study electrochemically-driven solid-state phase transformation due to its intriguing phase transformation behaviors[4-12]. At ensemble level, both particle-by-particle (de)intercalation[6, 8] and concurrent (de)intercalation[10, 13, 14] behaviors were observed, which were recently suggested to be controlled by the applied current densities. At single-particle level, two-phase and solid-solution mechanisms both exist[5-7, 12]. These complex phase transformation behaviors are likely related to the anisotropic lithium-transport property (lithium-channel along <010>, **b** axis direction)[15, 16] and low electron conductivity of $LiFePO_4$, which however has not been fully understood, possibly due to the lack of suitable *operando* techniques with good spatial and chemical resolutions and favorable model samples.

In situ X-ray diffraction[12], X-ray absorption[17], neutron diffraction[15] techniques have provided valuable insights into the phase transforming behaviors of $LiFePO_4$. However, the obtained information is spatially averaged over many different particles across a large volume of the electrode so that single-particle level understanding is not readily available. *In situ* transmission electron microscopy[18, 19] and soft X-ray microscopy[10, 11] can probe changes at the nanoscale but they require restrictively thin samples (typically < 150 nm) and specialized electrochemical cells, making the measurements very challenging. The recently developed synchrotron transmission X-ray microscopy (TXM) and spectro-imaging provide a unique and complementary tool to visualize solid-state electrochemical reactions both at the single-particle

level (state-of-the art spatial resolution ~25 nm) and in a large area of the electrode (40 μm × 40 μm in a single field-of-view; 400 μm × 400 μm in mosaic mode)[20-22]. Benefited from the strongly penetrating hard X-rays, the experiments can be performed on realistic electrodes that are tens of microns in thickness and contain all the key components such as carbon black and polymeric binder under battery *operando* conditions, using simple cell design such as a perforated coin-cell. However, a large sample (typically > 1 μm in thickness) is required to absorb sufficient X-ray in order to provide meaningful chemical information.

To correlate the phase transformation in $LiFePO_4$ with its crystallographic orientation, it is favorable to have a single-crystalline sample with well-defined morphology. Single-crystalline $LiFePO_4$ samples have been prepared with hydrothermal and solvothermal approaches[23-26]. Because {010} facets have the lowest surface energy in $LiFePO_4$,[27, 28] the synthesized $LiFePO_4$ samples usually exhibit a platelet-like morphology with large area of {010} facets exposed. These samples are relatively thin in the **b** axis direction (typically < 200 nm), which is highly desirable for high-rate lithium insertion/extraction but conversely making them unsuitable for studying phase transformations using TXM. Therefore, it is particular interesting to tune the synthesis parameter to prepare $LiFePO_4$ model samples that are longer or thicker in the **b** axis direction.

Here we report a ligand assisted hydrothermal synthesis of single-crystalline $LiFePO_4$ microrods. High-resolution transmission electron microscopy confirms that these microrods are grown along the <010> direction. Electrochemical delithiation of $LiFePO_4$ is studied using *operando* hard X-ray spectro-imaging. We observe anisotropic reaction that preferentially initiates at the end of the microrods and propagates towards the interior along the **b** axis direction,

providing the first direct evidence for one-dimensional lithium transport in $LiFePO_4$ under electrochemical conditions. Further, the comparison between chemical phase maps with phase-field simulations reveals insights into the kinetics of electrochemical delithiation of $LiFePO_4$.

A7.2 Experimental Methods

A7.2.1 Synthesis of the $LiFePO_4$ microrod

To prepare samples of lithium iron phosphate ($LiFePO_4$), 6 mmol of ammonium dihydrogen phosphate ($NH_4H_2PO_4$), lithium hydroxide (LiOH), and nitrilotriacetic acid [$N(CH_2CO_2H)_3$] were weighed out and transferred into a glass jar. 60 mL of deionized water was then added to the glass jar and the solution was stirred for 15 minutes by placing a magnetic stir bar into the jar containing the solution and setting the jar on a stir plate. After 15 minutes, 1–2 mL of NH_3·H2O were micropipetted into the solution until a pH of 9 was attained. 6 mmol of iron(II) sulfate heptahydrate ($FeSO_4 \cdot 7H_2O$) was then added to the solution and the solution was stirred for another 15 minutes. The resulting solution was transferred to a Teflon reactor in a stainless steel autoclave that was finally set in the oven at 200 °C for approximately 48 hours and allowed to cool down naturally. The greenish precipitate was collected by centrifugation and washed with deionized water and ethanol for three times before being left to dry in an oven at 60 °C. The product was further thermally annealed at 600 °C for 8 h under an atmosphere of Ar/H_2 (95:5).

A.7.2.2 Material characterizations

Scanning electron microscopy (SEM) images were acquired using a LEO 55 VP field emission scanning electron microscope at a working voltage of 5 kV. Transmission electron

microscopy (TEM) images and electron diffraction (ED) patterns were acquired using a FEI Philips FM200 transmission electron microscope (200 kV). The TEM samples were prepared by dropcasting the $LiFePO_4$ samples in ethanol onto lacey-carbon grids (Ted Pella Inc. lacey carbon type-A, 300 Mesh). Powder X-ray diffraction (PXRD) data were collected on a Bruker D8 diffractometer using Cu Kα radiation. The PXRD samples were prepared by drop-casting the ethanol suspensions of the samples onto glass substrates and dried.

A7.2.3 Electrochemical characterization

Electrochemical measurements were performed on electrodes pasted on aluminum foils (~25 μm thickness), which were prepared from slurries containing 70 wt% active material, 20 wt% conductive carbon black and 10 wt% PVDF binder using NMP as the solvent. CR2032-type coin cells were assembled in an argon-filled glovebox, using Li metal as the counter/quasi-reference electrode, 1 M $LiPF_6$ in EC/DMC (1/1 by volume) as the electrolyte, and electrolyte-soaked polyethylene films as the separator. All cells were aged a few hours before any tests. Cyclic voltammetry was performed using a Biologic SP-200 Potentiostat operated using EC-Lab software. Constant current discharge/charge tests were carried out using a MTI muti-channel cycler.

A7.2.4 *Operando* hard X-ray spectroimaging

The *operando* hard X-ray spectro-imaging experiments were performed using the full-field transmission X-ray microscope (FFTXM) at beamline X8c, National Synchrotron Light Source (NSLS), Brookhaven National Laboratory (BNL), using a perforated 2032-type coin cell with holes on both sides sealed by Kapton tapes. The holes were sealed using Kapton tapes. The

o*perando* measurements were performed on diluted electrodes made of 50 wt% $LiFePO_4$ active material, 30 wt% carbon black and 20 wt% polymeric binder to avoid overlapping between particles. Carbon papers (~110 μm thickness) are used as current collectors because they are quite transparent to hard X-rays. The cell was put into a custom-built holder mounted on a motorized *X, Y, Z,* θ stage and aligned to allow the X-ray beam to transmit through. A field of view of 40 × 40 μm^2 with a 2048 × 2048 CCD camera was used. The cell was continuously cycled in galvanostatic or potentiostatic mode and absorption-contrast images (X-ray transmitted through the sample) and reference background images (X-ray passing through air) were collected in sequence under dynamic conditions. To track the phase transformations in the electrode, a full series of TXM images were collected at each state of discharge and charge. Each TXM image series was collected by scanning across the Fe *K*-edge (7112 eV) from 7091 to 7285 eV, with a step size of 2 eV, and taking one TXM image at each energy step, which contains 256 × 256 XANES spectra when 8× 8 binned camera binning was used. The exposure time for each image was 2 seconds. Each chemical phase map took ~6 minutes to finish. After collection each set of data, the area of study (FOV 1) was allowed to rest for ~12 min (not exposed to X-rays) to minimize any potential impact induced by the X-ray beam, during which a new set of data was taken in another area of study (FOV 2) and background reference images (X-ray passing through air) were also recorded after that. The output pixel size is ~160 nm (camera binning 8).

The XANES spectrum at each pixel was normalized using an established method and then fitted with the linear combination of standard reference spectra collected from $Fe^{3+}PO_4$ and $LiFe^{2+}PO_4$ powders sealed between two pieces Kapton otherwise under the same conditions

using TXM. The spectrum fitting was carried out by minimizing the *R* value (a measure of misfit) for each spectrum at each pixel, which is defined as:

$$\boldsymbol{R} = \sum_{Ei}^{Ef} (dataE - refE)^2 / \sum_{Ei}^{Ef} dataE^2 \quad (2)$$

where *Ei* is 7091 eV, *Ef* is 7285 eV, *dataE* is the normalized spectrum at each pixel for the given energy *E,* and *refE* is the possible fitting reference value that is a linear combination of X-ray attenuation of $LiFePO_4$ and $FePO_4$. *R* values were minimized at each pixel to find the best-matched phase combination of different Fe oxidation states so that red ($Fe^{3+}PO_4$) and green ($LiFe^{2+}PO_4$) colors can be assigned accordingly to generate the chemical phase maps. We applied an *R-value* filter (misfit filter) to the resulting phase map in order to give the most accurate chemical phase information. *R* is typically smaller than 0.05 in the displayed chemical phase maps.

A7.3 Results and Discussion

We synthesized the $LiFePO_4$ microrods *via* a hydrothermal approach (see synthetic details in A7.2.1). Lithium hydroxide (LiOH), iron(II) sulfate heptahydrate ($FeSO_4 \cdot 7H_2O$), ammonium dihydrogen-phosphate ($NH_4H_2PO_4$) were used as precursors and nitrilotriacetic acid [$N(CH_2CO_2H)_3$, NTA] was used as a complexing reagent to Fe^{2+} to avoid the formation of iron hydroxide and control the supersaturation to favor the anisotropic growth. No microrods were obtained without the addition of NTA.

We first examined the microrods using scanning electron microscopy (SEM). The microrods are faceted and typically 2–7 μm in thickness/height and tens of microns in length (Figure

A7.1a). Many of them have a rectangular cross-section. The phase identity of the microrods was confirmed to orthorhombic $LiFePO_4$ (Space group *Pmna*) by powder X-ray diffraction (Figure A7.1b). We further examined the microrods (>15 microrods) using transmission electron microscopy (TEM), which confirmed that the microrods are single crystals and their long-axis direction is along <010> (Figure A7.1c and A7.1d). Because the lithium-ion channels in $LiFePO_4$ are also located along the <010> direction, the $LiFePO_4$ microrods provide a unique platform to study the electrochemical delithiation reaction (charge reaction of $LiFePO_4$), which is believed to be highly anisotropic but still not fully understood.

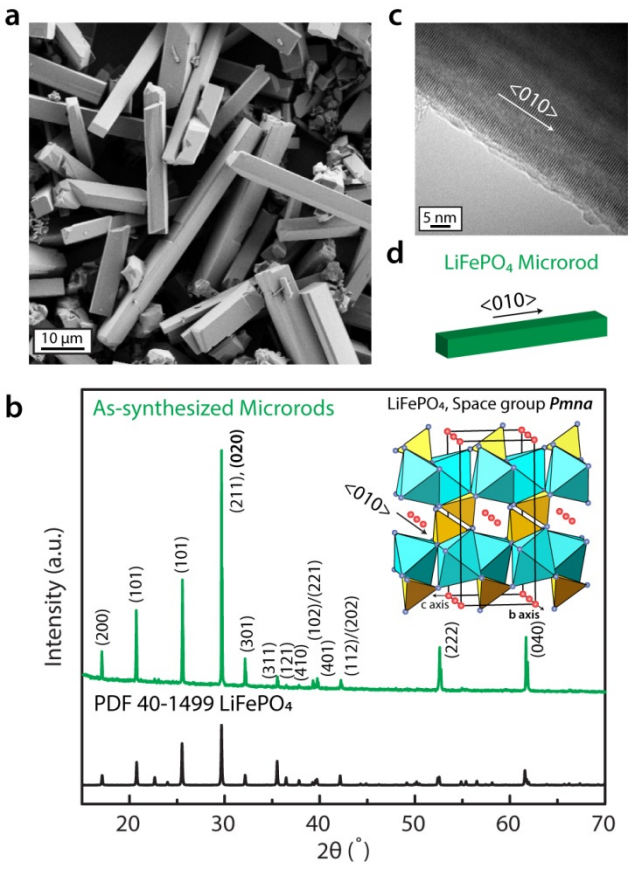

Figure A7.1 | Structural characterizations of the synthesized $LiFePO_4$ microrods. a. SEM image of the microrod; **b.** PXRD pattern of the microrods in comparison with the standard PDF card. Inset is the crystal structure of $LiFePO_4$, showing that the lithium-ion channels are located along the <010> direction; **c.** HRTEM image of a $LiFePO_4$ microrod, showing the growth direction is <010>; **d.** Schematic illustration of a $LiFePO_4$ microrod and its long-axis direction;

The electrochemical delithiation of the $LiFePO_4$ microrods was visualized using *operando* hard X-ray spectro-imaging. Before the delithiation experiment, we first took a cyclic voltammogram (CV, **Figure A7.2**) to confirm that the electrode was functioning normally. A pair of redox peaks that can be related to Fe^{2+} oxidation and Fe^{3+} reduction was observed. Compared with CV profiles taken on $LiFePO_4$ nanoparticles, the current density is smaller. This is expected. Because of the large size of the $LiFePO_4$ microrods, diffusion-limited condition was easily reached, which limited the current density. We also observed that the peak current density increased (marked by red arrows) as the cycle number increased, suggesting that increasing amount of electrode material participated in the electrochemical reaction.

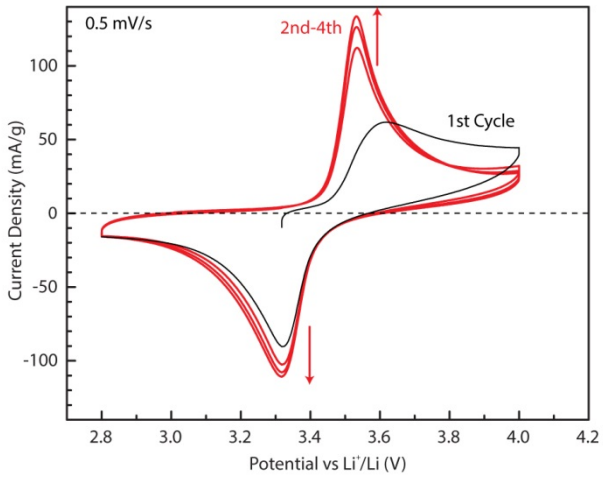

Figure A7.2 | Cyclic voltammogram of an *in situ* $LiFePO_4$ electrode. The scan rate is 0.5 mV s^{-1}. Four cycles of data were recorded.

The $LiFePO_4$ microrods were delithiated by holding a constant voltage at 4.0 V vs *E* (Li^+/Li). We took series TXM images in two different areas of the electrode over the course of delithiation (Figure A7.3a). The chemical phase maps (Figure A7.3b) were constructed from the TMM images using a previously established method. The spatial distribution of red ($FePO_4$) and green ($LiFePO_4$) pixels indicates the progression of electrochemical delithiation reaction. It is clear that the reaction is not uniform. Smaller particles reacted faster than the larger ones (see FOV 2 in Figure A7.3b). We also observed that the delithiation initiates from the end of the microrods and propagates preferentially along the axial direction (<010> direction). In both microrods that we examined, the reaction only occurred on one end, which is likely due to lack of electrical contact on the other end.

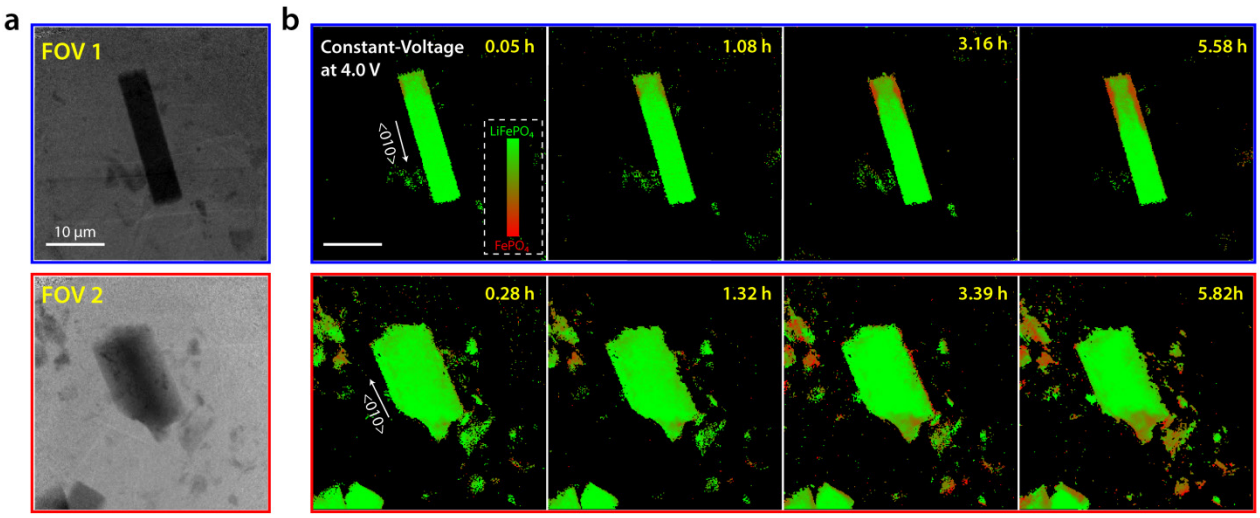

Figure A7.3 | Visualization of electrochemical delithiation of the $LiFePO_4$ microrods. a. TXM images of the two study area; **b.** Two series of chemical phase maps showing the progressing of the electrochemical delithiation.

A7.4 References

1. Padhi, A. K., Nanjundaswamy, K. S., Goodenough, J. B., Phospho-olivines as Positive-Electrode Materials for Rechargeable Lithium Batteries. *J. Electrochem. Soc.* **144,** 1188-1194 (1997).

2. Goodenough, J. B., Kim, Y., Challenges for Rechargeable Li Batteries. *Chem. Mater.* **22,** 587-603 (2009).

3. Chung, S.-Y., Bloking, J. T., Chiang, Y.-M., Electronically conductive phospho-olivines as lithium storage electrodes. *Nature Mater.* **1,** 123-128 (2002).

4. Delacourt, C., Poizot, P., Tarascon, J.-M., Masquelier, C., The existence of a temperature-driven solid solution in Li_xFePO_4 for $0 < x < 1$. *Nature Mater.* **4,** 254-260 (2005).

5. Yamada, A., et al., Room-temperature miscibility gap in Li_xFePO_4. *Nature Mater.* **5,** 357-360 (2006).

6. Delmas, C., et al., Lithium deintercalation in $LiFePO_4$ nanoparticles via a domino-cascade model. *Nature Mater.* **7,** 665-671 (2008).

7. Malik, R., Zhou, F., Ceder, G., Kinetics of non-equilibrium lithium incorporation in $LiFePO_4$. *Nature Mater.* **10,** 587-590 (2011).

8. Chueh, W. C., et al., Intercalation Pathway in Many-Particle $LiFePO_4$ Electrode Revealed by Nanoscale State-of-Charge Mapping. *Nano Lett.* **13,** 866-872 (2013).

9. Li, Y., et al., Current-induced transition from particle-by-particle to concurrent intercalation in phase-separating battery electrodes. *Nat Mater* **13,** 1149-1156 (2014).

10. Li, Y., et al., Dichotomy in the Lithiation Pathway of Ellipsoidal and Platelet $LiFePO_4$ Particles Revealed through Nanoscale Operando State-of-Charge Imaging. *Adv. Funct. Mater.* **25,** 3677-3687 (2015).

11. Ohmer, N., et al., Phase evolution in single-crystalline LiFePO4 followed by in situ scanning X-ray microscopy of a micrometre-sized battery. *Nat. Commun.* **6,** (2015).

12. Liu, H., et al., Capturing metastable structures during high-rate cycling of $LiFePO_4$ nanoparticle electrodes. *Science* **344,** (2014).

13. Badi, S.-P., et al., Direct synthesis of nanocrystalline $Li_{0.90}FePO_4$: observation of phase segregation of anti-site defects on delithiation. *J. Mater. Chem.* **21,** 10085-10093 (2011).

14. Laffont, L., et al., Study of the $LiFePO_4/FePO_4$ Two-Phase System by High-Resolution Electron Energy Loss Spectroscopy. *Chem. Mater.* **18,** 5520-5529 (2006).

15. Nishimura, S.-i., et al., Experimental visualization of lithium diffusion in Li_xFePO_4. *Nature Mater.* **7,** 707-711 (2008).

16. Morgan, D., Van der Ven, A., Ceder, G., Li Conductivity in $Lix MPO_4$ $(M = Mn, Fe, Co, Ni)$ Olivine Materials. *Electrochem. Solid-State Lett.* **7,** A30-A32 (2004).

17. Deb, A., Bergmann, U., Cramer, S. P., Cairns, E. J., Structural investigations of $LiFePO_4$ electrodes and in situ studies by Fe X-ray absorption spectroscopy. *Electrochim. Acta.* **50,** 5200-5207 (2005).

18. Niu, J., et al., In Situ Observation of Random Solid Solution Zone in $LiFePO_4$ Electrode. *Nano Lett.* **14,** 4005-4010 (2014).

19. Zhu, Y., et al., In Situ Atomic-Scale Imaging of Phase Boundary Migration in $FePO_4$ Microparticles During Electrochemical Lithiation. *Adv. Mater.* **25,** 5461-5466 (2013).

20. Li, L., et al., Visualization of electrochemically driven solid-state phase transformations using operando hard X-ray spectro-imaging. *Nat. Commun.* **6,** 6883 (2015).

21. Wang, J., Chen-Wiegart, Y.-c. K., Wang, J., In operando tracking phase transformation evolution of lithium iron phosphate with hard X-ray microscopy. *Nature Commun.* **5,** 4570 (2014).

22. Yu, Y.-S., et al., Nonequilibrium Pathways during Electrochemical Phase Transformations in Single Crystals Revealed by Dynamic Chemical Imaging at Nanoscale Resolution. *Adv. Energy Mater.* **5,** 1402040 (2014).

23. Yang, S., Zavalij, P. Y., Stanley Whittingham, M., Hydrothermal synthesis of lithium iron phosphate cathodes. *Electrochem. Commun.* **3,** 505-508 (2001).

24. Zhao, Y., Peng, L., Liu, B., Yu, G., Single-Crystalline $LiFePO_4$ Nanosheets for High-Rate Li-Ion Batteries. *Nano Lett.* **14,** 2849-2853 (2014).

25. Ellis, B., Kan, W. H., Makahnouk, W. R. M., Nazar, L. F., Synthesis of nanocrystals and morphology control of hydrothermally prepared $LiFePO_4$. *Journal of Materials Chemistry* **17,** 3248-3254 (2007).

26. Nan, C., et al., Solvothermal synthesis of lithium iron phosphate nanoplates. *Journal of Materials Chemistry* **21,** 9994-9996 (2011).

27. Fisher, C. A. J., Islam, M. S., Surface structures and crystal morphologies of $LiFePO_4$: relevance to electrochemical behaviour. *Journal of Materials Chemistry* **18,** 1209-1215 (2008).

28. Wang, L., Zhou, F., Meng, Y. S., Ceder, G., First-principles study of surface properties of $LiFePO_4$: Surface energy, structure, Wulff shape, and surface redox potential. *Phys. Rev. B* **76,** 165435 (2007).